Generation of Millimetre Waves from a Pseudospark Discharge Electron Beam

David Bowes

(B.Sc. Hons., University of Strathclyde, UK)

(M.Sc., University of Strathclyde, UK)

SUPA Department of Physics

University of Strathclyde

Submitted for the Degree of Ph.D.

November 2013

Contents

Acknowledgements

Firstly, I would like to thank my supervisors Dr. Adrian Cross and Dr. Huabi Yin for lending me their time, patience and knowledge throughout these past few years. This work would not exist if not for their assistance, and for that I offer my deepest thanks. I also wish to offer my sincere gratitude to EPSRC for their generous funding of this work, and Richard Wylde at Thomas Keating Ltd. for his considerable technical expertise in the manufacture of a 200 GHz BWO.

I would also like to acknowledge the contributions of the members of the Atoms, Beams and Plasmas group as a whole, in particular Dr. Wenlong He, for his assistance in every aspect of this work; Dr. Kevin Ronald and Prof. Alan Phelps, for their not inconsiderable knowledge and guidance; Dr. Liang Zhang, for his considerable expertise and assistance with the MATLAB-derived dispersion diagrams; and Dr. Craig Robertson and David Barclay, for their technical skill in constructing the components needed, often at the shortest of notice. I would also like to extend my thanks to my fellow Ph.D. students Kathleen Matheson, David Constable and Dr. Michael McStravick for showing that it *is* possible to make it through a research degree alive.

I thank my friends for their contributions to my continuing sanity, the staff at Rock-A-Rolla Magazine for the welcome distractions, the thousand-or-so bands who have soundtracked my degree, Linda Bowes for her care and constant support and, most of all, my wonderful partner Emma Herd for her love, patience and none-too-subtle prompting to write this thesis. Finally, I offer heartfelt gratitude to my family who can’t be here to enjoy this with me – my mother, my uncle and my gran. I would never have made it this far without all of you.

Selah.

Abstract

A backward wave oscillator (BWO) powered by a 4-gap pseudospark (PS) discharge-generated electron beam has been designed, modelled and constructed, and has been found to generate 2.7 W of RF power at a frequency of 199 GHz. This work presents numerical simulations and experimental results of this work, as well as the techniques, apparatus and diagnostics involved in the manufacture and testing of this device. The physics underlying both the BWO and the PS discharge, a low-pressure plasma phenomenon of high peak current, fast rise time and capable of generating a high quality, high brightness and high current density self-focussing electron beam, will be examined.

Also two other devices will be explored: a BWO operating at 67 GHz and a multi-cavity klystron, a form of linear beam amplifier, operating at 94 GHz. The operating and bunching mechanisms of the klystron shall be likewise explored, along with the steps taken for the physical construction of such a miniscule and technically demanding device.

A detailed exploration of the PS electron beam has been undertaken, with particular focus on the successful generation of electron beams of sub-millimetre radii. A PS discharge has also been applied for the generation of electron beams, successfully resolving a sub-mm diameter object and generating X-ray photons with energies of 15.83 keV when a 46 kV electron beam was directed towards a molybdenum target/witness plate. This is a step towards the development of a pseudospark-based small-point X-ray imaging source.

Pressure Conversion Table

To▶ / From ▼	psi	mbar	bar	atm	Pa	kPa	MPa	mmH_2O	$in.H_2O$	mmHg	in.Hg	kg/cm^2
psi	1	68.95	0.0689	0.0681	6895	6.895	0.006895	703.8	27.71	51.715	2.036	0.0704
mbar	0.0145	1	0.001	0.000967	100	0.100	0.0001	10.21	0.402	0.75	0.0295	0.00102
bar	14.504	1000	1	0.987	100000	100	0.1	10210	401.9	750.1	29.53	1.02
atm	14.7	1013.25	1.01325	1	101325	101.325	0.1013	10343	407.2	760.0	29.92	1.033
Pa	0.000145	0.01	0.00001	0.00001	1	0.001	0.000001	0.102	0.00402	0.0075	0.000295	0.00001
kPa	0.14504	10.0	0.01	0.00987	1000	1	0.001	102.07	4.019	7.5	0.295	0.0102
MPa	145.04	10000	10	9.87	1000000	1000	1	101971.6	4014.6	7500.6	295.3	10.2
mmH2O	0.001421	0.098	0.000098	0.000097	9.8	0.0098	0.0000098	1	0.0394	0.0735	0.00289	0.0001
in.H2O	0.0361	2.488	0.002488	0.00246	248.8	0.2488	0.00025	25.4	1	1.866	0.0735	0.00254
mmHg	0.01934	1.333	0.001333	0.001316	133.3	0.1333	0.00013	13.61	0.536	1	0.0394	0.00136
in.Hg	0.4912	33.86	0.03386	0.03342	3386	3.386	0.00386	345.7	13.61	25.4	1	0.0345
kg/cm^2	14.22	980.7	0.9807	0.968	98067	98.067	0.0981	10010	394.1	735.6	28.96	1

* Courtesy of Pascal Industries.

List of Figures

Chapter 1:

Aims & Background

1.1 Introduction

The aims of this work contained within this thesis are threefold:

1. To explore the capabilities of the pseudospark as an electron beam source for high frequency generation, particularly in regards current and propagation abilities with small-diameter beams (<1mm). Beam sizes shall be reduced through the use of collimating structures and examined via beam diagnostic techniques, both new and improved.
2. To design millimetre-wave devices suitable for operation with the pseudospark discharge, and to model and optimise their performance through the use of any suitable codes. In this case, the most suitable codes for use are MAGIC, a finite-difference time-domain particle-in-cell (FDTD PiC) code for simulation of beam-wave interactions and CST Microwave Studio for studies of microwave propagation. The design of the structures will include all aspects involved in device operation, i.e. power coupling, vacuum integrity and compatibility with existing systems.
3. To test and evaluate these designed systems with pseudospark-derived electron beams using available diagnostics and to compare experimental performance with that predicted by simulation, particularly with respect to output power and operational frequency, as well as examining the stability and repeatability of such performance. From this, it will be ascertained whether it is possible to scale such a system to higher frequencies.

From these goals, the suitability of the pseudospark discharge for frequency generation into the sub-millimetre wave range will be evaluated.

1.2 Overview of mm-Wave Sources

The millimetre-wave portion of the electromagnetic spectrum (30 – 300 GHz, corresponding to wavelengths of 10 to 1 mm) has grown in importance in the past decade with increased applications becoming apparent. The most frequently used frequency bands are becoming saturated with an ever-increasing demand for communications, radar and remote sensing applications. In consequence there has

been, in recent years, research into new sources to generate electromagnetic power in the relatively underused higher frequency bands in the 100s of GHz range, particularly solid state devices and vacuum electronic devices (VEDs). Complementary Metal-oxide Structure (CMOS) amplifiers have recently begun to catch up with VEDs, with researchers at National Chiao Tung University in Taiwan having developed a 40-nm digital bulk CMOS amplifier exhibiting 140 mW of power at 213.5 GHz, with an estimated 3-dB bandwidth of 13 GHz [1]. While this is impressive and outstrips many solid-state devices, where powers are typically limited to 10s of mW for InP Gunn devices operating at similar frequencies [2], it nonetheless falls short of figures achieved by many VEDs.

Vacuum tubes have been utilised for the generation of mm-wave frequency generation for decades and gyrotrons are one of the most frequently used, and powerful, of mm-wave sources. They operate by bunching free electrons within a strong magnetic field and have been shown to generate kWs of power in the mm-wave range, a 220 GHz device operating in the TE_{03} mode using an 8T pulsed magnet at the Terahertz Research Center, University of Electronic Science and Technology of China has achieved 11.5 kW with an efficiency of 12.8% [3]. The Research Centre for Development of the Far-Infrared Region in Fukui, Japan have pushed frequency capabilities, with a 388 GHz gyrotron achieving power of 62 kW [4], while also of note is the current work being undertaken to develop a 4 MW, 170 GHz coaxial cavity gyrotron for nuclear fusion projects such as ITER, which will push the power capabilities of gyrotrons even further [5]. Currently, the highest powers achieved at this frequency were by the European Gyrotron Consortium (EGYC), who developed a coaxial cavity gyrotron delivering 2.2 MW of power with 30% output efficiency [6].

Backward wave oscillators (BWOs) are linear beam tubes within which an electron beam is directed through a slow-wave structure, such as a folded or rippled-wall waveguide, with interactions between the slow space-charge wave of the electron

beam and the backwards eigenwave of the slow-wave structure supplying energy to an electromagnetic wave which travels backward along the structure. They are particularly well-adapted to high-frequency generation and commercially-available devices can generate radiation at up to 1.5 THz, though at sub-μW power levels, while 200 GHz devices operate with 50 mW output power [7]. Variations on the BWO, such as the clinotron, where a tilted beam is used over the slow-wave structure, and the orotron, which utilises two mirrors with the SWS to form a Fabry-Pérot cavity, have both outperformed traditional BWOs, with a 300 GHz clinotron generating 1 kW of pulsed power [8] while the Institute of Applied Physics of the Russian Academy of Sciences have produced mm-and-sub-mm-wave orotrons, with 180 GHz operation delivering 1 W of power for a current of 200 mA and a pulse duration of 4-10 ms [9].

Closely related to the BWO, the travelling wave tube (TWT) also utilises a slow wave structure in conjunction with an electron beam but amplifies a given signal rather than generating one from noise. There is currently a huge burst of interest in these devices, spurred on by improved manufacturing techniques such as LIGA (lithographie, galvanoformung, abformung, a technique which uses either x-rays or UV radiation to allow for the formation of minute, high aspect-ratio structures) as well as the DARPA HiFIVE (High frequency integrated vacuum electronics) program, which seeks to develop new generations of vacuum amplifiers at frequencies exceeding 100 GHz. Of note are Nothrop Grumman Electronic Systems, who have developed a 5-circuit folded-waveguide amplifier operating at 19.8 kV and 277 mA which has generated short pulses of 55.5 W at 214 GHz, with gain and efficiency of 28.5 dB and 2.3% respectively [10], and the Naval Research Laboratory in Washington, USA have similarly produced a serpentine waveguide amplifier, a 64-gap structure producing just over 60 W of power at 214.5 GHz using a beam voltage of 12 kV, with a total tunable range of 200 GHz to 240 GHz [11].

Along with TWTs, klystrons are one of the two main linear beam families of vacuum tubes and operate by using an RF signal to velocity-modulate an electron beam at discrete points, inducing longitudinal bunching in the beam and thus amplification at the RF frequency. They were one of the earliest vacuum tubes to be manufactured and while they typically exhibit high power and efficiency, the difficulties in manufacturing small-dimension interaction structures have seen them fall out of favour for high-frequency operation. However, klystrons operating as multipliers, where the resonant frequency of the input cavity is tuned lower in comparison to that of the output cavity to allow for extraction of higher multiples of the input frequency, have recently attracted renewed interest. Variations on klystrons, such as the reflex klystron oscillator and the extended interaction klystron (EIK) have become more prevalent at these frequencies, however. Communications & Power Industries, Ltd. have produced a range of EIKs at 220 GHz for several years, with pulsed EIKs delivering 100 W of peak power with 5% duty cycles and CW devices delivering 9W of power, while their reflex klystrons deliver 1 W of CW power and 50 W pulsed at the same frequency of 220GHz [12]. At lower frequencies, these powers may be several orders of magnitude greater.

Magnetrons are devices which use magnetic fields interacting with electron beams to induce high-frequency radiation within cylindrical cavities and research at the Institute of Radio Astronomy of the National Academy of Science of Ukraine has led to the production of a several spatial-harmonic magnetrons operating at, or near, 210 GHz with a peak pulsed power of 1.4 kW with a 0.95 T magnetic field, anode voltage of 15 kV and beam current of 15 A. The pulse duration was of 50 ns length, with a duty factor of 0.01% [13].

There are numerous other sources of mm-wave radiation, most notably free electron lasers (FELs) and relativistic beamline sources, with both capable of high power generation at frequencies stretching into the terahertz regime, though given their use predominately being focused at high frequencies, these may be discounted from

discussion here due to the need to use high energy (hundreds of keV) electron beams and the large size of such systems. A useful review of their capabilities has been given by Booske, et al [14].

While each of the above devices have their distinct limitations: gyrotrons require extremely high magnetic fields, BWOs and TWTs are restricted by manufacturing concerns, as are klystrons, which also suffer from breakdown effects at high voltages; magnetrons, meanwhile, may be difficult to properly tune. Many of these issues are overcome with careful design but one constant issue is that of the free electron sources for the devices, which must typically deliver higher beam current densities in order to deliver suitable operation with small beam diameters.

This work seeks to further develop a relatively new electron beam source for vacuum tubes, the pseudospark discharge. Pseudosparks are low-pressure discharges which utilise a distinctive hollow-cathode structure to generate extremely fast rise times [15], while simultaneously generating high-quality electron beams of high brightness ($10^{11\text{-}12}$ $Am^{-2}rad^{-2}$), high current density (~10^4 Am^{-2}) and low emittance due to the space charge neutralisation of the electron beam in a background plasma [16]. These beams have been shown to be scalable to smaller dimensions with little effect on current density and as they propagate, an ion channel is formed which acts to self-focus the electrons, eliminating the need for a guiding magnetic field. These features combined make the pseudospark an excellent tool for the generation of mm-waves.

The BWO has been deemed an appropriate device for gauging the suitability of the pseudospark for mm-wave generation due to its overall robustness, while the lack of BWOs in this frequency range offering more than 10s of mW of power makes it an attractive device to investigate. A 200 GHz BWO using a pseudospark electron beam source is therefore the primary focus of this work, although two other devices shall also be included: an experimental investigation of a W-band BWO operating at 67

GHz, and the design and cold testing of a three-cavity klystron with a centre operating frequency of 94 GHz. Through this work, the suitability of the pseudospark for higher-frequency generation into the THz regime will be evaluated.

1.3 Pseudospark Applications

Since the pseudospark's genesis, its primary application has been as a high-current switching device. Known by other names, such as the cold cathode thyratron and the backlit thyratron (a term used when optically triggered, rather than electrically), its performance as a high-power switch served to outstrip many of the alternatives available. Early switches demonstrated high performance in peak current, rate of current rise, efficiency, switching precision, recovery time and current reversal. Time delays of <40 ns and sub-ns jitter were possible and, due to the cold cathode operation, were also capable of long lifetimes [17]. Such devices are still in use today.

The pseudospark beam also has applications in some X-ray imaging capacity, due to its ability to produce a short-duration soft X-ray flash. Investigated by C.S. Wong in 1989 [18] using a hollow cathode impacting a focused electron beam onto a flat anode surface, X-rays of up to several kW in power were observed. The X-ray spectrum being emitted corresponded to the characteristic line emission of the anode material, which was interchangeable (copper, aluminium, tungsten and titanium were all tested), and using a copper anode with a 20 kV charging voltage, an average X-ray dosage of 18 ± 0.4 mGy was produced.

Perhaps the most attractive application for pseudospark cathodes is as a source of high-energy electron beams. Due to the properties described above there are numerous possible commercial applications, the most viable of which is in material processing (e.g. sputtering, electron beam drilling and the production of thin films) [19]. Additionally, the beam shows great potential as a source of electrons in some millimetre-wave generation devices and processes due to the ability to generate high

current density electron beams which can be propagated through small diameter structures without the need to apply a strong guiding magnetic field.

1.4 Atoms, Beams and Plasmas Group Research

The Atoms, Beams and Plasmas group at the University of Strathclyde has always had a strong drive towards research in beam-wave interactions and free-electron physics with attractive industrial potential, either in terms of high operating efficiencies, high attained power or frequency of operation. Megawatt-level radiation at frequencies ranging from 1-220 GHz has been obtained via investigations of the CRM (Cyclotron Resonance Maser) instability, FELs (Free Electron Lasers), gyrotrons [20] and loaded waveguides while the demonstration of a saturated FEL oscillator in 1996 spearheaded further research into high gain FEL amplifiers [21]. Research into CARM (Cyclotron Auto-Resonance Maser) instabilities at the second harmonic were the first of their kind [22], as well as being the first to demonstrate a novel broadband gyrotron amplifier possessing high output power and efficiency [23]. The group has also carried out extensive and invaluable research on AKR (Auroral Kilometric Radiation) phenomena [24], 1D and 2D Bragg reflectors [25] and FEM processes (Cherenkov and bremsstrahlung).

The group has also undertaken significant studies in the fields of cathodes and beam formation physics, documenting the first use of cold field-enhanced emission in high-power microwave devices [26], as well as investigating the emission of electrons from velvet surfaces in Pierce configurations and explosive emission of electrons in coaxial diodes [27].

1.5 Summary of Pseudospark Work at the University of Strathclyde

The University of Strathclyde's Atoms, Beams and Plasmas group has over fifteen years of experience in working with pseudospark discharges. H. Yin, whose

expertise has been invaluable in assisting with, and contributing to, this work, first started pseudospark research at Strathclyde in 1994, presenting her PhD thesis work on the topic of Pseudospark Discharge and Cherenkov Maser Experiments in 1998 [28]. Much of the work conducted was on single-gap pseudospark discharges using an experimental setup very similar to the one described in Chapter 4, varying gas, gas pressure, gap separation, cathode cavity depth, external capacitance, aperture diameter and applied voltage to form a rigorous deconstruction of the pseudospark discharge model. Beam performance was also studied, yielding 100 amps of current at an applied voltage of 10 kV [29].

Aside from the extensive work investigating single-gap discharges, much has also been done on multiple-gap pseudospark discharges, using alternating layers of Perspex insulators and stainless steel inter-electrodes between the cathode and anode. For an 8-gap pseudospark system, the measured beam could be seen to comprise a high-energy, low-current section, where the voltage was ~70 kV and current ~40 A, followed by a low-energy, high-current section of V ≈ 20 kV, I ≈ 350 A [30]. The high-energy phase is the one of most benefit in high-power RF applications.

The beam from a pseudospark discharge was later used as the electron beam source for a Cherenkov maser, a slow-wave RF amplifier which uses a dielectrically-loaded resonator to generate amplified radiation. Using a 70-80 kV, 10 A beam, generated by a 3-gap pseudospark discharge and fed through a 60 cm-long alumina-lined waveguide, an output power of 2 kW was generated in the frequency range 25.5-28.6 GHz, corresponding to a device gain of 29 dB [31].

In conjunction with this research, post-acceleration experiments were also carried out on the produced beam to compensate for the lower energy present during the latter high-current phase of the discharge process. The aforementioned 3-gap configuration was adapted to include an acceleration gap 30 mm downstream of the anode, driven

by a 40 kV, 125 ns voltage pulse, and then measured by a Rogowski coil situated 120 mm downstream of the gap. By correctly synchronising the electron beam and the accelerating pulse, a 100 A, 40 kV pulse was measured at the Rogowski coil without the aid of a guiding magnetic field, compared to a less substantial 200 V before acceleration [32].

Chapter 2:

Theory

2.1 Introduction

In this chapter the basics of electron beams and their production will be covered, up to and including the use of the pseudospark (PS) discharge as a generator of electron beams. In order to adequately explain the physical processes involved in the PS discharge, an analysis of gas discharges over various pressure regimes will be included. Methods of evaluating the quality of electron beams are reviewed, and the suitability of PS-generated beams for microwave generation is examined. This chapter also explains the operating principles behind the two millimetre-wave devices examined in this work, the klystron and the backward-wave oscillator (BWO), including a brief history of their discovery, their amplification mechanics and methods which may be employed to gauge their operating frequencies, power handling and expected output.

2.2 Electron Beams and Cathodes

The point of origin for many electron beams is a cathode, an electrode which allows the flow of electrons out of itself although, in the case of vacuum devices, it is more appropriate to replace the term electron with free electron. Initially, the term ‘cathode’ was used in Faraday’s descriptions of his early explorations of electrolysis in the 1830’s [33].

The deciding factor in choosing a material for an electrode is its conductivity; for this reason, metals are the materials most frequently used due to the phenomena of *metallic bonding*, involving the sharing of free and mobile valence electrons by metal atom nuclei. Metal cations are fixed in a solid network and immersed in a sea of freely moving electrons. The metal atoms are bound together by the interaction between the negatively charged electrons and positively charged metal ions and, given the freedom of the electrons, such a formation gives rise to high conductivity [34].

2.2.1 Electron Emission

Electron emission describes the process in which electrons may leave a material's surface and escape into space. This may be induced by a variety of methods, such as the application of heat (thermionic emission), light (photoelectric emission), a strong electric field (high-field emission) or particle bombardment (secondary emission) [35], with cathodes operating under any of these principles being known as *solid cathodes*.

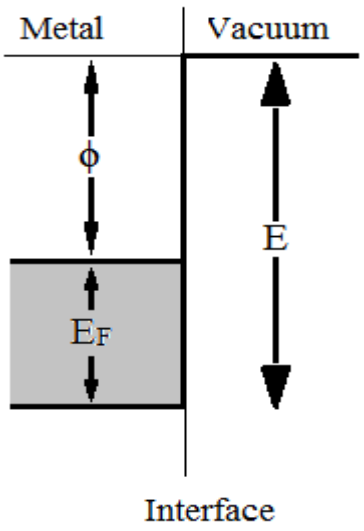

Figure 2.1: Potential barrier at a solid with the total energy, *E*, the electron energy in the solid, E_F, and the work function, ϕ.

The basis of electron emission is the free electron model, where electrons can be said to exist in a number of discrete energy levels, or states. Electrons with the highest energies are known as *valence electrons* and these are the most likely to be emitted. However, they do not have sufficient energy to escape on their own. For emission to occur the valence electrons must overcome a potential barrier which exists at the surface of the material, the energy required to surmount this being known as the *work function*, ϕ (figure 2.1). This is measured in electron volts (eV) and varies depending on several factors including the material, surface condition, and applied films. This potential barrier is usually surmounted but it may on occasion be tunnelled through, as is the case with field emission. For escape to occur, the electron must gain the energy required to equal that of a free electron in the surrounding medium.

2.2.2 Thermionic Emission

Thermionic cathodes were likely the first types of cathode to be discovered and put into general use, with knowledge of thermal emission from metals being acquired as far back as 1880 by Thomas Edison [36] although no serious experimentation on the process was undertaken for several years. The result of Edison's later work on filament lamps led to the invention of the thermionic diode in 1884 [37]

Thermionic emission is a process in which electrons are given sufficient energy to escape a solid by increasing the electron temperature, the degree of the effect varying with the surface material. The current induced by thermionic emission may be estimated by considering the density of electron energy states and the probabilities of their occupation. As such, the electron energy distribution as a function of energy may be obtained by multiplying the density of states by the probability of occupation.

Only those electrons which possess energy greater than the Fermi energy may overcome the work function barrier and be emitted. The thermionic emission current density is given by the Richardson-Dushman equation [38]

$$J = A_0 T^2 e^{-\frac{e\phi}{kT}} \text{ A/m}^2 \tag{2.01}$$

where T is the temperature, ϕ is the work function, k is the Boltzmann constant, e is the electronic charge and A_0 is a constant, given as

$$A_0 = \frac{4\pi m_e e k^2}{h^3} = 1.2 \text{ x } 10^6 \text{ A/m}^2\text{deg}^2 \tag{2.02}$$

m_e being the electron mass and h being Planck's constant.

This indicates an exponential variation of current density with temperature and work function. Typically, temperatures are stabilised at around 1500 K due to high temperatures limiting the lifetime of a thermionic cathode. As such, it is necessary to

minimise the work function as much as possible. Given that the work function varies with the orientation of the crystal of a material, metals with open lattices are normally preferable. Barium is a good choice for this, with a work function of 2.52 - 2.7 eV, but it tends to evaporate rapidly at high temperatures thus necessitating the use of a dispenser cathode to replenish the barium cathode surface.

The above analysis does not take into account the effect of an electric field on the cathode. In practice, it is found that upon the application of an electric field E_{ext} to a thermionic emission surface, current emission will increase in a process known as the Schottky effect. This is due to the lowering of the work function by a factor of $e\Delta\phi$, where

$$\Delta\phi = \sqrt{\frac{eE_{ext}}{4\pi\epsilon_0}} \tag{2.03}$$

The emitted current density now becomes

$$J = J_0 e^{\sqrt{\frac{eE_{ext}}{4\pi\epsilon_0}}} \tag{2.04}$$

where J_0 is the current density as calculated via the Richardson-Dushman equation, often termed the zero field current density. This equation will generally hold for electric field strengths of lower than 10^8 Vm^{-1}, after which Fowler-Nordheim tunnelling will contribute heavily to the electron emission process. It may be noted that at low electric field levels, electron space charge effects may alter the effective current density due to the influence of electrons near the current emitter.

2.2.3 Field emission

When electric fields in the region of 10^8 – 10^{10} Vm^{-1} are applied, there is a noticeable rapid increase in electron emission from the emitter surface which occurs independent of cathode temperature. Known as field emission, the phenomenon was

initially observed in 1897 by R.W. Wood [39] but no analytical consideration was put into the topic until 1923 when W. Schottky investigated it further [40].

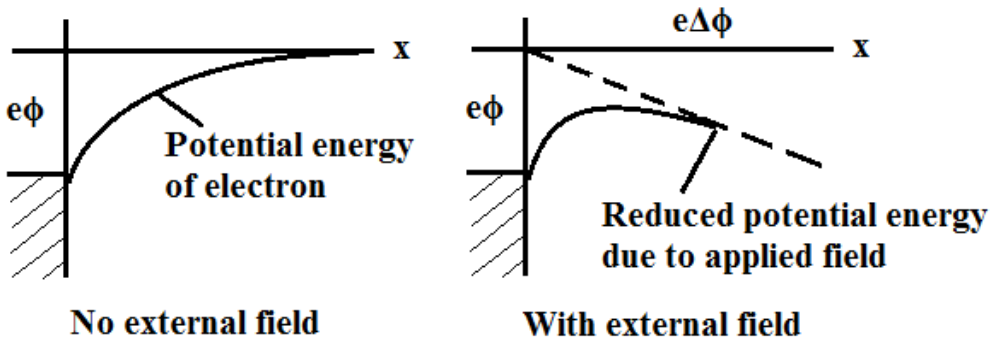

Figure 2.2: Illustration of the Schottky effect [38].

Figure 2.2 illustrates that when an electric field is applied there is a reduction of both work function and electron potential energy, known as the Schottky effect. With a sufficiently large field, the work function is reduced to the degree that it is no longer strictly necessary for an electron to possess the energy to surmount the work function barrier and it may tunnel through the reduced potential barrier (figure 2.3), a process which is derived from the quantum mechanical nature of electrons: this is what is known as Fowler-Nordheim tunnelling. The electric field which is required for tunnelling to occur may be approximated from the Heisenberg uncertainty principle to be [41]

$$E_{ext} = 2\left(\frac{2m_e}{(h/2\pi)^2}\right)\phi^{\frac{3}{2}} \tag{2.05}$$

The current density from a field emission device may be calculated by multiplying the tunnelling probability by the flux of electrons with a particular energy level and then integrating over all available incident electron energies. This is depicted in the Fowler-Nordheim equation, given as

$$J = AE^2 e^{-\frac{B_{cat}}{E_{cat}}} \tag{2.06}$$

where B_{cat} and E_{cat} are variables dependent on the cathode properties, with a weak variation with the electric field.

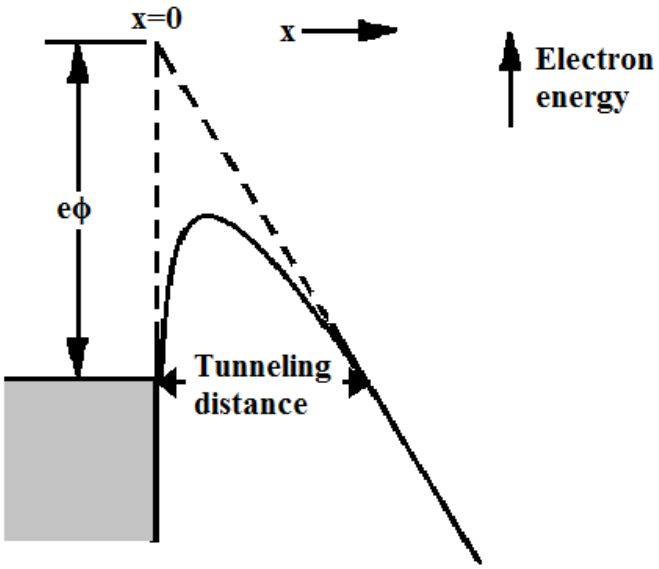

Figure 2.3: The presence of an extremely high electric field allows the possibility of quantum tunnelling [38].

In order to produce such high potentials, field emission structures are often comprised of arrays where emitters are shaped into very fine tips (tens of angstroms – microns radius of curvature) allowing the development of high fields at moderate potentials. With these fields, the potential barrier at the tip's surface is significantly narrowed and consequently the probability of electrons tunnelling into vacuum is increased [38].

2.2.4 Photoemission

Much as with field emission, the process of electron emission via the absorption of light can be envisioned as a quantum process, with devices which operate under such principles being based on Einstein's quantum theory of photoemission. This theory was further elaborated upon in 1958 in the Three-Step model for photoemission which describes the photoemitting process as being a three-stage one. Firstly, there is the optical absorption/photoexcitation stage which imparts electrons within the surface with the energy to leave the material. Following this is a transport stage,

where electrons travel through the material, giving the possibility of inelastic scattering through interactions with other electrons (common within metals) and, finally, the escape of the electron from the surface and into vacuum.

The photoemission current may be found from [42]

$$I(h\nu) = I_0(h\nu)[1 - R(h\nu)]\frac{\alpha_{PE}(h\nu)}{\alpha(h\nu) + \frac{1}{l(h\nu)}P_E(h\nu)} \tag{2.07}$$

where $I_0(h\nu)$ is the incident intensity of light with photon energy $h\nu$, $R(h\nu)$ is the light reflectivity, $\alpha(h\nu)$ the material's absorption coefficient, $\alpha_{PE}(h\nu)$ the absorption as it relates to electrons imparted with sufficient energy to escape, $P_E(h\nu)$ is the probability of the electrons reaching the surface having sufficient energy to escape and $l(h\nu)$ the scattering length of the electron. From analysis of this equation, it may be determined that if the absorption length L_a, given by $1/\alpha(h\nu)$, greatly exceeds the scattering length the photoemission will be very low, as is often the case with metals where the ratio of l_a to l tends to be extremely high, particularly where the incident radiation is in the high UV region. Meanwhile, the converse also holds true with photoemission being relatively high in situations where the ratio approaches unity, as is the case with some semiconductors.

Photocathodes are commonly used at low current densities in electro-optical devices, although devices which utilise high-intensity pulsed lasers allow for high power, high brightness electron beams. In addition, photocathodes have many advantages over thermionic cathodes; they are capable of operation at room temperature; the output electron beam may be modulated through the variation of the photon flux; they are capable of high current densities and; they possess a small transverse energy, allowing for high brightness beams. However, their continuing growth depends on the availability of high-power lasers, they are not suitable for long pulse-length generation and the photoemissive coatings required are typically sensitive to

poisoning, leading to clean vacuum of very low pressures (~10^{-10} Torr) being required.

2.2.5 Plasma Cathodes

Much of the original research on plasma electron emitters was performed by Y.E. Kreindel throughout the 1970s before eventually being presented in his work 'Plasma Electron Sources' in 1977 [43]. His research on the emission properties of low-temperature plasmas provided a foundation for later work on the control and stabilisation of plasma beams, as well as understanding the plasma emission process itself.

Plasma cathode electron guns, or plasma cathodes, use a pre-existing plasma as the basis of the production of a well-defined electron beam. Such systems contain two essential parts, namely a plasma generator, based on an electrical discharge, and some form of electron extraction method. They do not contain a hot filament, making them more reliable than thermionic cathodes, and can generate electron beams at higher pressures. They are also largely unaffected by back-streaming ions, a possible liability in some applications. Plasma cathode electron beams may be pulsed and possess current densities up to 100 Acm^{-2} [44].

These current densities are largely dependent on the properties of the plasma, namely the density and temperature, and on the extractor electric field distribution. As the extraction field is increased, so too does the plasma potential and, consequently, electron emission, although for electrons to be extracted and accelerated to the full beam energy, the increase in extractor potential should be greater than that of the plasma. Additionally, the emission surface should be significantly smaller (~ several %) than the total discharge electrode area, otherwise electrons will follow the distribution of the electric field and not be accelerated. It is possible to achieve high current densities due to a lowered potential barrier for emitted electrons due to the

applied acceleration voltage, while the potential barrier for electrons moving towards the anode increases to compensate.

Whilst simple planar systems have been in use for several decades, there has been a growth in more distinctive forms of plasma cathodes, such as those operating with hollow cathodes [45] and those based on arc discharges.

2.3 Gas discharges

For the understanding of plasma cathodes, and consequently pseudospark cathodes, it is necessary to understand the principles of gas discharges. Gas discharges occur when electricity is conducted through a gaseous medium by the movement of ions which have been produced by collisions between electrons and gas molecules. Within a system which consists of a gas, electrodes and a surrounding barrier, a current is carried by electrons in response to an applied electric field. There are a number of distinct discharge modes, and these can be broadly categorised as either self-sustaining or non-self-sustaining. In the case of non-self-sustaining discharges, the current ceases to be carried when the applied voltage is removed. These discharges are also known as 'dark' or, more commonly, *Townsend* discharges. In the case of self-sustaining discharges, the discharge undergoes *gas breakdown*low, arc, hollow cathode and pseudospark discharges are all self-sustaining.

Gas discharges may occur in a number of gases and over a wide range of pressures, ranging from ~10^{-5} Torr to ~760 Torr, and can carry currents between 10^{-6} and 10^{6} A. The exact point at which a discharge undergoes breakdown varies according to the type of gas being used, the pressure regime and the voltage being applied to the electrodes. In particular, the main factor is the current-voltage characteristic of the gas being used [46].

2.3.1 Non-Self-Sustaining Discharges

Non-self-sustaining discharges are so called due to the fact that in order to sustain current flow there must be a continuous applied voltage, in the absence of which the discharge ceases. If we consider any gas to contain a number of ions and electrons due to ultraviolet and cosmic radiation and radioactivity, then in a system with two electrodes we may expect emission of electrons from the same factors. Without an electric field, there is an equilibrium state achieved wherein the rate of generation of charged particles is counteracted by the recombination rate. By applying a small voltage (sufficient to produce a field strength E of ~1 Vcm^{-1}) then current will flow in the gas due to the pre-existing electrons and ions whilst barely upsetting the equilibrium state. The current density J is proportional to E. As E and J increase, the equilibrium is altered due to the number of positive ions reaching electrodes and being neutralised, resulting in an increased recombination coefficient and reducing the total charged particles within the gas and consequently reducing the rate of current increase with voltage [47].

It will eventually become the case that

$$J = de\frac{dn}{dt} \tag{2.08}$$

where dn/dt is the total rate of production of charged particles, e is the charge of an electron and d the anode cathode gap separation. The above state is known as the saturation current density, and is independent of both E and electron mobility. Current densities in these conditions are usually very small ($<10^{-9}$ Acm^{-2}) even when using a strong external radiation source and the voltage across the electrodes is in the order of 10 V, and this type of discharge is the primary cause of leakage in charged bodies as well as the initial state of many other gas discharges. It is also possible to produce a similar discharge through the use of a heated cathode to provide electrons, which would allow for a higher saturation current density.

When the voltage is further increased, eventually the current will begin to rise sharply, the rate of increase varying according to the gas pressure, but it is best to consider a low pressure case (~ few Torr) where there are several mean free paths between the electrodes. The rate will typically increase until the breakdown voltage V_B is reached (figure 2.4), normally in the order of 100s of volts although the precise value depends on the gas type and pressure, as well as the electrode separation, size and material. Between saturation and V_B the region is known as Townsend discharge and the peak current in this region is typically ~1 μA.

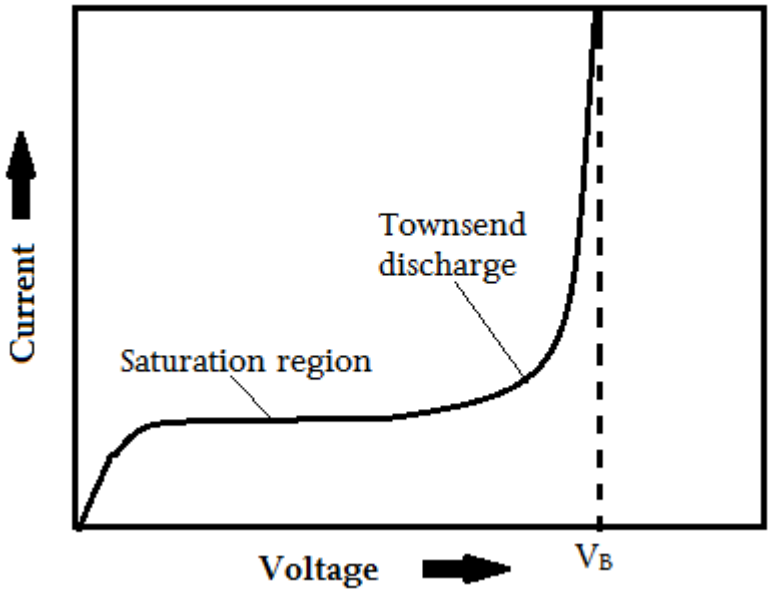

Figure 2.4: Townsend discharge characteristics.

In the low pressure region, it helps to assume the case of two electrodes with dimensions larger than their spacing where constant external radiation is incident only on the cathode to produce electrons. With increasing *E*, the electrons are further accelerated between collisions until their collisional energies are above the ionisation level. As such, some electrons ionise atoms during their traversal, producing ions and additional electrons which themselves may cause further ionisation, and so on. This effect may be quantified by Townsend's first ionisation coefficient α, defined as the number of ionising collisions made on average by an electron as it travels one centimetre between cathode and anode. From this it may be written that

$$dn = \alpha n dx \tag{2.09}$$

where dn is the rate of increase and dx the distance travelled. If α is taken to be independent of x, it may be integrated to

$$n = n_0 e^{\alpha x} \tag{2.10}$$

where n_0 is the number of electrons leaving the cathode per second. As such, the current in a tube of electrode spacing d is

$$I = n_0 e^{\alpha d} = I_0 e^{\alpha d} \tag{2.11}$$

where I_0 is the cathode electron current, dependent only on external radiation effects, and all electrons related to I_0 are known as primary electrons. The difference between I and I_0 is due to all ionising collisions caused by electrons within the gas, and can be significantly greater than I_0. In the case where there is no external source but rather photoionisation from the gas itself, the current is given as [47]

$$I = \frac{I_0(e^{\alpha d} - 1)}{\alpha d} \tag{2.12}$$

It is evident that the above description accounts only for α and d, neglecting gas conditions altogether. In order to effectively analyse this factor it is necessary to account for temperature and pressure separately and not simply density, due to the temperature theoretically affecting the possibility of ionisation. Nonetheless, the effect of heating is usually negligible and as such α can be deduced from the gas pressure p when the variations of the cross-sections for ionisation are known.

Taking the mean free path of an electron in the field direction as λ, the mean energy gained by an electron between collisions is $Ee\lambda$. α must depend on both this energy and the pressure, as well as the number of encounters per cm, therefore

$$\alpha = pf(Ee\lambda) \tag{2.13}$$

where *f* is an unknown function. It is reasonable to assume that the mean free path is inversely proportional to the pressure, therefore

$$\alpha = pf\left(\frac{Ee}{p}\right) or \frac{\alpha}{p} = \phi\left(\frac{E}{p}\right) \tag{2.14}$$

where both *f* and ϕ are functions similar in form to *f*. Townsend devised the latter equation from experiment due to α/p being determined from E/p, giving it the format

$$\frac{\alpha}{p} = Ae^{-Bp/E} \tag{2.15}$$

in which *A* and *B* are constants, variable according to the gas medium and electric field range [48]. There are several forms of Townsend's first ionisation coefficient but this generalised form is true in most cases.

The ratio of *I* to I_0 is known as the multiplication factor and within many devices there is a pressure where the multiplication will peak at constant voltage, meaning that α is also a maximum with respect to the pressure. This condition may be expressed as

$$0 = \frac{\partial \alpha}{\partial p} = p\phi\left(\frac{E}{p}\right)\left(-\frac{E}{p^2}\right) + \phi\left(\frac{E}{p}\right) \Rightarrow \frac{\partial \alpha}{\partial p} = \frac{E}{p}\phi'\left(\frac{E}{p}\right) \tag{2.16}$$

where the prime indicates differentiation with respect to E/p.

This all accounts for primary electron emission but in any system there is normally increased current flow at high values of *I* and *d*, usually attributable to secondary emission. At low voltages, emission of electrons by positive-ion bombardment of the cathode is a common occurrence for which Townsend introduced his second ionisation coefficient. This is applicable to other secondary effects as well, and can be applied to cathode emission as the cathode yield γ in electrons per incident ion. Now, the current may be expressed as [28]

$$I = I_0 \frac{e^{\alpha d}}{1 - \gamma(e^{\alpha d} - 1)} \tag{2.17}$$

where γ can be found from

$$\frac{n_+}{\gamma} = n_\alpha - (n_0 - n_+) \tag{2.18}$$

Here, n_+ is the electrons per second from the cathode due to secondary emission, and n_a the electrons per second from all sources arriving at the anode.

Aside from positive ion bombardment, the other secondary emission process common in Townsend discharges is photoelectric emission at the cathode due to photons produced by excited atoms. γ is variable depending on the gas being used, but its value is always less than 1, usually ~10^{-2}.

Figure 2.4 shows a rapid increase in current at the breakdown voltage, to the extent that the breakdown current theoretically becomes infinite. This could occur if the increasing voltage and field strength in the Townsend region affect γ and α as to induce this unstable condition and cause a rise in current which will be uncontrollable until an external limiter is introduced. In other words, this is the breakdown criterion, written as

$$\gamma e^{\alpha d} = \gamma + 1 \; or \; \gamma e^{\alpha d} = 1 \text{ since } \gamma \ll 1 \tag{2.19}$$

also known as the Townsend (or sparking) criterion. $\gamma e^{\alpha d}$ is the number of secondary electrons to be emitted from $e^{\alpha d}$ positive ions. At this point, a form of positive feedback takes over where each primary electron produces a secondary electron which can continue the process and as such has become independent of the external radiation source, assuming that the secondary electron yield is greater than unity and that secondary electrons are not recollected by the anode and thus can contribute to the discharge. At this point we may say that the discharge has become self-

sustaining. Additionally, at this point the gas becomes luminous and forms either an arc or glow discharge depending on the gas type and external circuitry.

By taking $V=Ed$ (as is the case in a uniform field), using $\gamma=\psi(E/p)$ and by varying equation 2.15, equation 2.19 may be written as

$$\psi\left(\frac{V_B}{pd}\right)e^{pd\phi\left(\frac{V_B}{pd}\right)}=1 \tag{2.20}$$

This is true only in the case of a fixed pd and fixed V_B, and as such it can be said that V_B depends only on the gas pressure and electrode spacing i.e.

$$V_B=f(pd) \tag{2.21}$$

which is also known as Paschen's law. This does not give a form for f or f', although it is possible to obtain theoretical forms which are limited in validity. It is notable that all combinations of gas and electrode material have a minimum breakdown potential, a minimum value of V_B, when plotted against pd which is usually in the order of several hundred volts. At low pressures ($pd<pd_{min}$), the breakdown will occur over the largest possible path and as such will require high voltages for breakdown to occur. In high pressure cases ($pd>pd_{min}$) the converse is true in that collisions occurring as an electron crosses the gap is greater than at the minimum, but the energy gained between collisions and the degree of ionisation are much lower and hence voltage must also be increased to allow breakdown.

2.3.2 Self-Sustaining Discharges

After breakdown, a self-sustaining discharge may take one of several forms. If the pressure is in the order of 1 Torr between DC electrodes, and the whole circuit is controllable via variable series resistance and voltage, a current-voltage characteristic such as the one depicted in figure 2.5 will result.

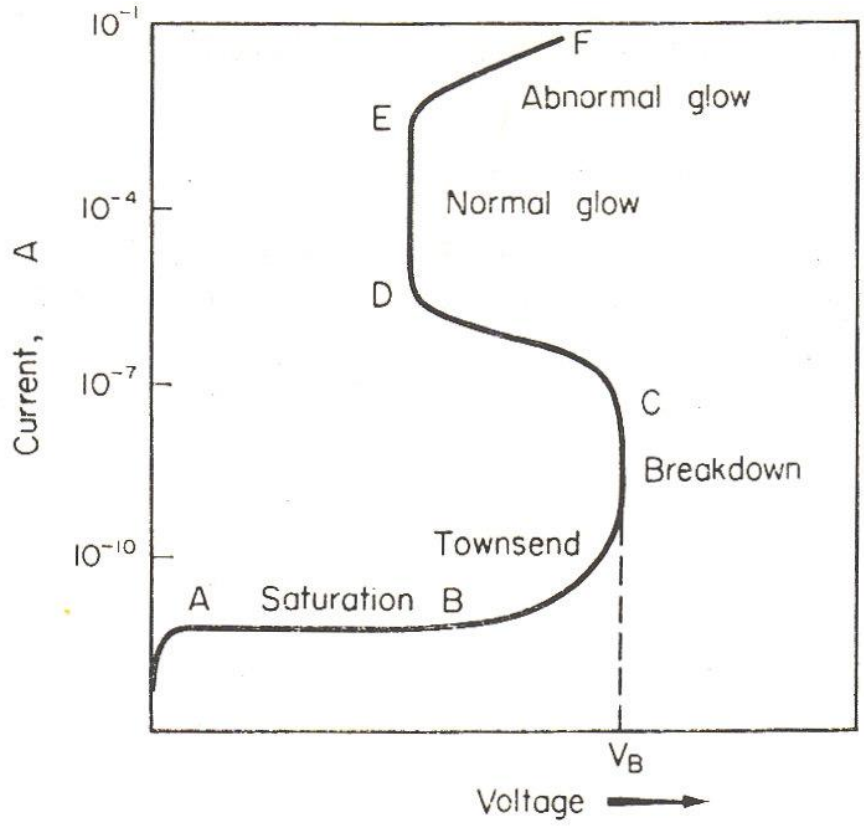

Figure 2.5: Current-voltage characteristics of a self-sustaining discharge.

The form which the discharge will take is determined by a combination of the gas and circuit conditions. If the pressure is relatively low (< 3 Torr) then a glow discharge will likely form, a type of moderate-current discharge which possesses a modest current (~1 μA-100 mA) whilst presenting a diffuse glow. Pressures nearer to atmospheric conditions combined with a low circuit resistance will cause the generation of an arc discharge, possessing a much more intense luminance than a glow discharge. At higher, atmospheric pressures within a varying *E* field, breakdown will cause the formation of a corona, slightly more akin to a glow discharge in appearance.

2.3.3 Glow Discharge

Glow discharges are one of the more common and well-known forms of plasma discharge and are also one of the simplest discharges to recreate experimentally, requiring only an evacuated tube and two electrodes (figure 2.6) [49].

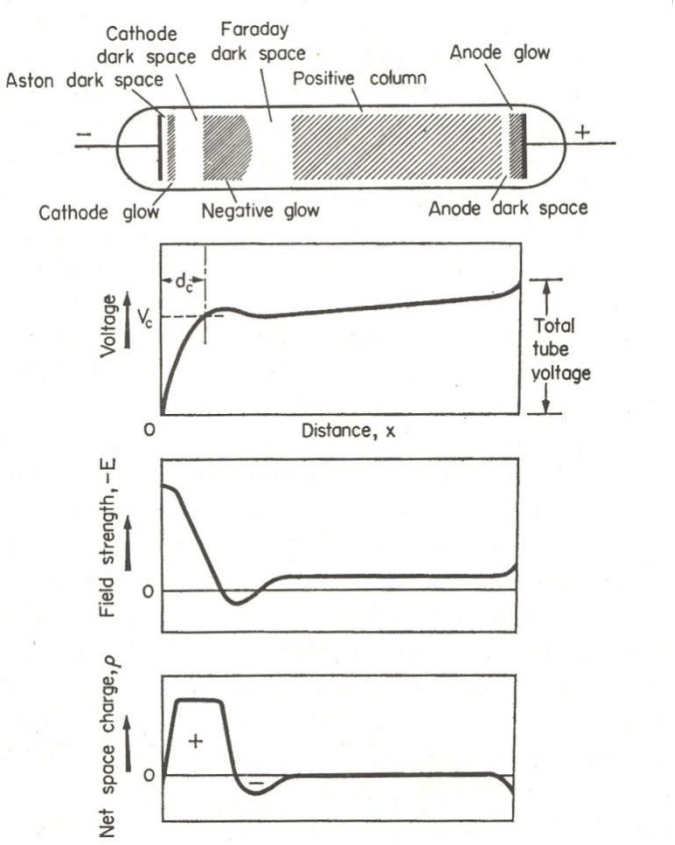

Figure 2.6: Form and characteristics of a glow discharge [49].

In such a system, a gas discharge may be initiated by increasing the external voltage until a luminous region begins to appear. In a 'normal' glow discharge the current density on the cathode will remain constant, with the glowing region spreading across the cathode surface with only a slight dip in voltage. If the current is raised further, beyond the point where the glow completely covers the cathode surface, then the current density will increase and the glow will move into the 'abnormal glow' region. This will initiate a steady rise in potential with current until an arc discharge begins, at which point the cathode will be sufficiently heated to begin to emit thermal

electrons. The potential existing between electrodes in a glow discharge is known as the maintaining potential, V_m.

A typical glow discharge at a pressure of ~1 Torr will appear as in figure 2.6, the length of the discharge comprising numerous regions which are named as shown. Slow ions drifting towards the cathode from the negative glow region, producing a region of positive space charge near the cathode which in turn produces a region of high electric field, coinciding with the sheath region of the cathode dark space. The strength of this field typically decreases linearly with distance from the cathode, reaching almost zero at the boundary of the cathode dark space and negative glow region. As ions enter the cathode dark space from the negative glow they are accelerated by the field and strike the cathode surface, producing secondary electrons, while metastable atoms and UV photons from the negative glow region also produce secondary electrons. The efficiency of electron production, γ, varies with the compositions of the gas and cathode, as well as with the energy of the electrons. It is this secondary production efficiency which determines the voltage necessary for current increase in the abnormal glow stage of the discharge. As the tube voltage increases, the voltage drop across the sheath region, or *cathode fall*, also increases, increasing the kinetic energy of accelerating electrons and thus releasing more secondary electrons. If the cathode fall is sufficiently large, sputtering may occur at the cathode surface, generating a thin surface glow directly in front of the cathode [50].

As the secondary electrons are emitted, they are accelerated away from the cathode and through the Aston dark space, where insufficient energy means that they cannot excite the gas. When they reach energies which correspond to the peaks of the excitation cross-sections of the background gas, some electrons will collide with gas atoms and produce the cathode glow layer. Due to the high electric field inducing rapid acceleration, the electrons rapidly gain the momentum and energy to surpass the maxima of the excitation cross-sections and, as such, the cathode glow layer is

relatively thin. At the boundary of the cathode dark space and negative glow regions, electrons reach terminal velocity and the electron energy distribution is found to contain a large amount of high energy electrons, with those electrons which have reached this point without suffering collisions possessing energies comparable to the cathode fall. Investigations have that the proportion of fast electrons at the boundary increases with the cathode fall, and with decreasing pressure [51] [52].

Beyond this boundary and into the field-free body of the negative glow region, typically the most luminous region of the discharge, the electron energies are diminished due to numerous inelastic collisions, while any secondary electrons move by diffusion due to the lack of an accelerating force in any one direction. The electrons take on an approximately beam-like form, with the energy distribution changing to favour lower energy electrons generated by ionising collisions as the distance from the boundary increases. It is these ionising collisions from fast-moving electrons which are instrumental in maintaining the discharge since ions generated by collisions involving slow-moving electrons are eventually lost, either by diffusion to the walls of the discharge tube, by collisions with the cathode face or by volume recombination with low-energy electrons in the negative glow. The current of positive ions and electrons lost to the tube is proportional not only to ion and electron densities but also to the circumference of the tube, while the tube current is directly related to the positive ion and electron densities and to the area of the tube. As such, the use of a large diameter tube is beneficial in the reduction of losses in the discharge [53]. While the discharge current within the cathode dark space was largely carried by fast-moving ions, discharge current here is carried by the fast moving electrons. Much of the negative glow's properties, as well as those of the cathode dark space, can be found in K. G. Emeleus' review of the subject [54].

The Faraday dark space is caused by electrons within the negative glow region being decelerated to the degree that they fall below the minimum threshold for excitation and begin to drift towards the anode, experiencing only elastic collisions in the

process. Because of the range in electron energies and the nature of collisions within the negative glow region, the boundary between the two regions is normally diffuse in appearance. As the slow electrons proceed they form a density gradient large enough to maintain electron flow towards the anode, despite the decelerating effect of the Faraday dark space's reversed electric field, although it necessary to introduce a longitudinal electric field for the electrons to reach the anode. The positive column achieves this with a constant low electric field along its length to compensate for charge losses. A charge sheath builds at the anode to repel ions and attract the slow electrons, producing a narrow anode glow, and the anode fall across the sheath is approximately equal to the ionisation potential of the background gas.

It may be found that the lengths of the various regions vary with pressure, with pressure extremes limiting the retention of the glow discharge characteristics. The existence of the dark regions is due to electrons being able to travel farther, on average, before striking a gas atom meaning that, if the pressure is sufficiently reduced, the cathode dark space will expand to fill the tube. At this point, most electrons can travel from cathode to anode in a straight line without collisions and, after being accelerated to high velocities by the applied voltage, the discharge is essentially behaving more and more like an electron beam. At pressures below 1 mTorr the supply of current cannot be maintained due to the drop in electron emission via positive-ion bombardment.

2.3.4 Arc Discharge

When pushing the input to higher currents using a lower resistance source, the glow discharge will become an arc, which is characterised by a higher current and significantly lower voltage (<50 V) than the glow discharge. The current density will markedly increase, producing an intensely luminous glow that acts to obscure the cathode region. At high pressures the arc possesses a dense core and flame-like outer regions. While the current varies along the discharge length, it is constant at the cathode and focused on a small cathode spot to which the current flows, although the position of this moves with time. The high current density is caused by a

combination of two processes, namely thermionic emission and field emission; thermionic, via a large bombardment of ions heating the cathode during the transition from glow to arc discharge; and field, or cold emission, from high fields present at various micro-peaks on the cathode surface. Thermionic arcs tend to have smaller current densities (~1000 Acm^{-2}), stationary cathode spots and sustainable glow-arc transitions, while cold-cathode arcs possess current densities of up to 10^6 Acm^{-2}, discontinuous transitions and moving beam spots. It is possible, however, for hybrids of these to exist with certain cathode materials or gases.

2.4 Pseudospark Discharge

Originally discovered in 1977 by Christiansen and Schultheiss, the pseudospark discharge operates under low pressures, in the region between the Paschen minimum and vacuum breakdown (figure 2.7), within a hollow cathode structure of unique geometry. The voltages required are typically quite high (up to 100s of kV) and is capable of producing current densities of 10^4 Acm^{-2} over short time periods (10s of ns). It is a three-stage process, consisting of an initial Townsend breakdown, a hollow cathode discharge and a final superdense glow discharge. During the latter two stages, the pseudospark can be made to emit a high current density, self-focusing electron beam possessing high brightness and low velocity spread.

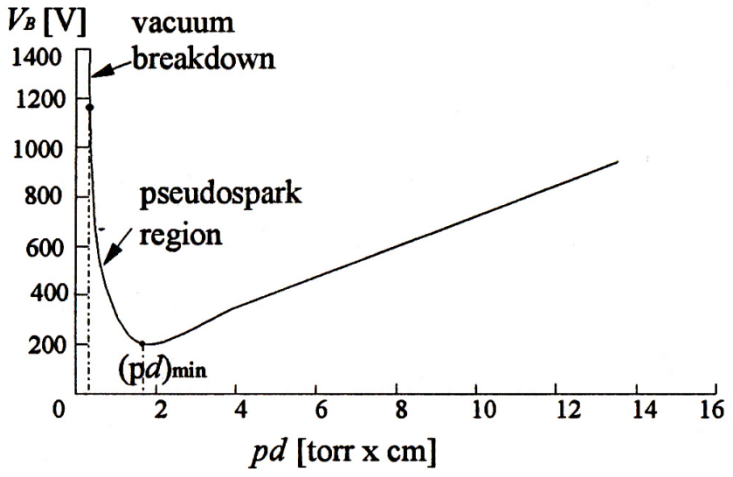

Figure 2.7: Typical Paschen curve showing region of pseudospark occurrence [28].

2.4.1 The pseudospark cathode

Before examining the physical processes within the pseudospark in greater depth, it is useful to examine the geometry of the pseudospark discharge chamber. Primarily, it consists of two plane-parallel electrodes, each with an on-axis aperture, separated by an insulating disc, typically several millimetres thick. Behind the cathode hole lies a closed cavity, as can be seen in figure 2.8.

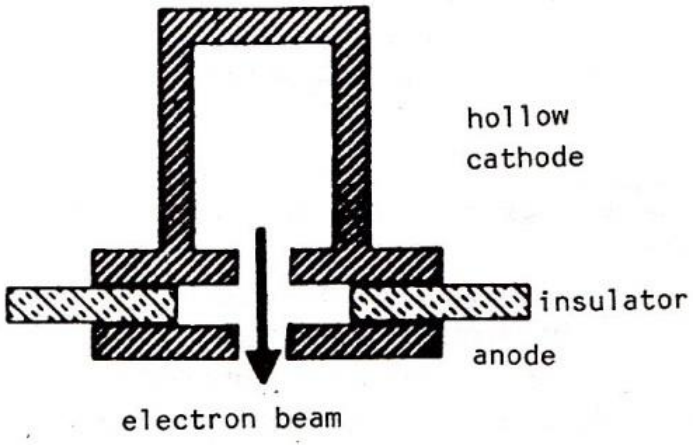

Figure 2.8: Configuration of a single-gap pseudospark discharge chamber [28].

The effective voltage hold-off varies both with the pressure within the discharge chamber and with the *gap separation*, the distance between the cathode and anode. In order to extend the voltage hold-off capabilities it is possible to create multi-gap pseudosparks using multiple insulating discs, each separated with an intermediate electrode (figure 2.9). In the case of a single-gap structure, the maximum usable voltage is ~40 kV, limited primarily by field emission and surface flashover, although higher voltages may be possible if using extremely low pressures which, while still feasible, may limit the cathode lifetime due to erosion effects.

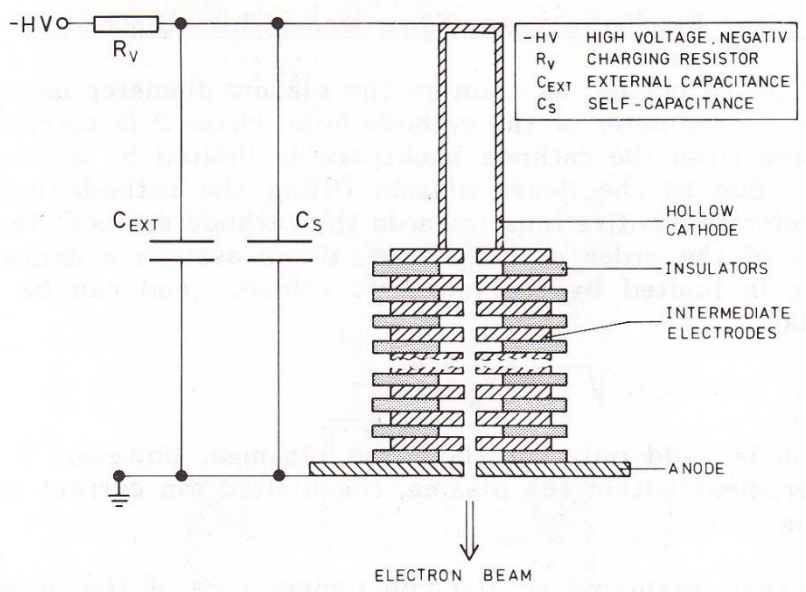

Figure 2.9: Configuration of a multi-gap pseudospark [28].

Typically, triggering the pseudospark discharge may be achieved using even a low power triggering system, either via a surface discharge within the cathode hole, a DC corona discharge within the hollow cathode (either DC or pulsed), optical triggering by means of an appropriate UV light source, or through the use of an external secondary glow discharge to inject charge carriers into the cathode. Discharges may be operated periodically either by repeated triggering using one of the above methods, or in a repetitive self-breakdown state.

When operated as a self-triggered source, achieved by maintaining constant pressure and charging voltage at breakdown, the frequency of repetition is given as [28]

$$f = \frac{1}{R_0(C_{ext} + C_S) ln \frac{V_0}{V_0 - V_B}} \tag{2.22}$$

with V_0 and R_0 the charging voltage and resistance respectively, C_{ext} the external capacitance and V_B the breakdown voltage for the given gas.

2.4.2 Evolution of a pseudospark discharge

When analysing the temporal development of the pseudospark discharge, it is beneficial to break the process down into three processes, namely the pre-discharge, or ignition, of the pseudospark, the development of the hollow cathode discharge and the superdense glow phase (figure 2.10). The superdense glow discharge will only occur if enough energy has been imparted to the electrode system to compensate for the recovery of voltage hold-off capability after the hollow cathode phase.

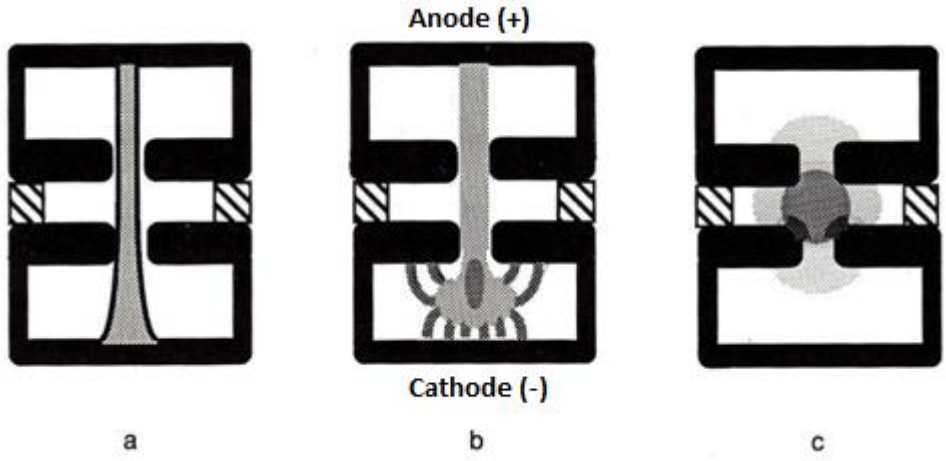

Figure 2.10: The three stages of the pseudospark discharge process: (a) low-current Townsend discharge, (b) hollow cathode discharge and (c) superdense glow discharge. These show the expansion of the plasma column (light grey), with regions of increased plasma density in the hollow cathode in dark grey [55].

To initiate the pseudospark discharge, a negative voltage is first applied to the cathode via one of the aforementioned methods, causing a highly divergent applied field to be established within the hollow cathode region ($E/n \sim 10^{-14}$ Vcm^2), peaking on axis ($E/n \sim 10^{-11}$ Vcm^2) where a very low current Townsend discharge will develop on axis due to the electric field's focusing effect.

At the beginning of the application of voltage, the field in the region between the cathode and anode is almost uniform, with distortions appearing in the region surrounding the electrode holes. Once the initial electrons have begun to be drawn towards the anode ionisation of the gas begins to occur, with much of the ionisation

occurring outside of the hollow cathode. Secondary electrons produced by the volume ionisation are accelerated towards the anode and subsequently absorbed due to their increased mobility, leaving behind a growing ion-space-charge field.

This causes the electric field in the cathode and the cathode-anode gap to become distorted, with the resulting changes in field distribution and potential causing further electron multiplication increase. As ion density in the gap increases, the electric field on the anode side decreases and increases on the cathode side, while the ion-induced space-charge field eventually grows to an order comparable to that of the geometric field. Electrons at this point are no longer being accelerated towards the anode but are slowed down by the high ion space-charge density, resulting in the development of a plasma close to the anode. As the plasma is field-free, the anode potential moves to the plasma surface, becoming a *virtual anode*. The result of the plasma formation is an increased potential near the cathode hole, with both field penetration into the hollow cathode and electron multiplication increasing. The anode potential begins to approach the cathode hole in this phase [28].

2.4.2.1 Hollow Cathode Discharge

As time progresses, the ionisation process moves to the space between the cathode and virtual anode, causing the plasma and, consequently, the virtual anode to approach the cathode, resulting in increased potential at the cathode hole. As the plasma grows, it enters the hollow cathode, at which point the potential around the cathode hole inside the cathode is almost at the full anode potential, resulting in increased ionisation efficiency in the region. The cathode surface is surrounded by a high field sheath of varying thickness. Soon after the plasma enters the cathode, the maximum ionisation efficiency is achieved, accompanied by a fast increase in current. Electron emission from the walls occurs due to primary photons, ions and atoms. This is the hollow cathode discharge, originating from the hollow cathode behind the cathode hole.

The hollow cathode helps to increase the discharge current through two separate mechanisms. The first is through its confining effect, due to which any electrons emitted and accelerated in the sheath on one side of the hollow cathode cavity can be reflected by the opposite sheath, with each electron possibly incurring several reflections before being ejected through the cathode hole to the anode. This increases the possibility of ionisation due to the electron spending more time inside the hollow cathode. The second is through electron multiplication by means of the sheath thickness in the hollow cathode, with variations in sheath thickness affecting electron multiplication by several orders of magnitude.

This means that a large part of the ionisation process occurring within the hollow cathode takes place in the sheaths. Secondary electrons generated here are accelerated by the high sheath fields and can generate further secondary electrons, with the acceleration allowing these electrons to reach high energies leading to a very substantial increase in electron multiplication in the hollow cathode. Whilst this increase is considerable, it is a transient process, related to the confining geometry and the higher energies gained when a fraction of the ionisation processes take place within the sheaths. With this, the plasma expands and the sheath contracts, the bulk of the ionisation processes now occurring in the low field plasma regions. The drop in ionisation processes within the sheath is compensated for by the confining geometry, the effect substantial enough to maintain the discharge.

Due to the extremely high reduced electric field around the cathode hole an axial electron beam consisting primarily of runaway electrons will be generated, the duration of which is limited by voltage breakdown. As such, the moment of maximum beam current (several 100s of A) marks the end of the second phase of the pseudospark discharge, which lasts in the region of 10-30 ns.

2.4.2.2 Superdense Glow Discharge

Once the plasma diameter becomes large enough to shield the cathode hole the second phase ends due to electron emission from the backspace becoming limited due to the dense plasma buildup. Hence, the anode-facing surface of the cathode takes over the entirety of the discharge current, leading to the final superdense conductive phase of the pseudospark discharge.

Following the hollow cathode phase there is a sizeable voltage drop in a thin sheath region bordering the cathode surface leading to a vacuum arc cathode-like situation, where the nearby bulk plasma acts as a virtual anode. Additionally, the bulk plasma will adapt to the cathode morphology resulting in a high uniform electric field between the cold cathode surface and the plasma. As the bulk plasma density increases during the process the cathode sheath, d_c, contracts in accordance with [56]

$$d_c = \sqrt{2\epsilon_0 U_c / e n_e} \tag{2.23}$$

where U_c is the cathode voltage drop.

Ion acceleration to the cathode surface is now possible, the accelerating field strength in the order of $kT_e/\lambda_D e$. The ion drift velocity limits the current density to

$$j_+ = 0.5 n_+ e v_+ \approx 0.5 n_+ e \sqrt{2kT_e/m_+} \tag{2.24}$$

This results in current densities of approximately 100 of A/cm^2 for field-free plasmas, though in the case of plasmas containing an electric field gradient, this current can be substantially higher.

During this phase gas particles are released from the cathode surface via ion impact or through thermal desorption which, after ionisation, contributes greatly to the ionic number density. Such ions are then accelerated through the cathode fall, which lies on the order of 10^6 V/cm, impacting on the electrode surface and rapidly heating it

(3000-4000 K in 30-100 ns) which, according to thermionic field emission theory is sufficient to generate the high discharge current observed.

A contributing factor to this is the occurrence of small arc-like discharge between microtips on the electrode surface resulting in field enhancement for the microprotrusion. Taking these into account, the electric field at the cathode surface may be estimated by [56]

$$E_c \approx \beta \frac{U_c}{d_c} = \beta \sqrt{\frac{e n_e U_c}{2\epsilon_0}} \tag{2.25}$$

where the field enhancement factor, β is given as $\beta = h/r$, h and r being the height and tip radii of the microtips respectively. With sufficient field strength these microtips will explode and form a metal plasma which will contribute to the bulk plasma, the transition from non-explosive to explosive being an almost instantaneous one.

From equations 2.23 and 2.25, it is evident that the electric field at the cathode surface varies with the properties of the bulk plasma, in particular its electron density, therefore it is possible to determine a critical electron density, beyond which the field will induce explosive emission from the cathode microtips. This criterion is stated as

$$n_e \geq n_e^{cr} \frac{2\epsilon_0}{e U_c} \left(\frac{E_c^{cr}}{\beta} \right)^2 \tag{2.26}$$

where E_c^{cr} is the surface field strength at which a material will reach an explosive state within nanoseconds. For a tungsten cathode, this would be ~ 1×10^{10} V/m, with a value of n_e^{cr} of roughly 5×10^{10} m^{-3}. While the critical field strength of a given material depends entirely on a combination of the material and surface morphology, the critical electron density also varies with the applied voltage and with electron temperature. Through the combination of ion bombardment and the hundreds of

cathode microexplosions which occur on the surface, each producing a current of several amps, current densities in excess of 1 kA/cm^2 are possible over considerable surface areas.

Evidence of this behaviour can often be seen directly from examination of the post-discharge cathode surface in the region of the cathode hole where signs of erosion are usually visible. The symmetrical pattern of erosion around the axis suggests an erosion mechanism that is homogeneously distributed around the hole's edge, whilst the size of the erosion pattern lies in keeping with measured dimensions of the dense plasma core during the superdense glow phase of the pseudospark discharge [55].

2.5 Electron Beams

Electron beams are streams of free electrons moving in approximately a single direction, parallel to the axis of the beam. Electron trajectories are often rectilinear though exceptions do occur, such as with free electron lasers (FELs), and beam axes may be either straight or curved. Cross-sectional shapes vary with design, such as sheet beams or cylindrical beams. They have numerous applications, the most relevant to this work being acting as a beam source in vacuum electronics devices, and are also found in electron optics devices [57], accelerators, electron microscopy, beam tubes in televisions [58] and radar, and high-resolution lithography [59].

Electron beams may be evaluated via a number of factors, most notably according to their current, power, kinetic energy and spread, pulse length, transverse dimensions and parallelism. In order to describe the last two quantities, the concept of phase space must be introduced.

Traditionally, when describing the motion of particles, 3D or configuration space is utilised, in which particle positions are described by a position vector [x(t), y(t), z(t)] whilst their velocities are given by a velocity vector [v_x(t), v_y(t), v_z(t)] in order to

take account of forces acting on the electrons. For large groups of moving particles, such as would be the case in an electron beam, this method is unsuitable and so phase space is adopted.

Phase space is a 6-dimensional representation of particle motion, where the first three dimensions represent the particle position and the latter describe the motion of the particle. In the case of a non-relativistic beam, where electron velocities lie far below the velocity of light, particles are represented in a system which takes account of velocity ($x(t)$, $y(t)$, $z(t)$, $v_x(t)$, $v_y(t)$, $v_z(t)$) but for relativistic electrons (generally, this corresponds to accelerating voltages of over 20 kV) momentum is instead considered ($x(t)$, $y(t)$, $z(t)$, $p_x(t)$, $p_y(t)$, $p_z(t)$). Whilst it is impossible to display all six dimensions simultaneously, by showing the projection of a particle's motion in one direction (x, v_x) it is possible to show the development of particle orbits in two dimensions.

There are numerous consequences of the utilisation of phase space. The first is that by plotting large numbers of particles in a system where forces vary smoothly with space, the particles will display a large degree of order in that, barring collisions, two particles which begin with similar phase-space coordinates will always be neighbours. This implies that trajectories exhibit laminar behaviour and therefore follow non-intersecting streamlines [60]. This streamlined behaviour is the basis of most equations of particle motion in electron beams.

The main condition for laminar flow is that the forces acting on particles are smooth, but this is usually when long range forces are acting on the particles. In contrast, short range forces are usually classed as collisions, either between electrons or with a background. Such collisions normally result in only a discrete change in phase-space trajectories, but this often means that two neighbouring particles may become separated in velocity space to a large degree. In most particle beam accelerators and transport systems, however, the effect of collisions is small and changes in phase

trajectories occur slowly in comparison with the particle motions observed under the action of long range forces.

2.5.1 Beam emittance

The term emittance is a measure of the quality of a beam, in that it describes the beam's parallelism. It may be thought of as characterising the effective phase volume of a particle beam distribution. In an ideal focussing system, emittance is conserved and therefore imperfections in transport systems may be gauged by measuring emittance growth. It is expressed in terms of particle position and transverse angle. The transverse angle of a particle is defined as the angle which a particle makes with the beam axis, where

$$x' = \frac{dx}{dz}, y' = \frac{dy}{dz} \tag{2.27}$$

However, in the case of paraxial beams, where the angles which the particles make with the axis are very small, a more useful definition may be derived from the particles' transverse velocities, such that

$$x' = \frac{v_x}{v_z}, y' = \frac{v_y}{v_z} \tag{2.28}$$

The coordinates (x, x', y, y') are often expressed as functions of z rather than time, t, and describe the trace of a particle orbit in the z-direction rather than the time-dependent position. With this in mind, the coordinate space is termed *trace space*.

The emittance, ε_x, at a given position along the beam's axis may be defined as the projected area of the x,x' plane of the beam divided by π. The projected area of a beam is conveniently defined as the smallest ellipse in trace-space which can successfully capture every particle within its boundary, as depicted in figure 2.11. The emittance may then be defined as the area of said ellipse divided by π, i.e.

$$\varepsilon_x = \iint dx\, dx' /\pi \tag{2.29}$$

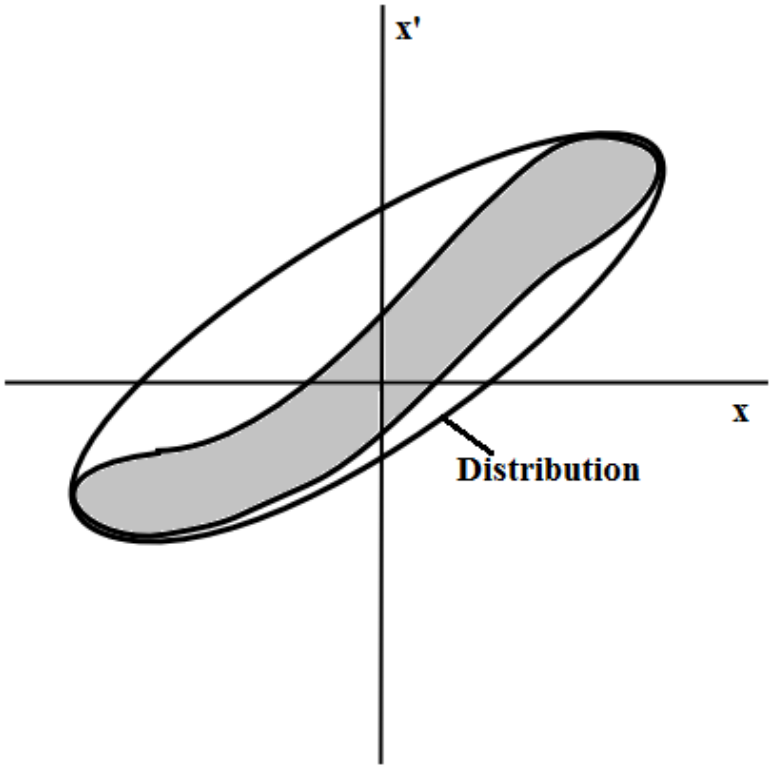

Figure 2.11: Particle distribution as enclosed by an ellipse of minimal area [60].

When the major and minor axes are aligned to the coordinate axes and x_0 and x_0' are the ellipse dimensions, as in figure 2.12, this equation may be simplified to

$$\varepsilon_x = x_0 x_0' \tag{2.30}$$

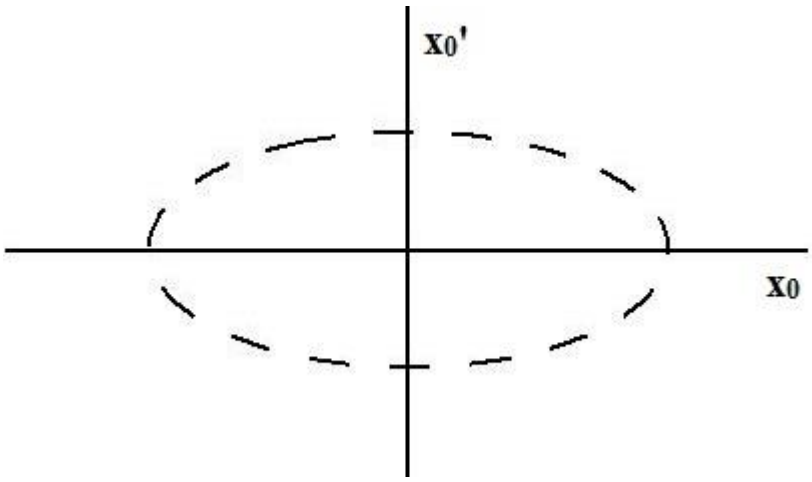

Figure 2.12: Hyper-emittance in the xx' plane [60].

Occasionally, the value of emittance is taken as the area of the ellipse without the use of the divisor of π and so it is recommended to mention which convention is used when quoting values. Modern definitions of emittance include the 1/π factor and give emittance values in π-m-rad, although either convention may acceptably be used..

In a transport system where the beam is not accelerated, the beam emittance is in proportion to the beam's effective phase volume and will remain constant along its length due to the continuity of the distribution being preserved by beam focussing, assuming linear forces, but this is not the case in a system with irreversible processes which act to distort the boundaries of the beam. When this occurs, the ellipse must enclose an even larger area of phase space, known as emittance growth. This is undesirable as it leads to a loss of parallelism in the beam. Nonetheless, it is often unavoidable in beam systems and so a final emittance value for a beam is used, itself being a sum of the intrinsic emittance and emittance growth.

Previous discussion of emittance has only taken account of one-dimensional beams or those in which motion in the x and y directions are independent but in many focussing systems transverse particle motions are inseparable, and so the emittance definition must be extended to encompass four dimensions. One such example is a paraxial beam in a focussing system in which x and y motions couple but the

transverse motion is independent of axial motion, resulting in emittance in the x and y directions no longer being separately conserved quantities but the four-dimensional trace-space volume is constant in the absence of acceleration.

At this point it is useful to define hyper-emittance, a four-dimensional extension of emittance. If a parallel beam possesses uniform distribution in four-dimensional trace-space, it shall fit into a four-dimensional ellipsoid, given by

$$\left(\frac{x}{x_0}\right)^2 + \left(\frac{x}{x_0'}\right)^2 + \left(\frac{y}{y_0}\right)^2 + \left(\frac{y}{y_0'}\right)^2 = 1 \tag{2.31}$$

then the hyper-emittance, ε_4, is defined as

$$\varepsilon_4 = \frac{V_4}{\pi^2} = x_0 x_0' y_0 y_0' \tag{2.32}$$

where V_4 represents the four-dimensional volume encompassed by the ellipsoid.

In a situation where the particle motions in x and y are independent, then we can specify separate emittances, ε_x and ε_y, and the hyper-emittance may be calculated as

$$\varepsilon_4 = \varepsilon_x \varepsilon_y \tag{2.33}$$

When a beam is accelerated, its emittance is generally decreased. This is because the transverse momentum of particles remain constant but the axial momentum increases, thus reducing *x'*. To reflect this, the quantity normalised emittance is used, a measurement of emittance which remains constant during acceleration. Given that acceleration may be neglected, any decrease in normalised emittance may be due to beam degradation through either non-linear forces or beam perturbations.

During acceleration, the trace-space volume of a beam will decrease but in a linear focussing system the phase-space volume will remain constant. Normalised emittance is calculated from the boundary of the distribution of orbit vector points in

modified trace-space (x, βγx') where $\beta\gamma=1/m_0c$ is a correction factor included to ensure that normalised emittance remains constant during acceleration. The normalised emittance may then be given as [60]

$$\varepsilon_{nx}=(\beta\gamma)\varepsilon_x=(\text{Area in } x\text{-}p_x \text{ space})/\pi m_0 c \tag{2.34}$$

or, for the case of non-relativistic beams

$$\varepsilon_{nx}=\beta\varepsilon_x=v_x\varepsilon_x/c=(\text{Area in } x\text{-}p_x \text{ space})/\pi c \tag{2.35}$$

2.5.2 Brightness

When discussing charged particle beam applications, the term brightness is the current density per unit solid angle in the axial direction. A beam which has high brightness has a high current density and good parallelism. If a beam has current *I*, average radius Δr and divergence angle $\Delta\theta$, then in the limit $\Delta\theta \ll 1$ the brightness may be defined by

$$B \cong \frac{I}{(\pi\Delta r^2)(\pi\Delta\theta^2)} = \frac{J_b}{\pi\Delta\theta^2} \tag{2.36}$$

where J_b is the average beam current density [60].

When a beam exhibits symmetry in the transverse direction it is possible to define the brightness in terms of emittance. Considering a beam with perfect distribution and orbit vectors filling an ellipse with axes (x_0,x_0') and (y_0,y_o'), the brightness may be written as

$$B \cong \frac{I}{(\pi x_0 x_0')(\pi y_0 y_0')} = \frac{I}{\pi^2 \varepsilon_x \varepsilon_y} \tag{2.37}$$

For isotropic beams with average emittance ε, we may approximate the brightness as

$$B = \frac{I}{\pi^2 \varepsilon^2} \tag{2.38}$$

For small beam angles, this definition may be approximated as [61]

$$B \approx \frac{J}{\Omega} = \frac{J}{\pi\alpha^2(z)} \tag{2.39}$$

where J is the beam current density, Ω is a solid angle which encompasses all rays emitted from a point on the z-axis and α(z) is the angle between the z-axis and the beam edging rays.

In the same manner as emittance is not conserved during acceleration, neither is brightness and so we may define a normalised brightness as a counterpart to normalised emittance. In a relativistic system, this is written as

$$B_n = \frac{I}{\pi^2\varepsilon_n^2} = \frac{B}{(\beta\gamma)^2} \tag{2.40}$$

2.5.3 Beam Focussing

In any beam transport system, there will be a radial spread of the beam. This may be due to electrons possessing a radial velocity component, but may also be due to space charge forces causing repulsion effects, resulting in an increase in the beam radius. The solution to counteracting this is to use some form of confinement system. In most cases, the confinement method shall be through the use of a magnetic field [62] (either periodic or permanent) or an array of electrostatic lenses, although this latter method is less common [60].

An alternative is to utilise ion channel focussing, in which an electron beam is passed through a cloud of weakly-ionised gas in order to confine the beam. Also known as the ion focus regime (IFR), this effect occurs due to the effect of the beam head as it enters the plasma, dispersing the plasma electrons and causing the formation of a uniform ion channel. As the beam progresses through this channel, the space-charge forces of the ions act to constrain radial growth of the electron beam. It is this

principle which lies at the heart of the plasma-focused free electron laser [63] and other such devices.

Assuming an electron beam with density n_{b0}, radii r_b, zero transverse velocity and initial longitudinal velocity v_{z0} entering a plasma, the tip of the electron beam will induce the formation of an ion channel with a density of n_{i0} via the expulsion of electrons. The force induced on the beam due to beam electric and magnetic self-fields is [64]

$$\boldsymbol{F}_{b,p} = \frac{n_{b0} e^2 \boldsymbol{p}}{2\epsilon_0 \gamma^2} \tag{2.41}$$

where $\boldsymbol{p}$ is the radial vector in the x_0y plane. Similarly, the force exerted on the beam by the ionic space charge fields is

$$\boldsymbol{F}_{i,p} = -\frac{n_{i0} e^2 \boldsymbol{p}}{2\varepsilon_0} \tag{2.42}$$

When the force exerted by the ion channel exceeds the beam's own space-charge forces, it is known as a strong ion channel effect and will induce betatron [65], or periodic transverse, oscillations in the electron beam with a frequency defined as

$$\omega_b^2 = \frac{\omega_p^2}{2\gamma} \tag{2.43}$$

where the plasma frequency is obtained from $\omega_p^2 = \frac{e^2 n_{i0}}{\varepsilon_0 m_0}$.

From equations 2.41 and 2.42, equilibrium between the ionic and electronic space-charge forces and, consequently, radial confinement will be achieved when

$$\gamma^2 n_i = n_b \tag{2.44}$$

2.5.4 Pseudospark electron beam performance

The electron beam produced by a pseudospark discharge generally possesses many desirable attributes and can be considered to be of high quality. Beam emittances of 15 mm mrad are typical, as are brightness values of 4 x 10^{10} A/m^2rad^2 [66]. Beam current densities may exceed 10^4 Acm^{-2} and the beam does not require a guiding magnetic field due to its confinement via the process of ion channel focusing. As such, this makes it particularly beneficial in devices for which magnetic confinement methods may be problematic, either due to size or operational constraints. A comparison of electron beam performance is shown in table 2.1 [28] [67].

Beam Parameters	**Pseudospark cathode**	**Thermionic cathode**	**Plasma flare cathode**	**Field emission cathode**	**Photocathode**
Current density [$kAcm^{-2}$]	> 1	< 0.1	> 10	~5	~0.2
Energy spread	Small	Small	High	Small	Small
Time duration	ns - μs	ns – DC	ns - μs	ns-DC	~ns
Brightness [$Am^{-2}rad^{-2}$]	10^9 - 10^{12}	10^2	10^7 - 10^8	10^{12}	10^{12}
Max. beam current [A]	10^3	10^2	10^6	<10	10^2
Beam diameter [mm]	1 - 5	1 – 100	1 - 100	<1	~10

Table 2.1: Comparison of pseudospark electron beam performance with other electron beam sources using typical obtained parameters.

The attributes and performance of the pseudospark electron beam make it a good choice for generation of high-frequency radiation. It may be scaled down to

diameters of several mms, allowing for application to smaller interaction structures, and is second only to field emission devices in terms of current density, an important factor in realising respectable output powers at higher frequencies. What makes it preferable to field emission devices is that beam focussing is typically achieved through the formation of an ion channel immediately after the anode, constraining the beam without the need of an external magnetic field. Although some limitations exist with pseudospark-sourced electron beams, such as noise generation, the quality of the beams, as well as their self-focussing properties, make them well-suited for use with some types of plasma-filled electron tubes.

2.6 Beam-wave Interactions

In order to function, all microwave devices require the presence of beam-wave interactions, resonant interactions occurring between the normal electromagnetic wave modes of a waveguide or cavity and the natural oscillatory modes of an electron beam. Within electron beams, these modes of oscillation occur as a result of longitudinal spatial bunching or rotational phase bunching. In the cases of both normal electron beam modes of oscillation and the natural electromagnetic wave modes of cavities and waveguides, the modes may be described by dispersion relations between the angular frequency ω and the axial wavenumber k_z. Electron beam modes and resonant modes exist independent of each other in the $\omega - k_z$ plane, except when the wave modes or electron beam modes of oscillation are modified such that they intersect. In these situations, there is a resonant exchange of energy between the two for certain wavelengths and frequencies.

The dispersion relations for electron beams vary according to the motion and oscillation mode of the electrons within the beam. The most basic form of oscillatory mode is the *space-charge oscillation wave*, which occurs as a result of electron bunching. Without considering axial confinement factors, the dispersion relation describing the space-charge wave for a beam progressing along the z-axis is given by

$$\omega = k_z v_z \pm \frac{\omega_b}{\gamma_0} \tag{2.45}$$

where $\omega_b = (|\rho_0|e^2/\varepsilon_0 m\gamma_0)^{1/2}$ is the beam plasma density, with ρ_0 the beam charge density, v_z the axial velocity and $\gamma_0 = (1 - v_z^2/c^2)^{-1/2}$ the relativistic factor. Depending on the use of '+' or '-', these are described as being 'fast' or 'slow' space-charge waves respectively [68]. This equation does not give any radial boundaries as could be expected in a real-world scenario. At $k_z = 0$, this equation gives a wave with a phase velocity exceeding the speed of light, as can be seen in figure 2.13.

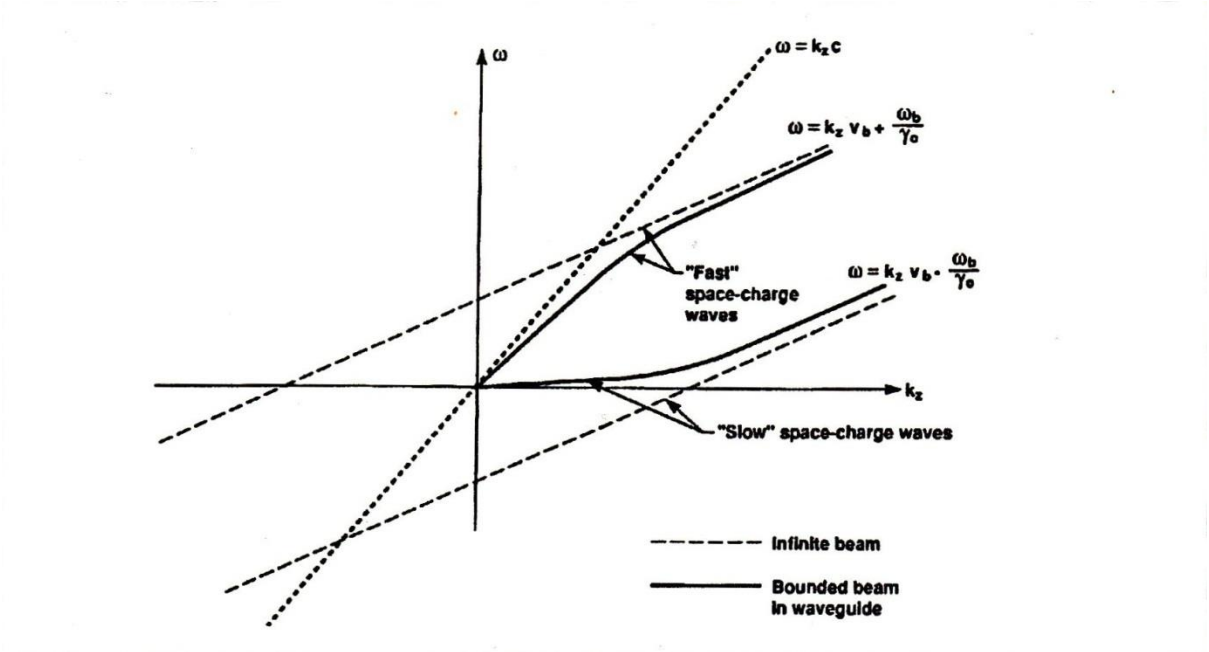

Figure 2.13: Dispersion curve for an electron beam [68].

This also shows the result of radial boundaries being considered, as would be the case of a beam travelling within a waveguide. In such an instance, the phase velocity of the beam always remains less than c, resulting in a fast space-charge wave which, in a sense, may still be considered a slow wave. In all instances, however, the fast space-charge has positive energy while the slow space-charge wave has negative energy.

The reason for this is that, in the case of slow waves, ac current and velocity are antiphase, i.e. [69]

$$I_1 = \pm \frac{\omega \rho_0 v_0 A}{\omega_p} \left(\frac{2V_1}{V_0} \right) = \pm \frac{1}{2} \frac{\omega}{\omega_p} \frac{I_0}{V_0} V_1 \tag{2.46}$$

where I_1 is the ac current and V_1 is the beam kinetic voltage. As such, when the velocity exceeds v_0, the charge density drops below the equilibrium charge density J_0 and it can then be said that the kinetic energy of an unmodulated beam is greater than that of one carrying a slow wave. In other words, it is necessary to remove power from the beam to setup a slow wave, which is the key to understanding many beam-wave interactions and microwave devices.

2.6.1 Microwave Devices

Devices which generate microwaves vary in a number of ways, most notably in their waveguide and cavity modes; in their electron and oscillation modes; their beam-wave interaction mechanisms; their operational effects; and their electron beam intensity.

In the first case, that of electromagnetic modes, microwave sources are considered to be slow-wave or fast-wave. Fast-wave interactions involve waveguide modes with phase velocities exceeding that of light; slow-wave interactions involve waveguide modes with velocities below that of light.

Electron movement involved in interaction processes may be subdivided into three types: O-type, or linear beam, devices, where the electron beam travels in the direction of the magnetic field (e.g. klystrons, travelling wave tubes); M-type, or crossed-field, devices, where the electron beam runs across crossed electric and magnetic fields (e.g. magnetrons); and space-charge devices, where microwaves are generated purely as a result of intense space charge interactions (e.g. virtual cathode oscillators) [68].

Operationally, devices are generally classed as being amplifiers or oscillators. In the case of amplifiers, the output signal is an enhanced version of an input, or seed, signal. Without this seed signal, there will be no noticeable output other than low-level noise. Oscillators, meanwhile, require feedback in order to generate microwaves, as well as sufficient gain to overcome the losses incurred per cycle. In such a way, an output signal may be generated spontaneously without the presence of an input signal.

Beam current densities further subdivide devices into two groups of operation: a low-current Compton regime, with negligible space-charge effects and electrons acting as a coherent array of individual emitters, and the Raman regime of operation, with high current densities and beam current verging on the space-charge limit.

In the next two sections, two devices which operate under such principles are examined. The klystron, covered in section 2.7, is a linear beam, O-type amplifier which enhances a microwave signal fed into a resonant cavity to modulate the velocities, and consequently the space-charge densities, of an electron beam. Section 2.8 outlines the theory of the backward-wave oscillator, or BWO, is a slow-wave, O-type oscillator, in which microwaves are generated from the interaction of an electron beam and the backward electromagnetic modes of a slow-wave structure.

2.7 Backward Wave Oscillators

Backward wave oscillators (BWOs), also known as carcinotrons or backward wave tubes, are linear beam vacuum tubes which operate in a similar fashion to travelling wave tubes (TWTs) in that they involve the interaction between an electron beam and a slow wave structure, a periodically varying transmission line, over a number of cycles of the beam oscillation frequency. While TWTs propagate a wave in the direction of electron flow, the structures in BWOs allow for the propagation of

backward waves, with phase and group velocities travelling in opposing directions. This situation may only arise when space-charge waves are present, as shall be discussed in section 2.7.1. Oscillations originally begin with noise signals growing in the interaction circuit at the far end of the interaction structure, with some of the energy generated travelling back towards the electron source. This induced wave will have a phase velocity in the opposite direction. If an electron current, i.e. an electron beam, is introduced, possessing a velocity greater than the phase velocity, the electron kinetic energies will be transferred to the wave, increasing the circuit wave energy and inducing energy growth near the beginning of the tube. This is effectively a regenerative process in that this increased energy induces velocity modulation in the electron beam, which becomes current modulation at the 'catcher' end, inducing energy in the circuit in the form of a wave which travels back towards the electron source, producing further bunching, and so on. At high beam currents, oscillation will occur in the tube. The amplification frequency is restricted by the properties of the slow-wave structure and may be tuned by means of varying the beam voltage [70].

2.7.1 Slow Wave Structures

To begin an analysis of the effect of slow wave structures, some assumptions must be made. In a structure that is periodic along z with a period L, where an electromagnetic field as a harmonic function of time is given by [71]

$$\mathbf{E}(r,t) = \mathbf{E}(x,y,z)e^{i\omega t} \tag{2.47}$$

Then a modulus of the field will likewise be periodic. As such, the complex amplitude after a single-period shift along z is multiplied by the phase multiplier $e^{-i\varphi}$, where φ is a real constant, i.e.

$$\mathbf{E}(x,y,z+L) = \mathbf{E}(x,y,z)e^{-i\varphi} \tag{2.48}$$

Considering the coordinates function $\mathbf{F}(x,y,z) = \mathbf{E}(x,y,z,)e^{i\beta_0 z}$, where $\beta_0 = \frac{\omega}{v_{\varphi 0}} = \frac{\varphi}{L}$. This function may be verified to be periodic from

$$\mathbf{F}(x,y,z+L) = \mathbf{F}(x,y,z) \tag{2.49}$$

And so the field in a periodic system, with period L as a function of z, up to the factor $e^{-i\beta_0 z}$, is given as

$$\mathbf{E}(x,y,z) = \mathbf{F}(x,y,z)e^{-i\beta_0 z} \tag{2.50}$$

These equations express Floquet's theorem, which may be written as

$$\mathbf{E}(x,y,z,t) = \mathbf{F}(x,y,z)e^{i(\omega t-\beta_0 z)} \tag{2.51}$$

Using the periodicity of the coordinates function **F**(x,y,z), it may be expressed as a Fourier series

$$\mathbf{F}(x,y,z) = \sum_{-\infty}^{\infty} \mathbf{F}_n(x,y)e^{-i(2\pi/L)nz} \tag{2.52}$$

Substituting into Floquet's theorem,

$$\mathbf{E}(x,y,z,t) = \sum_{-\infty}^{\infty} \mathbf{F}_n(x,y)e^{i(\omega t-\beta_n z)} \tag{2.53}$$

where

$$\beta_n = \beta_0 + \frac{2\pi}{L}n, \qquad n = -\infty, \dots, -1,0,1, \dots, \infty$$

In the above-described periodic structure, it may be seen that the field is a superposition of *spatial harmonics*, waves of the form $\mathbf{F}_n(x,y)e^{i(\omega t-\beta_n z)}$, with equal

frequencies yet varying spatial structures, transversal distributions and wavelengths. The function $F_n(x,y)$ may be found from Maxwell's equations in conjunction with the corresponding boundary conditions.

The wavelength of a spatial harmonic is defined as

$$\lambda_n = \frac{2\pi}{\beta_n} = \frac{2\pi}{\beta_0 + 2\pi/L}, \quad n = \cdots, -1, 0, 1, \ldots, \tag{2.54}$$

the phase velocity as

$$v_{ph,n} = \frac{\omega}{\beta_n} = \frac{\omega}{\beta_0 + 2\pi/L}, \tag{2.55}$$

and the group velocity as

$$v_g = \frac{\partial \omega}{\partial \beta_n} = \frac{\partial \omega}{\partial \beta_0} \tag{2.56}$$

As can be seen, the group velocity remains the same for all harmonics.

While the field for any given harmonic satisfies Maxwell's equations, they do not satisfy the boundary conditions as the harmonic period λ_n does not equal a multiple of the structural period; only the total field satisfies the boundary condition. Therefore, if any single period is excited, all other harmonics will also emerge, their amplitudes and phase relationships determined by the slow-wave structure's geometry and frequency. Each specific set of harmonic determines a mode, and an infinite number of modes are possible for any given structure.

In cases where n is sufficiently large, harmonics are slow waves (i.e. they possess phase velocities less than the speed of light) and have the properties of surface

waves. The field of the *n*th harmonic decreases with distance *x* from the SWS boundary as

$$e^{-\sqrt{\beta_n^2-k^2}}x = e^{-(2\pi x/\lambda_n)\sqrt{1-\left(v_{ph,n}/c\right)^2}} \tag{2.57}$$

And so it may be said that the slow harmonic's field is diminished by $e^{2\pi\sqrt{1-\left(v_{ph,n}/c\right)^2}}$ in a direction normal to the direction of propagation.

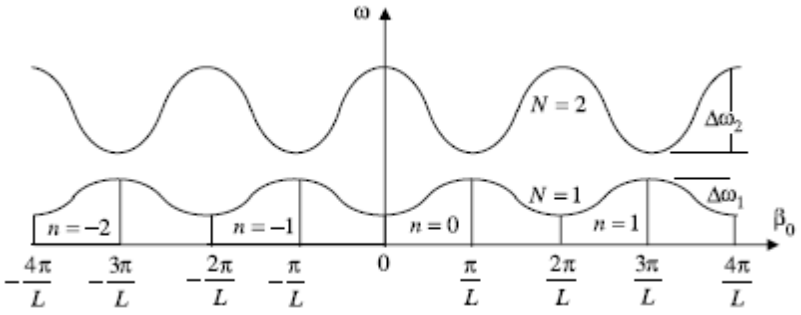

Figure 2.14: Dispersion diagram for a periodically-varying structure [71].

Figure 2.14 shows a dispersion diagram for a slow-wave structure, where the function $\omega(\beta_0)$ is periodic with period $2\pi/L$. As β_0 is increased by $2\pi/L$, β_n becomes β_{n+1} and so, while the label of each β_n is altered, there is no variation in any of the harmonics. The same can be seen in the –ve direction. The lower curve of the dispersion diagram illustrates the fundamental mode, $\Delta\omega_1$ denoting the frequency bandwidth over which it is possible to propagate in this mode, $\Delta\omega_2$ the propagation bandwidth for the second mode, and so on.

From analysis of the dispersion function $\omega(\beta_0)$, the propagation constant of the zero harmonic β_0 lies between

$$0 \leq \beta_0 L \leq \pi$$

thus setting the maximum possible phase shift of the 0th harmonic to π. The group velocity at the range boundaries $\beta_0 = 0, \pi$ is zero, while from our earlier definition of the group velocity, it may be said that the modulus of the -1th harmonic propagation constant lies in the range $\pi/L \leq |\beta_{-1}| \leq 2\pi/L$ and therefore the propagation constants may be arranged as

$$|\beta_0| \leq |\beta_{-1}| \leq |\beta_1| \leq |\beta_{-2}| \leq |\beta_2| \leq \cdots \tag{2.58}$$

It may be shown that the fields of the harmonics decrease with $|\beta_n|$, and equation 2.58 is known as the law of harmonic amplitude decrease, indicating that the 0th harmonic has the greatest amplitude. Given that the field of a harmonic decreases with distance from the boundary, there eventually reaches a point where only the zero harmonics are detectable and the field begins to resemble that of a regular waveguide.

All positive harmonics (those with n ≥ 0) possess a positive phase velocity while negative harmonics (those with n < 0) have a negative phase velocity. Assuming a positive $\omega = \omega(\beta_0)$ slope similar to that of figure 2.14 for the first mode in the range $0 \leq \beta_0 L \leq \pi$, it may be observed that all positive harmonics have coinciding phase and group velocity directions and as such are forward waves, while the reverse is true for negative harmonics, making them backward waves. For coupled-cavity slow wave structures, the propagation in this mode may be forward or backward wave depending on the form of coupling between cells. At the 2nd mode, the converse is true. When phase and group velocities of a structure's fundamental harmonic coincide in direction, the structure has positive dispersion; when they oppose, it has negative dispersion. If the group velocity for an nth order harmonic is defined as

$$\frac{1}{v_{g,n}} = \frac{\mathrm{d}\beta_n}{\mathrm{d}\omega} = -\frac{2\pi}{\lambda_n^2}\frac{\mathrm{d}\lambda_n}{\mathrm{d}\omega} \tag{2.59}$$

Then, in the case of positive dispersions, the wavelengths of the 0th and all positive harmonics are decreased in frequency.

Based on this description, it may be deduced that when the electron beam is synchronised with some negative harmonics as defined in equation 2.55, i.e.

$$|\beta_{-n}| \approx \beta_e \text{ or } \frac{2\pi n}{L} - \frac{\omega}{v_{ph,0}} \approx \frac{\omega}{v_0}, \qquad \text{n} > 0, \tag{2.60}$$

which, in the limit of zero space-charge, is known as the synchronous condition, then energy will be transferred from the electron beam to the field and transported towards the buncher end of the SWS. In other cases, it is the interaction between the structure and the slow space-charge wave which dictates operation. Due to the direction of energy travel, field amplitude is strongest nearer the cathode, with electron bunching occurring in the lowering field.

2.7.2 Analysis of backward-wave oscillator operation

In effectively analysing the operation of the BWO, there are two forces which must be considered: the effects on current in an electron beam due to the fields present in the SWS, and the field induced in the SWS due to a current in an electron beam. These may be solved separately, and then combined to give an overview of the simultaneous interactions occurring within the tube [72].

The matter of excitation of the field by a current may be expressed in the form

$$(\delta^2 + q)\tilde{\boldsymbol{I}} = i\frac{I_0}{2U_0\beta_e C^2}\widetilde{\boldsymbol{E}_W} \tag{2.61}$$

where C is the Pierce parameter, δ the incremental propagation constant, q the space-charge parameter, Ĩ the ac current and $\widetilde{\boldsymbol{E}_W}$ the ac field. The first of these three variables are dimensionless and are explained in more detail in [73].

In addressing the field excitation by means of backward wave propagation in a plane ξ

$$\widetilde{E_W} = \widetilde{E_0} e^{-i\beta_o z} - \frac{\beta_0^2 Z}{2} \int_z^L \tilde{I}(\xi) e^{i\beta_o (z-\xi)} d\xi \tag{2.62}$$

We must then factor in not only the opposing phase and group velocity directions and the input signal amplitude, taken as $\widetilde{E_{in}} = \widetilde{E_0} e^{-\beta_0 L}$ at $z = L$, transforming this into

$$\widetilde{E_W} = \widetilde{E_{in}} e^{-i\beta_0 (z-L)} - \frac{\beta_0^2 Z}{2} \int_z^L \tilde{I}(\xi) e^{-i\beta_o (z-\xi)} d\xi \tag{2.63}$$

or, in the differential form,

$$\frac{d\widetilde{E_W}}{dz} + i\beta_0 \widetilde{E_W}(z) = \frac{\beta_0^2 Z}{2} \tilde{I}(z) \tag{2.64}$$

Substituting $\widetilde{\boldsymbol{E}_W}$, $\tilde{I} \sim \tilde{A} e^{-i\beta z}$, this may be represented using Pierce's variables,

$$(\delta + ib) \widetilde{\boldsymbol{E}_W} = \frac{\beta_0^2 Z}{2\beta_e C} \tilde{I} \tag{2.65}$$

From this, as well as the definition of the Pierce parameter $C = \frac{I_0 Z}{4U_0}$, where I_0 is the beam current, Z the impedance and U_0 the beam voltage, we may find the dispersion equation for a backward wave oscillator,

$$i(\delta + ib)(\delta^2 + q) = -(1 + Cb)^2 \tag{2.66}$$

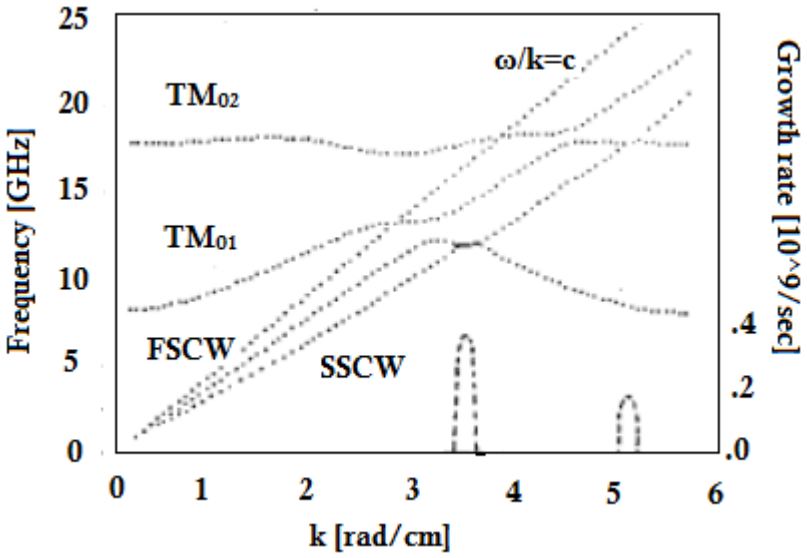

Figure 2.15: Calculated BWO dispersion curve showing interaction between slow space charge wave and lower harmonics of a slow wave structure, with growth rate indicated to indicate tuneable range [74].

Figure 2.15 shows the dispersion diagram for a BWO, as designed by Butler et al. [74], showing the interaction between the slow space charge wave and the backward phase of the -1 (TM_{01}) harmonic. It can be noted that there is a degree of deformation in the TM_{01} mode at the point of interaction and this is a product of space-charge effects, which will be considered later. The growth rate is marked here to show the range of k over which amplification is possible.

If δ_1, δ_2 and δ_3 are the complex roots of this, the partial solutions are given as

$$\widetilde{E_k}(z) = e^{-i\beta_e z} e^{\beta_e C \delta_k z}$$

$$\widetilde{I_k}(z) = i\frac{I_0}{2U_0\beta_e C^2}\frac{1}{\delta_k^2 + q}\widetilde{E_k}(z) \tag{2.67}$$

$$\widetilde{v_k}(z) = \frac{1}{\omega\rho_0}(\omega - v_0\beta_k)\widetilde{I_k}(z) = \frac{\eta}{v_0\beta_e C}\frac{\delta_k}{\delta_k^2 + q}\widetilde{E_k}(z)$$

While general solutions are given as

$$\widetilde{E_k}(z) = \sum_{k=1}^{3} A_k \widetilde{E_k}(z)$$

$$\begin{aligned} \widetilde{I_k}(z) &= \sum_{k=1}^{3} A_k \widetilde{I_k}(z) = i \frac{I_0}{2U_0 \beta_e C^2} \sum_{k=1}^{3} \frac{1}{\delta_k^2 + q} A_k \widetilde{E_k}(z) \\ \widetilde{v_k}(z) &= \sum_{k=1}^{3} A_k \widetilde{v_k}(z) = \frac{\eta}{v_0 \beta_e C} \sum_{k=1}^{3} \frac{\delta_k}{\delta_k^2 + q} A_k \widetilde{E_k}(z) \end{aligned} \tag{2.68}$$

Assuming the boundary conditions

$$\tilde{E}(0) = \widetilde{E_0}, \quad \tilde{I}(0) = \tilde{v}(0) = 0 \tag{2.69}$$

then the constant, A_k, is stated as

$$A_k = \frac{\delta_k^2 + q}{(\delta_k - \delta_l)(\delta_k - \delta_m)} \widetilde{E_0}, \qquad \text{k,l,m = 1,2,3} \tag{2.70}$$

The input complex amplitude is determined by the first part of equation 2.69, its amplitude may be given as $\widetilde{E_k}(L) = e^{-i\beta_e z} e^{\beta_e C \delta_k L}$, giving a complex gain for the tube of

$$G_E = \frac{\tilde{E}(0)}{\tilde{E}(L)} = e^{i\beta_e L} \frac{1}{\sum_{k=1}^{3} \frac{\delta_k^2 + q}{(\delta_k - \delta_l)(\delta_k - \delta_m)} e^{\delta_k \beta_e C L}} \tag{2.71}$$

When the denominator of this equation equals zero, it will correspond to infinite gain and from this condition may be found the start-up conditions for a BWO.

When losses are factored into the system, the dispersion equation 2.66 for cases where $Cb \ll 1$ may be altered to compensate, becoming

$$i(\delta - d + ib)(\delta^2 + q) = -1 \tag{2.72}$$

where *d* is a negative variable to represent the attenuation of the backward wave as it traverses the SWS.

In order to compute the starting current, however, it is best to consider the lossless case. It is possible to represent equation 2.72 as a cubic equation with real coefficients,

$$(\chi + b)(q - \chi^2) = 1 \tag{2.73}$$

where $\delta = i\chi$. Typically, this presents an equation with three roots; one real, and two complex, where the former represents a wave of constant amplitude while the latter two have increasing and decreasing amplitude, though the growing wave will not become dominant near the output due to the start-up condition as defined by equation 2.71. It is also possible for the output signal to consist of the interference between three waves with comparable amplitudes in the case where certain values of *b* and *q* to allow for three real roots.

The start-up current may be found from the solutions for δ_1, δ_2 and δ_3, as well as the definitions of C and b, and is given as

$$I_{st} = 4U_0 \frac{(CN_{st})^3}{ZN^3} \tag{2.74}$$

$$\frac{v_0}{v_{ph,0}} = \frac{b_{st}}{N}(CN_{st}) + 1 \tag{2.75}$$

When the dispersion of the slow wave structure is known, equation 2.75 may be used to determine the oscillation frequency of the tube. Start-up conditions, as well as calculated values of CN_{st}, may be found in the work of Johnson [70] and Heffner [72].

When q = 0, the dispersion relation may often be expressed as

$$(\beta_0 - \beta_e)L = (2n + 1)\pi \tag{2.76}$$

Equations 2.75 and 2.76 form the criteria for effective interaction, in that they are instrumental in selecting the wave that is synchronous with the electron beam for modulation of the electrons, thus allowing for stationary oscillations to be maintained within the system. This is especially necessary in that oscillations within the system begin from noise, as previously expressed, and as such consist of waves of varying phase velocities, with these being determined by the SWS dispersion. As such, a process for selection is required for coherent generation of a backward wave.

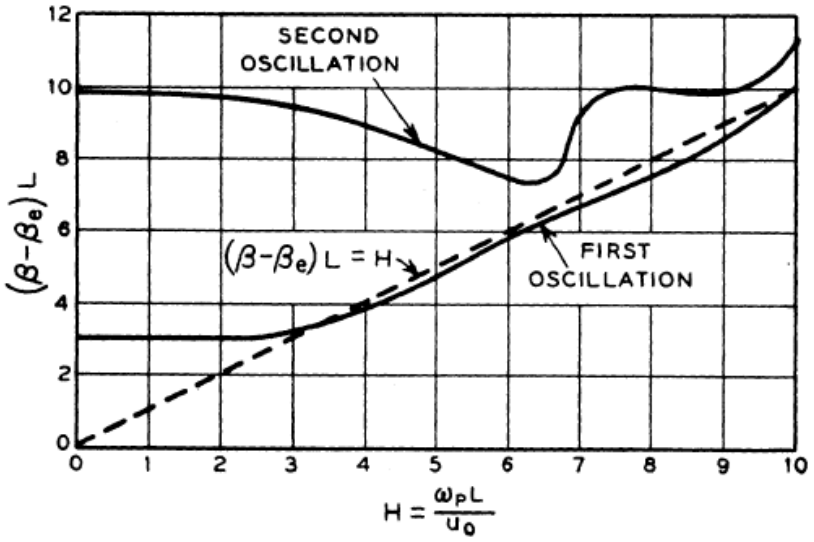

Figure 2.16: (β-βe)L required for oscillation to begin as function of the space charge parameter H [72].

It may also be noted that the conditions for start-up oscillation may vary with space-charge. Figure 2.16 shows the variation in the start-up conditions with the space charge parameter *H*, which may be defined as the number of effective plasma

wavelengths in the length of the tube. For large values degrees of space charge, the start-up conditions approach

$$(\beta - \beta_e)L = H$$
$$CN_{st} = \left(\frac{H}{16\pi}\right)^{1/3} \tag{2.77}$$

That $(\beta - \beta_e)L$ for the first oscillation point is a rising function of current indicates that rising current will cause a downshift in frequency of oscillation, though this shift will be relatively minor.

The conditions for oscillation also determine the tuning operation of the BWO in that the starting difference $(\beta_0 - \beta_e)$ is independent of $\beta_e = \omega/\sqrt{2\pi U_0}$. This means that a change in the accelerating voltage U_0 will have a corresponding effect on $\beta_e = \omega/v_{ph,0}(\omega)$. Careful SWS design and tube construction allow for band frequency tuning of up to three octaves.

2.7.3 Relativistic BWOs

As velocities are increased into the relativistic regime, many limitations of linear beam tubes are diminished and with this weakening of space-charge limitations, tubes are capable of both higher frequencies and energies.

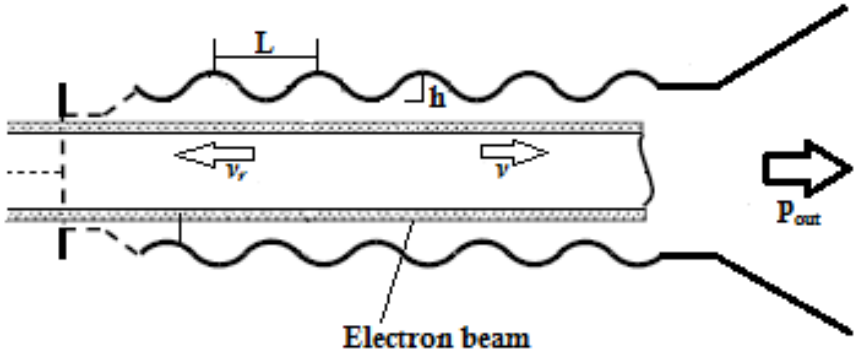

Figure 2.17: Relativistic single-stage BWO schematic.

Figure 2.17 shows the operation of a relativistic BWO with a sinusoidally corrugated waveguide. The electron beam interacts with the -1 harmonic of the structure, which is typically the TM_{01} mode in the case of cylindrical structures, and due to the small degree of deceleration of relativistic electrons, the depth of corrugation in the structure is small ($h/\lambda \ll 1$). The entrance to the beam tube is typically tapered up to the SWS and is cut off at its smallest point, preventing leakage into the cathode and reflecting the backward wave. As the backward wave propagates back through the structure it does not interact with the electron beam and is eventually radiated through an output window. The window is typically widened so as to prevent high-frequency breakdown occurring.

2.8 Klystrons

Klystrons are a family of linear beam amplifiers which use RF cavities to velocity modulate electron beams at a frequency dictated by the cavity resonances. Originally devised by the Varian brothers, Russell and Sigurd, in 1939 they are a variation in principle of lumped-element LC resonators [75] wherein an electron beam is passed through gridded gaps, between which are oscillating electric fields with sufficient field strength to modulate the velocities of any electrons passing through them. These electrons are subsequently accelerated or decelerated in accordance with the phase of the field at the time of modulation, the resultant variations in velocity causing bunching along the length of the beam and thus amplification at the frequency of the electric field. The amplified RF signal is then extracted by an output 'catcher' cavity. It was found that the ac fields required for bunching and RF energy extraction were best obtained by making the grids form part of the surfaces of cavity resonators [76].

While the mesh grid approach is useful in understanding the principles of klystron operation, it is seen to be inappropriate for general usage, with higher-energy beams destroying it in transit, and as such gridless gaps are standard. The past 60 years have seen the klystron as an amplifier grow in importance, first as a frequency source for

radar devices and, in more recent times, as a frequency-driving component in LINAC systems. Several variations to the core two-cavity design have also come to the fore, including reflex, multi-beam, extended interaction and multi-cavity klystrons, as well as hybrids like the travelling wave tube-klystron hybrid, the twystron.

Whilst two cavity klystrons are useful for understanding the operation of klystrons, in practice it is more common to use multiple-cavity structures. By introducing a cavity, up-tuned in frequency, prior to the output cavity it is possible to increase the degree of bunching in the beam. This is due to the cavity being excited by the bunch's presence and inducing a similar electric field which acts to accelerate any lagging electrons into the bunch. In such a way gain may be increased.

A similar method is used to increase the device bandwidth, through the use of a five-cavity klystron. The purposes of the first, fourth and fifth cavities have already been explained. In such a device, the second cavity is down-tuned to effectively demarcate the lower desired bandwidth limit while the third cavity is up-tuned to determine the upper limit. In this way, bandwidths of as high as 10% have been achieved, but this approach relies on having an output cavity capable of coupling out microwaves across the full frequency range.

However, the gridded two-cavity klystron is a useful starting point for understanding the operation of the klystron amplifier.

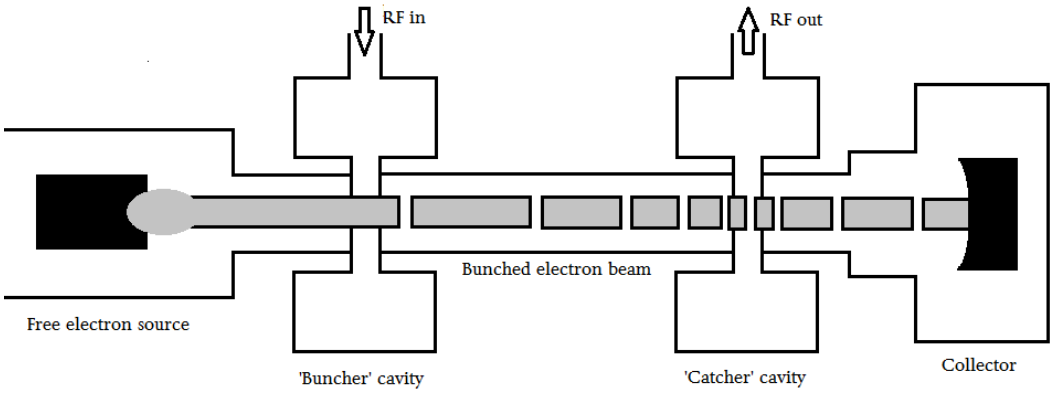

Figure 2.18: A 2-cavity klystron amplifier.

In a basic klystron (Figure 2.18), there are a number of key elements, namely the electron beam source, the buncher cavity, the catcher cavity, the drift tube and the microwave coupling system to allow an RF signal to be fed into the buncher cavity, and for the amplified microwave signal to be extracted. In addition, a depressed collector may be situated after the extraction cavity to salvage the spent electron beam and thus increase the overall efficiency, while additional cavities are typically introduced along the length of the drift tube to increase the device gain, efficiency and/or bandwidth.

A microwave signal matching what is typically the fundamental mode of the input cavity is fed in through some coupling method, often a coupling loop although slot coupling is another option, which excites the mode and induces an oscillating electric field across the cavity's interaction gap, the opening which allows coupling between the cavity and the electron beam as it passes through the drift tube. As electrons are emitted from the beam source, they proceed through the drift tube region, which is of sufficiently small dimensions that the feed signal is cut-off and thus cannot propagate from cavity to cavity without the beam's presence. The maximum drift tube radius may be calculated for a TE_{11} mode as [68]

$$f_{co}(TE_{11}) = \frac{\omega_{co}}{2\pi} = \frac{1}{2\pi}\left(\frac{1.84c}{r_0}\right) = \frac{8.79}{r_0} GHz \Rightarrow r_0(cm) < \frac{8.79}{f(GHz)} \tag{2.78}$$

If the electron beam has been accelerated by a voltage V_0 to a velocity v_0 and passes the first, gridded, gap it will be acted upon by an oscillating voltage $V_1 \sin \omega t$, the effect of which is reduced by a coupling coefficient, *M*. It is reasonable to assume that $V_1 \ll V_0$. *M* is always less than 1 and lowers the voltage to account for transit time effects. The electrons enter the gap with energy

$$\frac{1}{2}mv_0^2 = eV_0 \tag{2.79}$$

and exit with velocity *v* and a modified energy

$$\frac{1}{2}mv^2 - \frac{1}{2}mv_0^2 = eMV_1 \sin \omega t \tag{2.80}$$

The exit velocity may consequently be found as

$$v = v_0 \sqrt{1 + \frac{MV_1}{V_0} \sin \omega t} \tag{2.81}$$

or, from the assumption that V_1 is much less than V_0,

$$v \equiv v_0 \left(1 + \frac{MV_1}{2V_0} \sin \omega t\right) \tag{2.82}$$

Under the assumption that the input cavity's interaction gap is narrow enough that the electrons' transit times may be neglected, then it may be said that electrons enter then leave at a time t_1, travel a distance *l* and arrive at the second gap at a time t_2, which can be found from

$$t_2 = t_1 + \frac{l}{v} = t_1 + \frac{l}{v_0\left(1 + \frac{MV_1}{2V_0} \sin \omega t\right)} = t_1 + \frac{l}{v_0} - \frac{lMV_1}{2v_0V_0} \sin \omega t_1 \tag{2.83}$$

which, in terms of phase, is given as

$$\omega t_2 = \omega t_1 + \theta_0 - X \sin \omega t_1 \tag{2.84}$$

where the transit angle $\theta_0 = \omega l / v_0$ and the bunching parameter $X = MV_1\theta_0/2V_0$. When X is of a value greater than unity, it implies electron overtaking although this can be counteracted by space-charge effects, as shall be seen later.

At time $t_1 = 0$, when the beam is entering the buncher, the DC current is given as I_0 but in the time interval t_1 to $t_1 + dt_1$, the charge leaving the buncher and entering the catcher in the interval t_2 to $t_2 + dt_2$ is $I_0 dt_1$. Letting I_t be the sum of the DC and RF currents transported via the beam to the catcher then, through conservation of charge,

$$I_0 dt_1 = I_1 dt_2 \tag{2.85}$$

which may be combined with the differentiated equation 2.84 to give

$$I_t = \frac{I_0}{(1 - X \cos \omega t_1)} \tag{2.86}$$

For the fundamental mode (n = 1) I_t may be obtained from [76]

$$I_t = 2I_0 J_1(X) \cos(\omega t_1 - \theta_0) \tag{2.87}$$

where J_1 is a Bessel of the first kind. The maximum possible value of $J_1(X)$ is 0.582, which corresponds to $X = 1.84$.

With an output power calculated as the product of the RF current I_1 and the maximum achievable output gap voltage, which cannot exceed 90% of the beam voltage if the electrons are to retain sufficient energy to reach the collector [77], the output power may be found from

$$P_{out} = \frac{1.16I_0}{\sqrt{2}} \times \frac{V_0}{\sqrt{2}} = 0.58 I_0 V_0 = 0.58 P_{in}, \tag{2.88}$$

implying a peak operating efficiency of 58% for a two-cavity klystron, disregarding space-charge effects. Modern klystrons commonly achieve efficiencies higher than this (~65%) due to the fact that they do not operate at maximum beam modulation, as the above analysis describes.

In the above description of klystron operation, perhaps the most important factor is the gap coupling coefficient, *M*. It not only affects the velocity modulation and, consequently, the bunching process but it also plays a part in the eventual extraction of RF energy to the output cavity. Klystron gain may be said to scale with the coupling factor to the order of M^{2n}, where *n* is the number of cavities.

M may be defined as the ratio of the effective voltage presented across the interaction gap to the integral of the applied field, i.e.

$$M(\beta_e) = \frac{\int_0^g E_z(z) e^{j\beta_e z} dz}{\int_0^g E_z(z) dz} \tag{2.89}$$

where g is the gap length and $\beta_e = \omega / v_0$ is the beam propagation factor. It can be seen that *M* is a dimensionless quality and depends largely on f(z), also known as the field shape factor. In the case of gridded gaps, where a constant field is present, the denominator integral is trivial. However, by integrating over the entire z-axis, a more general case suitable for gridless gaps may be found. This takes the form

$$M(\beta_e) = \frac{\int_{-\infty}^{\infty} E_z(z) e^{j\beta_e z} dz}{\int_{-\infty}^{\infty} E_z(z) dz} = \frac{V_{eff}}{V_1} \tag{2.90}$$

While as many calculations for the coupling coefficient exist as there are types of gap edges (e.g. rounded, knife-edge, square) the knife-edge assumption is perhaps

the most common. In such a structure, the field at a gap with an RF voltage V_1 at a drift tube radius of a is found from [78]

$$E_z(a,z) = \frac{1}{\pi g/2} \frac{V_1}{\sqrt{1-\left(\frac{z}{g/2}\right)^2}} \tag{2.91}$$

Inserting this into the generalised coupling efficient equation and integrating, the coupling factor for gridless gaps at $r = a$ is obtained,

$$M(a,\beta_e) = J_0\left(\frac{\beta_e g}{2}\right) \tag{2.92}$$

where J_0 is the beam current density. Taking this as the boundary condition, M can then be calculated at any point in the gap and averaged over the beam. The result of this is found in the form

$$M = J_0(\beta_e g/2)\frac{\sqrt{I_0^2(\gamma b) - I_1^2(\gamma b)}}{I_0(\gamma a)} \tag{2.93}$$

where $\gamma = \sqrt{\beta_e^2 - k^2}$, a is the drift tube radius and b is the beam radius.

2.8.1 Space-Charge Effects

As electrons leave the gap, the effect of their acceleration and deceleration is the formation of electron bunches along the length of the electron beam, an effect that is countered by rising space-charge forces in the electron bunches as the electron density increases, causing them to repel and thus for debunching to occur. The bunching process is reflected in the dispersion relation

$$\omega = k_z v_b \pm \frac{\omega_p}{\gamma_b} \tag{2.94}$$

where the + sign is associated with the fast space-charge wave and the – sign with the slow. ω_p, the relativistic beam plasma frequency, is found from $\omega_p = \sqrt{\rho_b e/\varepsilon_0 m \gamma_b}$, ρ_b being the charge density on the beam. The interaction of these two

waves determines the bunching peak z_b, the point of maximum amplification at which the extraction gap should be situated. In a simple, linear regime, this is given as

$$z_b = \frac{\pi\gamma_b v_b}{2\omega_b} \equiv \frac{\lambda_b \gamma_b}{4} \propto \frac{\gamma_b^{3/2} v_b^{3/2}}{J_b^{3/2}} \tag{2.95}$$

where J_b is the beam current density and $\lambda_b = 2\pi v_b/\omega_b$. Beyond z_b, debunching occurs, eventually resulting in the bunch disappearing at $z = 2z_b$ (figure 2.19).

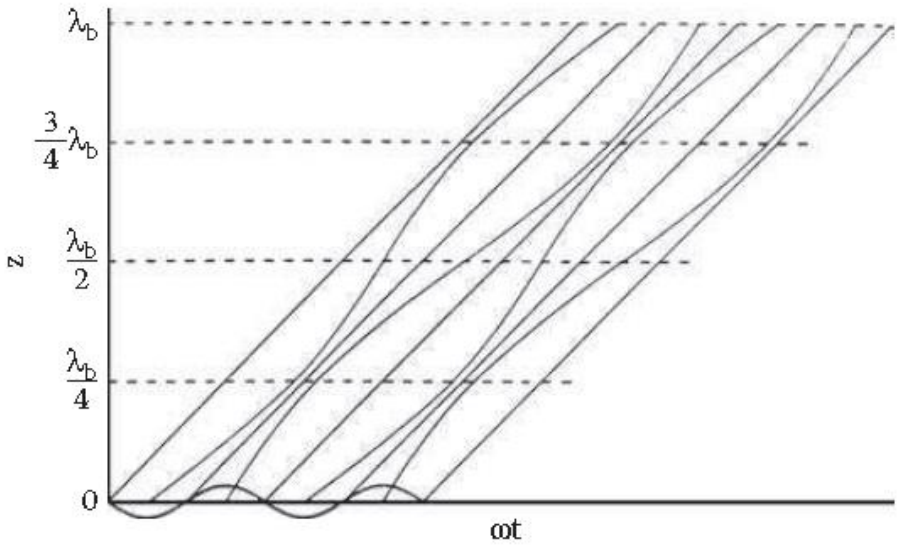

Figure 2.19: Applegate diagram showing bunching with distance in a klystron, taking into account space-charge effects [38].

While this typically holds true for an infinite beam, where the electric fields and, consequently, space-charge forces, are constrained to only contribute in the axial direction, finite beams also possess electric fields with a radial component, thus reducing the axial component and, by extension, the plasma frequency by a *plasma reduction factor*, *R*. The reduced plasma frequency is expressed as ω_q and varies non-linearly as a function of the beam radius and the ratio of the drift-tube radius to the beam radius. The plasma reduction factor is defined as [76]

$$R = \frac{1}{\sqrt{\left(1 + \frac{T_n^2}{\beta_e^2}\right)}} \tag{2.96}$$

where the various values of T_n correspond to space-charge wave-numbers. Calculated values of these may be found in work by Branch and Mihran [79].

As a bunch approach the interaction gap of the next cavity it induces a positive charge on the nearest side of the interaction region. As this bunch progresses into the gap, the charges redistribute themselves over the length, flowing to the other side of the gap by means of the loaded cavity. If these charges are understood to be ac charges, then the polarity of the charges will change with time and current will begin to flow in the opposite direction. This current flow across the load of the cavity will act to produce a potential difference across the gap and slow down the bunch, extracting energy which is then dissipated in the load resistance. The rate at which energy is extracted from the bunch [69]

$$F_{v_0} = \int_{-g/2}^{g/2} E|I_1|e^{-jk_e z}dz \tag{2.97}$$

where g is the gap width, I_1 the beam ac current, E the electric field strength and k_e the electronic wavenumber.

This must equal the rate of energy dissipation in the load, given by the product of the gap voltages and current $I_g V_g$, and it may be shown that the ac current may be related to the gap current by the gap coupling coefficient, M, i.e.

$$I_g = M|I_1| \tag{2.98}$$

As such, it stands that the gap coupling coefficient also affects how the beam drives the cavity gap.

The beam RF current, as modified by space-effects, may now be found from

$$I_1 = -j\frac{MI_0V_1}{2V_0}\frac{\omega}{\omega_p}\sin(\beta_p z)e^{-j\beta_e z} \tag{2.99}$$

where $\beta_p = \omega_p/v_0$. This holds only in the limit of small signals, however.

2.8.2 RF Cavities

Klystron cavities may be analysed as being analogous to LC resonant circuits. As the frequency for a simple lumped-element circuit is increased, the circuit is modified a closely-spaced parallel-plate capacitor replacing the multiple-capacitor arrangement and a single half-turn replacing the multi-turn inductor. Further frequency increases are achieved by adding inductors in series and increasing the capacitor plate separation until the inductors become a hollow toroid, concentrating the magnetic field in the capacitive (gap) region and the electric field within the central cavity region [80]. Typically, this is simplified to such a structure as is illustrated in figure 2.20.

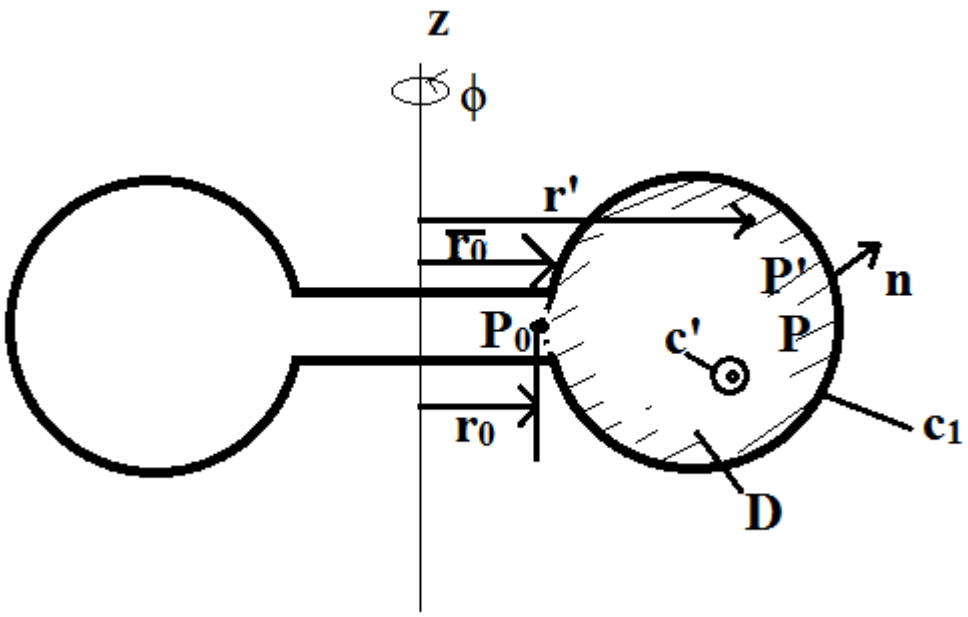

Figure 2.20: Re-entrant klystron cavity cross-section [81].

A re-entrant cylindrical cavity is depicted in figure 2.20, where the cylindrical co-ordinates of *r*, ϕ and *z* are used. In such a cavity, the fundamental mode is excited with the field components defined as

$$E_z = \frac{1}{j\omega\epsilon_0}\frac{1}{r}\frac{\partial u}{\partial r}, E_r = -\frac{1}{j\omega\epsilon_0}\frac{1}{r}\frac{\partial u}{\partial z}, u = rH_\phi \tag{2.100}$$

In this case, *u* satisfies the wave equation

$$\frac{\partial}{\partial r}\left(\frac{1}{r}\frac{\partial u}{\partial r}\right) + \frac{\partial}{\partial z}\left(\frac{1}{r}\frac{\partial u}{\partial z}\right) + \frac{k^2}{r}u \equiv L(u) + \frac{k^2}{r}u = 0 \tag{2.101}$$

under the boundary condition stating that at

$$\frac{\partial u}{\partial n} = 0 \tag{2.102}$$

where c_1 is the wall section of the boundary of *c* in D, and $k^2 = \omega^2\epsilon_0\mu_0$ [81].

This may be solved through the application of Green's function, G(P, P'; k^2) for the points P and *P'* in *D*. It is possible to determine the input admittance for a given cavity at the gap edge $\overline{P_0}$ by

$$\vec{Y}(\overline{P_0}) = 2\pi[u(P_0) - u(\overline{P_0})] - j\omega\epsilon_0 \int_{c_0} G(P, P'; k^2)\boldsymbol{E}' \cdot ds' \tag{2.103}$$

The admittance may also be defined as

$$\vec{Y}(\overline{P_0}) = \frac{1}{j\omega L} + j\omega C_1 \tag{2.104}$$

where C_1 is the capacitance of the cavity and is found from

$$C_1 = 4\epsilon_0 r_0 \ln \frac{e\sqrt{(r_1 - r_0)^2 + h^2}}{2d} \tag{2.105}$$

and the inductance, *L*, is found from

$$L = \frac{\mu_0}{2\pi} \int_D \frac{dS'}{r'} \tag{2.106}$$

The gap capacitance, $C_{0,}$ is given as

$$C_0 = \epsilon_0 \frac{\pi \overline{r_0^2}}{d} \tag{2.107}$$

However, this does not take account of the effect of the gap on the circuit. Assuming a space constant electric field on the curved surface, radius r_i, of the gap region, the new gap capacitance C_0, is stated as

$$C_0 = \epsilon_0 \frac{\pi\left(\overline{r_0^2} - \overline{r_i^2}\right)}{d} + \epsilon_0 \frac{\pi\left(\overline{r_i^2}\right)}{d} \gamma\left(\frac{d}{\overline{r_i}}, k\overline{r_i}\right) \tag{2.108}$$

where γ is a capacitance reduction factor, the values of which may be found in [81].

In either situation, the total capacitance, *C*, is calculable as the sum of C_0 and C_1. While the above calculations give a good approximation of the properties of many of the more common cavity types, there has been a wealth of work done on the subject in recent years [82] [83], particularly with the rise in availability of fast, powerful modelling codes.

In using the resonant circuit analog for a cavity resonator, it is possible to determine the properties of the cavity. The cavity's resonant frequency may be given as

$$\omega_0 = \sqrt{\frac{1}{LC}} \tag{2.109}$$

and we also introduce the cavity quality factor, Q. A factor which highly influences cavity losses and bandwidth, it is defined as

$$Q \equiv \omega_0 \tau_{RC} = \omega_0 RC \tag{2.110}$$

where R is the parallel combination of the resistance from the beam, R_b, from the circuit, R_c and from external sources, R_e.

Each cavity also possesses a characteristic impedance, Z_c, which is set with the geometry of the cavity without beam coupling. The impedance peaks when the driving frequency and resonant frequency are matched and drops when there is a mismatch, the sharpness of the drop dictated by Q. It is defined as

$$Z_c \equiv \frac{R}{Q} \approx \frac{1}{\omega C} \tag{2.111}$$

Physically, the description of R/Q is that it is the ratio of the square of the voltage across the cavity gap and the energy stored within the cavity [76], i.e.

$$\frac{R}{Q} = \frac{V^2}{2\omega_0 W} \tag{2.112}$$

2.8.2 Klystron Gain and Bandwidth

In multiple-cavity klystrons, penultimate cavities largely exist in order to present an inductive load to the passing electrons, shortening the electron bunch lengths and increasing the RF current component of the beam. The output circuit then acts to present a total impedance of R_T to the RF current, the product of these two being equal to the beam voltage V_0, which is necessary in order for RF current extraction. Assuming a simple cavity resonator, the half-power bandwidth is given by

$$\frac{\Delta\omega}{\omega_0} = \frac{1}{Q_T} = \frac{R}{Q}\frac{1}{R_T} \tag{2.113}$$

thus showing that the bandwidth of a klystron is largely set by the R/Q of the output circuit.

The total impedance is typically matched to the load impedance, R_L, to allow for effective RF extraction. Taking this assumption in conjunction with the output voltage and gain being proportional to R_T, the relationship

$$G \times BW \propto R_L \times \frac{\Delta\omega}{\omega_0} = \frac{R}{Q} \tag{2.114}$$

may usually be held to be true [76].

In multiple cavity klystrons where gain is to be maximised, the cavities are normally stagger-tuned to frequencies above the operating band. As the beam is velocity modulated by a cavity, the subsequent bunching causes an increased RF current due to tighter bunching. These higher RF currents then excite subsequent cavities, thus increasing bunching further, and so on. However, the original modulation still exists and the RF current at the output gap is a sum of all previous RF currents. The current gain between cavities is given as

$$\begin{aligned} \frac{I_n}{I_m} = G_{mn}(\omega) &= g_{mn}(\omega)Z_m(\omega) \\ &= \frac{1}{2}jZ_m(\omega)\frac{I_0}{V_0}\frac{\omega}{\omega_q}M_m M_n \sin(\beta_q l_{mn})e^{-j\beta_e l_{mn}} \end{aligned} \tag{2.115}$$

where

$$Z_n(\omega) = \left(\frac{R}{Q}\right)_n \left[\frac{1}{\frac{1}{Q_{Tn}} + j\frac{\omega^2 - \omega_{0n}^2}{\omega\omega_{0n}}}\right] \tag{2.116}$$

For a three-cavity klystron, the overall current gain may be expressed as

$$G(p) = \frac{I_3}{I_1} = (g_{12}g_{23}Z_2 + g_{13})Z_1 \tag{2.117}$$

where p is a complex variable $p = \sigma + js$, with an imaginary part s shifted in relation to ω_0 in accordance with the following relations:

$$\begin{gathered} p = \sigma + js \\ js = j\frac{\omega - \omega_0}{\omega_0} \\ \frac{\omega - \omega_0}{\omega_0} \approx 2 \end{gathered} \tag{2.118}$$

From the above approximation, equation 2.21 may now be written as

$$Z_n(p) = \frac{1}{2}\left(\frac{R}{Q}\right)_n \left[\frac{1}{p - p_n}\right] \tag{2.119}$$

with

$$\begin{gathered} p_n = -\frac{1}{2Q_n} + js_n \\ s_n = \frac{\omega_n - \omega_0}{\omega_0} \end{gathered} \tag{2.120}$$

Finally, the power gain may be obtained from

$$\begin{aligned} G(p) &= \frac{4}{Q_{e1}Q_{e3}} \frac{|Z_3 G_{13}|^2}{(R/Q)_1 (R/Q)_3} \\ &= \frac{4}{Q_{e1}Q_{e3}} \frac{|(g_{12}g_{23}Z_2 + g_{13})Z_1 Z_3|^2}{(R/Q)_1 (R/Q)_3} \end{aligned} \tag{2.121}$$

2.9 Summary

Electromagnetic waves may propagate through any conductive medium with a frequency governed by the dimensions of the transmitting structure, as well as the

medium's permeability and permittivity, in a fashion dictated by Maxwell's equations. By combining these structures' inherent electromagnetic properties with a charged particle beam, it is possible to generate amplified EM radiation at a frequency dictated by the structural dimensions. In the case of klystrons, the effects of a field within a resonant cavity can modulate the velocities of passing electrons, leading to bunches of high electron density, and thus amplification. For backward wave oscillators, the beam is passed through a structure which allows for the generation of slow space-charge waves which are reflected within the structure and used as a seed to initiate oscillations within the beam. Both have their own benefits in regards bandwidth, gain, efficiency and manufacturability, although the electron beam generated from the pseudospark discharge has the potential for effective operation within both types of device, as well as many others.

Chapter 3:

Design, Simulation & Construction

3.1 Introduction

The generation of millimetre waves is a complex process that has, in recent years, been made simpler through the use of mathematical analysis software (MathCAD, MATLAB); electromagnetic modelling software capable of analysing and simulating complex geometries and operational parameters within relatively short periods of time and to a high level of accuracy; and computer-aided design (CAD) packages such as Autodesk Inventor, thus reducing both cost and the time required to optimise mm-wave generating structures.

This chapter shall describe the realisation of such structures, charting the analytical design, simulation and construction of a 200 GHz BWO and a multi-cavity klystron with a centre frequency of 94 GHz. This includes the coupling to and from the devices, as well as the steps taken to ensure vacuum integrity and for the injection of the pseudospark electron beam. The design, construction and testing of a prototype coupling system for use with the W-band klystron shall also be presented.

Design shall primarily be based around the use of the theory outlined in chapter 2, and further refinement and optimisation is achieved through numerical simulation. Two software packages were used in the analysis of the aforementioned structures: MAGIC, a finite-difference time-difference (FDTD) particle-in-cell code, and CST Microwave Studio, a finite integration technique (FIT)-based electromagnetic modelling package geared towards high-frequency component analysis. The operating features of these packages shall be briefly mentioned, along with pertinent simulation results.

Finally, the stages involved in the physical construction of each device will be presented, detailing as far as is possible the motivation for the particular

manufacturing techniques used and any concessions made with their eventual realisation.

3.2 The Simulation Codes

Of the two simulation codes used throughout the design phases of this work, CST Microwave Studio was primarily chosen during the 'cold' test analysis of microwave structure, in that no electron beam was present. This included the eigenmode testing of resonant structures, transmission and loss calculations for coupling systems and the generation of dispersion diagrams for comparison with those obtained by numerical analysis. In contrast, MAGIC has many applications in the modelling of plasmas as well as RF structures and so this was used not only for the eigenmode testing of some RF structures, namely resonant cavities, but also for examining the beam-wave interactions within the examined microwave tubes, including calculations of device output power, gain and efficiency.

3.2.1 CST Microwave Studio

CST Microwave Studio is known as a finite integration technique (FIT) code [84] which uses a generalised form of the finite-difference time-domain (FDTD) technique used in packages such as MAGIC. Based on the premise that all electromagnetic problems may be solved through the use of Maxwell's equations, it allows for their reformulation in an integral form adapted for a computer simulation environment. It is a finite volume discretisation scheme but allows for these volumes to be defined in any way that they may be slotted neatly together, thus hexahedra and tetrahedra may be used to construct meshes for geometrically complex shapes, and the use of integral balances allows for stability and conservation properties to be proven before numerical calculations begin.

This process begins with the restriction of electromagnetic fields to a simply connected and bounded space region Q, containing the region to be analysed. This is then broken down into a series of simplicial interconnected cells, which forms the computational grid, with each edge being given an orientation. In this way, the union

of these edges may be termed a directed graph. Within this system, the integral forms of Maxwell's equations may be applied and solved for the various facets, edges and volumes and the results calculated as a series of matrices. These are then extrapolated forwards in time and space and averaged across the surrounding volumes, thus allowing for the development of a comprehensive model of an electromagnetic system. FIT systems are highly adaptable to complex geometries and may be improved further using adaptive mesh techniques, such as those applied in CST Studio Suite, though the effect these systems have on runtimes may sometimes be restrictive.

3.2.2 MAGIC

MAGIC uses the FDTD method for the calculation of electromagnetic field effects but is also known as a particle-in-cell code (PiC), using Lagrangian and Eulerian mesh frames to track the movements of individual particles in continuous phase space and to analyse the development of currents and densities [85]. Using these techniques, it is possible to model the behaviour of plasmas and, in the case of this work, the effects of electromagnetic structures on the flow of particles, namely electron beams. MAGIC renders structure using either a 2-and-a-half-dimensional framework (MAGIC-2D) for rotationally symmetric structures, or in three dimensional space (MAGIC-3D), rendering structures via either Cartesian (x, y, z), polar (φ, r, z) or cylindrical (r, φ, z) coordinate systems.

Typically, PiC codes represent groups of particles as *super-particles* which, due to the Lorentz Force equations relying only on charge-to-mass ratios, behave in a similar fashion to how individual particles would. The ratio of particles to super-particles must be sufficiently low to allow for accurate behavioural models to be generated, yet large enough to allow for manageable runtimes. These details, along with other macro-quantities such as current density, are assigned to the super-particles as particle weighting.

Super-particle behaviour relies largely on the 'pusher' system behind them, moving the particle from one cell to the next and predicting its state when it does so. Pushers are generally expected to be both accurate and efficient, yet these still contribute much of a simulation's runtime. For MAGIC, the leapfrog method is typically used, an implicit solver system which calculates particle velocity from fields updated prior to calculation. In brief, the leapfrog method calculates the position, x, and velocity, v, of super-particles over a time step Δt using

$$\begin{aligned} \frac{\mathbf{x}_{k+1} - \mathbf{x}_k}{\Delta t} &= \mathbf{v}_{k+1/2}, \\ \frac{\mathbf{v}_{k+1/2} - \mathbf{v}_{k-1/2}}{\Delta t} &= \frac{q}{m}\left(\mathbf{E}_k + \frac{\mathbf{v}_{k+1/2} + \mathbf{v}_{k-1/2}}{2} \times \boldsymbol{B}_k\right) \end{aligned} \tag{3.01}$$

where *k* refers to quantities carried over from the previous time step, *k* + 1 to the quantities calculated for the next time step and velocities are calculated in the interval between the two time steps. Electric fields are calculated using the FDTD method above.

While simulation particles may be positioned anywhere within a cell, macro-quantities are evaluated only on the cell edges, just as with fields. Particles, therefore, are modelled to have a shape determined as $S(\mathbf{x} - \mathbf{X})$, where **x** is the position and **X** the observation point, which satisfies the conditions for space isotropy, charge conservation and convergence for higher-order terms. Similarly, calculated fields cannot be used directly in the particle mover and have to be interpolated through field weighting,

$$\mathbf{E}(\mathbf{x}) = \sum_i \mathbf{E}_i S(\mathbf{x}_i - \mathbf{x}) \tag{3.02}$$

where *i* labels the grid point. By using the same weighting scheme for both particles and fields and ensuring the correct space symmetry, accuracy through conservation of momentum may be obtained. Due to the linear nature of the structures and particle behaviour examined in this work, collisional models may be neglected in this thesis.

3.3 G-band BWO

A G-band (140 – 220 GHz) BWO using a sinusoidally rippled wall as a slow wave structure was designed for operation with the pseudospark discharge acting as an electron beam. Rather than coupling the RF signal out near the PS electron gun, the BWO was designed as a mildly relativistic device, reflecting the amplified microwave signal from a cut-off structure at the beam input point and outputting via a launching horn. In simulations with MAGIC-3D, this reflection was achieved by setting the beam tube radius to less than the cut-off radius for the selected frequency of 200 GHz but in experiments this was enhanced by placing a tungsten mesh adjacent to the inside face of the PS anode and to the entry point to the device. Such mesh structures have been used with PS e-beams in the past and have been found to have little effect on beam current and plasma development.

A sinusoidally rippled SWS may be expressed in the form

$$R(z) = R_0(1 + h\cos(k_0 z)) \tag{3.03}$$

where R_0 is the mean radius of the structure, h is the amplitude of the corrugation and $k_0 = 2\pi/L$ is the corrugation wavenumber. It is typical in these types of SWSs to select a value of R_0 that lies close to the cut-off for a selected frequency in order to prevent the propagation of higher-order modes. If it is intended to operate the device at 200 GHz, as was stated in chapter 1, then the circular waveguide cut-off is, from equation 2.79,

$$R_0(cm) = \frac{8.79}{f(GHz)} = \frac{8.79}{200} = 0.044$$

Based on this, a mean radius of 0.5 mm was used. Not only does this lie close to the cut-off value but it also coincides with the minimum machinable radius for wire-spark erosion manufacture. While this may not be relevant for manufacture of the more complex SWS, it can be used in the construction of collimating structures for the testing of the PS e-beam with similar cross-sectional dimensions.

In order to establish cut-off at the beginning of the structure, the beam entry point was selected to lie below the cut-off radius and was therefore selected to be 0.41 mm. For the SWS corrugations, three variables had to be determined: the corrugation depth, periodic length and number of corrugations. The first two were determined by means of the analysis of corrugated waveguides determined by Barroso [86]. Using the definition declared in equation 3.01 and assuming spatial periodicity along z, azimuthally symmetric TM electric fields are expanded in a spatially harmonic series according to Floquet's theorem. This eventually results in an infinite series of equations for the amplitude coefficients A_n

$$\sum_{n=-\infty}^{n=\infty} A_n C_{n,m}(\omega, k_{z0}, h, R_0, L) = 0 \tag{3.04}$$

where

$$C_{n,m} = \left[1 + \frac{2\pi}{L}(n-m)\right]\frac{k_{zn}}{k_{\perp n}^2}\int_0^L dz J_0\left(k_{\perp n}R(z)\right)\cos\left((n-m)\frac{2\pi}{L}z\right), \tag{3.05}$$

$$k_{zn} = k_{z0} + \frac{2\pi}{L}n, 0 \leq k_{z0} \leq \frac{2\pi}{L}\text{and} \tag{3.06}$$

$$k_{\perp n}^2 = \frac{\omega^2}{c^2} - k_{zn}^2 \tag{3.07}$$

Setting

$$det\left\|C_{n,m}\right\| = 0 \tag{3.08}$$

it is possible to determine the eigenvalues for a given h, R_0 and L. With the assistance of Dr Liang Zhang and with reference to the dimensional profile of an existing BWO within the department, a peak-to-peak amplitude of 0.2 mm was found to meet the guideline of $h < \frac{\lambda}{4}$ typically applied to relativistic BWOs [86] while a periodic length of 0.467 mm yielded a fundamental operating frequency of ~197 GHz. A decision was made to use a 30-period BWO structure to ensure the structure was long enough to provide sufficient feedback and gain to achieve oscillation.

3.3.1 BWO Dispersion

While the analysis of the SWS dispersion outlined previously takes account of both geometry and the electron beam, it does not fully hold for a PS-derived beam. This is

due to the ion channel which forms during the beam propagation and acts to constrain radial growth. In order to plot the dispersion of such a configuration, the inclusion of the plasma must be accounted for.

A solid, uniform electron beam of density n_b and radius $R_b < R_0 - h$ propagates through an SWS filled with a collisionless, cold and uniform plasma with a density of n_p, with plasma frequency and beam plasma frequencies of $\omega_p = \sqrt{e^2 n_p / m_e \epsilon_0}$ and $\omega_b = \sqrt{e^2 n_b / m_e \epsilon_0}$ respectively. The beam current lies below the space-charge-limiting current for a smooth-walled waveguide with similar dimensions, beam electrons all possess identical axial velocity, v, the beam has an equilibrium position and it is free from any deformation. If an infinitely large guiding magnetic field is assumed then the only non-vanishing terms in the relative dielectric tensor lie along the diagonal [87], i.e.

$$[\epsilon] = \begin{bmatrix} 1 & 0 & 0 \\ 0 & 1 & 0 \\ 0 & 0 & \epsilon_{zz} \end{bmatrix} \tag{3.09}$$

where

$$\epsilon_{zz} = 1 - \left(\frac{\omega_p}{\omega}\right)^2 - \frac{\omega_b^2}{\gamma^3(\omega - k_n v)^2}, \tag{3.10}$$

γ is the relativistic factor and k_n is the wavenumber.

In a corrugated structure, only the TM waves may perturb the beam density and axial velocity, so considering only these, the axial and radial electric fields are given from

$$E_z(r,z) = \sum_{-\infty}^{\infty} E_{zn} e^{i(k_n z - \omega t)} \tag{3.11}$$

$$E_r(r,z) = \sum_{-\infty}^{\infty} \frac{ik_n}{\frac{\omega^2}{c^2} - k_n^2} e^{i(k_n z - \omega t)} \frac{dE_{zn}}{dr} \tag{3.12}$$

where k_z is the axial wavenumber and

$$k_n = k_z + nk_0$$

$$E_{zn} = A_n J_0\left(\frac{x_n}{R_o} r\right), 0 \le r \le R_b$$
$$= B_n J_0\left(\frac{y_n}{R_o} r\right) + C_n J_0\left(\frac{y_n}{R_o} r\right),\ R_b \le r \le \mathrm{R(z)} \tag{3.13}$$

$$x_n^2 = R_0^2\left(\frac{\omega^2}{c^2} - k_n^2\right)\left[1 - \frac{\omega_p^2}{\omega^2} - \frac{\omega_b^2}{\gamma^3(\omega - k_n v)^2}\right] \tag{3.14}$$

$$y_n^2 = R_0^2\left(\frac{\omega^2}{c^2} - k_n^2\right)\left(1 - \frac{\omega_p^2}{\omega^2}\right) \tag{3.15}$$

From the conditions of continuity of E_r and E_z at $r = R_b$, the constants B_n and C_n may be expressed in terms of the constant A_n, i.e.

$$B_n = -\frac{\pi\delta}{2} K_n A_n, C_n == -\frac{\pi\delta}{2} L_n A_n$$

$$K_n = y_n J_0(x_n\delta) N_1(y_n\delta) - y_n J_1(x_n\delta) N_0(y_n\delta)$$
$$L_n = y_n J_0(x_n\delta) J_1(y_n\delta) - y_n J_0(x_n\delta) J_1(y_n\delta) \tag{3.16}$$
$$\delta = R_b/R_0$$

The definitions of the RF electric fields are subject to the boundary condition

$$E_t\big(r = R(z)\big) \propto E_z\big(r = R(z)\big) + E_r\big(r = R(z)\big)\frac{dR(z)}{dz} = 0 \tag{3.17}$$

i.e. that at the perfectly conducting waveguide surface, the tangential electric field $E_t = 0$.

Through substitution into equation 3.10, a dispersion relation determining ω from k_z is found, based on a nontrivial set of solution of amplitude A_n. However, this is based on the coordinate z and the as-yet-unknown constant A_n. These may be eliminated by multiplying 3.10 by $e^{-imk_0 z}$ and integrating from $z = -\pi/k_0$ to $z = \pi/k_0$. The resulting dispersion relation is

$$\sum_{n=-\infty}^{\infty} A_n \int_{-\frac{\pi}{k_0}}^{\frac{\pi}{k_0}} e^{i(n-m)k_0 z} \cdot \left(1 + \frac{ik_n}{\frac{\omega^2}{c^2} - k_n^2} \frac{d}{dz}\right) \times \left[K_n J_0\left(\frac{y_n}{R_0} R(z)\right) + L_n N_0\left(\frac{y_n}{R_0} R(z)\right)\right] dz = 0 \tag{3.18}$$

This dispersion relation was then solved using methods outlined by Minami et al. [87] and plotted for beam voltages ranging from 10 to 50 kV. Whilst the plasma densities in the device have yet to be experimentally measured, they have been determined through simulation to have values of n_p = 6 x 10^{12} cm^{-3} and n_b= 7 x 10^{12} cm^{-3} [88].

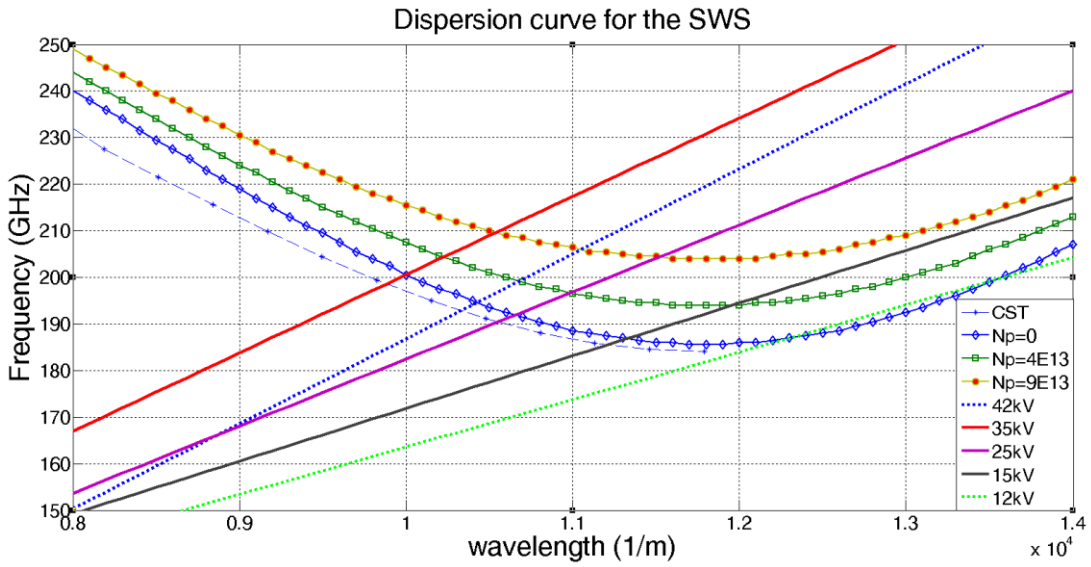

Figure 3.1: Dispersion diagram for various beam lines and plasma densities.

Figure 3.1 shows the TM_{01} mode dispersion for the desired BWO geometry, with and without the presence of the plasma taking into account the change of the discharge current as a function of voltage [89]. Taking n_p to be 4 x 10^{12} cm^{-3}, it can be seen that the expected point of intersection at 200 GHz lies between the beam lines for 25 kV and 35 kV. However, in MAGIC simulations the plasma ion channel was not accounted for, and so the dispersion for n_p = 0 was used in order to determine the

beam voltage for simulation. This allowed for the determination of a beam voltage of 35 kV for simulation purposes.

3.3.2 BWO Simulation

The designed BWO structure was subsequently created in the FDTD-PiC code MAGIC-3D and comprised of a cylindrical waveguide of length 0.89 mm and radius 0.41 mm, a single-period-length (0.47 mm) taper up to the SWS and a 30-period SWS with a mean radius of 0.5 mm and a peak-to-peak amplitude of 0.2 mm. The tube was filled with vacuum and the outer walls of the structure were set as a perfect conductor. The MAGIC rendition of this structure may be seen in figure 3.2.

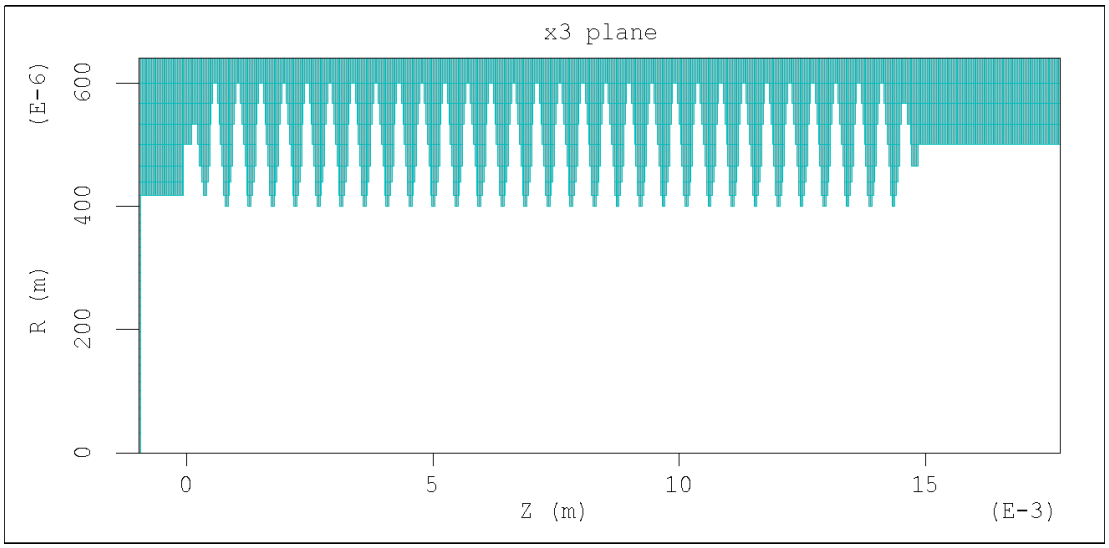

Figure 3.2: Cross-section of BWO geometry as rendered in MAGIC-3D.

The axial and radial resolutions, Δz and Δr, were taken as functions of the periodic length and corrugation depths respectively, while the azimuthal resolution, $\Delta\phi$, was set at a value of $\Delta\phi = 2\pi/6$. The axial resolution was set to $\Delta z = L/15 \approx 0.03$mm while two values of Δr were used, defined as

$$\Delta r_{min} = \frac{2.5h}{7.5} \approx 0.03 \text{ mm}, \qquad \Delta r_{max} = \frac{8h}{7.5} \approx 0.11 \text{ mm}$$

Δr_{max} was used to mark the drift tube, beam entry tube and the thicker parts of the conducting walls, while the SWS was rendered with the smaller Δr_{min}.

The electron beam was input as a hollow beam of 0.35 mm mean radius and a thickness of 0.2 mm from the left-hand side of the device pictured in figure 3.2. A hollow beam was used in order to reduce simulation time, although comparison with a single run with a solid beam found that the error in using the hollow beam was < 5%. To better illustrate PS performance, the 35 kV input beam voltage was pulsed, with a rise-time of 1.2 ns and a total pulse length of 10 ns (figure 3.3). The beam current of 1.5 A was kept constant.

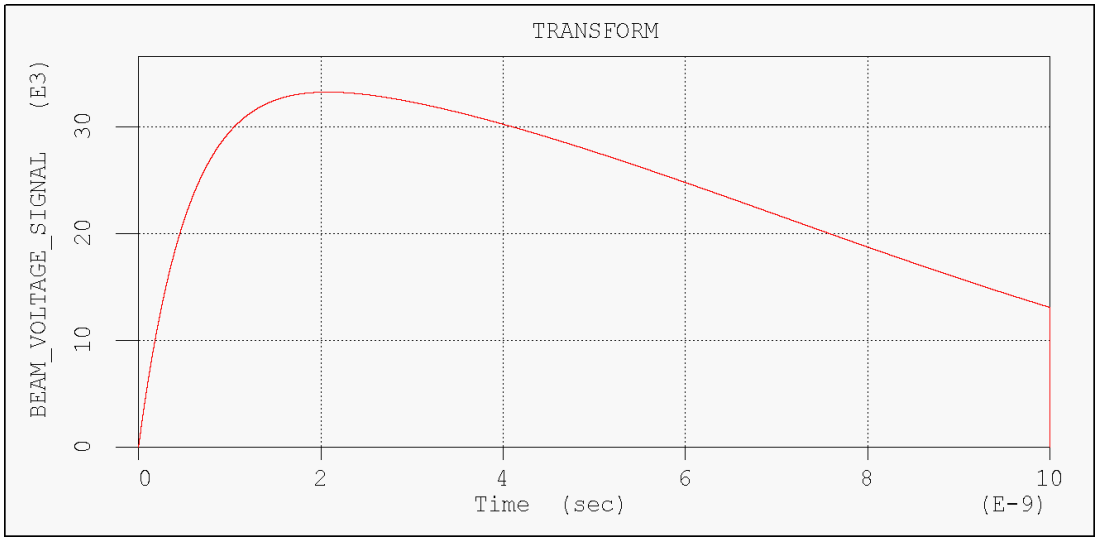

Figure 3.3: Beam voltage swept over time.

Whilst MAGIC is capable of modelling ion environments, for the purposes of calculating the performance of the BWO, it was deemed sufficient to constrain the electron beam using a simple solenoidal magnet along the length of the device, with a magnetic field strength of 5 T. This is large enough to constrain the beam but not enough to induce pinching effects. The effect of the focussing may be seen in the plot of pitch angle as a function of axial position, z (figure 3.4). It can be clearly seen that there is little in the way of radial spread of the beam over the interaction length (15 mm), which is in keeping with the performance of the PS-derived e-beam.

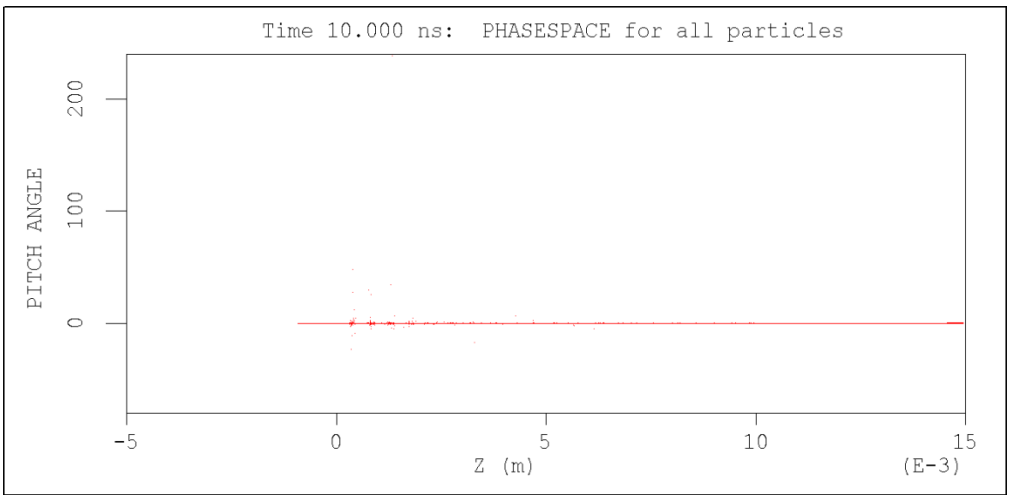

Figure 3.4: Beam pitch angle measured over interaction length, showing little deviation from the normal.

A run-time of 10 ns was set to fully allow the oscillations in the tube to develop, and the simulation was run at double precision to allow for more accurate measurements. Figure 3.5 shows the development of the electron beam as it progresses through the SWS, focussed and keeping an approximately constant density. The backward wave progresses towards the left hand side of the structure before being reflected by the cut-off waveguide section and the peak power measured via the 'observe field_power s.da' command at an outlet port situated at the right-hand side of the structure. Points were declared along the length of the SWS and the electric field integrals observed, along with fast Fourier transforms of the observed values, in order to determine the frequencies of the generated signal.

Figure 3.5 shows the electron beam's path as it travels in the z-direction.

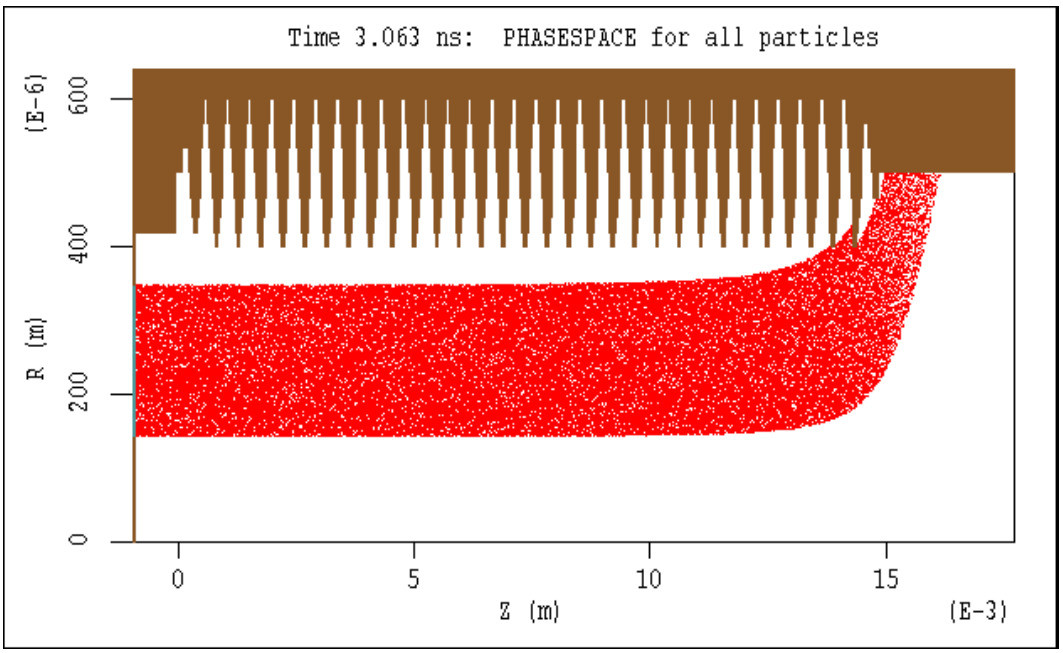

Figure 3.5: MAGIC-simulated G-band BWO operation.

Over the 10 ns runtime, a TM_{01} wave was generated at the device output, with the mode pattern approximated through the cross-sectional analysis of the electromagnetic field pattern at discrete moments, most notably at the end of the slow-wave structure. A measurement of the power flow through the output port with time detected an average output power of 2.5 W from the tube (Figure 3.6). While the efficiency of this device was admittedly low (< 1%), particularly with respect to the efficiencies typically achieved by some BWOs, the generation of several watts of power at such frequencies is uncommon and, as such, showed enough usefulness to warrant further investigation with the view to further improving the design upon demonstration of a working device.

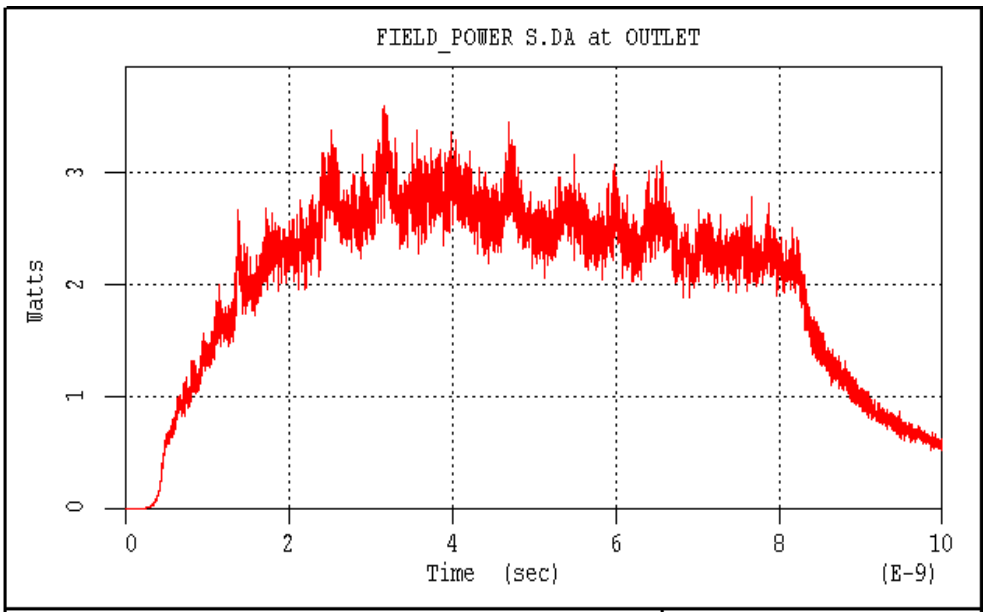

Figure 3.6: Predicted output power of the G-band BWO.

The frequency of the output TM_{01} wave was determined through the FFT of the electric field in the axial direction at the end of the SWS (figure 3.7), which yielded frequency spectrum ranging from 186 to 208 GHz.

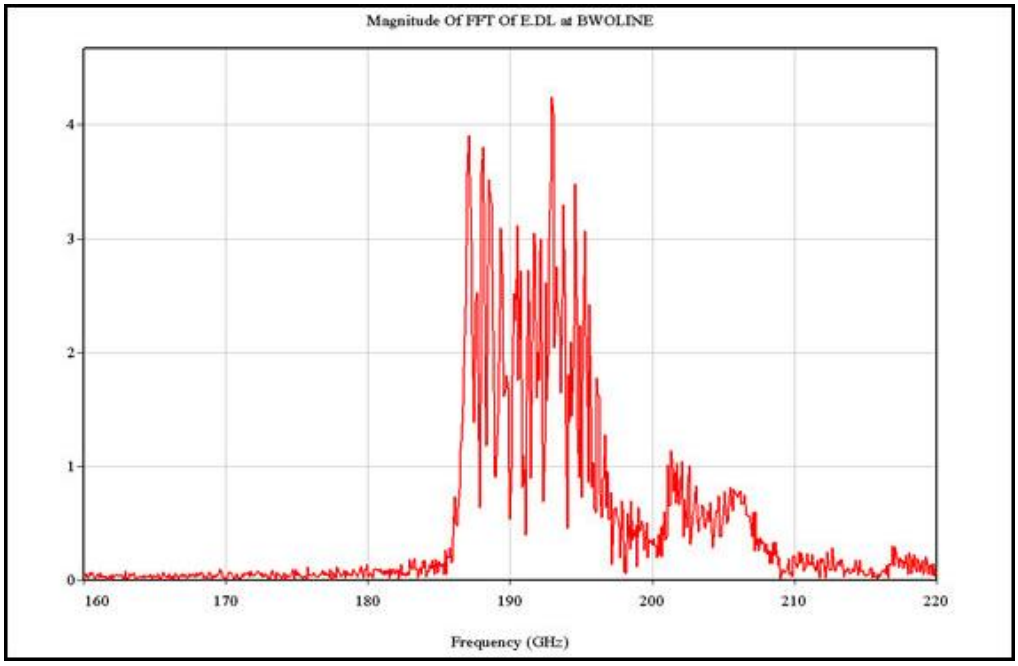

Figure 3.7: FFT of BWO output signal, showing frequency spectrum.

This result confirms that millimetre waves in the G-band frequency range can be generated from the structure, as well as providing an approximation of the power levels achievable using the PS e-beam with such a structure, and this was deemed sufficient to proceed with manufacturing. BWOs operating at 200 GHz with watts of power are not especially common, although the main issue was the manufacturing of the SWS, which shall be discussed later in this chapter. The MAGIC-predicted output frequency showed good agreement with the analytical dispersion calculations taking into account the swept beam voltage and the corresponding current.

3.3.3 BWO Horn Design and Simulation

A conical horn was designed and modelled for use with the 200 GHz BWO. An optimum horn may be defined by the equation [90]

$$d = \sqrt{3\lambda L} \tag{3.19}$$

where d is the aperture diameter, λ the wavelength and L the slant length, defined as the length from the horn aperture to the apex. An aperture diameter of 7 mm was chosen, based on material restraints, which gave an optimum slant length of 16.3 mm. This equation only defines the optimum aperture diameter for a given horn length and, as such, was treated as a starting point to determine a practical horn length for the BWO. The horn was simulated in CST Microwave Studio and a parameter sweep was used to vary the horn length from 15 to 20 mm in 0.2 mm increments, with a 1D measurement of the peak measured gain used as an indicator of horn performance.

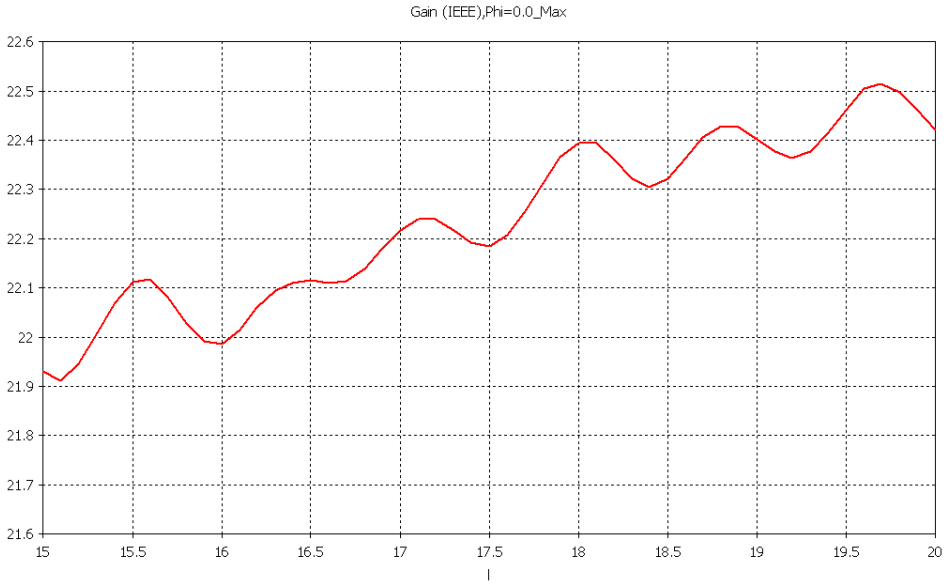

Figure 3.8: maximum predicted gain from an antenna horn at 200 GHz as a function of length.

As illustrated in figure 3.8, gain increases almost indefinitely with length, which is in keeping with aperture-limited antenna theory. In practice, however, any increase in length results in an increased chance of the horn's edge breaking off during manufacture, thus necessitating a degree of compromise between length and performance. A horn length of 18 mm was deemed a sufficient balance between these mutually exclusive attributes.

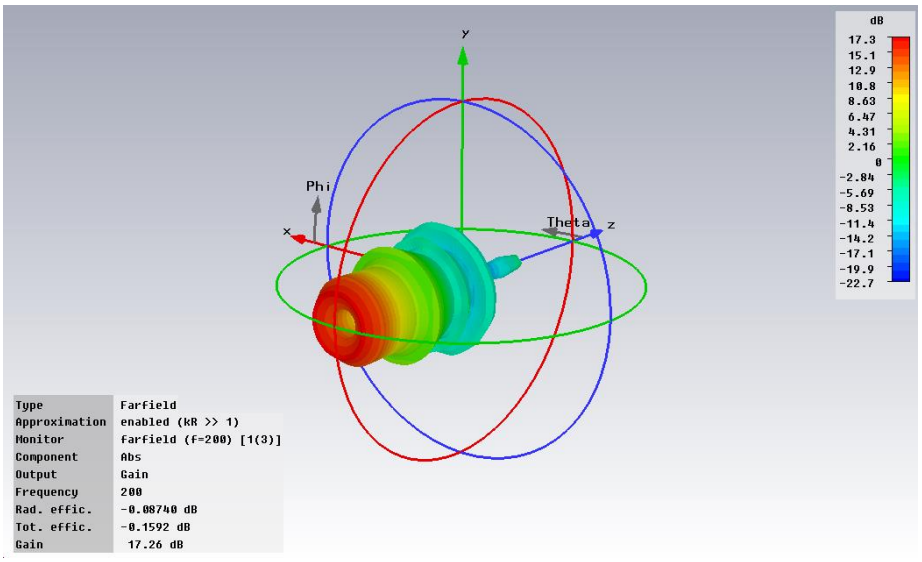

Figure 3.9: TM_{01} far-field pattern of conical horn.

Removing any symmetry planes, such a horn was stimulated with a TM_{01} wave and the far-field pattern calculated within an automatically generated closed volume. Figure 3.9 shows the resulting distinctive 'donut' far-field pattern of a TM_{01} wave, with relatively large sidelobes resulting from interference due to the presence of undesirable modes. Due to the positions of these sidelobes, their presence could be neglected as being inconsequential to the detection of the main lobes.

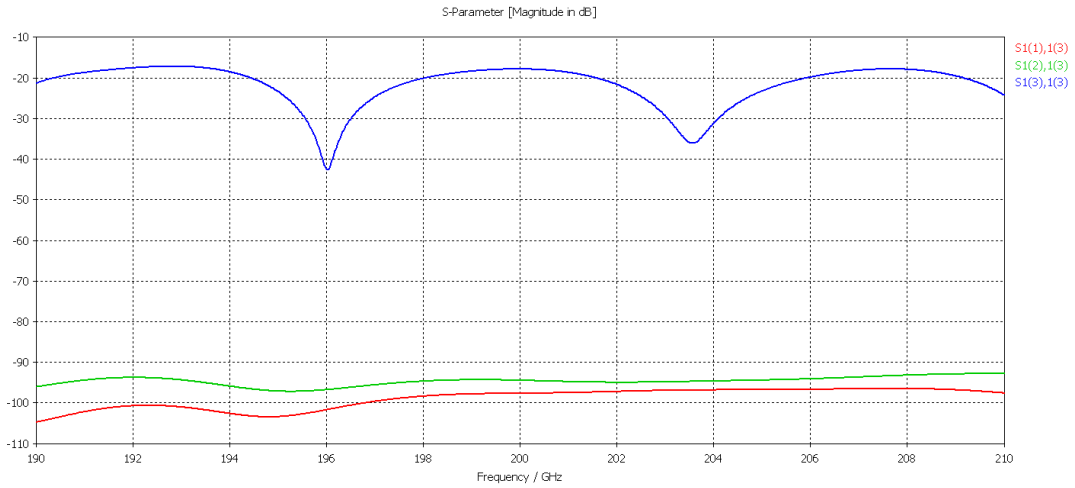

Figure 3.10: S_{11} parameters for first three modes of the BWO launching horn.

Using a linear estimation of the horn performance, a horn gain of 17.3 dB at 200 GHz was predicted. Figure 3.11 shows a 2D Cartesian plot of the resultant mode pattern, showing transmission maxima at ± 5.1º. Reflection from the horn was also determined to be low, with an average predicted reflection of -20-40 dB for the TM_{01} mode (figure 3.10). Whilst any reflection could run the risk of interfering with the operation of the BWO by feeding back the output signal, this low level of reflection was deemed to be inconsequential for the purposes of the experiment.

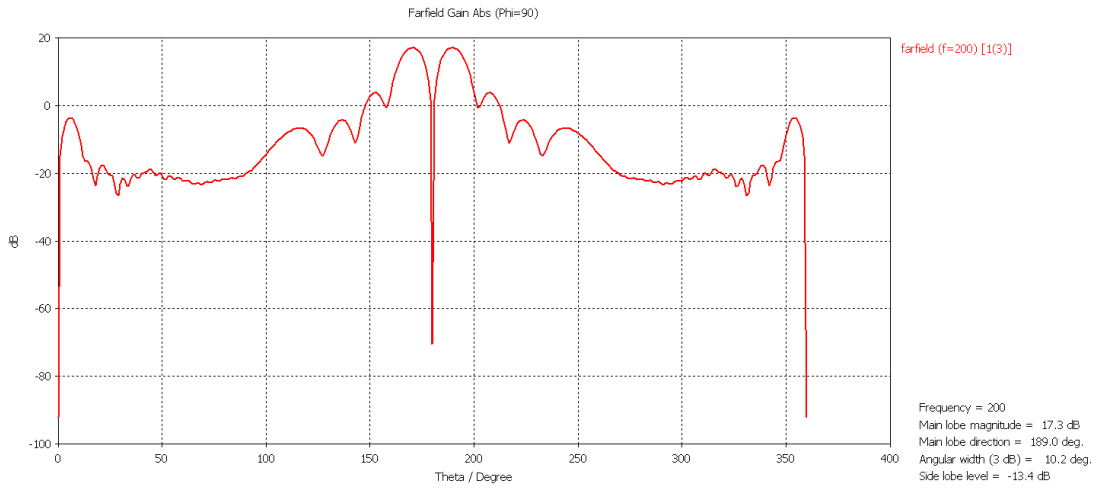

Figure 3.11: 2D Cartesian plot of predicted mode pattern, showing maxima at ± 5.1°.

Due to possessing a respectable gain and well-defined main lobes, the horn was deemed fit for purpose and the design adapted for construction.

3.3.4 BWO Construction

The body of the slow wave structure was formed by the electrodeposition of copper on top of a machined aluminium mandrel, created through the use of a high-speed milling process. The 1 mm mean radius structure possessed a 30-period, sinusoidally varying surface of 0.2 mm peak-to-peak amplitude and a periodic length of 0.47 mm. The beam entry point is a cylinder of 0.41 mm radius, serving to cut off the backward wave. The SWS tapers out at the beam/microwave exit point at an angle of 5° (figure 3.12, right hand side). This taper was to allow for fitting to the finished launching horn. The former may be seen in figure 3.13 (a) and (b), with additional waste lengths to provide machining stability, as well as to allow electrodes to be attached during the electrodeposition stage.

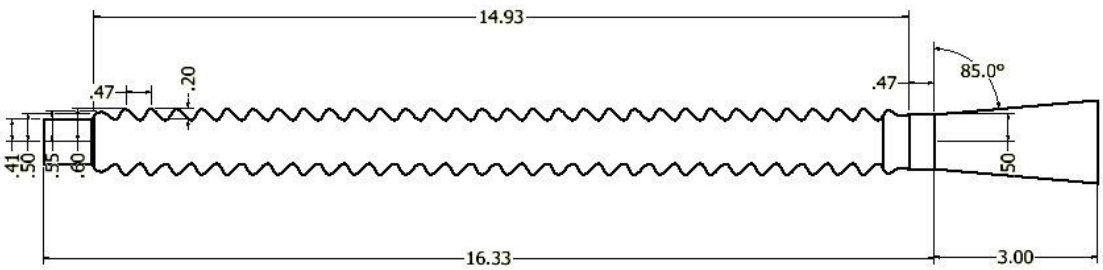

Figure 3.12: Design of aluminium former for a 200 GHz BWO.

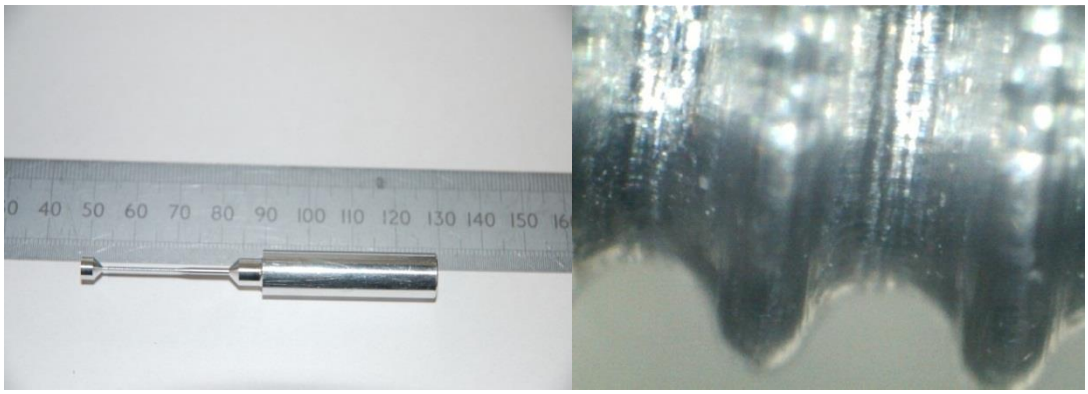

Figure 3.13 (a) and (b): BWO aluminium former, left, and high-magnification image of one period of structure.

Analysis of the finished former showed that some dimensions were out by over 0.1 mm. The final former had a mean radius of 610 μm, a periodic length of 470 μm and a sinusoidal variation of 130 μm. Based on these observations, the dispersion was recalculated (including plasma ion channel effects) by Dr. Liang Zhang and interaction at 200 GHz was seen to occur at a beam voltage of 35 kV (figure 3.14) [91].

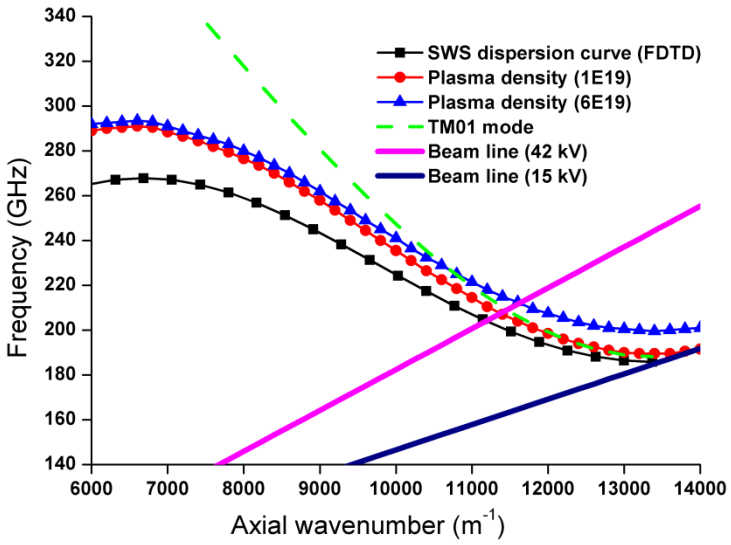

Figure 3.14: Recalculated dispersion for manufactured BWO.

Following copper growth, the aluminium was dissolved in an alkaline solution before further machining to allow for the device to be directly inserted into the PS anode and for the launching horn to be attached separately. A 14.7 mm length of radius 3mm was machined at the beam entry point to allow for direct entry into the anode while a longer, 5 mm radius section prevented further movement into the anode.

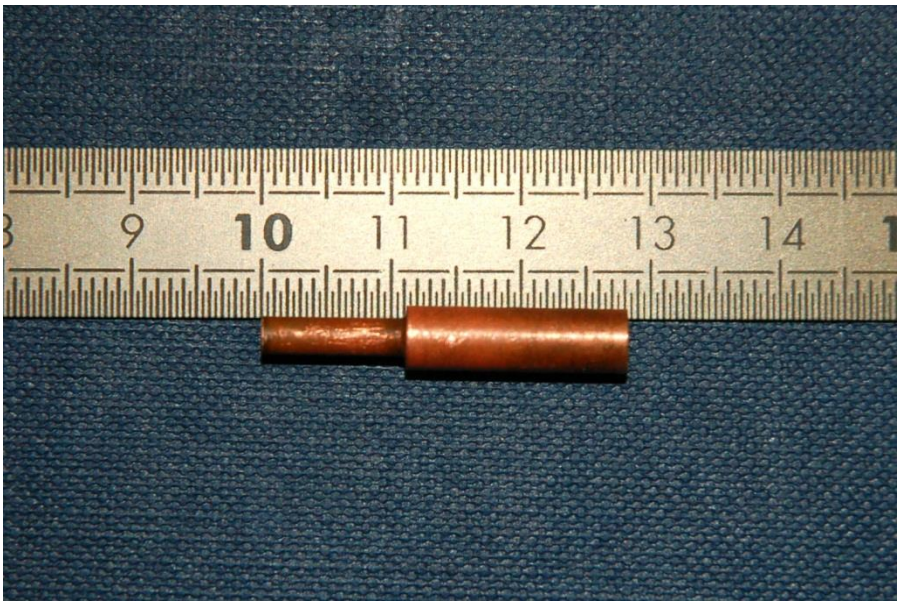

Figure 3.15: BWO following copper deposition and former dissolution.

The horn antenna was machined by drilling a 5 mm diameter hole, 4 mm deep recess in a 7 mm diameter, 22 mm long copper cylinder before drilling an on-axis, 1 mm hole through the copper (Fig 3.16 (a)). Through wire erosion, the horn was machined from the structure and could then be fitted neatly on to the BWO (Fig 3.16 (b)).

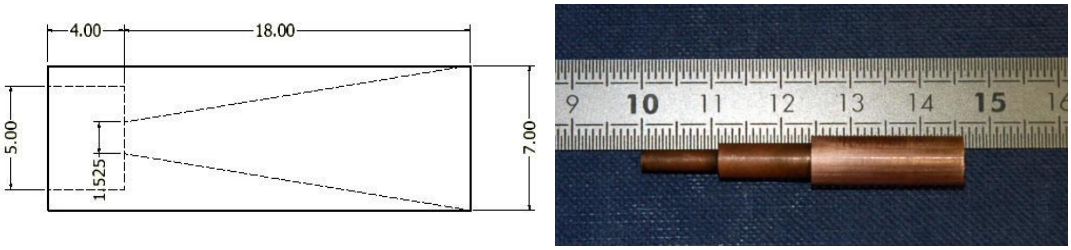

Figures 3.16 (a) and (b): CAD design of launching horn, left; and completed BWO-horn assembly, right.

3.4 W-band Klystron

In designing a klystron for W-band operation, it may be useful to classify the parameters to be determined as either being related to the device's physical construction or to the generation of the electron bunches. From the theory outlaid in section 2.8.2, it can be seen that, if a frequency of operation may be specified beforehand then it is possible to determine the dimensions of a klystron resonant cavity as well as the radius for the inter-cavity drift tube. Beam parameters may then be calculated via expected performance parameters of pseudospark-derived electron beams, as was the case with simulation of the BWO described earlier in this chapter, while the interaction length can then be determined via equation 2.96. A drift tube radius of 100 μm was chosen due to the limitations placed on the machining of metals. Whilst smaller diameters are possible, these cannot generally be sustained over distances greater than ~ 1 mm without a major effect being observed on the quality of the machined tube. With this in mind, the dimensions of a pillbox resonant cavity could be chosen. Due to the method of coupling, the cavity width was kept as close as possible to the width of a G-band waveguide section (1.27 mm) while, similarly, cavity width and outer radius were kept to similar dimensions.

Such a cavity was designed and modelled in both CST Microwave Studio and MAGIC-2D. Possessing inner and outer cavity radii of 0.14 mm and 0.635 mm respectively, it was found that in order to resonate close to the 94 GHz target, the gap width had to be set at 0.28 mm (plus 0.2 mm radius rounded tips in order to minimise breakdown effects). The structure was created in CST Microwave Studio and an adaptive mesh used along with CST's eigenmode solver, which found the fundamental frequency to be 93.55 GHz. This was then modelled in MAGIC-2D using its own eigenmode solver. A mesh density of 6 cells per 0.04 mm (the thickness of the drift tube) was chosen; below a density of 4, the eigenmode solver was prone to erratic behaviour, over 8 and run-times became lengthy for anything other than small computational tasks. Through MAGIC, the frequency was determined to be 93.60 GHz. In hot test simulations, the cavity Q was determined to be 800 while a cavity R/Q was calculated to be 143. While this cavity was suitable in many ways, a second design was devised in order to further optimise cavity performance.

A second cavity design consisted of an inner and outer radius of 0.14 mm and 0.56 mm, while cavity width was 1.04 mm. This is narrower than the waveguide width but the coupling structure could be adjusted to compensate for this. A gap width of 0.14 mm allowed for better coupling between beam and cavity. The cavity structure was determined to have a resonant frequency of 93.76 GHz from simulation in CST Microwave Studio using an adaptive mesh. Simulations in MAGIC, using a similar mesh density to the previous cavity, determined the cavity resonance to be 94.43 GHz. This showed a reasonably large disparity from the CST simulation, which owed to the difference in meshing techniques, particularly when resolving rounded edges, as at the interaction gap ends. In practice, the CST-determined value is likely more accurate due to the more refined meshing system but, for MAGIC simulations, the latter frequency was adopted. Here, the cavity Q and R/Q were determined to be 880 and 140 respectively. Owing to the improved cavity performance and to the shorter interaction gap, it was decided to use this cavity design for the three cavity klystron.

For simulation purposes, a drift tube radius to beam tube radius ratio of 1:0.8 was adopted. This allowed for effective bunching of beam electrons while reducing the voltages presented across the output interaction gap and, consequently, the risk of breakdown. Beam voltage was kept reasonably low (10 kV) and a beam current of 15 mA was adopted, a reasonable value for a small-diameter PS electron beam. Calculations determined an optimal drift-tube length of 2 cm but it was found that, in simulations with the three-cavity structure, device gain was higher at a length of 1 cm. The reasons for this are yet to be investigated. While no magnetic field would be present in a PS beam, a field strength of 0.8 T was implemented in simulations in order to constrain the beam.

3.4.1 Klystron Simulation

A three-cavity test of the designed klystron was implemented in MAGIC-2D. The choice for the number of cavities was based on a compromise between device performance and the difficulty in manufacturing such a structure. A two-cavity design was felt to be too simple and for the device performance to lie under what was felt to be desirable, while having too many cavities would have run the risk of misalignment upon the device's eventual construction. As such, a three-cavity structure allowed for a challenging design while minimising the possibility of failure.

Three identical cavity designs were used for simulation, although the cavity conductivities were varied, with the input cavity set to 7 mΩ·m while the penultimate and output cavities were set to 3.3 mΩ·m. The change was implemented in order to reflect the effects of cavity loading from the input source, while the values assumed cavity conductivities of 3.5×10^7 and 1.5×10^7 Sm^{-1}, reasonable values for copper cavities assuming average roughness [92].

Initial simulations of the device used an electron beam of constant voltage and current which, although dissimilar to the pulsed sweep of PS beams, provided a

method of gauging klystron performance. The klystron simulation was run at an axial mesh resolution of 2 cells per 0.04 mm while the radial mesh was varied between 2.25 cells per 0.04 mm for larger, less essential areas (cavity walls, drift tube, cavity body) and 3 cells for areas which required finer resolutions, such as the interaction gap. While this was a less refined resolution than for cavity cold testing, it was found that the effects of having a larger mesh were less pronounced in the simulation of the individual cavities, although the reason for this is currently unknown. In addition, efforts to simulate the klystron at comparable resolutions resulted in run-times too large for practical usage.

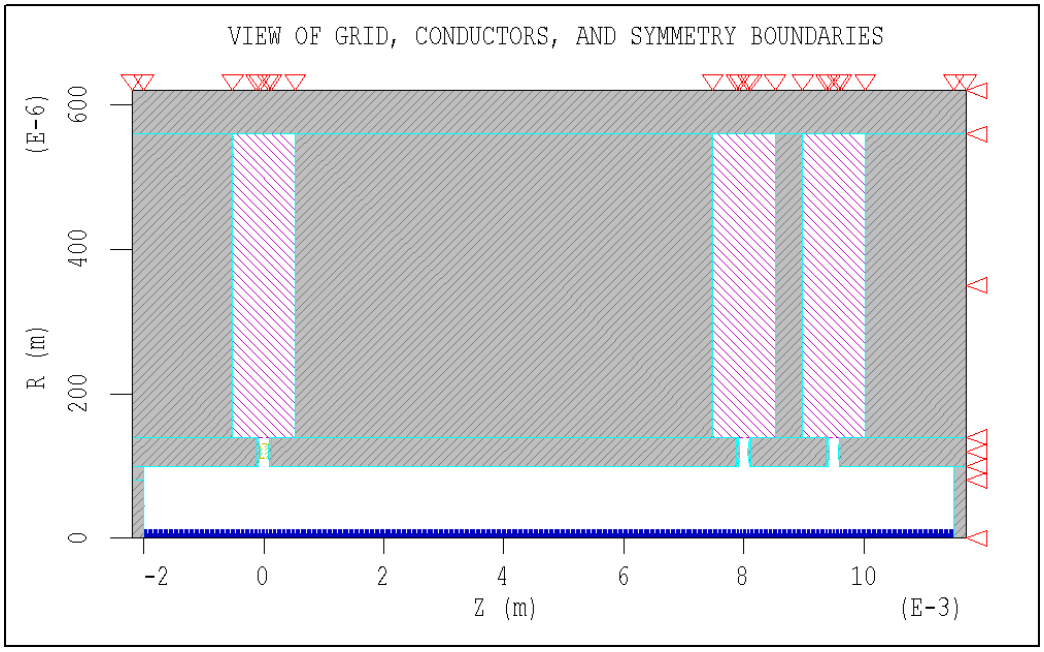

Figure 3.17: MAGIC-2D-rendered three-cavity klystron geometry.

Figure 3.17 shows the klystron structure as it was simulated in MAGIC. Using a run-time of 50 ns, the simulation was run. Peak power was measured across each of the three interaction gaps using MAGIC's 'observe field_power' command while field monitors examined the development of the electric fields at each of these points. Particle motion was monitored and showed clear signs of bunching during operation. By defining the beam power, it was possible for MAGIC to output the device gain and efficiency as a function of time.

Following this, RF input power and beam current were varied in order to determine the optimum operating parameters. Variations in RF current were found to induce a trade-off between gain and efficiency, with the optimum drive current lying between 2.05 and 2.1 mA. An RF current of 2.05 mA was chosen, delivering 8.7 % efficiency, 18 dB gain and an output power of 10.5 W.

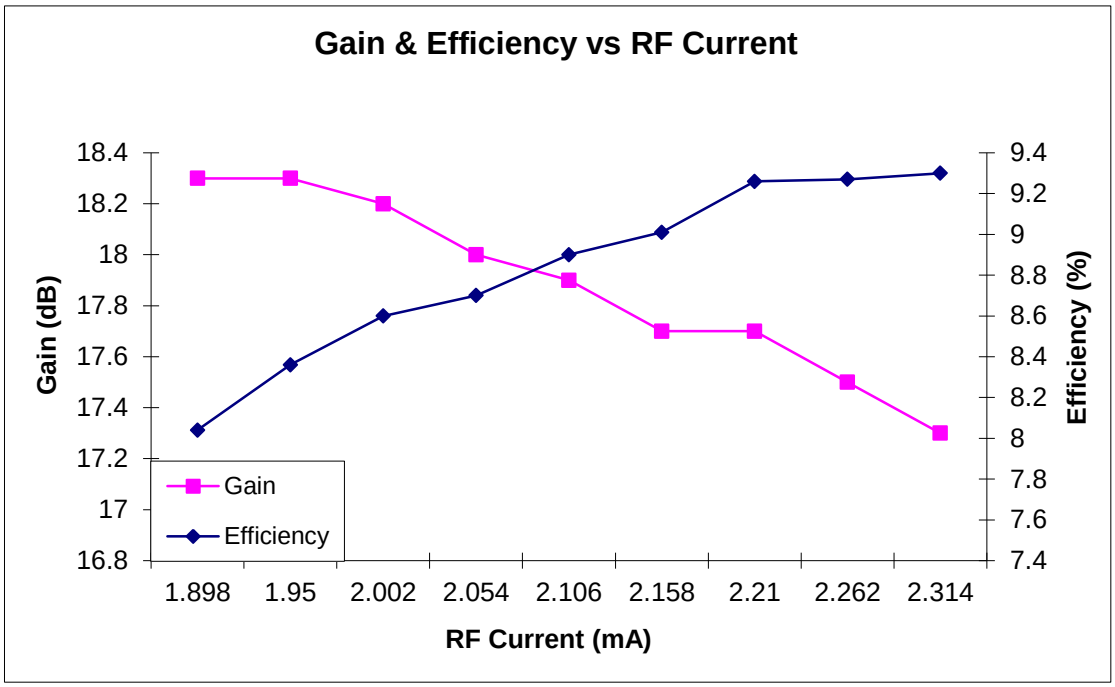

Figure 3.18: Variation in klystron gain and efficiency with RF current.

The effect of beam current was decidedly more linear, with both gain and efficiency increasing until a beam current of 22.5 mA, at which point device efficiency started to drop. A current of 25 mA was chosen for the constant-current beam, delivering 10.5% efficiency and 21 W of power. This figure was treated as a highly idealised marker of performance due to its neglect of coupling factors and the pulsed nature of the pseudospark.

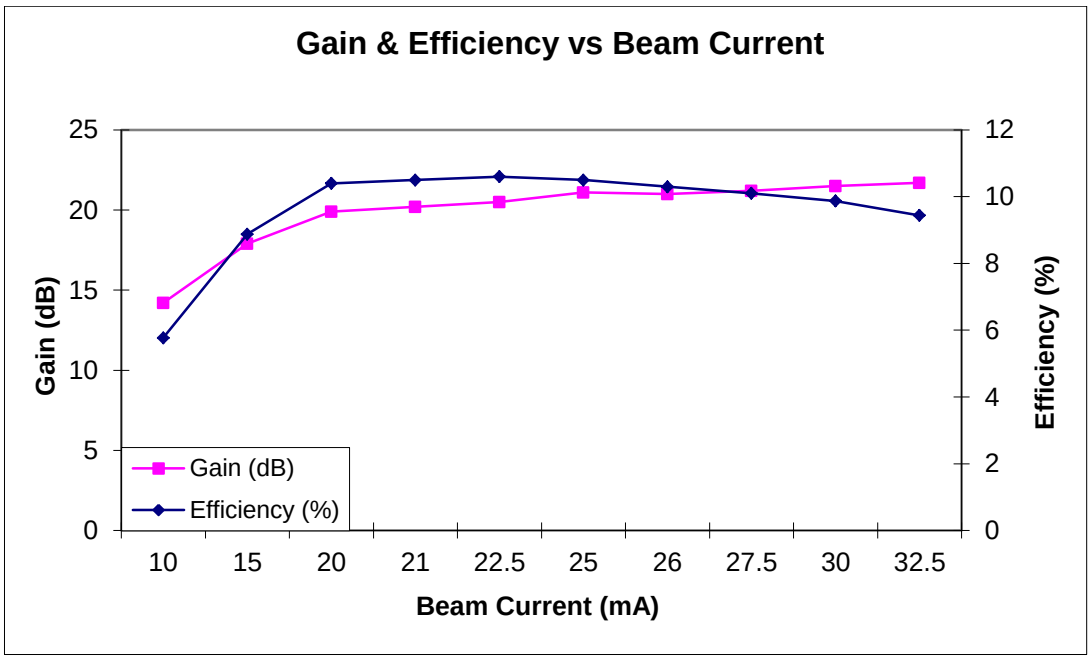

Figure 3.19: Variation in klystron gain and efficiency with beam current.

Following these optimisations using the constant-voltage, constant-current beam, a pulsed electron beam was used to excite the three resonant cavities with the accelerating voltage dropping from 16 kV to 8 kV between 5 and 10 ns into the simulation runtime before dropping to 0 kV between 25 and 30 ns. The beam current, meanwhile, rose to 15 mA with a 10 ns risetime from simulation start-up before dropping to zero after 25 ns. These parameters were chosen to give an approximation of device performance using a PS electron beam. Pulse durations of 25 ns are not uncommon with PS discharges, while the chosen voltages lie at the limits of performance for single-gap pseudosparks. The use of larger voltages would run the risk of damaging the klystron due to the large currents that they sometimes carry. A 100 mW seed signal, tuned to the input cavity resonance, stimulated beam bunching. Figures 3.20 (a) and (b) show the development of fields within the interaction cavity during interaction at a given point in time, illustrating the effect of the beam-wave interaction on the structure's fields.

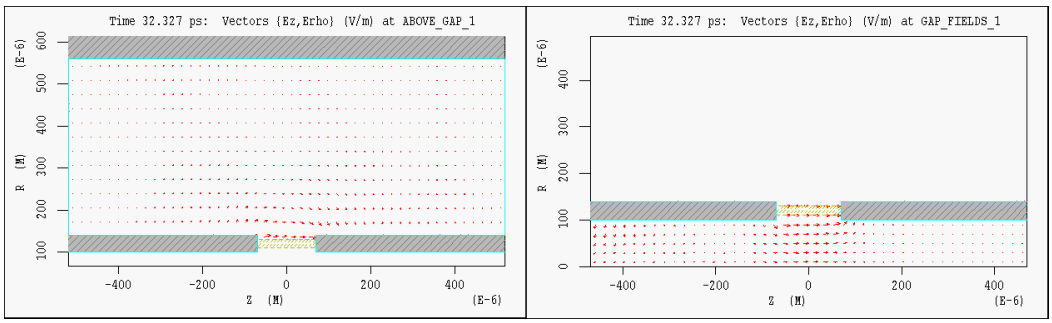

Figures 3.20 (a) and (b): Development of field lines above, left, and below cavity, right.

A cavity Q of 880 for the input cavity and 1860 for the second and third cavities was predicted by the simulation. Following a 50 ns run-time, an output power of 8.4 W at 94.427 GHz was predicted.

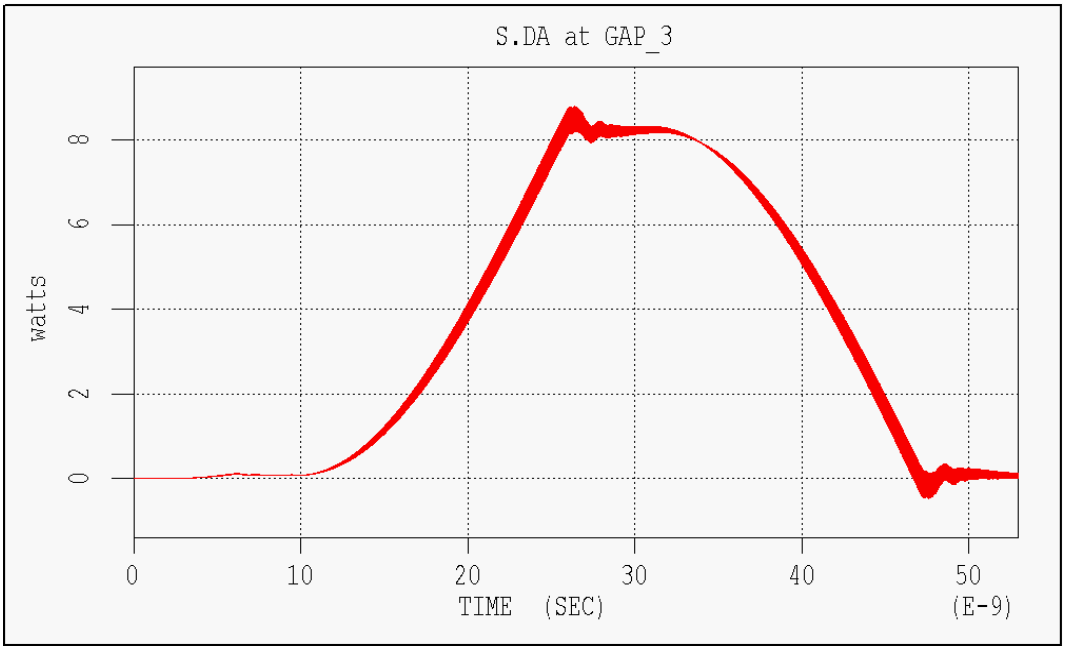

Figure 3.21: Simulated output power of klystron.

Calculating the device gain and efficiency as

$$G = 10\log_{10}\frac{P_{out}}{P_{RF,in}} \tag{3.20}$$

$$\eta = \frac{P_{out}}{P_{beam,in}}, \tag{3.21}$$

device gain and efficiency were calculated as 20 dB and 7%, respectively (figures 3.22 (a) and (b)).

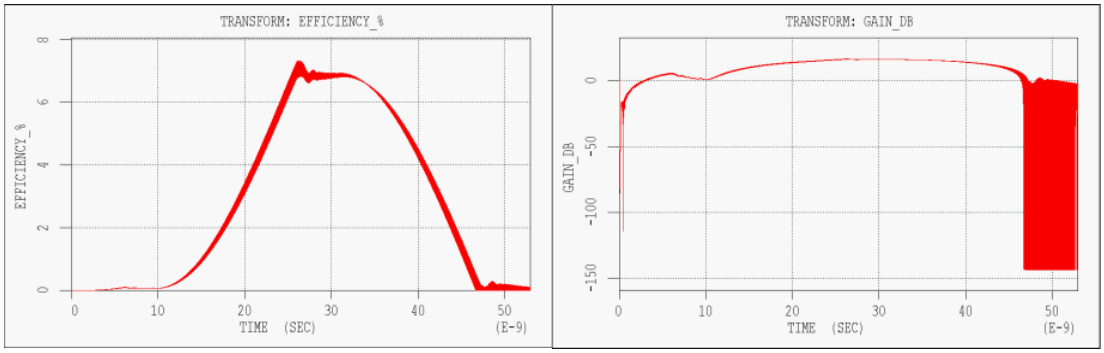

Figures 3.22 (a) and (b): Simulated efficiency, left, and gain, right, of klystron.

3.4.2 Klystron Cavity Coupling

The use of fundamental-mode klystron cavities presented issues in coupling. Whilst coaxial coupling, where discrete coupling points are placed around the structure in order to feed the signal to the cavity, would be possible in theory, the dimensions in use and the difficulty in manufacturing at these dimensions to high tolerances rendered it inapplicable. Meanwhile, iris coupling [93] was not possible due to the large reflections which would be incurred in coupling through an undersized aperture which could damage more sensitive frequency sources. As a result, a novel coupling method was proposed in which a slot would be cut along the width of a resonant cavity and coupled to a standard dimension waveguide via a tapered section. Whilst this would result in the propagated signal being attenuated and/or reflected where the taper reaches cut-off, a dielectric insert would be used in order to effect a change in cut-off frequency. In order to maximise transmission, two criteria were set: to minimise reflection to the source and to minimise dielectric loss.

The first criterion could be met by tapering the dielectric structure, thus allowing a gradual transferral from air to dielectric. The smaller the angle with which the mm-wave signal entered the transition, the lower the reflection coefficient. For the second

criterion, the size and type of dielectric were of greater importance. It was concluded that a reduction in the volume of the dielectric transition would result in a lower dielectric loss for the coupled signal. Likewise, a low-loss material would be preferable but this is restricted by the fact that the material must be machinable and possess a high enough dielectric constant that transmission of the signal could be achieved.

3.4.2.1 X-band Coupler

Due to the novel nature of the dielectric coupling system, the principle was examined, modelled and tested at a lower frequency band both in order to validate the efficacy of the technique and to verify the reliability of the simulated model. A coupling system for operation between 8 and 12 GHz was designed, using a 22.86 x 10.16 mm rectangular input waveguide which could be used to couple to a resonant cavity. Using CST Microwave Studio, a TM_{01} mode was input from port 1 and underwent a 90° phase shift during the course of coupling. Direct transmission measurements were taken from directly at the end of the dielectric region, while reflection coefficients were also measured. In addition, simulations were conducted where the dielectric fed directly into an X-band waveguide section. While this presented an obvious impedance mismatch, it allowed the system to be compared with single-coupler experimental measurements.

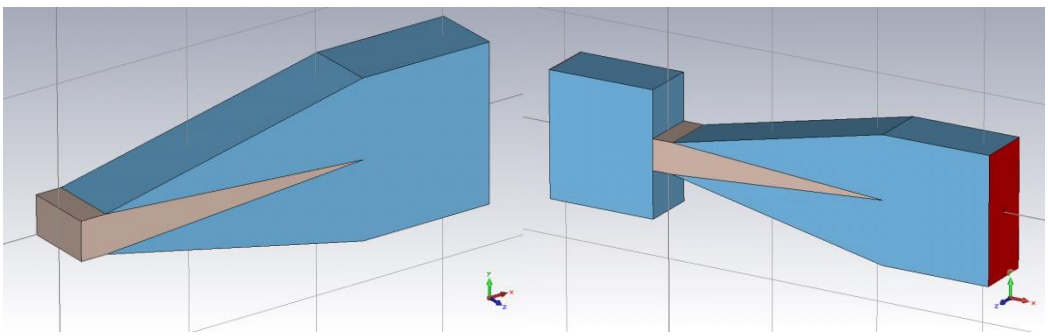

Figures 3.23 (a) and (b): CST representation of X-band coupling structure, left, and coupling directly into waveguide, right.

In order to measure the coupler's performance using a coupled cavity, a 10.16 mm wide cavity was designed in order to maintain structural simplicity, with other

dimensions adjusted to accompany this. A cavity of outer radius 4.45 mm fit this demand, yielding a resonant frequency of 10.26 GHz.

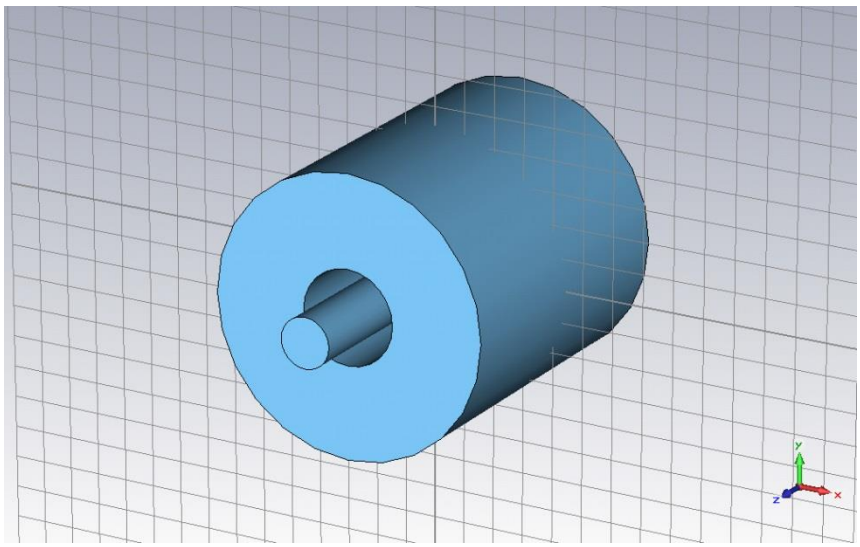

Figure 3.24: X-band cavity rendered in CST Microwave Studio.

Two possible dielectrics were deemed to have sufficiently low losses and a dielectric constant high enough to overcome the waveguide dimensions necessary to couple to an aperture of this size; alumina, with a dielectric constant of 9.1, and BNP-2, a form of machinable aluminium nitride possessing a dielectric constant of 7.9. Three factors were considered during the coupler's design: these were the length of the tapered section, L_1; the length of the cut-off waveguide, L_{cut}; and the height of the coupling slot, h_{cut}. It was found that while the effect of varying L_{cut} was negligible, S_{21} measurements increased both with an increase in L_1, thus reducing reflections, and with an increase in h_{cut}, thus reducing cut-off effects. Figure 3.25 shows the effect of taper length on reflection, while figure 3.26 illustrates the shift in cut-off and increased transmission demonstrated from the increase of $h_{cut.}$

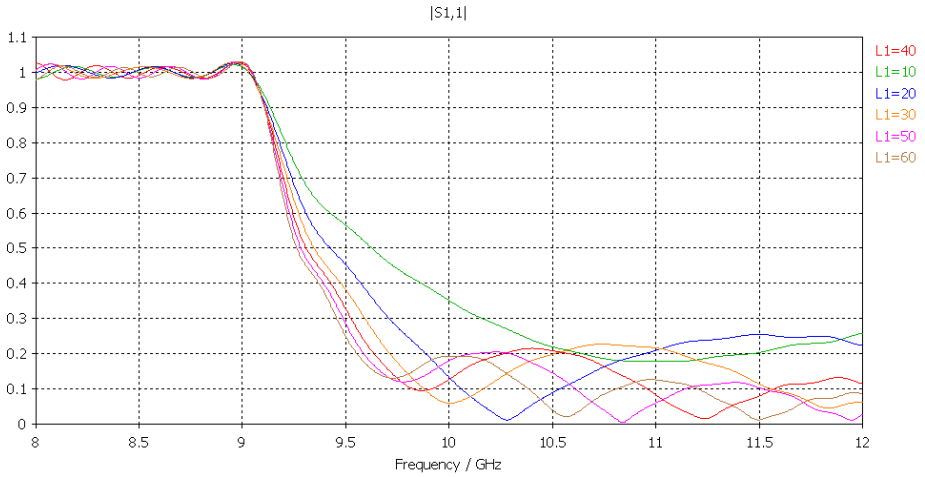

Figure 3.25: S_{11} measurements with variation in taper length.

Using BNP-2 as a dielectric, it was found that an h_{cut} of greater than 5 mm was necessary in order to achieve any transmission at X-band frequencies. In addition, sharp resonances may be seen in the S_{21} measurements, an effect of the dielectric's intrinsic resonance. The final structure consisted of a coupling slot height of 5.6 mm, along with taper and cut-off lengths of 40 mm and 6 mm, respectively.

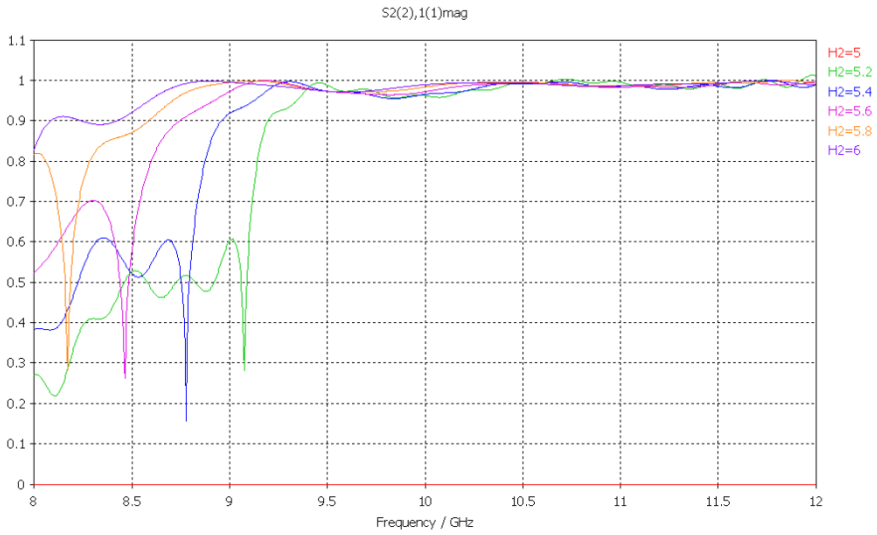

Figure 3.26: S_{21} measurements with variation in dielectric height.

Physically, the simulated design was reconstructed in the form of a solid copper block with a tapered aperture, 22.86 x 10.16 mm at one end and 10.16 x 5.6 mm at the opposite end, machined through the use of wire spark erosion (figure 3.27). An attachable copper plate allowed for the insertion of a dielectric which could then be slotted through the smaller aperture. In addition, a cavity which could be slotted onto the structure was machined from two copper parts which were then held together via three screws. Dimensions of the slot in the plate and the dielectric insert were kept as close as possible so as to ensure a tight fit and, as such, no adhesive or bonding agent was required. This also allowed a small amount of freedom in positioning the dielectric and gave limited ability to tune the cavity.

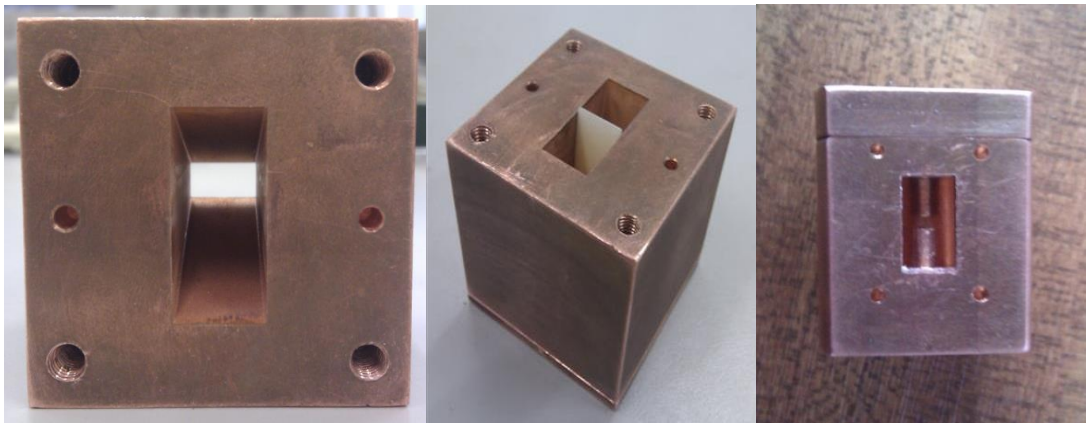

Figures 3.27 (a), (b) and (c): Dielectric-based coupler, left; with dielectric insert, centre; and X-band cavity with coupling aperture, right.

As may be seen in figure 3.28, the behaviour of the coupler was similar in its transmission behaviour to the simulated predictions for both dielectric materials, with higher frequencies transmitting through the tapered transition region more readily due to the shortened wavelengths. Attenuation was considerable at lower frequencies, ranging from -17 dB at 8 GHz to -4 dB at 11.5 GHz in the case of alumina and – 26 dB at 8 GHz to -7 dB at 12 GHz for BNP-2. While the behaviour of both materials matched simulations well, the BNP2 performed slightly worse than predicted due to approximations being made in regards material properties due to a lack of full information on the dielectric's properties.

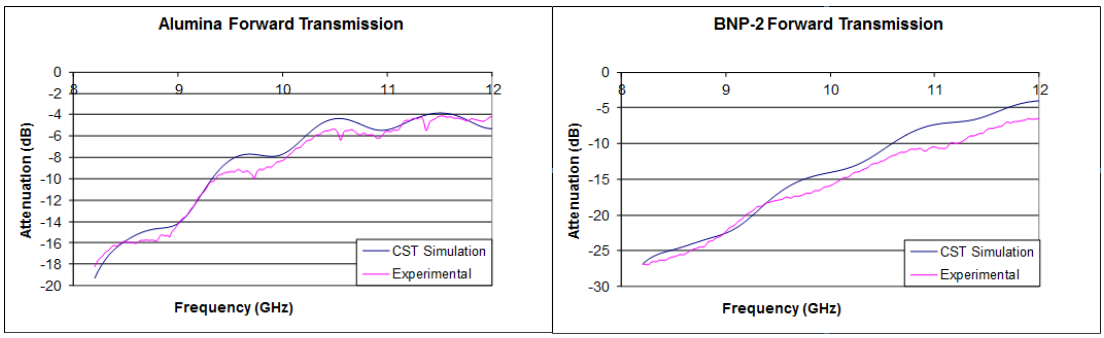

Figures 3.28 (a) and (b): Comparison of simulated and experimentally obtained transmission coefficients for alumina, left, and BNP2, right.

With the cavity connected, both materials showed signs of resonance at ~9.8 GHz when the coupler's reflection coefficient was measured, with BNP2 showing a sharper resonance but a higher degree of loss (figure 3.29). While this resonance differed from CST Microwave Studio predictions, the resonant frequency was found to shift with the position of the dielectric and so this result could be seen to be a measurement of cavity resonance as opposed to intrinsic behaviour from the dielectric. These experiments not only confirmed that the coupling device performed as expected but also that alumina was the superior choice of material for coupling at higher frequencies.

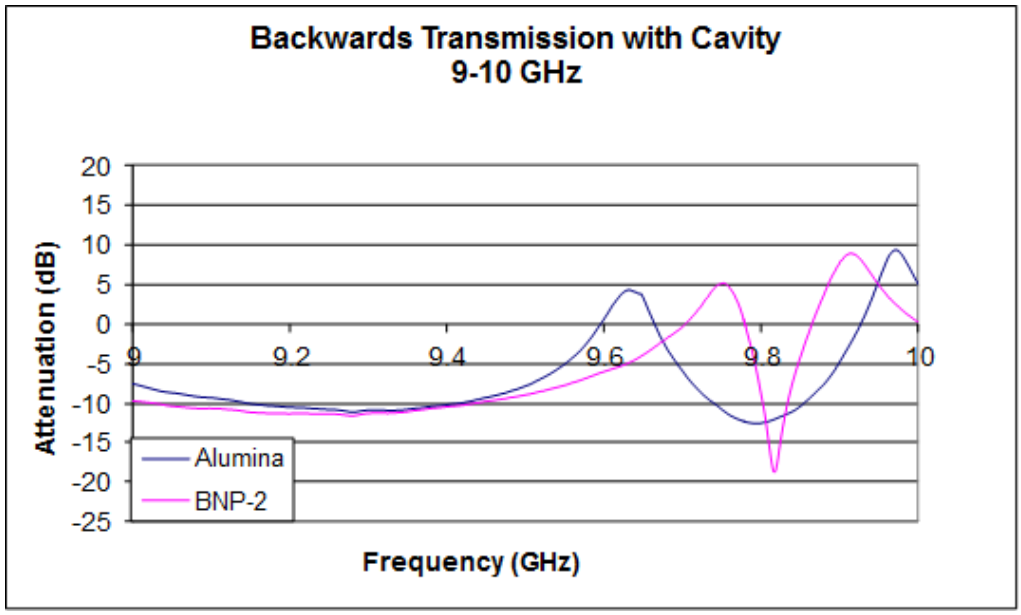

Figure 3.29: Cavity resonance as measured through both coupling dielectrics.

3.4.2.2 W-band Coupler

While the X-band coupler showed that the theory behind a dielectric coupler could be applied to a real-world system, the performance was poorer than could be expected for a typical coupling system. Further investigation revealed that by using a taper which expands from the waveguide wall, as opposed to being placed in the centre of the waveguide, reflections could be reduced. Such an asymmetrical coupler design was simulated in CST Microwave Studio using alumina as the transition material. Using a 2.52 x 1.27 mm waveguide (WG27) as an input port and transitioning along a 2.73 mm long tapered region, the signal is fed into the cavity via a 1.054 x 0.56 mm rectangular coupling slot, with the dielectric positioned to minimise the degree of reflection the signal may experience (figure 3.30).

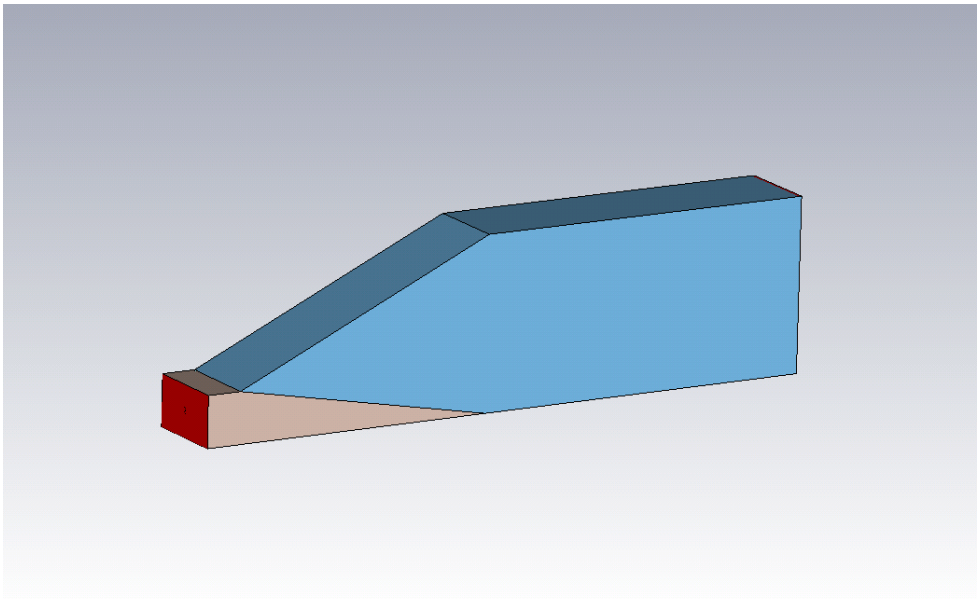

Figure 3.30: Microwave Studio rendering of W-band coupling structure.

Using the asymmetrical design, the W-band coupler performed admirably, with a transmission loss of -2.6 dB at 90 GHz and -1.45 dB at 95.5 GHz. Reflection ranged from -3.25 dB to -5.5 dB. While this is still not ideal, they were nonetheless a notable improvement on the X-band design while the fact that the coupler would be used with relatively low power levels (mWs) meant that damage to the source from these reflections would be minimal.

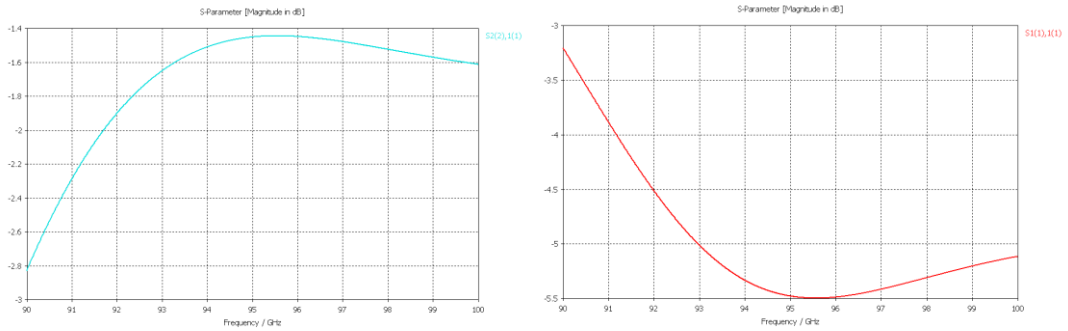

Figures 3.31 (a) and (b): Transmission, left, and reflection coefficients, right, of simulated coupling structure.

When simulated with the attached cavity, the coupler showed a very clear resonance, although with an offset of several GHz. This may have been due to the section of cavity removed in order to allow for the coupling slot. While this would occur in practice also, an effort was made to allow a degree of tunability in the finished structure in order to compensate for this phenomenon.

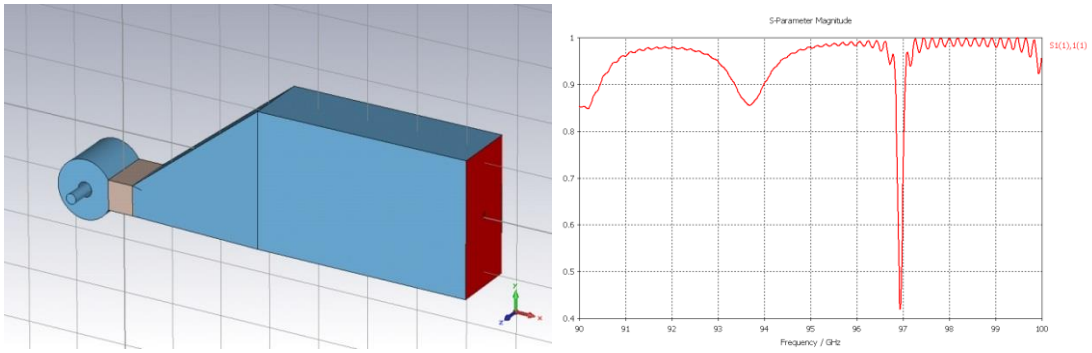

Figures 3.32 (a) and (b): W-band coupling structure with cavity, left, and reflection coefficient showing cavity resonance.

3.5.3 Construction

After simulation in CST Microwave Studio, the resonant cavities, beam tube and coupling slot were designed in a series of 7.3 x 7.3 mm copper segments, each of varying length and features, which were then stacked as in figure 3.33, as is often the case in MEMS manufacturing techniques where structures will be etched into silicon wafers before being aligned and placed end-to-end. Machining of these structures was achieved via a combination of high-speed milling and wire erosion to tolerances

of ± 0.05 mm. Alignment was achieved through the use of the housing structure. In total, the full klystron interaction region was constructed of 10 tiles, three of which included the cavities, five incorporated the nose sections necessary for beam-wave interaction and the remainder making up the 200 μm diameter drift tube. The 3 mm long drift region between the input and intermediate cavities was broken down into two thinner sections due to difficulties in effectively machining a 200 μm diameter channel of such length.

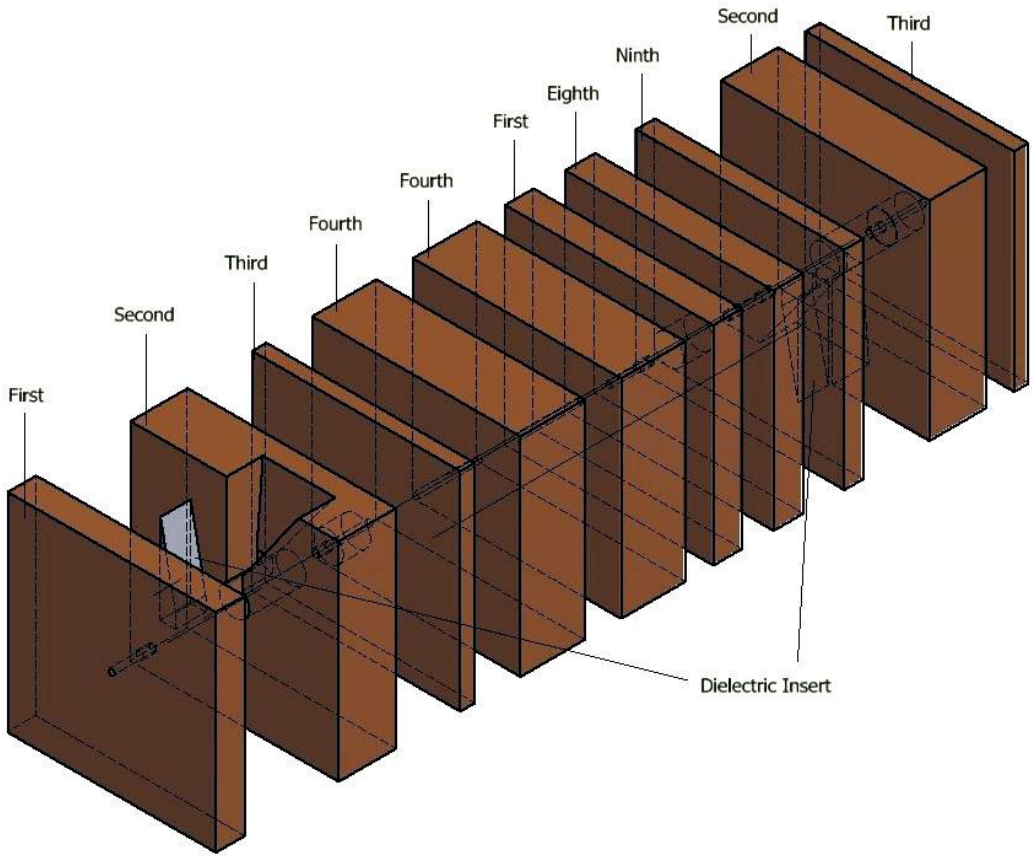

Figure 3.33: Klystron interaction region assembly.

These parts were checked after construction and dimensions found to lie within 0.05% of the design specifications. For the input and output cavities, two further backups were also manufactured. This allowed for an element of inter-changeability when matching cavity frequencies and thus for tuning the device. Tuning could

further be made possible by compressing the cavities by mechanical means (e.g. by tightening the screws affixing the housing structure to the pseudospark anode).

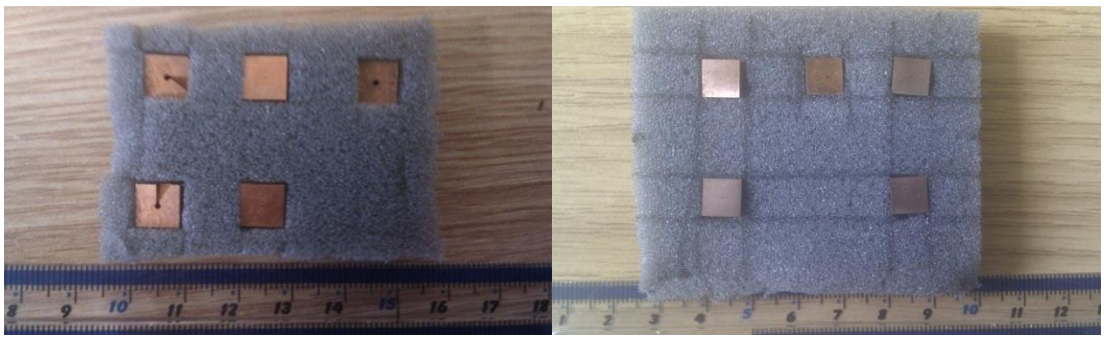

Figures 3.34 (a) and (b): Copper klystron segments.

After simulation and the results of the X-band coupling system test, it was decided to use a modified version of the dielectric tapered insert which was adopted before, tapering it from only one side rather than adhering to the symmetrical design which was used in the proof of theory experiment. By placing the structure flat against the coupling slot wall, it allows for a smoother transition and involves less reflection than placing the transition to the dielectric in the centre of the electric field.

Five tapered alumina inserts were manufactured. As with the backup cavities, this not only offers a degree of safety against accidental damage due to the small size and fragility of the structures but also offers a degree of tunability. The tapered inserts were inserted by hand and, to aid in alignment against the cavity edge, a rod was constructed from stainless steel which was inserted into the cavity section. In this way, it was possible to align the dielectric and cavity edges to the highest accuracy.

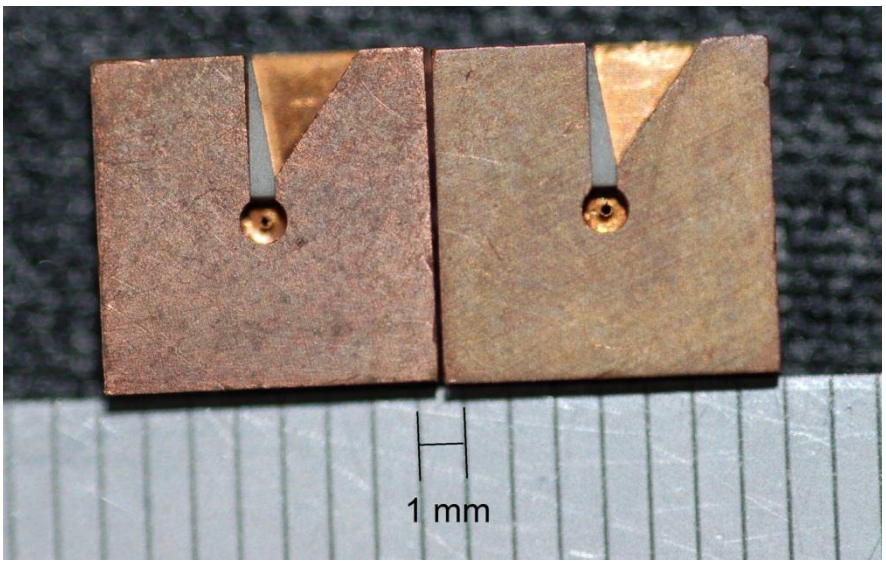

Figure 3.35: Assembled input and output cavities, with dielectric tapers in white.

The aim of the housing structure was to allow it to be connected to the PS anode, for the klystron interaction region to be inserted and aligned, to allow a mm-wave signal to be fed to the input cavity, to allow extraction of the amplified mm-wave signal and to allow the entire structure to be placed under vacuum. Using a 50 x 50 x 30 mm copper block as a base, a central 7.3 x 7.3 mm channel was created using wire electrical discharge machining (EDM), as were two W-band waveguides (2.56 x 1.28 mm) which, due to the limitations of the wire EDM process, were machined through the full length of the block. These passed through the centre channel and were located so that they would feed directly into the input and output cavities. The two unneeded holes were then expanded using a 4 mm drill before cylindrical copper plugs were inserted and vacuum brazed. The brazing material was layered in a series of concentric rings around the cylindrical plug before firing as to better maintain vacuum integrity. The central channel was then re-machined to allow for the insertion of the interaction region, as well as to remove any residue from the previous drilling and brazing.

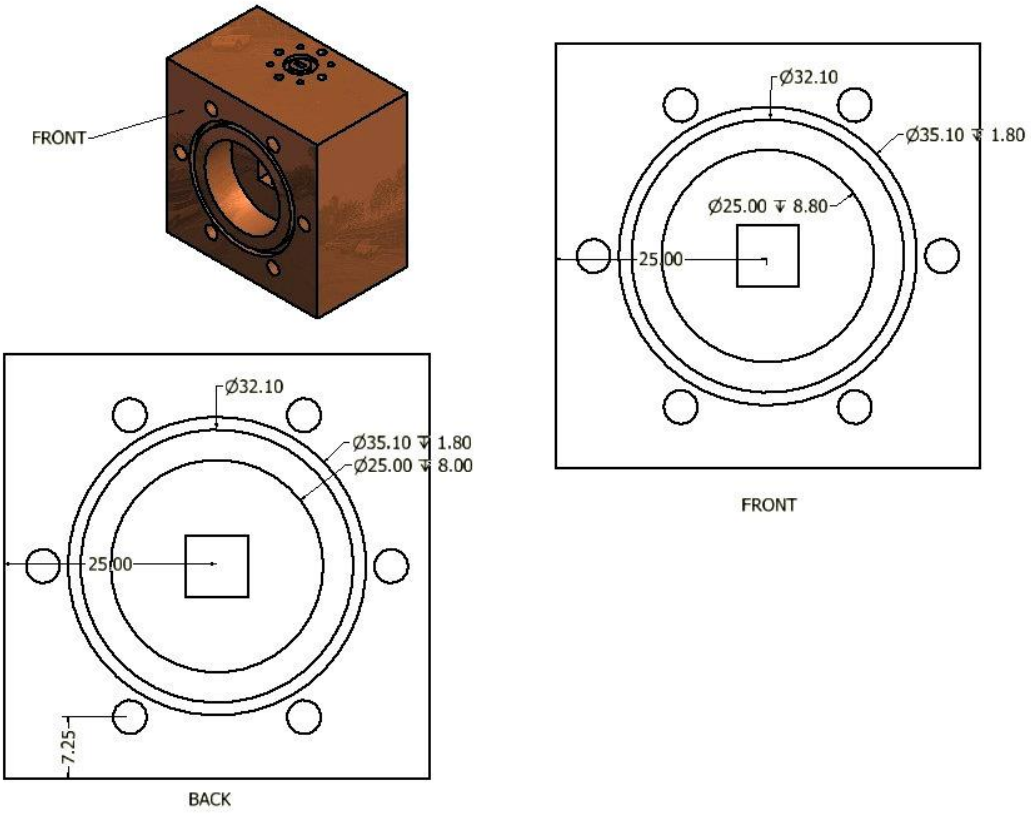

Figure 3.36: Design of klystron housing structure.

In order to accommodate the W-band waveguide flange fittings required for coupling to and from the klystron, the length of the housing block was designed to be larger than the interaction length, yet kept as low as possible to allow for minimal beam travel between the pseudospark anode and interaction region. 8 and 8.8 mm diameter recesses were machined on the beam input and output sides of the housing respectively to compensate for this and, to correctly align the cavity coupling apertures with the machined waveguides, close-fitting plugs were inserted, each with 1 mm diameter centre-located apertures to allow for beam entry and extraction from the klystron drift region. One plug was machined with a protuberance for insertion into the anode, acting as a centring structure, and the opposite plug, a 3mm thick copper disc, was held in place using a machined plastic ring situated between it and the surface of the Rogowski coil.

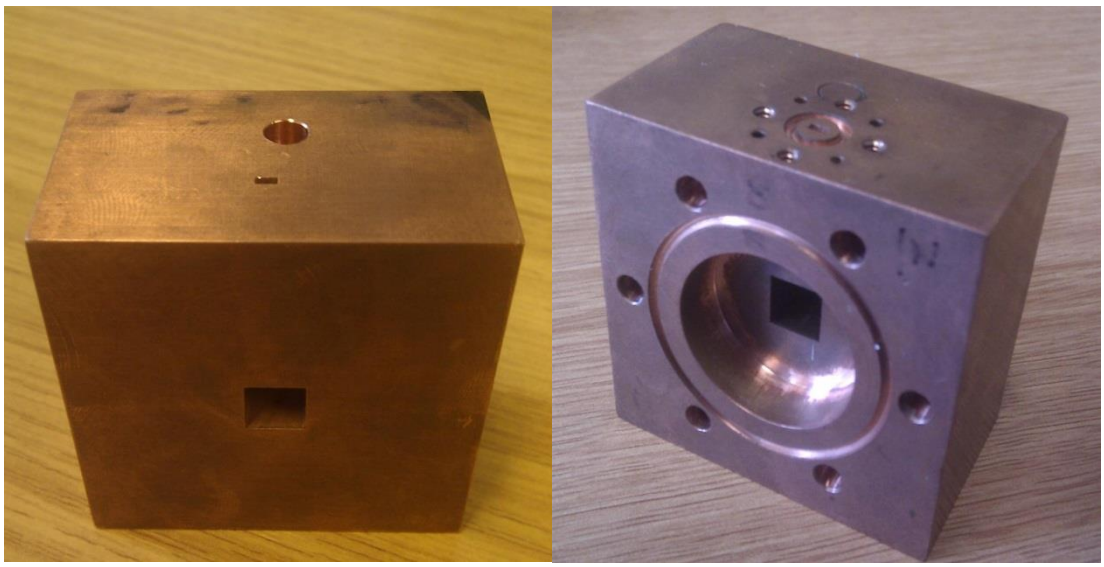

Figures 3.37 (a) and (b): Klystron housing structure during machining process, left, and completed block, right.

Vacuum sealing was achieved through the use of nitrile 32 mm inner diameter (ID) O-rings on either side of the housing structure and with 0.1 mm thick Mylar windows affixed over the mm-wave coupling slots, bound on both faces by 5 mm ID O-ring seals.

Input of the seed electromagnetic wave was performed via the use of standard dimension rectangular waveguide, 2.54 x 1.27 mm in size. The dimensions of the coupling slot were determined by the cavity width and the dielectric-adjusted cut-off, which changed with the square root of the material's dielectric constant. This led to a coupling slot width of 0.56 mm, sufficient to allow for coupling of much of the frequency band with limited attenuation, while the slot length was shortened to 1.054 mm due to the difficulty in achieving the desired resonance with cavities of 1.27 mm length.

3.5 Pseudospark Discharge Chamber Construction

The pseudospark discharge chamber as used in the course of the work of Dr. H. Yin, is constructed to an easily-adjustable, modular, vacuum-tight design, consisting of a hollow, stainless steel cylindrical cathode with two on-axis apertures, one to allow the insertion of an adjustable stainless steel inner electrode. The cathode has outer and inner diameters of 63 and 50 mm respectively, and the cathode depth may be adjusted from 0 to 100 mm before being fixed in position by a removable fixing plate. A recess in the centre of the outer cathode face allows for the inclusion of small discs of varying material, thickness and aperture size, although for most experiments a 3.25 mm thick copper disc with a central aperture of 3 mm diameter is used. This may be seen in figure 3.38.

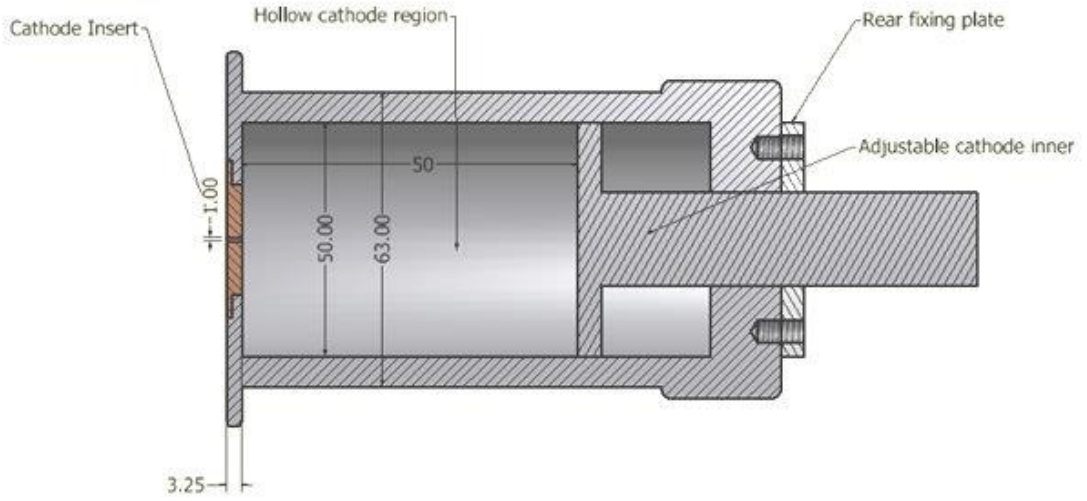

Figure 3.38: Cross-section of pseudospark cathode.

The anode is constructed from 12 mm thick stainless steel with a 3 mm diameter on-axis aperture and an outer radius of 120 mm. Screw fittings on the outer anode face allow for the attachment of diagnostics, beam collimators, drift regions in the form of cylindrical pipes, and microwave structures. An attached NW10 vacuum flange connected to a 4 mm diameter channel runs through to the central channel, allowing for evacuation of the discharge chamber. Multiple-gap pseudosparks are made possible through the inclusion of Perspex insulating discs, each 4 mm thick with

outer and inner diameters of 120 mm and 5.5 mm respectively, interspersed with intermediate electrodes, 3.25 mm thick stainless steel discs with an outer diameter of 80 mm and on-axis holes of 3 mm diameter. The Perspex insulator disks are designed with a convex shape in order to extend the surface flashover length. Figure 3.39 shows a four-gap configuration. Vacuum integrity is maintained through the use of nitrile O-rings between each anode and insulator face.

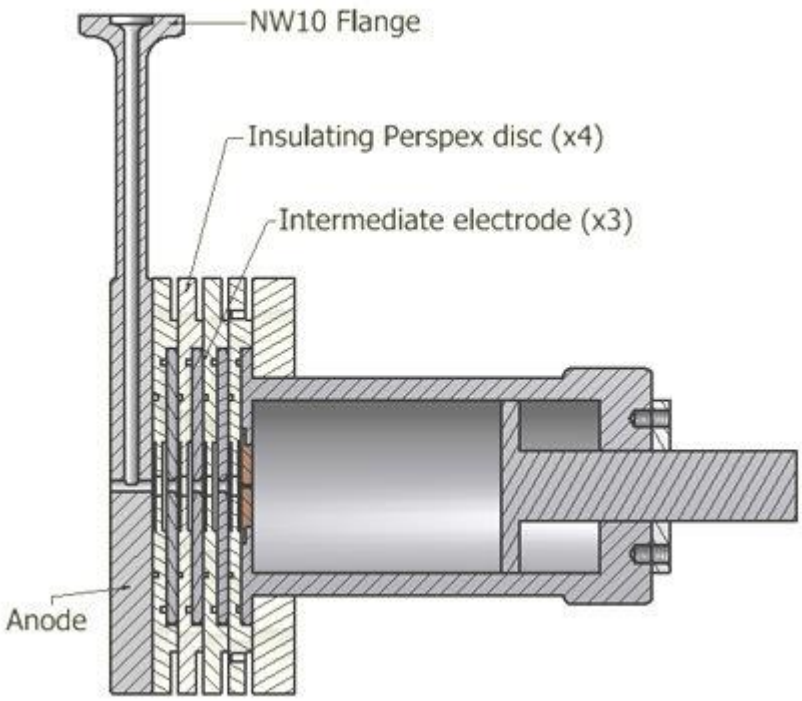

Figure 3.39: A four-gap pseudospark discharge chamber assembly.

3.6 Summary

In this chapter, the design, simulation and construction of a 200 GHz BWO and a 94 GHz klystron were presented, along with the design and construction of a novel dielectric-based coupling system. A description of the pseudospark discharge chamber and its construction was likewise included.

Analytical analysis of a G-band BWO using a 35 kV, 1.5 A electron beam yielded a dispersion diagram showing microwave generation at 190 GHz. Simulation of such a

structure in MAGIC-3D corroborated this, predicting 2.5 W of output power at 194.8 GHz. The design of a horn antenna for the device was predicted to produce 17.8 dB of gain, while an existing horn structure showed poor gain yet performed well in regards the elimination of undesirable modes due to internal reflection effects. As with the previous structure, manufacture of the device was accomplished through copper electrodeposition on an aluminium mandrel, though the conical horn was created separately through the use of wire spark erosion.

Through the analysis of an analogous LRC circuit design, a resonant cavity was designed and analysed using MAGIC-2D's eigenmode solver to have a resonant frequency of 94 GHz. This was used as the basis for a 3-cavity klystron, with cavities exciting an 8 kV, 36 mA electron beam. Interaction length, coupling factors and gain were predicted with small-signal analysis using MathCAD and verified through simulation, which predicted a peak output power of ~8 W, a gain of 20 dB and efficiency of 7.5%. In order to couple to the undersized cavities, a novel tapered coupler was devised which used wedge-shaped dielectric inserts in order to compensate for cut-off effects. A test of the principle was designed and tested in Microwave Studio before being manufactured in copper and tested using an Anritsu Lightning VNA. Cold-test analysis of the structure showed good agreement with simulated results, allowing for the design and simulation of a W-band analog. The klystron interaction structure was machined as a series of copper slates to compensate for limitations in manufacturing ability, assembled and housed within a copper housing block.

A modular design for a pseudospark electron beam source was constructed from stainless steel. A hollow cathode used a movable base to allow for its depth to be varied, while a hollow anode with 3 mm diameter central aperture allowed for electron beam extraction, as well as vacuum evacuation. Voltage hold-off could be achieved through the addition of Perspex insulating discs interspersed with intermediate stainless steel electrodes.

Chapter 4:

Apparatus & Diagnostics

4.1 Introduction

The purpose of the following chapter is to discuss the diagnostics involved in PS-driven mm-wave experiments, as well as to provide an overview of the experimental environment. Operating principles of the PS beam diagnostics, namely the Rogowski coil and the capacitive voltage divider, are presented, as are the specifics of the secondary equipment necessary for the operation of the PS discharge, e.g. high-voltage supply, vacuum system, and so on. Diagnostics for the measurement of other beam parameters, such as the cross-sectional area, shall be presented. Millimetre-wave diagnostic techniques shall also be introduced to ascertain the frequency and power of millimetre wave signals generated from the G-band BWO and W-band klystron, as well as to determine the resonant frequencies of the klystron cavities.

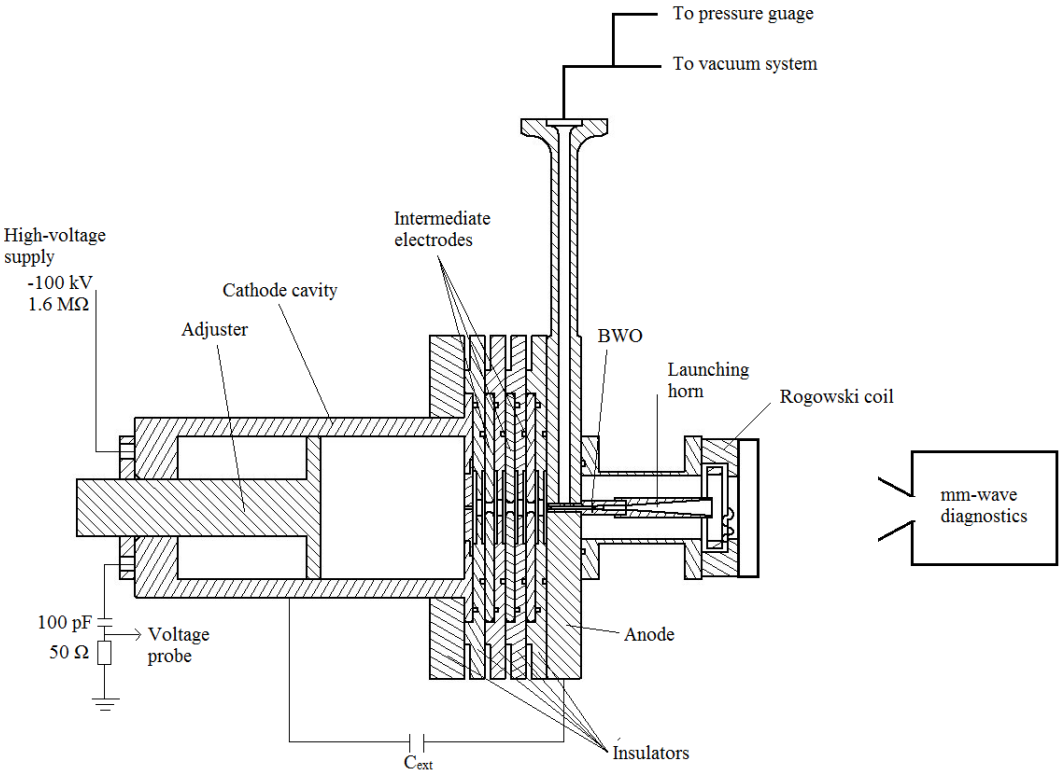

Figure 4.21: Experimental configuration for PS-BWO experiments.

Figure 4.1 shows the experimental configuration for 4-gap PS-BWO experiments and from it may be seen the main components. In addition to the PS discharge chamber and BWO, the specifications of which were described in Chapter 3, these are the

negative voltage supply, the beam diagnostics, most notably the voltage and current measurement systems, the vacuum system and the millimetre-wave diagnostics.

4.2 Electron Beam Diagnostics

Throughout the course of these experiments, there are two parameters of the pseudospark discharge that are necessary to monitor, and these are the discharge voltage and the electron beam current. Diagnostics should ideally have a fast response time, be relatively simple, and should be non-intrusive. With this in mind, discharge voltage was measured using a capacitive voltage divider circuit while beam current measurement was achieved through the use of a Rogowski coil. The design principles of these methods are discussed in Dr H. Yin's thesis [28].

4.2.1 Voltage Measurement

The PS discharge is marked by a number of features, one of which is its high amplitude, fast rise-time and sharp discharge voltage drop-off. To measure the voltage in a discharge circuit, there are numerous methods which may be used. The first option is to use an electrostatic voltmeter in conjunction with the discharge circuit, while a second is to make use of the breakdown characteristic of a calibrated sphere gap in air to calculate the breakdown voltage. The use of a voltmeter is the most appealing choice due to its increased accuracy, although neither are truly suitable since both methods only measure the magnitude of the voltage and not the voltage change in time.

In order to ascertain the temporal response of the discharge voltage in addition to the magnitude, one may use an optical measurement technique such as a Kerr cell [94] or a voltage divider in conjunction with an oscilloscope. Of these two options, the voltage divider is the more attractive due to the simplicity of its design and construction.

Voltage dividers are linear circuits which deliver an output voltage that is a fraction of their input, the ratio determined by the components involved in their construction. They may be purely resistive, for use in simple, low-frequency attenuation; purely capacitive, which allows for measurement over a wider bandwidth; or a combination of the two. While purely resistive circuits are low-noise, they are not as accurate as capacitive dividers. Conversely, a capacitive voltage divider will pick up noise and therefore will not prove effective for sub-μs rise-times [95].

A voltage monitor with a fast response and high load impedance is desired in order to measure the discharge voltage of the PS experiment. To this end, a capacitive probe based on the differentiation and integration of the input signal was designed.

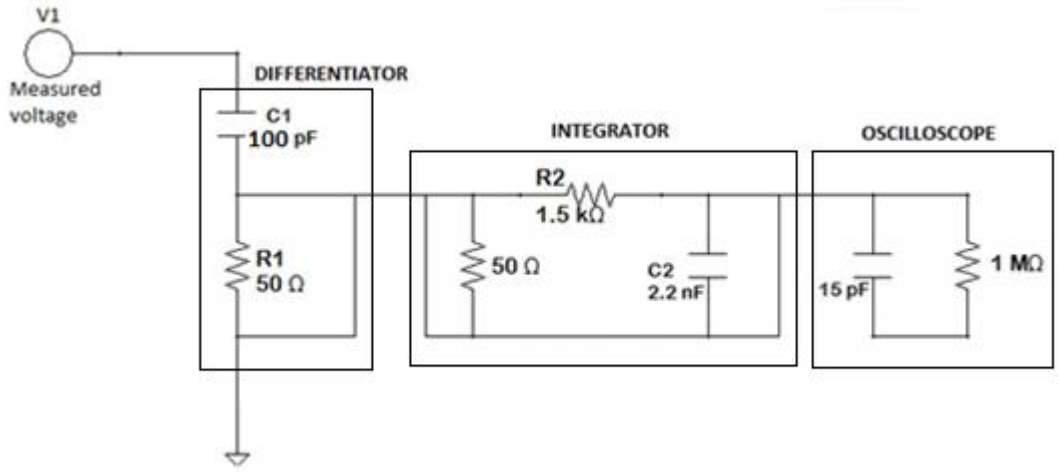

Figure 4.22: Configuration of capacitive probe for voltage measurement.

Working from the circuit in figure 4.2, the voltage change with time leaving the differentiator circuit may be calculated from V_{om} [96]

$$V_{om}(t) = R_1 C_1 \frac{dV_i(t)}{dt} \tag{4.1}$$

while the voltage entering the oscilloscope is given by

$$V_0(t) = \frac{R_1 C_1}{R_2 C_2} V_i(t) \tag{4.2}$$

In order to resolve the signal correctly, the differential condition $R_1C_1 \ll t_i$ must be met while the integrating condition $R_2C_2 \gg \tau$ should be satisfied by a factor of between 10 and 20, where t_i and τ are the rise-time and pulse duration of the measured signal, respectively.

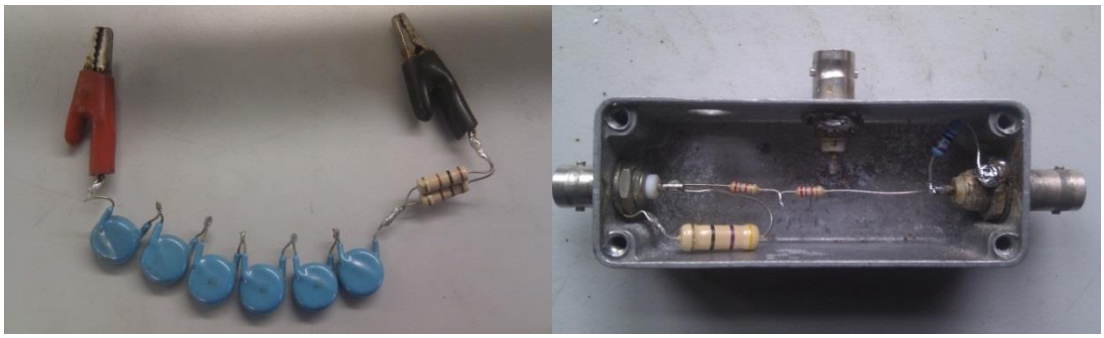

Figure 4.23 (a) and (b): Differentiating circuit, left, and integrating circuit, right.

The capacitor C_1 was constructed from 6 x 600 pF capacitors connected in series (figure 4.3 (a)), while C_2 consisted of a standard 2.2 nF capacitor. The capacitors were each rated to a voltage of 15 kV, allowing for failure of several capacitors without risk of system failure. For larger charging voltages the capacitors could be immersed in oil, thus increasing the breakdown field strength. The voltage divider was previously calibrated against a calibrated metal resistive voltage divider by comparing measurements using a pulse generator, and was concluded to have a rise-time of $\leq$ 15 ns and a sensitivity of 1.38 kV/V [28].

4.2.2 Beam current measurement

When measuring high-impulse currents there are a number of methods available, with the most popular non-destructive methods being the magnetic probe method, the resistive shunt method and the use of current transformers, which includes Rogowski coils. Destructive methods, such as Faraday cups and scintillation counters, are also possibilities for some situations. For the purposes of these experiments, a self-

integrating Rogowski coil was used for beam current measurement and verified using a Faraday cup.

4.2.2.1 Rogowski Coils

Rogowski coils are probes which are capable of measuring up to tens of MA with no interference and without any connection to high voltage conductors. They have been used in the monitoring of currents for over a century, and are particularly well-adapted to measuring currents from relativistic electron beams. Essentially a toroidal winding of *n* turns in a small area, it operates according to the principles of Ampère's law, which states that *the line integral of the magnetic field H around a single closed path is equal to the current enclosed*, and the Faraday-Lenz law, which describes the generation of an electromagnetic field by a changing magnetic field and that when this field appears in a closed circuit, it will induce a current in a direction that opposes that of the magnetic change [97].

The induced voltage in a coil of path length *dl* is given by

$$v_{dl} = -\frac{d\Phi}{dt} = -\frac{d}{dt}\left(\iint_S \vec{B}.d\vec{S}\right) = -\frac{d}{dt}\left(\iint_S \mu_0\vec{H}.d\vec{S}\right) = -\mu_0 A\frac{dH}{dt}\cos\alpha \tag{4.3}$$

The flux is then found by integrating along the coil and, given that the number of turns is finite, the induced voltage is then calculable. Hence, the measured current may be related to the induced voltage via the mutual inductance of the coil, *M*:

$$v_{coil} = -M\frac{dI}{dt} = -\mu_0 An\frac{dI}{dt} \tag{4.4}$$

The Rogowski coil may be considered equivalent to the circuit shown in Figure 4.4, where R_c is the coil resistance, L_c the inductance and C_c the capacitance.

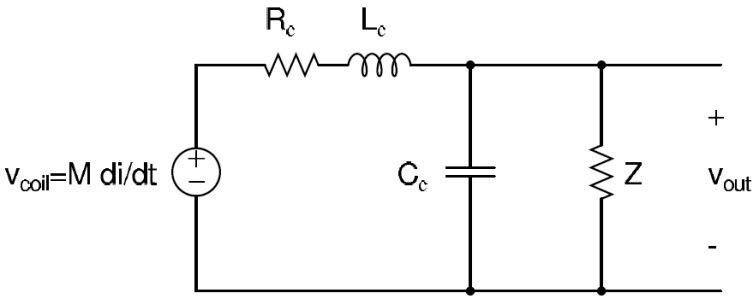

Figure 4.24: Equivalent circuit for a Rogowski coil.

When presenting a measurement impedance Z in the coil terminals, the transfer function may be defined as

$$\frac{v_{out}}{v_{coil}} = \frac{Z}{L_c Z C_c \omega^2 + (L_c + R_c Z C_c)\omega + R_c + Z} \tag{4.5}$$

Given that integration is necessary in order to observe a voltage signal proportional to the current waveform, a method of integrating v_{coil} is required. This integration may be performed mathematically, i.e. manually integrating the data received by the oscilloscope; electronically, through the use of a passive integration network; or through the use of a self-integrating Rogowski coil.

The latter method involves using a low enough resistance as the terminating impedance *Z* that equation 4.5 may be rewritten as

$$\frac{v_{out}}{v_{coil}} = \frac{R_{out} || (1/\omega C_c)}{R_c + \omega L_c} = \frac{R_{out}}{R_c + \omega L_c} \tag{4.6}$$

which may be simplified to

$$\frac{v_{out}}{v_{coil}} = \frac{R_{out}}{\omega L_c} \tag{4.7}$$

once we consider that, in the case of high frequency currents, the term ωL_c will be significantly larger than R_c, resulting in the above transfer function. The voltage produced by the measured current *i* is therefore

$$v_{out} = \frac{R_{out}}{\omega L_c} \cdot v_{coil} = \frac{R_{out}}{\omega L_c} \cdot Msi = \frac{R_{out}}{L_c} \cdot Mi \tag{4.8}$$

When considering designs for the Rogowski coils for use with the PS-driven electron beam a self-integrating type, as described above, is seen as preferable due to its improved sensitivity. To satisfy the conditions of L_c, ω and R_{out} above and thus maximise the output signal, the coil is designed and constructed from a ferrite core. It consists of ten turns of wire around the ferrite core with a 10 Ω external resistor connected in series. Inductance of the coil is measured to be in the region of 400-600 μH.

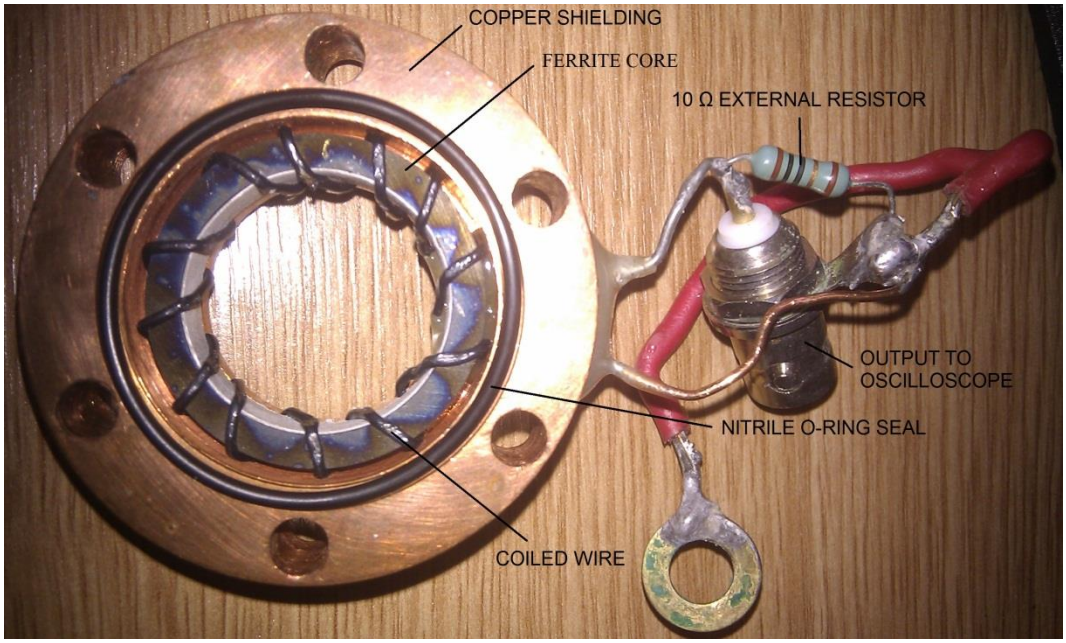

Figure 4.25: Rogowski coil for beam current measurement.

The Rogowski coil has been calibrated using a calibration test bench. A line current from a non-inverting type Blumlein was passed through the coil, with a 200 Ω fixed load attached in order to prevent current reflection in the circuit, and the current was adjustable by altering the charging voltage of the Blumlein. The cable Blumlein voltage was monitored and measured using the voltage divider described in section 4.3.1. Given that the load resistance was known, it was then possible to calculate the calibration current from the attached oscilloscope. The results showed that the Rogowski coil demonstrated linear sensitivity, and the calibrated sensitivity was determined to be 1.37 ± 0.05 A/V with a rise time of less than 10 ns. A more in-depth examination of the calibration process may be found in the thesis of Dr H. Yin.

4.2.2.2 Faraday Cup

Whilst not applicable to all situations, it is also possible to measure the current of an electron beam using a Faraday cup, generally considered one of the simplest forms of electron beam measurement techniques available. Named after 19th century electromagnetic and electrochemical pioneer Michael Faraday, it consists of a metal cup placed in the beam path. As electrons enter strike the surface of the cup collector they induce a current which then flows to ground via a resistor, typically measured using an oscilloscope for short pulses or a multimeter for longer duration pulses. Ideally, the cup should be shaped such that as few electrons as possible entering the collection area are able to escape. Given that it is a destructive method of beam current measurement its use is not applicable in all situations but when beam recovery is not an issue it is considered a highly accurate diagnostic device.

There are two main sources of error in faraday cup measurement: secondary electrons impinging on the conducting surface, and back-scattering from the cup surface. The first may be remedied by a number of methods, with the application of a biased electric field to the cup or a metallic mesh preceding the collection area being the most common while back-scattering effects may be minimised either through the shape and positioning of the cup and through the use of a low-z material, either to

line the cup surface or for construction of the faraday cup itself. Copper, with a backscatter coefficient of 0.30, is a common choice [98].

4.2.3 Beam Observation

Two methods of observing the size and position of the pseudospark-generated electron beam within this system have been used: witness plates and scintillator discs. Witness plates are sheets of metal which are placed perpendicular to a high-energy electron beam. From the resulting damage, it is possible to calculate the diameter of the beam at the position of impact, its position within the beam tube and, by extension, the electron beam divergence, accomplished through the insertion of several witness plates along the length of the beam transport region. By approximating the witness plate as an infinite slab, it is also possible to estimate the beam power flux and current [99]. For the following beam measurements, a 0.1 mm-thick molybdenum disc was used as witness plate, as well as an X-ray backscattering target (see section 4.2.4).

The other method used was that of a scintillator disc, a thin foil coated in a phosphorescent powder and situated in the beam tube downstream of the anode. As electrons strike the scintillator surface they in turn excite electrons within the scintillator material from the valence band to the conduction band or exciton band, leaving a hole in the valence band behind. Excitons, loosely bound electron-hole pairs, remain in the crystal lattice until they are captured as a whole by impurities within the material. This process causes the excitons to rapidly de-excite by emitting scintillation light, with the choice of activator impurities within the material determining the wavelength of the emitted light. With the correct material, it is possible to observe the cross-sectional profile of the electron beam, either with the naked eye or, in the case of higher voltage experiments where X-ray exposure may be an issue, with a digital camera (Nikon D40) and a sufficiently long exposure time.

4.2.4 X-ray Detection

A major application of electron beams is their use in the generation of X-rays. If an e-beam is directed at a target material possessing a high atomic number, the resulting exchange of energy will result in X-ray emission from the target; as such, detection and quantification of these X-rays may be used as a measure of beam energy.

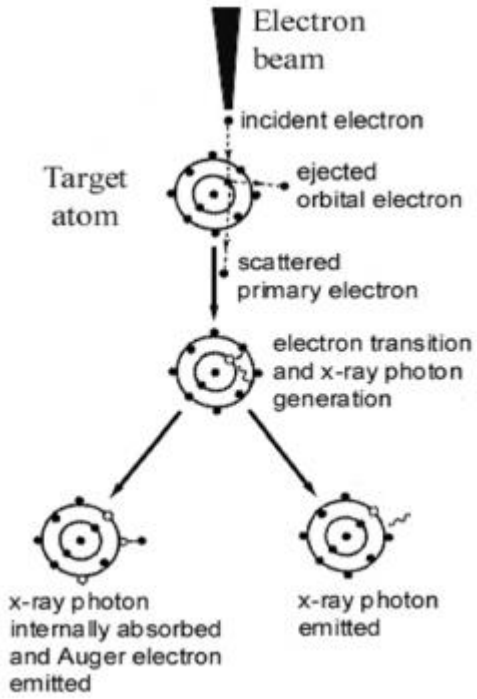

Figure 4.6: X-ray emission process from electron impact [100].

Figure 4.5 shows the X-ray emission process. As electrons strike the target surface there will be a degree of inelastic scattering. If the beam energy surpasses the critical excitation energy, E_c (also known as the X-ray absorption edge energy), of the target atomic shell, it can induce the ejection of inner shell electrons. For ionisation to occur, the overvoltage, U, of the electron beam, given as [100]

$$U = E/E_c, \tag{4.9}$$

must be greater than 1. The e-beam energy will be diminished by E_c as the target atom relaxes from its excited state via the transfer of an outer shell electron to the ionised inner shell and a characteristic X-ray photon will be generated. These X-rays

are either emitted or internally absorbed during the process of ejecting another outer shell electron, also known as an Auger electron. The fraction of X-rays emitted increases with the atomic number for a given shell, while the Auger yield decreases.

The wavelength of the emitted X-rays is given as

$$\lambda = \frac{hc}{E} \tag{4.10}$$

where λ is in Å and E is in keV.

The cross-section of inner shell ionisation is

$$Q = 6.51 \times 10^{-20}[(n_s b_s)/(UE_c^2)]ln(c_s U) \tag{4.11}$$

ionisations.cm^2/electron.atom, where n_s is the number of electrons per shell and b_s and c_s are constants which vary depending on the shell and overvoltage [101]. Energy lost by beam electrons due to inelastic scattering is given as

$$\frac{dE}{ds} = -7.85 \times 10^4 \left(\frac{Z\rho}{AE_m}\right) \ln\left(\frac{1.166E_m}{J}\right) \tag{4.12}$$

where the constant is equal to $2\pi e^4 N_0$ (N_0 being Avogadro's number), Z is the atomic number, A the atomic weight in g/mole, ρ the density in g/cm^3, E_m the average energy along path segment s in keV and J is the mean ionisation potential,

$$J(keV) = (9.76Z + 58.82Z^{0.19}) \times 10^{-3} \tag{4.13}$$

The electron stopping power of a material, S, is defined by

$$S = -\left(\frac{1}{\rho}\right)\left(\frac{dE}{ds}\right) \tag{4.14}$$

Q is found to be at a maximum with overvoltages of between 3 and 5.

Since characteristic X-rays are only generated when E_c exceeds the beam energy, the X-ray range is always smaller than the electron range. This range, in μm, is given as

$$R = \frac{K(E_0^n - E_c^n)}{\rho} \tag{4.15}$$

where K = 0.064 and n = 1.68 [100]. It is found that upper layers of the material produce more X-rays than equivalent freestanding layers due to incident electrons travelling randomly between layers through multiple scattering. As depth increases, electrons lose their energy and thus bring the overvoltage below unity.

Another method of X-ray generation is through Bremsstrahlung generation, where electrons lose energy to the Coulombic field created by the outer shell of a target atom. This lost energy is converted into Bremsstrahlung X-rays with maximum energies up to the initial electron energies. The maximum energy limit is known as the Duane-Hunt limit and it allows for accurate measurement of the electron beam energy.

The pseudospark X-ray diagnostic used a molybdenum target (Z = 42) of 0.1 mm thickness situated within a beam tube under vacuum and adjacent to the PS anode. Molybdenum is often used as an X-ray target for mammography systems and as well as possessing a high atomic number it also exhibits a high melting point, good thermal conductivity and low vapour pressure.

Detection of X-rays was achieved through the use of a Photonic Science Ltd. CoolView FDI 1:1 X-ray photodetector, with an available input area of 9.0 x 6.7 mm (1392 x 1040 pixels) and an optical resolution of 6.45 microns, situated 52 mm downstream from the anode. Capturing the image using an X-ray detector was a very similar process to that of capturing a beam cross-sectional image using a scintillator

and digital camera. The X-ray source sends a beam of X-rays through the object (in this case, two crossed copper wires of 0.1 mm diameter), with any rays not absorbed striking a scintillator layer, here a 30 micron-thick polycrystalline layer of Gadolinium Oxysulphide, optimised for resolution with X-ray energies of 5-60 keV, which then converts the X-rays into visible photons. To prevent contamination, an aluminium foil light exclusion membrane exists in front of the scintillator layer.

4.3 Millimetre-wave Diagnostics

Whilst electron beam diagnostics may normally be constructed and calibrated in-house, millimetre-wave diagnostics tend to bought intact and pre-tested. This is not only due to their complexity but also due to their small dimensions which, due to the wavelengths involved in frequencies of W-band and upwards, may drastically affect measured results. In the analysis of mm-wave signals, the components involved were the mm-wave detector, the frequency mixer and the vector network analyser. In addition, a combination of observed measurements and simulated results allowed for the calculation of the measured device's total mm-wave power.

4.3.1 Millimetre-wave Detector

Figure 4.7: Zero-biased detector for 140 - 220 GHz signals.

For detection of G-band (140 – 220 GHz) signals, an ELVA-1 ZBD-05 zero-biased detector was used. Based on a Schottky barrier lead diode design and using a WG5 feed as an input port, it exhibits >150 mV/mW sensitivity (~350 mV/mW at 200 GHz) and outputs a positive signal via an SMA connection, with 10 MHz video bandwidth output and 1 V maximum output. In addition, a buffer amplifier was connected between the SMA output and monitoring device, a Tektronix oscilloscope. Power levels were garnered from a calibration chart provided by ELVA-1, showing signal sensitivity across the detector's full bandwidth.

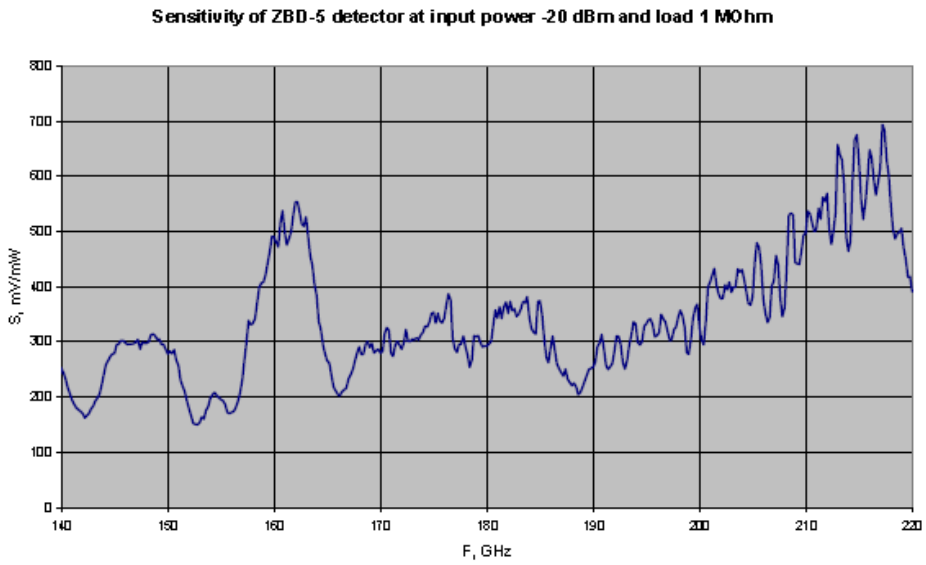

Figure 4.8: Calibration chart for ZBD-5 zero biased detector.

At W-band frequencies, a Flann Microwave 2701 detector, with a working frequency range of 75-110 GHz, was used in conjunction with a matched load and fed via a WR10 horn antenna.

4.3.2 Frequency Mixer

Frequency mixers are devices which take two input frequencies, one from a local oscillator (LO) and the other a radio-frequency (RF) signal, and output a composite intermediate frequency (IF) signal equal to

$$f_{out} = f_{in1} \pm f_{in2} \tag{4.16}$$

There also exists a subset of frequency mixers known as sub-harmonic mixers which use a lower-frequency source as an input and operate at a higher-order harmonic, i.e.

$$f_{out} = f_{in1} \pm k f_{in2} \tag{4.17}$$

where k is an integer.

In G-band experiments, a Militech MSH-05 sub-harmonic mixer, which operates at the second harmonic of the LO frequency, was used. It achieves noise figures of 5-9 dB and uses a band-pass filter to clean up LO harmonic signals while a notch filter reflects 3rd harmonics of the LO back into the mixer, thus providing optimum mixer conversion efficiency.

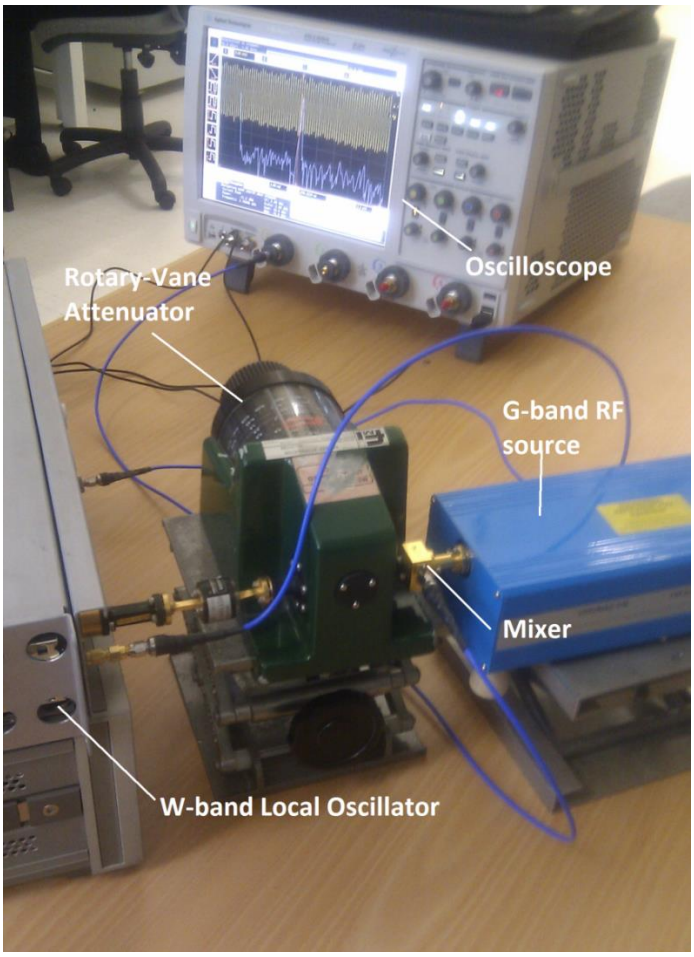

Figure 4.9: Experimental configuration for the calibration of a sub-harmonic mixer.

The sub-harmonic mixer was calibrated by connecting the LO port to a W-band high-frequency source at a frequency of 91 GHz, attenuating the power via a rotary vane attenuator with a maximum attenuation of 70 dB. The RF port was connected to an Anritsu Lightning Vector Network Analyser (VNA) via an OML S05MS signal generator extension module, capable of generating and analysing frequencies from 140-220 GHz. The VNA was operated in continuous wave, single frequency mode at frequencies of 185 to 191 GHz in approx. 1 GHz steps. The IF was output to an oscilloscope and attenuation was lessened until a composite frequency signal was output. An FFT analysis was performed on the output signal and the peak frequency of the composite signal was recorded and compared with calibration results observed at the University of St. Andrews, from whom the frequency mixing unit was on loan. Figure 4.10 shows the output of both the composite signal and its FFT transform at an RF frequency of 190 GHz while table 4.1 shows the observed IFs and conversion losses for the full scan.

Figure 4.10: Oscilloscope display of an IF signal in yellow and its Fourier transform in blue.

RF Frequency (GHz)	185	186	187	188	189	190	191
IF Frequency (GHz)	1.2	0.1	0.8	1.8	2.8	3.8	4.8
Conversion Loss (dB)	10.1	9.2	8.9	8.7	8.5	8.7	9.1

Table 4.1: Calibration observations of a sub-harmonic mixer using a 93.1 GHz LO input signal.

The observations were found to lie within 0.05 GHz of the previously recorded measurements.

Frequency detectors may also be used to determine the spectrum of a millimetre wave signal by capturing and recording the output of the LO signal and calculating the difference between the LO spectrum and that generated through the FFT of the generated IF signal, i.e.

$$\begin{aligned} f_{RF} &= f_{LO} - f_{IF}, ; f_{LO} > f_{RF} \\ f_{RF} &= f_{IF} - f_{LO}, ; f_{LO} < f_{RF} \end{aligned} \tag{4.18}$$

This not only eliminates the need for filters to determine the frequencies of signals but also returns a more accurate measurement of the frequency of the generated signal. To achieve this, an input horn was attached to the G-band RF input of the mixer while the LO signal was provided by the W-band signal generator. An output was fed to an oscilloscope and the signal was triggered by means of the collapse of the PS voltage pulse. As the PS discharges, the resultant IF signal can be scanned and, via an FFT of the mixed pulse signal, the dominant frequency of the device can then be determined by addition to, or subtraction from, the LO frequency. This technique allows for an accurate and repeatable method of determining the signal frequency, though the decision to add or subtract the IF may be unclear at lower frequencies, it may be inferred by means of repeated shots with varying LO frequencies.

4.3.3 Vector Network Analyser

Whilst frequency mixers and detectors may be used to detect and analyse microwave signals transmitted from antenna sources, vector network analysers (VNAs) provide an effective diagnostic technique for determining cavity resonances as well as transmission loss and reflection.

VNAs generally consist of a signal generator, a test set and a receiver and use them in order to determine the network parameters of high-frequency networks. These are normally output as scattering parameters, or S-parameters) in the form S_{mn}, where m is the input port and n is the output port. In practice, this equates to S_{11} denoting input port reflection, S_{12} the reverse voltage gain, S_{21} the forward voltage gain and S_{22} output port reflection. Many VNAs carry the ability to be fitted with extension modules in order to increase their effective frequency range.

Figure 4.11: Anritsu VNA with 140 - 220 GHz extension modules connected.

An Anritsu ME7808B broadband VNA, comprised of a 37397D VNA (40 – 65 GHz), a 3738A broadband test set, a MG3692A /15A / 3 Signal Generator (10 MHz to 20 GHz) and a MG3694A /15B / 3 Signal Generator (2 to 40 GHz), was used to test microwave components. For operating at W-band frequencies two Anritsu 3742A-EW extension modules were used, operating in the 65-110 GHz frequency band, while for G-band testing, two OML V05VNA2 T/R VNA extension modules, with a working frequency range of 140 – 220 GHz, were used. In order for the VNA to compensate for the adjusted frequency range, the band definition was adjusted by setting the start and stop frequencies (220 GHz and 140 GHz, respectively) and either multiplying or dividing the processed input and output frequencies by integers and introducing offset frequencies. Source 1 was set with a divisor of 12 and an offset of -0.27 GHz, source 2 was configured with a divisor of 12 and the receiver had an offset of +0.27 GHz.

The VNA was calibrated with a full 12-term, 1601 point SSLT (Short-Short-Load-Thru) calibration using an appropriate calibration kit (OML V05CAL for G-band, Anritsu 3635 for W-band). This involved a complete frequency sweep with attached matched loads, in order to provide an isolated reading. Next, offset shorts of differing offset distances were attached, and, after scans, the offsets were applied to the opposite heads. Finally, a thru, port-to-port sweep was performed, providing the reading necessary for the VNA to adjust for systematic errors in the test sets, cables and fixtures. This calibration was typically performed each day.

At X-band frequencies (8-12 GHz), an integrated Anritsu 37397A VNA with a frequency band of 45 MHz to 65 GHz was used, fitted with coaxial to rectangular waveguide converters. The calibration process for this VNA followed the same pattern and criteria as for higher-frequency operation.

4.3.4 Power Calculation

It is possible, using general antenna theorem, to estimate the total output power of a radiating mm-wave device. If an antenna horn radiates a total power of $P(\theta,\phi)$ at an angle of (θ,ϕ) the total power P_0 can be found through [102]

$$P_0 = \int_0^{2\pi} \int_0^{\pi} P(\theta,\phi) \sin\theta \, d\theta d\phi \tag{4.19}$$

where $\theta(0 \rightarrow \pi)$ and $\phi(0 \rightarrow 2\pi)$, with angles presented in the polar co-ordinates system with the radiating horn at the origin.

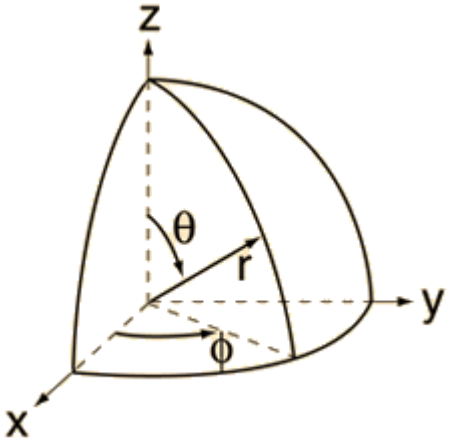

Figure 4.12: Spherical polar coordinates system with antenna at origin.

In practice, $P(\theta,\phi)$ is independent of ϕ and as such the above equation may be simplified to

$$P_0 = \int_0^{2\pi} \int_0^{\pi} P(\theta,\phi) \sin\theta \, d\theta d\phi$$

$$= \int_0^{2\pi} \int_0^{\pi} r^2 P(\theta, \mathrm{r}) \sin\theta \, d\theta d\phi \tag{4.20}$$

$$= 2\pi r^2 \int_0^{\pi} P(\theta) \sin\theta \, d\theta$$

where r is the distance between measuring point and launching antenna, $P(\theta,\phi)$ is the power density per unit angle and $P(\theta,r)$ is the power density per unit area. The integration in equation 4.21 may be completed by numerically integrating the normalised TM_{01} profile of the antenna and multiplying this by the maximum power density observed. In some cases an experimental observation of the TM_{01} profile may be unachievable and as such a simulated equivalent may be used to give an approximation.

4.4 Apparatus and Experimental Setup

As discussed in Chapter 2, the pseudospark discharge operates within a specific pressure range, and at a voltage governed by that pressure. As such, devices to supply these pressures and voltages are required, as well as the ability to monitor them. Additionally, an environment equipped to absorb the X-rays generated from high-energy usage is a necessity.

4.4.1 DC Voltage Supply

The PS discharge chamber is charged by a Glassman PK100N40 high-voltage DC power supply (-100 kV, 40 mA), connected to the chamber via a 3 MΩ charging resistor. External capacitance is added via three chains of capacitors, each consisting of seven 15 kV, 1000 pF capacitors, connected in parallel, resulting in 428 pF effective capacitance to reduce the inductance in the discharge circuit. The discharge voltage amplitude and, consequently, the beam energy vary with the pressure within the PS discharge chamber.

4.4.2 Vacuum System

Vacuum is achieved using an Edwards RV12 rotary vane pump, capable of speeds of $12 m^3 h^{-1}$ and an ultimate vacuum of 2×10^{-3} mbar, connected via an NW25 outlet to a Speedivac vacuum valve, normally closed, and an Edwards PV10EKA solenoid isolation valve, and to the anode by means of a Nupro needle valve, opened to allow for slow gas leakage.

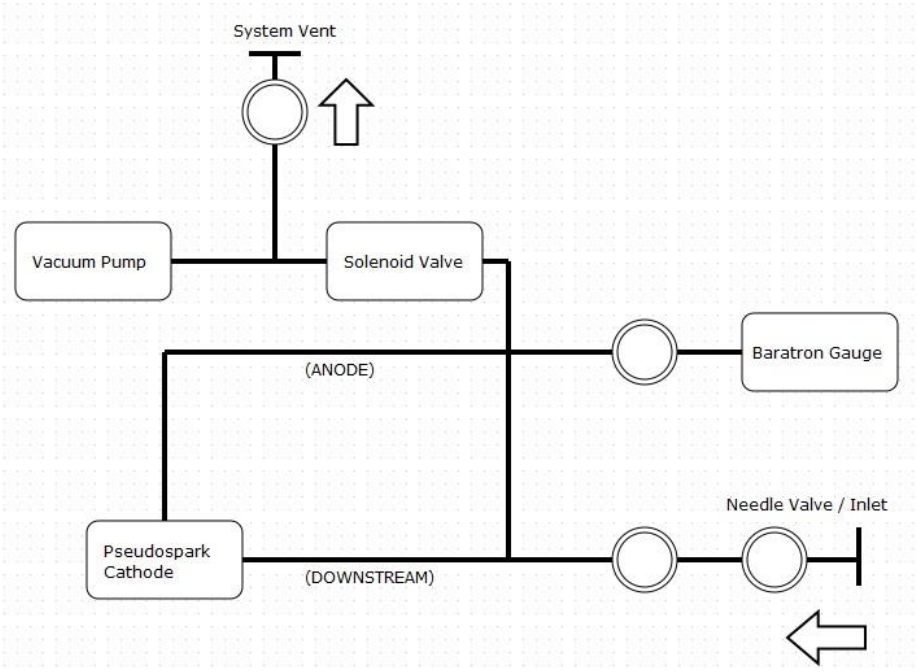

Figure 4.13: Schematic showing configuration of vacuum system.

This allows for control of gas leakage from outside the radiation shielding area by means of powering down the solenoid isolation valve, thus allowing the needle valve to leak air into the system at a preconfigured rate. After discharge occurs, the solenoid may be switched on and the system pumped down to a static base pressure. Pressure is monitored by means of a Baratron-type pressure gauge in conjunction with an MKS 250 gas inlet pressure/flow control module situated outside the shielded room. While this does not allow for monitoring of pressure throughout the system, the low vacuum requirements of the PS discharge mean that this is not of utmost importance.

The decision to use air as a working gas is largely a practical one. Whilst experiments on PS discharges with gases such as helium, argon and nitrogen have been conducted and argon has been found to deliver the most stable performance [28], air provides a cheap and abundant working gas which may be readily pumped and evacuated quickly and effectively. For this reason, air is an acceptable choice of gas for the experiments outlined in this thesis.

4.4.3 Safety System and Radiation Shielding

The discharge chamber is situated in a room bound on three sides by 50 cm-thick concrete walls, and on the floor and ceiling by a 6 mm steel wall flanked on either side by 3 mm-thick lead plates, with a steel outer wall of ~9 cm thickness. Movable lead shielded doors are constructed to the same specifications. Due to the presence of a gas-operated interlock system, all control and adjustments to be made to the pseudospark configuration must be performed from outwith the shielded area whilst the high-voltage supply is in operation. A full risk assessment of the pseudospark experimental area may be found in Appendix III.

4.5 Summary

A pseudospark electron beam source has been constructed with a simple, modular design, allowing for control of voltage hold-off through the use of Perspex insulating discs and stainless steel inter-electrodes, and with the ability to attach a variety of interaction structures to the anode whilst maintaining vacuum integrity. The discharge chamber is charged by a 100 kV, 40 mA DC Glassman power supply via a 3 MΩ charging resistor.

Vacuum has been achieved via a rotary vane pump, whilst pressure is controllable from outwith the experimental area via an electrically operated solenoid valve in conjunction with a needle valve. This configuration allows for both single and repeated shots and for both the power and the cross-sectional diameter of electron beams to be adjusted.

Electrical diagnostics for the circuit include measurement of the discharge voltage and the electron beam current. Voltage is monitored through the use of a capacitive probe with a risetime of $\leq$ 15 ns and a calibrated sensitivity of 1.38 kV/V. Beam current measurement utilised a compact, self-integrating, high sensitivity Rogowski coil based on a high permeability ferrite core with a risetime of $\leq$ 1ns and a

sensitivity of 1.37 A/V, as well as a copper and brass Faraday cup for downstream measurements of current. Beam cross-sectional imaging was achieved through the use of a molybdenum witness plate and a phosphorescent scintillator disk paired with a long-exposure digital camera. The X-ray emission properties of the pseudospark electron beam were probed using a molybdenum back-scattering target and an X-ray photodetector.

Experiments are conducted within a concrete and lead shielded environment whilst measurements are observed outside this area using a variety of oscilloscopes with frequency bandwidths of up to 20 GHz and sample rates of 20 GSa/s situated within an electromagnetically isolated room.

Chapter 5:

Experimental Results

5.1 Introduction

The pseudospark-based experiments undertaken as part of this work can be placed under two categories: those involving pseudospark beam diameters of 3 mm, which are a continuation of the PS e-beam work carried out at the University of Strathclyde in previous years under Dr Huabi Yin, and reduced-diameter beam experiments, where a collimating structure is used to reduce the e-beam's cross-sectional diameter carried out by D. Bowes. Such a structure may be one constructed solely for that purpose or the beam entry point for some other device. Reduced diameter experiments carry smaller currents and beam powers and, as such, diagnostics are generally more difficult to implement in relation to unconstrained beams. This may be alleviated through the use of higher charging voltages and, consequently, increased beam energies, which may be realised via the use of multi-gap PS configurations.

This chapter aims to present the results of experiments using pseudospark discharges to generate millimetre-wave radiation from a G-band BWO interacting with a 1 mm diameter beam and high-frequency radiation from a 94 GHz klystron, as well as preliminary experiments conducted with Dr. Huabi Yin using a W-band BWO. The experimental configuration of all apparatus shall be presented, along with operating procedures and any diagnostic measurements pertaining to the beam qualities and performance, while experimentally obtained results shall be compared, where possible, with estimated performance parameters from numerical calculations.

5.2 Pseudospark e-beam Experiments

5.2.1 3mm e-beam Measurements and X-ray Emission

A4-gap pseudospark system was configured as in figure 5.1 before being sealed with an electrically operated solenoid valve and evacuated to a pressure of ~100mTorr. The discharge chamber was connected to a Glassman negative voltage supply via a 30 MΩ resistor and DC voltages in the range of 40-46 kV were applied. An external

energy storage capacitor of 428 pF across the cathode and anode consisted of three chains of capacitors in parallel to reduce the inductance in the discharging circuit. Each chain consisted of seven 15 kV, 1000 pF resin dipped ceramic capacitors connected in series. The anode was grounded, while voltage and current were measured using the capacitive voltage probe and Rogowski coil outlaid in the previous chapter. Power to the solenoid valve was removed and the working gas (air) was allowed to enter the system through a fine control needle valve, opened to allow air to enter at a slow and controlled rate, maintaining gas uniformity within the discharge chamber. Pressure was monitored via a Baratron pressure gauge and the solenoid was re-engaged following discharge.

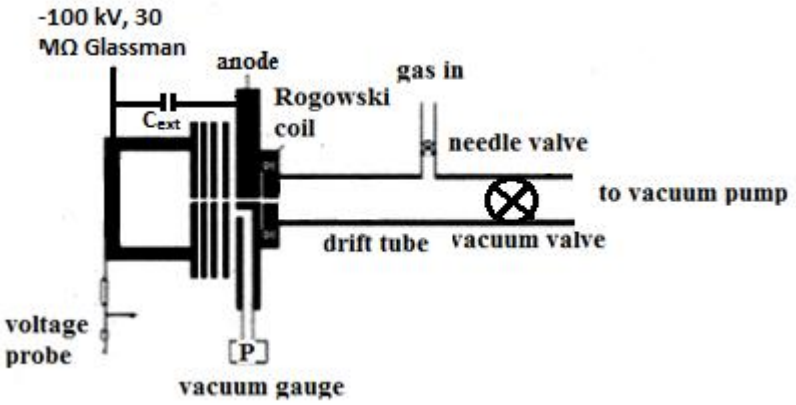

Figure 5.1: Schematic of 4-gap pseudospark beam experiments

Discharge occurred at a pressure of ~400 mTorr. Figure 5.2 shows a typical recorded beam current trace from a 4-gap pseudospark electron beam along with subsequent voltage collapse, with hollow cathode and superdense glow currents of 70 A and 200 A respectively measured by the Rogowski coil and a triggered oscilloscope, set to record with the current rise. The trigger level was set at 200 mVs which was equivalent to a measured beam current of 50 A in order to eliminate noise signals. Repeated shots showed a variation of ± 10% in the beam current, while the maximum pulse length of ~ 110 ns remained approximately constant.

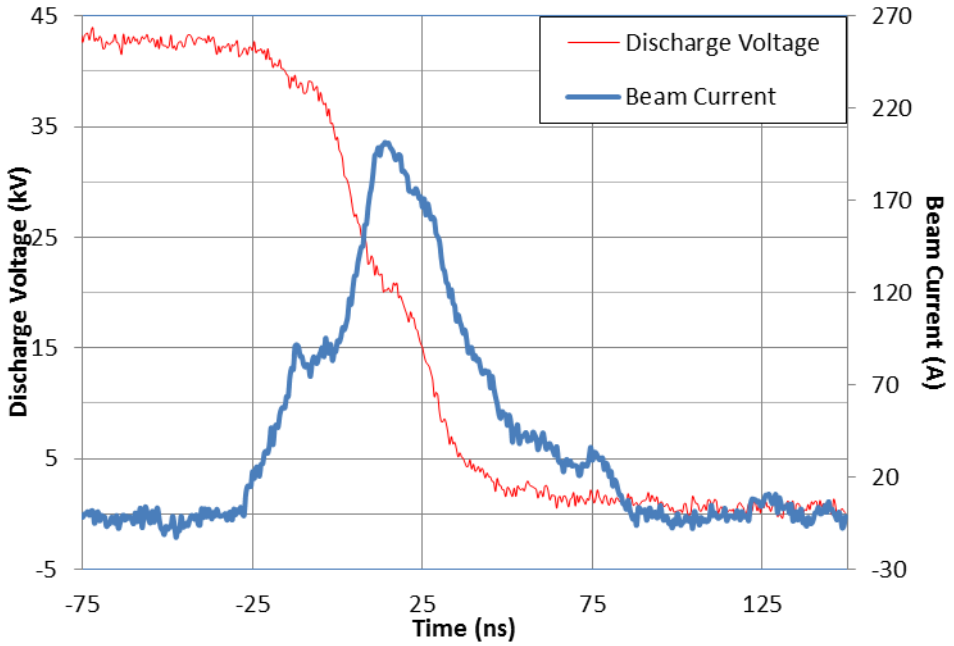

Figure 5.2: Beam current trace of a 4-gap, 43 kV, 3 mm diameter pseudospark e-beam.

Cross-sectional images of the produced electron beam were captured using a scintillator constructed from a disc of 0.1 mm-thick copper foil coated in a layer of phosphorescent scintillator powder, held within a copper frame and situated in a length of drift tube downstream of the PS anode and Rogowski coil. As the electrons strike the scintillator disk they impart energy sufficient for the powder to emit a diffuse glow which was then captured using a high-speed digital camera placed adjacent to the output window. A 3-gap PS was configured, although all other apparatus remained as before. Figure 5.3 shows a cross-sectional image obtained from an electron beam generated at an applied voltage of 23 kV, with a central bright spot of 3 mm diameter within a drift tube of diameter 22.5 mm (thin circle).

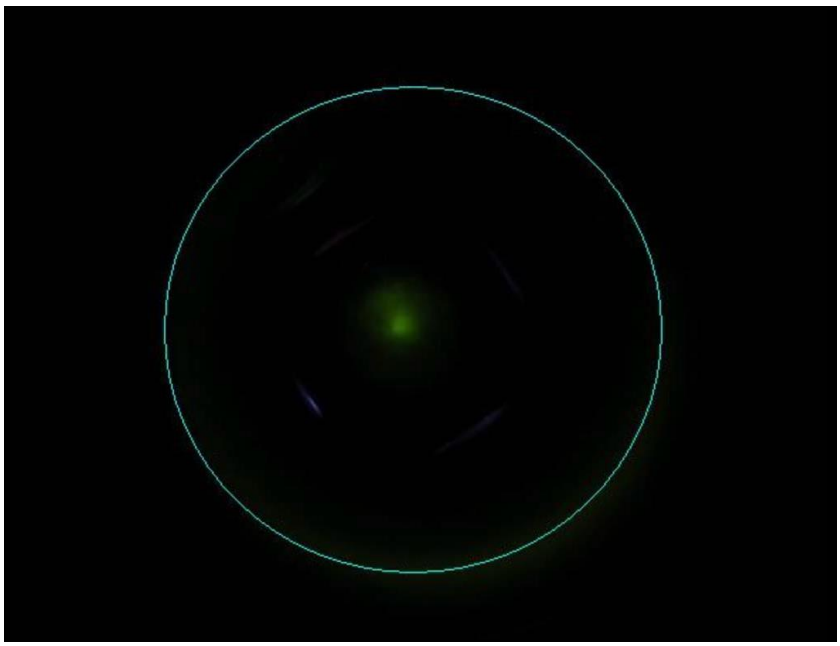

Figure 5.3: Image of a single-shot pseudospark electron beam with a cross-sectional diameter of 3 mm.

Figure 5.4 shows an image captured after 3 successive shots at 23 kV, with a central bright spot of approximately 3 mm diameter, the increase in size being due to the fact that the electron beam focal point often moves slightly between shots. The bright specks are an effect caused by the scintillator disk holder. A thin halo of light may be seen around the edges of the drift tube, which is an indicator of ion channel formation. This illustrates the presence of an ion channel, caused by the initial high-energy electrons ionising the background gas. As the electron beam progresses into this region, it causes the channel electrons to be displaced while the heavier ions remain fixed. These expelled electrons then strike the scintillator disk, causing the halo effect seen in figure 5.4, while the ion channel both guides and focuses the electron beam.

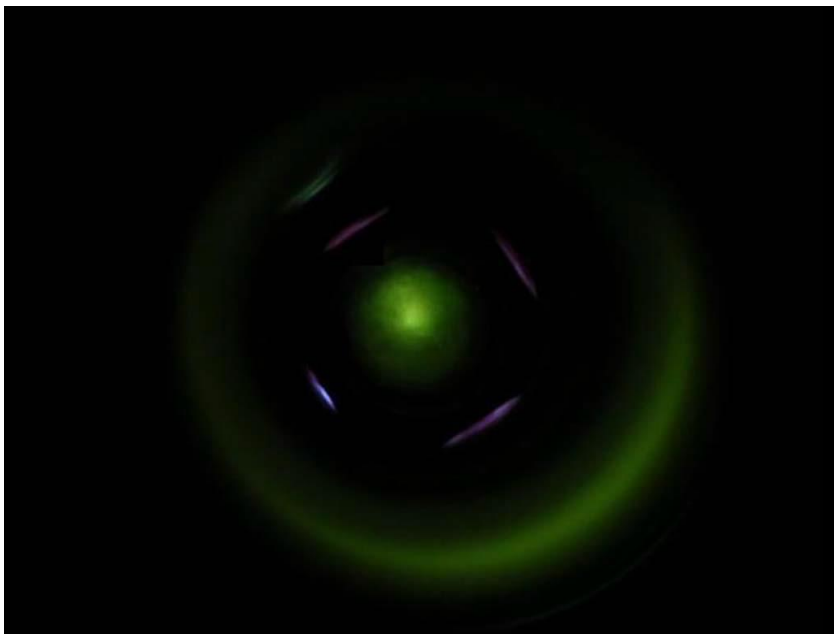

Figure 5.4: Captured image of 3 mm diameter beam using a phosphorescent scintillator. Integrated over the course of three successive shots, the surrounding ring is an indication of ion channel formation.

Using a magnetic-field-free collimator with an axial diameter of 3.5 mm and a length of 5 cm, a time-dependent beam brightness of up to $10^{11\text{-}12}$ A $m^{-2}rad^{-2}$ was measured [28].

The electron beam from the 4-gap PS discharge system was further used in X-ray generation as shown in figures 5.5 and 5.6.

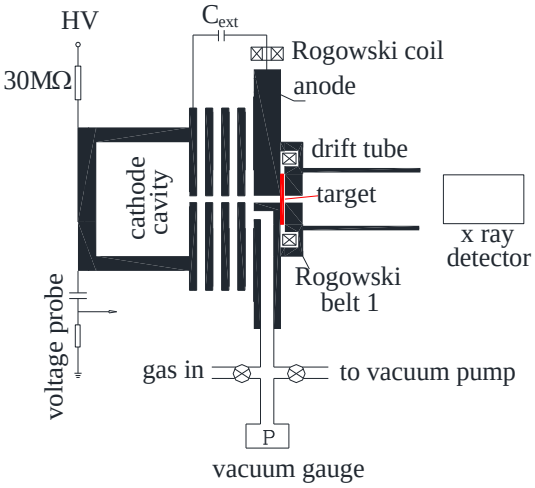

Figure 5.5: Pseudospark X-ray experimental schematic.

A molybdenum target of 0.1 mm thickness was situated adjacent to the anode followed by the X-ray photodetector, situated 52 mm from the anode. The choice of target material met the requirements of a high melting point (2896 K), good thermal conductivity (138 $Wm^{-1}K^{-1}$), low vapour pressure (1 Pa at 2743 K) and high atomic number (42),and is commonly used in mammography. This target also served as a witness plate for the PS-generated electron beam.

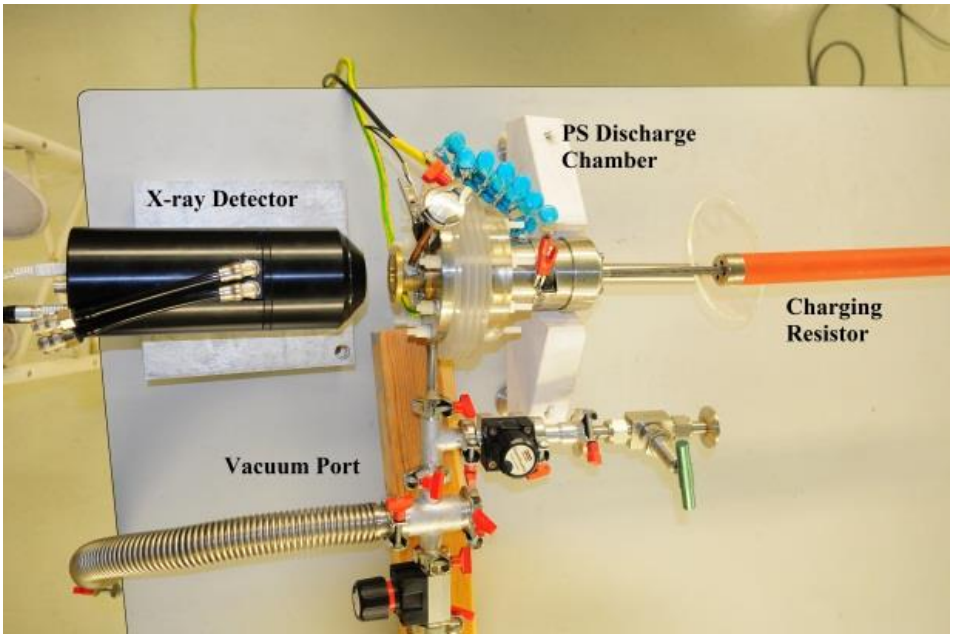

Figure 5.6: Experimental setup for pseudospark X-ray imaging.

An object, in this case two crossed lengths of 0.1 mm diameter wire, was placed between the anode and detector as the X-ray imaging target (Figure 5.7) while the detector itself was a Photonic Science Ltd. CoolView FDI 1:1, with an available input area of 9.0 x 6.7 mm (1392 x 1040 pixels) and an optical resolution of 6.45 microns. The object served to act as a contrasting image which, upon generation of X-rays, would act as a barrier for any radiation and would thus appear as a darker, undeveloped region on any image captured via the X-ray photodetector.

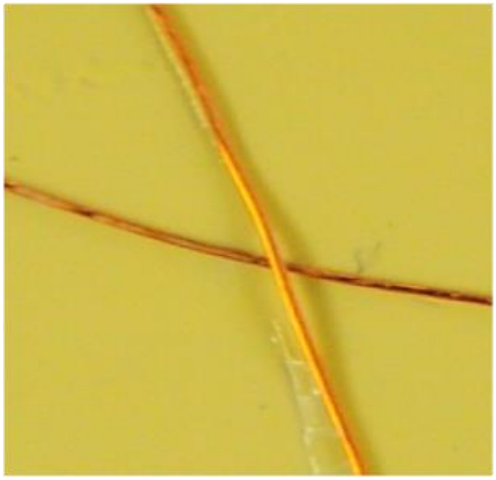

Figure 5.7: Crossed 0.1 mm diameter wire X-ray image target.

Capturing the image using an X-ray detector was a very similar process to that of capturing a beam cross-sectional image using a scintillator and digital camera. The X-ray source sends a beam of X-rays through the object, with any rays not absorbed striking a scintillator layer, here a 30 micron-thick polycrystalline layer of Gadolinium Oxysulphide, optimised for resolution with X-ray energies of 5-60 keV, which then converts the X-rays into visible photons. To prevent contamination, an aluminium foil light exclusion membrane exists in front of the scintillator layer.

Following evacuation to 100 mTorr, a steady voltage was applied and, after closing the vacuum pump with an electromagnetic valve, the working gas (air) was allowed

into the system at a slow rate (*dp/dt* of ~0.5 mTorr/s) by means of the adjustment of a fine control needle valve until discharge occurred, at which point the discharge pressure was recorded and thus the relationship between applied voltage and breakdown gas pressure was obtained.

Repetitive-shot discharges were then initiated via the adjustment of the needle valve while the pump was still in operation; in such a fashion, a desired steady-state pressure of 450 mTorr was achieved. Voltage was applied at 50 kV, reduced until breakdown occurred and kept at a steady voltage for repetitive breakdowns with a frequency of 1 Hz over a length of one minute, allowing the X-ray detector to continuously acquire image data with each successive shot. While the detector was continually acquiring data, the captured image was based on observations from a single discharge. The practice of repetitive breakdown simply eliminated the need to time the image capture to coincide with the PS discharge by increasing the chances of capturing a single shot in a relatively brief period of time, in this case approximately 1 minute.

Discharge voltages of between 22 and 46 kV were applied with the molybdenum target present, an X-ray beam was generated as shown in figure 5.8 (a).The target also served to act as a witness plate for the beam, and illustrated the 3 mm beam cross-section (figure 5.8 (b)).

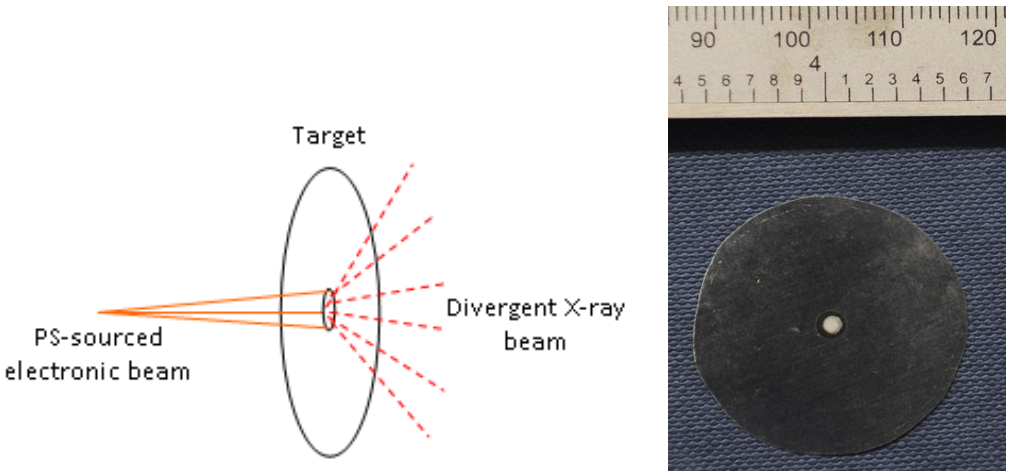

Figure 5.8 (a) and (b); Schematic diagram of X-ray generation, left; and molybdenum target showing incident region of 3 mm cross-section beam, right.

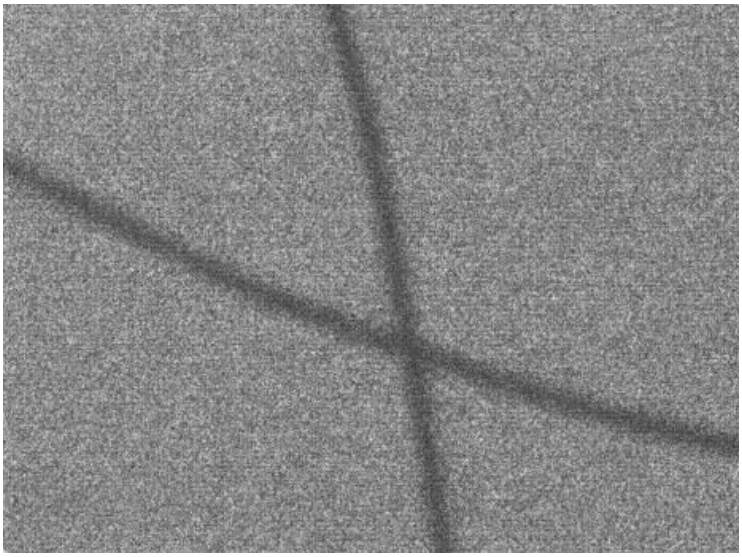

Figure 5.9: X-ray image of crossed-wire object at 46 kV.

Through the use of Siemens' simulator the spectrum of the generated X-ray photons was predicted for a 34 kV beam impacting on the molybdenum target with an air kerma of 1 Gy, showing an average X-ray photon energy of 15.83 keV (figure 5.10). Given the low energy, the aluminium membrane of the detector was removed and the integration time of the charge-coupled device (CCD) was selected to be 800 ns.

Images of the cross-shaped target were then received by the X-ray detector, with the clearest images being generated at 46 kV (figure 5.9).

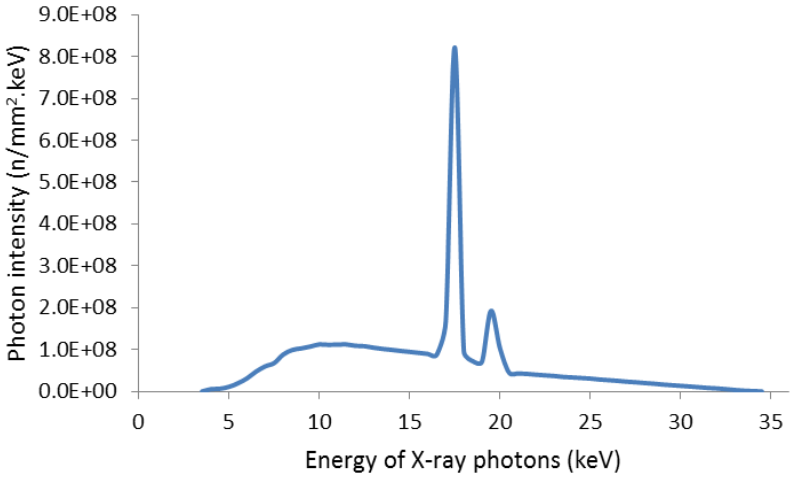

Figure 5.10: Observed spectrum of X-ray photons, showing an average energy of 15.83 keV.

The captured X-ray image acted as proof of the existence of the electron beam. Image capture was attempted at voltages of as low as 40 kV but the observed images lacked resolution and definition, indicating that the 46 kV applied voltage acted as a threshold for the generation of detectable X-rays with a molybdenum target. Due to voltage collapse during discharge, the actual beam voltage which generated the X-ray image was likely in the region of 34 kV, which could be verified in the future by means of spectral analysis of the emitted X-ray photons and subsequent comparison to the spectrum produced by Siemens' simulator. This would provide a good basis for the development of the PS discharge as a small-spot X-ray imaging source.

5.2.2 Reduced-Diameter Beam Measurements

In order to generate beam diameters of 1 mm, a stainless steel collimator was machined from a 0.5 mm thick stainless steel disc, attached directly to the anode via six M4 screws. A two-gap pseudospark discharge was configured as above and sealed using a stainless steel plate. The system was evacuated to an equilibrium state (~ 100 mTorr) before voltages of 5-10 kV were applied via a 30 MΩ resistor and the solenoid valve was disengaged.

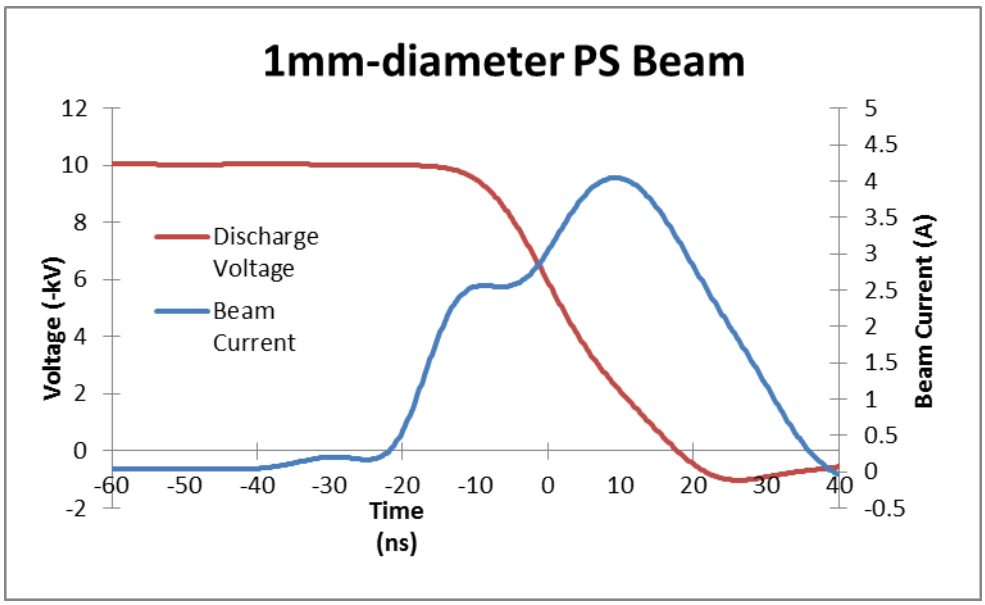

Figure 5.11: Beam voltage and current traces from a 1 mm diameter electron beam.

The pressures at which discharge occurred were similar to those witnessed in 3 mm experiments, as was to be expected. Figure 5.11 shows such a discharge at an applied voltage of 10 kV, with a peak beam current of 4 A and a pulse duration of 60 ns. This corresponds to a current density of approximately 500 Acm^{-2}, slightly larger than that observed in 3 mm beam experiments.

A 4-gap pseudospark discharge was configured in order to capture an image of a reduced-diameter beam using the existing scintillator apparatus. External capacitance, charging resistance and diagnostics were identical to those used in 3 mm experiments and the scintillator was placed within a cylindrical drift tube, attached directly to the Rogowski coil. In order to observe the beam adequately, the distance from the scintillator surface to the drift tube end was measured, allowing for the DSLR (digital single lens reflex) camera used for image capture to be correctly focussed, and the discharge chamber was sealed using a glass window before evacuation.

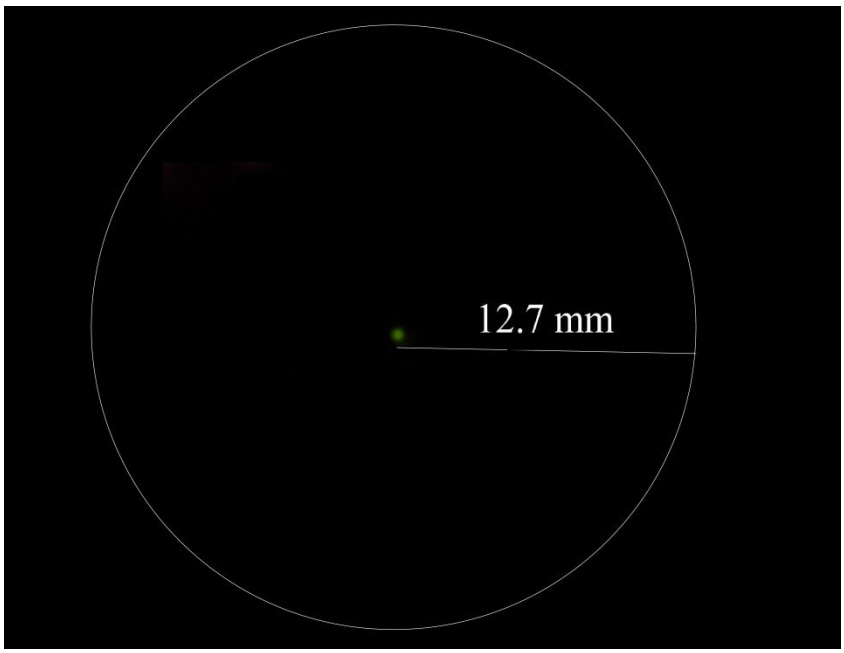

Figure 5.12: Scintillated image of a 1 mm diameter PS-generated electron beam.

Figure 5.12 shows the captured image from a 1 mm diameter PS e-beam at an applied voltage of 34 kV, with a beam current of ~8 A. The sharpness of the image shows a lack of visible beam spread and whilst the 'halo' effect witnessed in 3 mm beam images is not present, this is likely due to the decreased overall current.

A series of 8.1 mm-diameter collimating discs were machined from 0.1 mm-thick stainless steel with on-axis aperture diameters of 400 μm, 200 μm and 140 μm. They were affixed to the anode by means of a stainless steel alignment structure, as seen in figure 5.13.

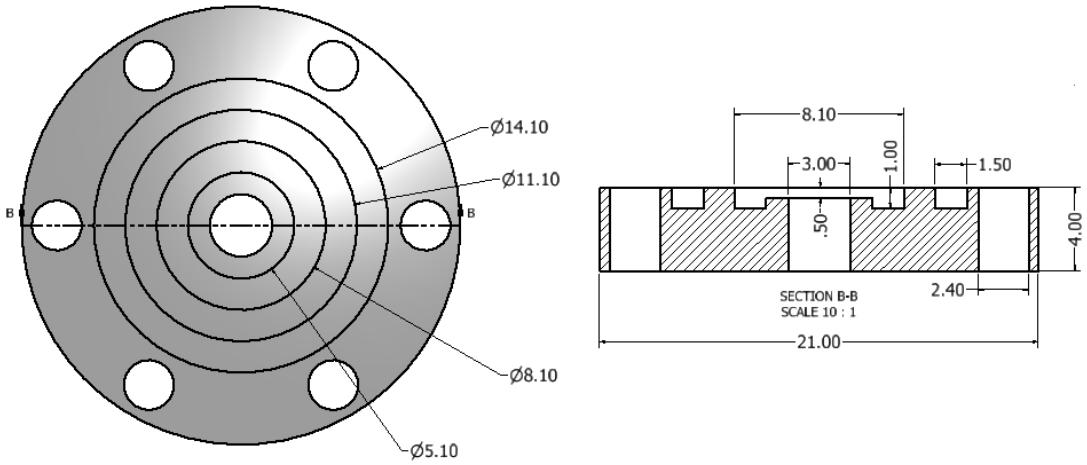

Figure 5.13: Structure for holding and centring beam scrapers.

A two-gap pseudospark was configured and evacuated to a pressure of 100 mTorr before voltages of 8-12 kV were applied. The solenoid valve was then disengaged and air leaked into the system at a controlled rate of ~0.5 mTorr/s via a fine-tuned needle valve.

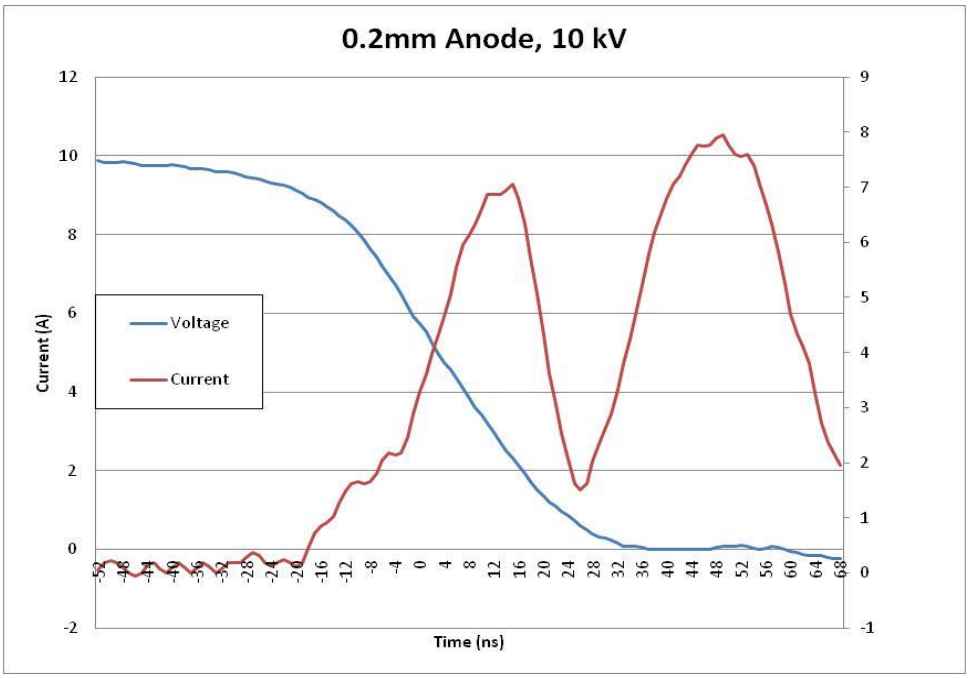

Figure 5.14: Voltage and current traces of a 10 kV, 0.2 mm radius PS e-beam.

Whilst shots were captured for most voltages with all three apertures and showed marked similarities to PS discharge current traces previously achieved, there were some anomalies with the results achieved from all three structures. Firstly, each shot exhibited a significant degree of post-discharge noise, as may be seen in figure 5.14, which was observed over numerous attempts. However, this is common with many PS current traces, even at larger beam diameters. Secondly, the current densities observed from these shots were higher than what are typically observed, with 0.2 mm radius aperture PS-generated beam at 10 kV delivering a current density of 5.6 kA/cm^2. Figure 5.15 shows how this scales with voltage using the smallest aperture size (70 μm radius). While these current densities are large, they are not outside the scope of current densities achievable in PS discharges and can be accepted as being feasible.

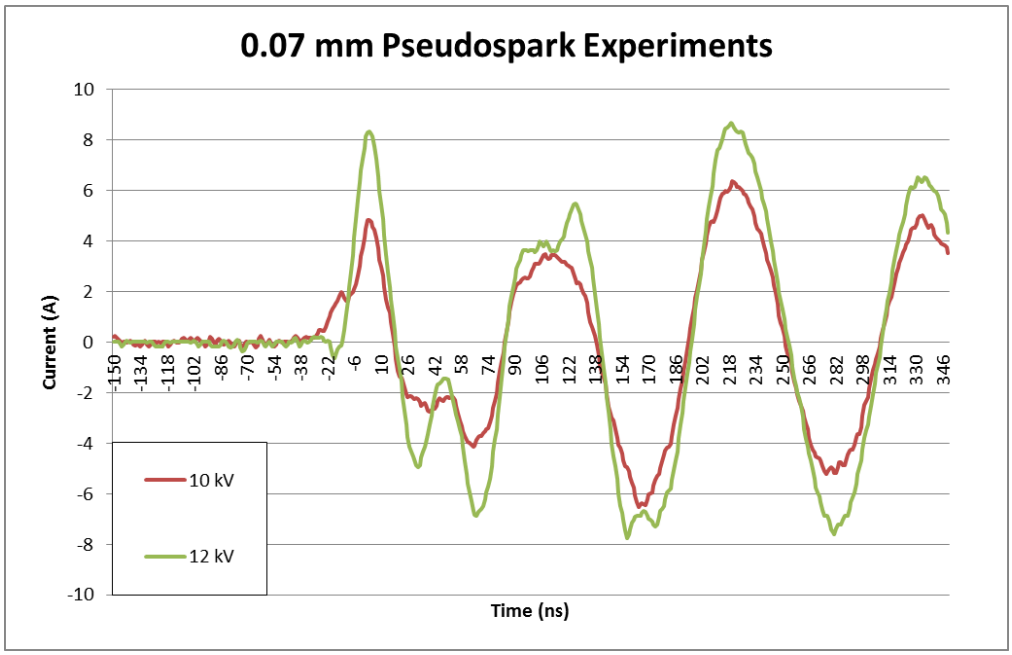

Figure 5.15: Current traces from a 70 μm diameter PS e-beam at charging voltages of 10 and 12 kV.

It was observed that scaling was approximately linear with voltage, although some shot-to-shot variations were observed, such as at an applied voltage of 8 kV. In this situation, the current could occasionally be seen to be even larger than normal and achieve higher peak currents than a 10 kV beam. However, in such situations the current trace did not exhibit the distinctive two-stage shape of a typical PS-generated

beam and was likely an abnormality, possibly a simple spark discharge generated due to the low voltage. This indicates that, for such beams, 10 kV acts as a threshold voltage for two-gap PS performance.

Table 5.1 shows the performance achieved by the PS for various voltage and aperture combinations.

Aperture Radius (μm)	**Applied Voltage (kV)**	**Discharge Pressure (Torr)**	**Hollow Cathode Current (A)**	**Superdense Glow Current (A)**
70	8	1.16	---	3.4
70	10	1.052	1.3	2.75
70	12	1.045	---	5.1
100	10	1.064	0.7	2.7
200	12	0.998	1.6	7.1

Table 5.1: Beam currents of reduced-diameter PS e-beams.

The results for the 100 μm and 200 μm diameter apertures were found to be replicable for approximately 40% of the shots attempted, with the observed currents varying little (± 0.2 A) from shot-to-shot but the smaller-diameter beam currents were more difficult to replicate. However, beam current was observed just as often as with the larger beams. Attempts were made to capture images of the smaller-diameter electron beams but it was found that the scintillator sensitivity was too low to allow for the images to be captured using the digital camera.

5.3 W-band BWO Experiments

To produce a suitably high energy electron beam pulse, a fourteen-gap pseudospark was configured, powered by a cable pulser capable of 170 kV, 120 ns duration pulses. Using as its foundation a 20 kV pre-trigger pulse applied to the pseudospark chamber, the cable pulser consisted of the addition of the output voltages from two

Blumlein circuits, created from high-voltage cables. Through the careful adjustment of two delay units and the addition of a load impedance significantly greater than the characteristic impedance (200 Ω), a voltage pulse of approximately four times the charging voltage was applied following the initiation of the pseudospark discharge, thus producing the high-energy electron beam.

The formed BWO interaction region was inserted into the PS anode. A millimetre-wave launching horn was then placed downstream of the interaction region, followed by a Perspex output window (figure 5.16). The mm-wave detector was situated 3 cm downstream of the output window at an angle of 5 degrees.

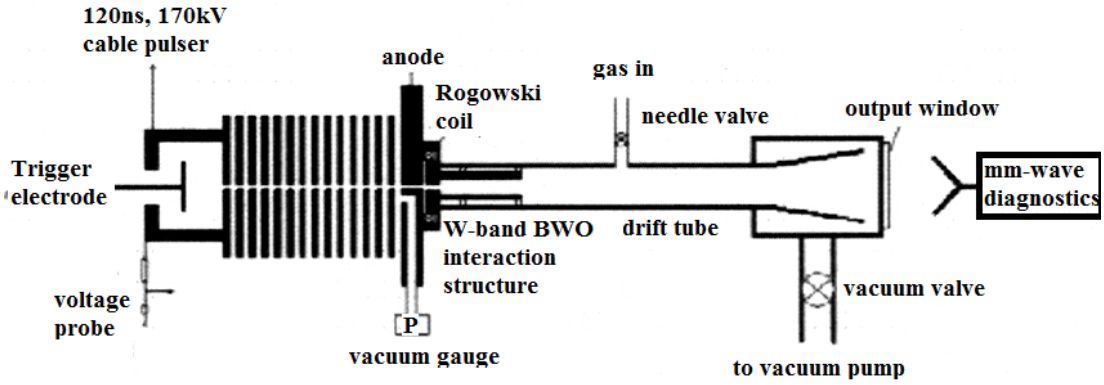

Figure 5.16: Experimental configuration of a 14-gap, pseudospark-driven, W-band BWO.

Due to the high voltages, the system was evacuated to a lower pressure than in the 4-gap experiments, namely a pressure of ~ 50 mTorr. A 20 kV charging voltage was applied and the gas allowed into the system via the fine-tuned needle valve. The Blumlein cable pulser was able to produce a 100 kV pulse of 100 ns duration to drive the PS discharge, the results of which may be seen in figure 5.17.This shows the resultant voltage pulse of ~100 ns duration the subsequently generated electron beam current, as measured by the Rogowski coil, which had a hollow cathode phase current of 25 A followed by a final peak current exceeding 100 A, as measured by the Rogowski coil. Millimetre waves were generated during the hollow cathode

phase at a voltage of 100 kV and were detected using a W-band detector system with a cut-off frequency of 59 GHz.

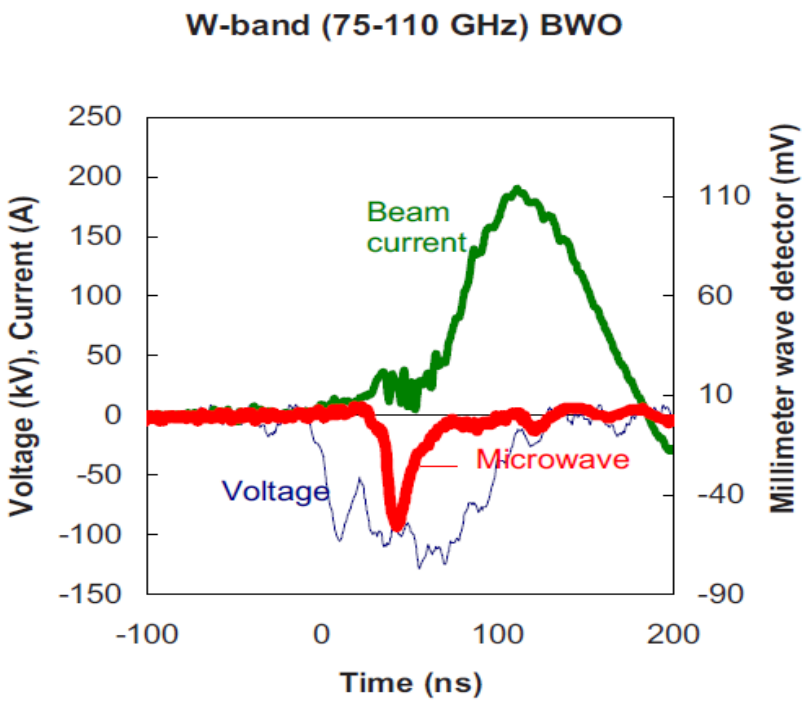

Figure 5.17: Time-correlated beam current pulse, applied voltage pulse and detected microwave pulse from BWO.

The experiments clearly showed the presence of microwave radiation from the BWO via the microwave pulse which followed the high-energy, hollow-cathode phase of the pseudospark discharge, although it was not possible to detect the exact frequency and power at the time of the experiments (first year of my PhD studies) due to the group not possessing a W-band mixer or W-band source to calibrate the detector. It was therefore not possible to compare the performance of the W-band BWO with that predicted in the simulations carried out by Dr. H. Yin. However, the successful generation was sufficient impetus for myself to design, simulate and construct a higher frequency G-band BWO experiment where the model could be successfully measured and compared with predicted values. This could provide additional support to simulations of higher-frequency devices.

5.4 W-band Klystron Experiments

5.4.1 Cold Testing

The W-band klystron input and output cavities were connected to a calibrated VectorStar VNA via a 65 - 110 GHz extension module. The cavities were stacked within the housing structure in the manner shown in Figure 3.34 and the unit was held in place by attaching the device securely to the PS anode, while the rear of the unit was held in place by a copper backplate followed by a plastic spacing ring. This configuration allowed for the coupling slots of the input and output cavities to be matched to the waveguides etched within the housing structure whilst tightening of the screws allowed the cavities to be lightly compressed, affording a degree of tuning of the cavities. The construction of multiple coupled cavities and dielectric inserts allowed for some inter-changeability in the experiment and gave a better chance of matching the input and output cavity resonances. The dielectrics could then be fixed in place using a ceramic bonding agent. However, it was not possible to determine the frequency of the penultimate cavity via direct VNA measurement techniques due to the absence of a coupling slot. Whilst the system was not placed under vacuum, the conditions of the hot experiments were replicated as best as possible, in that the input and output cavities were sealed with Mylar and the fixing screws were tightly fastened.

Through analysis of S_{11} parameters, it was observed that the tightening of these screws caused a degree of misalignment in the coupling slots caused by the pressure exerted on the copper, with the dip in the S_{11} parameter caused by the cavity resonance becoming attenuated as the tightening increased. This was likely a product of the softness of the material (copper), the sensitivity of the device to small changes in movement, or a combination of both.

By loosening the pressure of the fixing screws, clear resonances could be observed in the S_{11} parameters of both the input and output cavities of the W-band klystron. Due to the sensitivity of the klystron to stress and movement, however, it was found to be very difficult to match the frequencies of the input and output cavities.

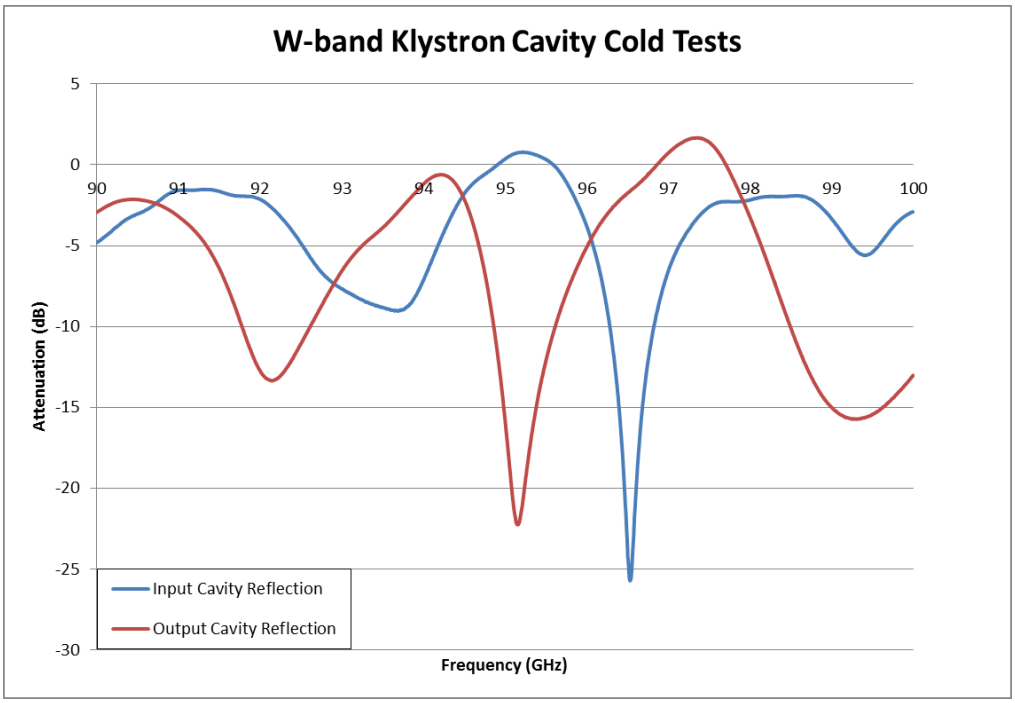

Figure 5.18: Input and output cavity resonances of W-band klystron.

Figure 5.18 shows the closest simultaneous match which was achieved using any combination of cavity and dielectric, where the input cavity showed a frequency of 96.5 GHz and the output demonstrated resonance at 95.1 GHz. It was possible to obtain cavity resonances nearer the predicted frequency of 94.5 GHz but this would often be lost in any attempt to fine-tune the remaining coupled cavity. Resonance was found to be extremely susceptible to movement of the housing, meaning that any frequency matches would likely be lost when configuring beam experiments, reducing frequency matching to chance. Frequency typically varied by several GHz for each cavity/dielectric combination while placement of the dielectric could alter the frequency further. As such, it was concluded that the construction of the klystron could not be accomplished by piecing the structure together in segments, and will likely necessitate forming the structure as a single unit. In doing so, the contact

resistance which arises between the segments could also be eliminated. The precise method of achieving this is a matter for further consideration, perhaps using recent advances in 3D printing of metal structures.

5.4.2 Klystron Beam Experiments

The assembled W-band klystron was connected to a two-gap pseudospark as seen in figure 5.19. The coupling ports were sealed with nitrile O-rings and Mylar discs before a W-band frequency generator was connected to the input port via a 6 cm length of W-band waveguide. The power source was housed within a grounded, air-cooled shielded metal box. A W-band horn was affixed to the klystron output port and directed toward a feed horn and mm-wave detector with a cut-off frequency of 59 GHz housed within a shielded box and connected to the oscilloscope via a copper braiding-shielded line. The Rogowski coil was affixed to the klystron housing and the structure sealed with a Mylar window.

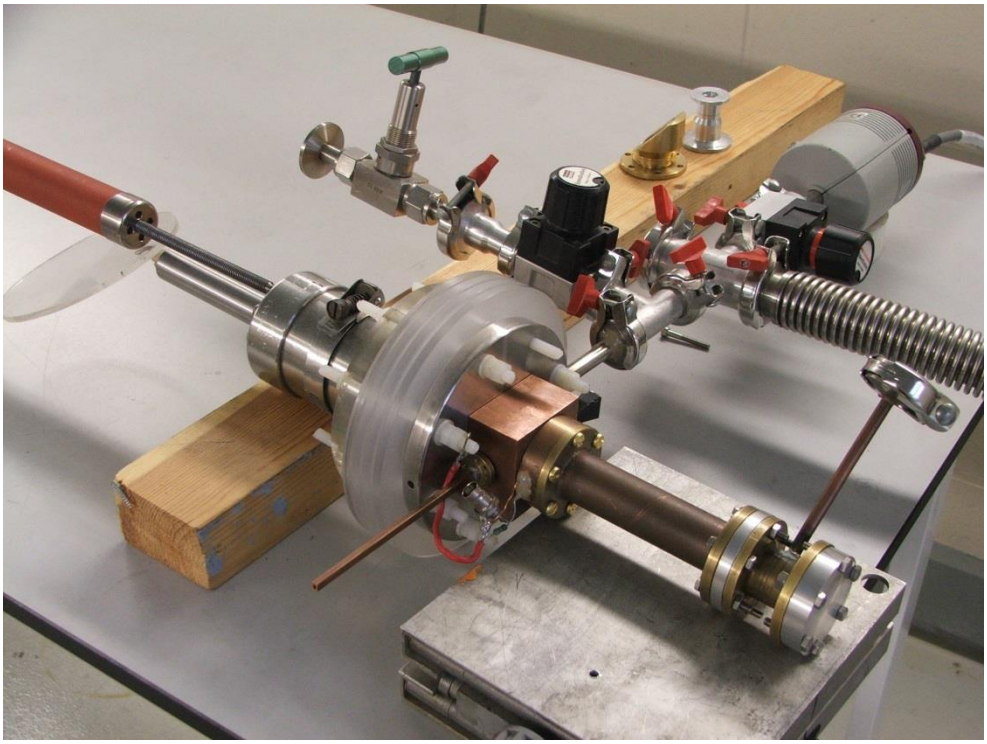

Figure 5.19: Configuration of PS-klystron apparatus, before inclusion of W-band source and diagnostics.

The input waveguide was connected to an air-cooled W-band oscillator house within a fan-cooled shielded metal box inputting ~25 mW of power and the system evacuated to 300 mTorr before applying a voltage of 12 kV and disengaging the electrically-operated solenoid valve and leaking working gas into the system. Discharge occurred at a pressure of ~800 mTorr but no microwave pulse or beam current at the output side of the klystron were detected using the beam and millimetre wave diagnostics feed into the oscilloscope. This observation was repeated as the frequency of the input signal was varied from 93 GHz to 96 GHz in 0.1 GHz increments, while the detector horn position was varied between 1 and 10 cm, with the same results achieved. Discharges at a 9 kV charging voltage likewise did not achieve millimetre wave generation or beam detection at the Rogowski coil, with any observed signals being attributable to noise. These results were an indication that while the simulated design of the klystron may have been reasonable, the difficulty in manufacturing such a minute structure makes physical realisation extremely difficult. As such, a redesign of the klystron should be considered as future work.

From the above observations, the failure of the W-band klystron can likely be traced back to three faults, or a combination thereof. The first is the difficulty in matching the frequencies of the three interaction cavities, largely due to the effect of minor changes in cavity geometry relating to manufacturing tolerances and dielectric placement. One possible solution to this issue would be the use of higher-order mode cavities with larger, less restrictive dimensions, or to implement a more refined method of cavity tuning.

The second issue was the misalignment of the coupling slots in the klystron with the input and output waveguides, particularly when physical stresses were involved. As copper is generally an excellent choice for devices such as klystron and BWOs, a method of integrating the coupling and housing structures in a single unit should be considered a possible avenue of research.

Finally, the alignment of the drift tube and its effect on beam propagation was obviously detrimental to klystron performance. The fault of this likely lay in the use of numerous ‘tiles’ to form the interaction region, with the possibility of drift tube misalignment growing with each successive tile, an issue which becomes even more serious as the drift tube radius is decreased. Composing the interaction region as a single structure, likely through the growth of copper on an aluminium mandrel (as with the BWOs) or 3D printing the structure in metal direct, is the ideal solution for this, although the machining of such a complex former with the required resolution is a subject of future work. This once again leads back to a redesign of the klystron as a whole as the likely candidate for achieving a working PS-klystron at these frequencies.

5.5 G-band BWO Experiments

A 4-gap PS discharge was configured as in figure 5.20 and sealed using a Mylar window. The mm-wave diagnostic, a G-band zero-biased detector, was housed within a shielded box in order to eliminate signal contamination from external microwave sources. A small aperture was cut in the box wall to allow for the ingress of the millimetre wave signal while the coaxial cable connection from the detector to the screened oscilloscope room was encased in copper braiding.

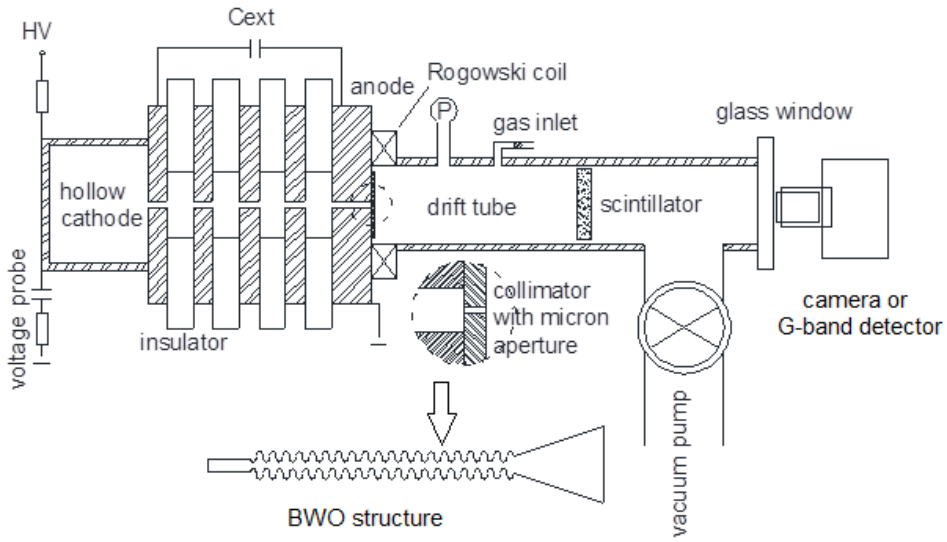

Figure 5.20: Schematic of G-band BWO experiments.

In order to maximise the received signal strength, the detector aperture was aligned off-centre by an angle of 5°, at a distance of 6.5 cm from the horn aperture. The angle was determined by the maxima predicted in CST Microwave Studio far-field calculations while the distance was calculated from the Fraunhofer distance, defined as

$$d_f = \frac{2D^2}{\lambda} \tag{5.1}$$

where D is the diameter of the horn aperture. This distance marks the delineation between the near- and far-field regimes.

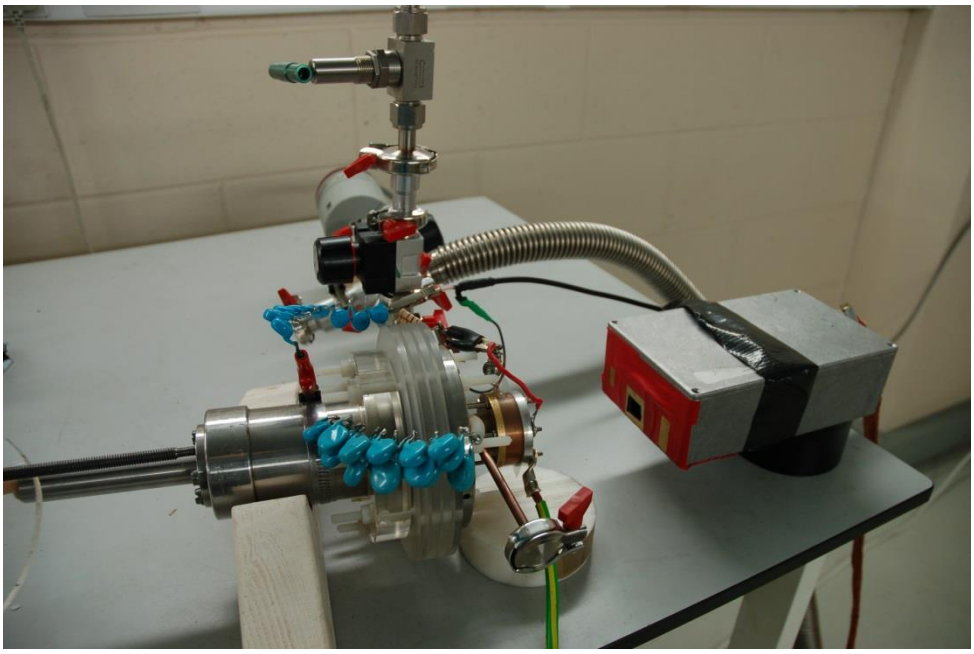

Figure 5.21: PS-BWO experimental environment.

Due to the lack of a cut-off region in the structure of the BWO, it was necessary to introduce a tungsten mesh capable of reflecting the microwave signal back towards the slow-wave structure and the output horn. Hence, a 95% transparency tungsten mesh was attached to the cathode-facing wall of the PS anode, flush with the entrance to the BWO and completely covering the central aperture. In order to ascertain the effects this may have on the electron beam's power, pseudospark

discharges were performed, both with and without the presence of the mesh structure.

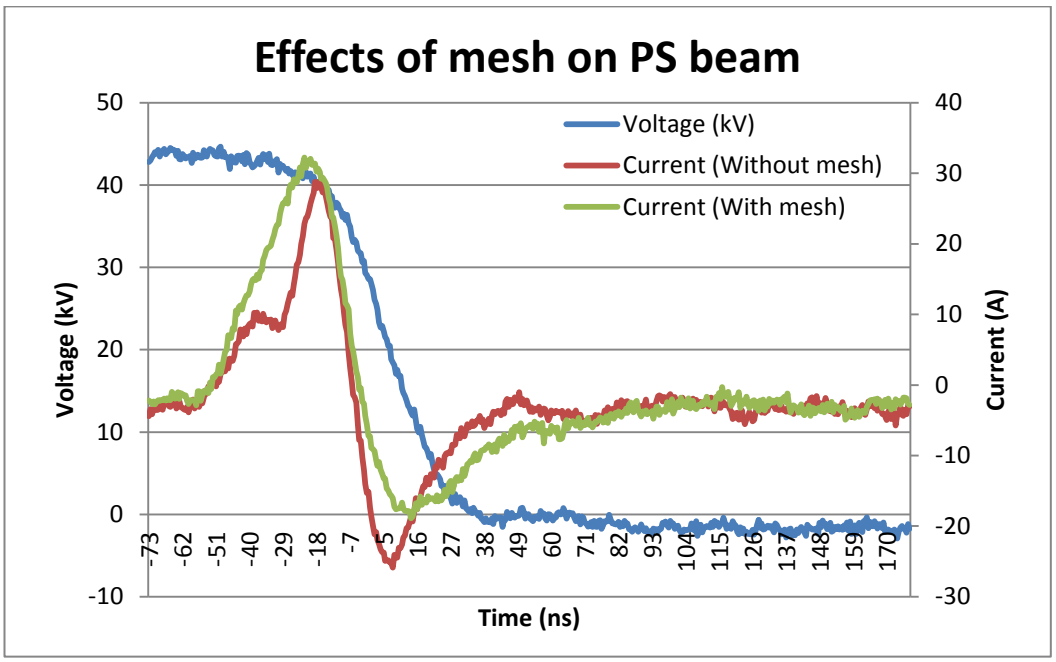

Figure 5.22: PS beam current measurements at 42 kV, with and without the presence of tungsten mesh.

Figure 5.22 shows the beam current measurements of a 3 mm diameter, 42 kV PS beam, both before and after the introduction of the tungsten mesh. Beam current was measured by a Rogowski coil situated 10 cm downstream of the anode. The presence of the mesh introduces a degree of smoothing of the current rise portion of the signal, most notably during the hollow cathode phase of the discharge, but there is little to no effect on either the pulse duration or the amplitude of the electron beam current. Repeated shots showed little variation in the performance of the PS discharge, with a discharge pressure of 700 mTorr being common to both configurations. The BWO was then inserted into the anode aperture.

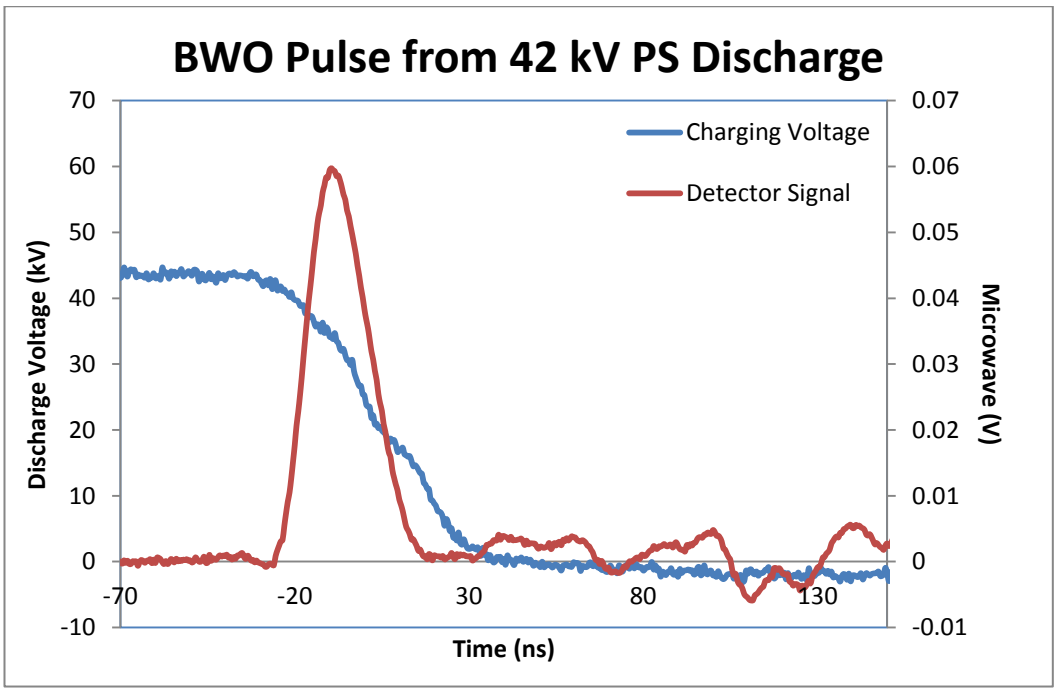

Figure 5.23: Measured microwave detector signal from a G-band BWO.

A charging voltage of 42 kV was applied to the sealed hollow cathode and pressure was evacuated to ~100 mTorr. Following disengagement of the solenoid valve, the working gas was leaked into the system at a slow, controlled rate until discharge occurred. A microwave pulse was captured via a triggered oscilloscope, with repeated shots yielding further measurements. It was found that the amplitude of these shots typically stayed within an order of magnitude in scale, but were only generated in approximately 60% of shots. The shot-to-shot variation rendered any attempts to replicate the far-field predictions of CST Microwave Studio impossible without the presence of a second, reference detector.

Measurements were performed with both the original, formed horn and the detachable conical horn. The conical horn transmitted the high-frequency signal with a sharper TM_{01} far-field pattern, as predicted in CST Microwave Studio simulations. The recorded signals from the detector were also noticeably larger, again in keeping with the higher predicted gain of the horn. This trend continued from shot to shot,

with the largest recorded microwave power from the detector recorded at an angle of 5 degrees.

5.5.1 Microwave Pulse Power

Using the calibration information provided by the device manufacturer, a maximum detected signal of 1 mW was observed. As was outlined in chapter 4, it is possible to ascertain the total output power of a device through the integration of the normalised far-field mode pattern of a horn combined with its dimensions and the observed signal. Due to the narrowness of the simulated pattern as well as technical limitations, a mode sweep, where the detector signal is measured at various angles from the normal, was deemed impractical and so only the normalisation of the simulated pattern was used. This was deemed acceptable due to the high manufacturing tolerances used in the construction of the horn.

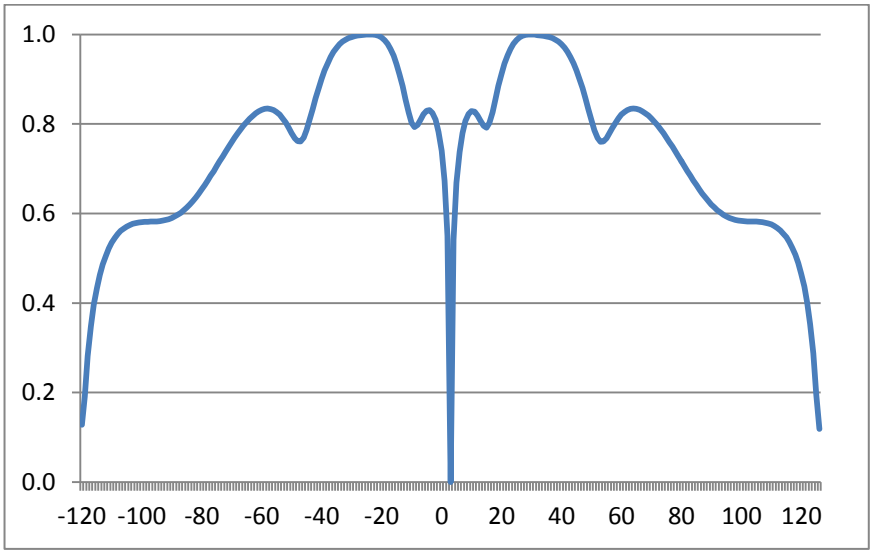

Figure 5.24: Normalised TM_{01} mode pattern of conical launching horn.

The TM_{01} profile was normalised and integrated from 0° to 60°, and the result combined with equation 4.21 to yield a value of 0.32. The measure maximum power density was obtained from the maximum power divided by the effective receiving horn area. The effective area of the launching horn, with gain of 17 dB and a wavelength of 1.5 mm at 200 GHz, was calculated as

$$A_{eff}(\theta,\phi) = \frac{G(\theta,\phi)\lambda^2}{4\pi} = 3.04 \text{ mm}^2$$

The maximum measured power was 1 mW at a distance of 65 mm and angle of 5 degrees, giving a maximum power density of 0.32 mW/mm^2. Therefore, the maximum power from the BWO was calculated to be 2.7 W. This shows a good degree of agreement with simulated results.

5.5.2 Frequency Determination

A four-gap PS was configured with the G-band BWO inserted in the anode's on-axis aperture and sealed with a Mylar window while a receiving horn was connected to a 2nd-harmonic frequency mixer using a W-band local oscillator (LO) source, configured to output at 95 GHz, which the mixer doubled, generating an effective LO signal of 190 GHz. The mixer, horn and oscillator were placed in a screened stainless-steel box and the intermediate frequency (IF) output line connected via a 20 GHz-bandwidth microwave cable to a high-speed oscilloscope, triggered via a second oscilloscope acting on the current rise detected by the Rogowski coil. The position of the horn was at a similar distance and angle from the launching horn as in earlier G-band BWO experiments.

Figure 5.25: Experimental setup of BWO frequency determination experiments.

The system was evacuated to a pressure of 100 mTorr and a steady voltage of -42 kV applied to the cathode. Following the opening of the solenoid valve, working gas entered the system at a controlled rate and discharge occurred at a pressure of ~400 mTorr. The output IF signal was scanned for signs of a microwave pulse and the frequency component analysed by means of a Fast Fourier Transform (FFT), displaying the frequency difference between the generated BWO microwave pulse and the LO frequency. This was repeated for several successive shots, the output shown in figure 5.26

Figure 5.26: Oscilloscope reading of IF signal derived from a BWO pulse, showing pulse amplitude, green, and FFT of signal, purple.

As the discharge voltage occurred at a time of rapidly falling voltage the resultant effect was to induce frequency sweep in the output. As such, the most effective method to determine the dominant frequency was to analyse over the length of the pulse, with the dominant peak being the one remaining largely unaffected. Over several discrete measurements, IF frequencies were measured, and the BWO was determined to possess an output frequency spectrum spanning from 188 to 202 GHz.

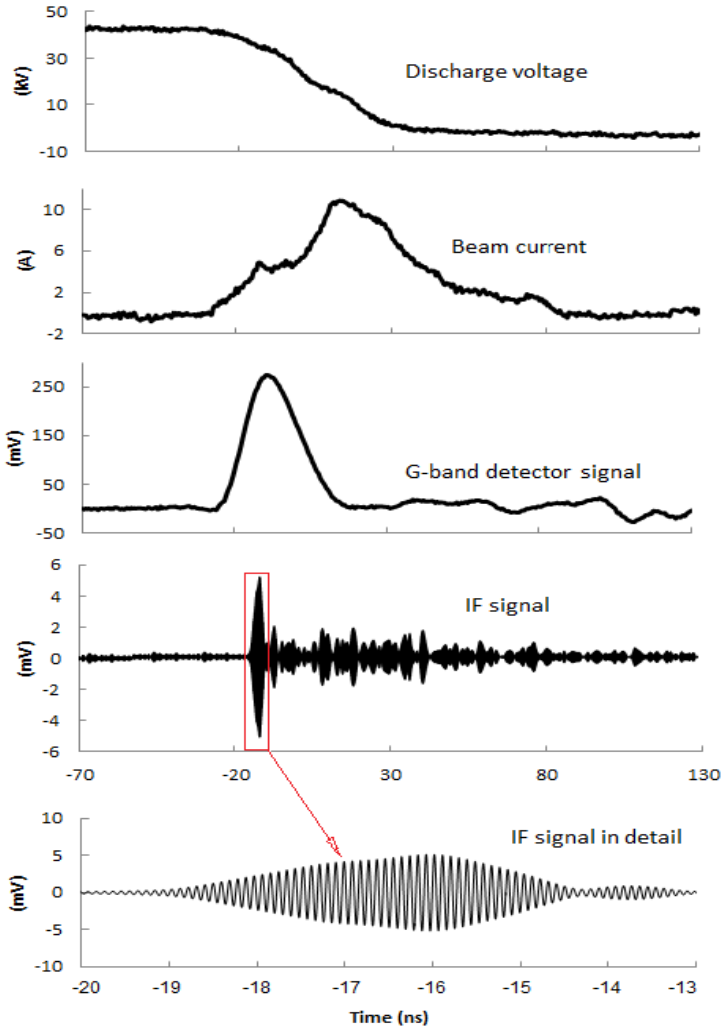

Figure 5.27: Time-correlated analysis of frequency-mixed BWO pulse.

Figure 5.27 shows a time-correlated analysis of a pulse, with the rising edge of the detected signal coinciding with the 5 ns-duration IF pulse, the hollow-cathode phase of the PS current trace and the falling discharge voltage. The voltage can be seen to be at approximately 35-40 kV, as in keeping with MAGIC simulations and the numerical dispersion calculations.

However, frequency performance of the BWO is largely dependent on beam voltage. As such, the measured frequency was that which coincided with the flat, high-energy

hollow-cathode phase of the pseudospark discharge, the remainder of the signal consisting of a swept frequency. While the addition of external capacitance to the discharge circuit may allow for the hollow-cathode phase to be extended, this issue will need to be addressed for the PS-BWO to function as an effective mm-wave radiation source.

5.6 Summary

A 3 mm diameter electron beam from a 4-gap pseudospark discharge chamber was measured at 43 kV using a Rogowski coil, yielding a superdense glow current of 200 A. Single and multiple-shot images from a PS electron beam were observed using a 0.1 mm thick copper foil coated with a layer of phosphorescent powder situated downstream of the anode and a long-exposure digital camera. These images showed good focusing of the electron beam as well as the presence of a surrounding ion channel. A time-dependent beam brightness of up to $10^{11\text{-}12}$ A $m^{-2}rad^{-2}$ was measured using a magnetic-field-free collimator.

Electron beams from pseudospark discharges have been shown to be a novel source for both coherent, low energy X-rays and millimetre-wave radiation. To ascertain the electron beam's effectiveness as an X-ray source, the beam was directed at a 0.1 mm thick molybdenum target, which also acted as a witness plate. The scattered X-rays were able to produce an image of two crossed sections of 0.1 mm thick copper wire, which were placed in front of an X-ray detector. The X-rays photons emitted were analysed and observed to have an average energy of 15.83 keV. Using higher energy beams, it is believed that this may have valid potential as a general-purpose X-ray source for the scanning of biological and non-biological materials.

A W-band klystron was cold tested using a vector network analyser. Although various cavity combinations were measured, it was found to be impossible to match the input and output cavity resonances. This was compounded by a coupling slot misalignment which presented itself when the klystron housing structure was

securely affixed to the anode. The klystron was later tested using a two-gap pseudospark discharge at voltages of 12 kV and 9 kV, using a mm-wave oscillator as a microwave seed source. The input frequency was swept from 93 GHz to 96 GHz but no beam trace or microwave signal was detectable from the system. A redesign of the klystron is currently underway in order to remedy some of the issues which led to the device's failure under laboratory conditions.

A backward wave oscillator consisting of a corrugated copper waveguide section was able to generate W-band radiation when a 100 kV, 25 A, 3mm diameter electron beam pulse was applied to the structure. From this result, proof that a PS-derived electron beam could be used to generate microwave radiation from a BWO was gained and the principle was applied to devices operating at higher frequencies.

This same principle was tested and validated in the G-band frequency range. A copper BWO was driven by a 42 kV PS discharge, using a 95% electron beam transparency tungsten mesh combined with a cut-off waveguide to reflect the millimetre wave generated signal towards the output horn. Discharge occurred at ~ 400 mTorr and a millimetre wave signal corresponding to 1 mW of power detected by a zero-biased detector. Through the calculation of the effective area of the horn and integrating the normalised TM_{01} profile of the horn, a total output power of 2.7 W was calculated, matching that predicted by MAGIC simulations. Using a 2^{nd}-harmonic frequency mixer connected to a 95 GHz LO source, the frequency spectrum of the output signal was measured to be in the range from 188 to 202 GHz, again showing good agreement with simulations and calculations.

Chapter 6:

Conclusions & Future Work

6.1 Overview

The pseudospark discharge is a low-pressure plasma phenomenon occurring within a modified hollow cathode cavity and is notable for its sharp, distinctive two-stage current rise, the first stage corresponding to a hollow cathode discharge and the latter to a superdense glow discharge resulting from enhanced field strengths between the cathode and anode inducing field emission and contributing energy to the plasma. It has found widespread use in the field of high-speed switching applications but it is also finding increased usage as an electron beam source due to the high-quality particle beam emitted from the anode aperture during the later stages of the discharge. Such a beam possesses high brightness and current density, a variable pulse duration, which may be extended through the introduction of external capacitance in parallel with the discharge circuit, and requires no guiding magnetic field due to the presence of an ion channel surrounding the beam as it exits the anode, focussing it in the axial direction. While these features are attractive, it is its ability to scale these beams down to sub-mm cross-sectional diameters that make it useful in the generation of millimetre and sub-millimetre waves.

One such frequency source, a backward wave oscillator (BWO), generates radiation via the interaction of the electron beam's space-charge wave and the backward wave of a periodic slow-wave structure, in the case of this work a sinusoidally-rippled waveguide wall. The generated microwave signal travels backwards along the tube where it may be coupled out using a coupler or reflected and extracted in the forward direction via a horn antenna. A BWO was designed, modelled and tested with a pseudospark-generated electron beam at a frequency of 200 GHz. In order to test the viability of this, a larger BWO based on a pseudospark discharge operating at 67 GHz was also designed, modelled and tested.

Additionally, a klystron operating at 94 GHz was designed, modelled and tested, with further testing to occur in the future. Klystrons are amplifiers which use a low-power microwave signal matched to the frequency of a resonant cavity to modulate a

passing electron beam, with electrons being accelerated or retarded depending on the phase of the signal at the time of traversal. This induces electron bunching and, consequently, increased current density at the selected frequency, which may then be extracted via a suitable coupling structure. A novel coupling method using a dielectric region to couple to undersized cavities was also devised.

6.2 Summary of Results

6.2.1 Pseudospark Beam Experiments

The pseudospark discharge relies on plasma formation within a unique hollow cathode / planar anode geometry, with on-axis apertures at the cathode and anode walls. Utilising a modular, stainless steel PS cathode designed by Dr Huabi Yin, with cathode inner and outer radii of 50 mm and 63 mm respectively, experiments were conducted on the effects of electron beam collimation in order to assess the suitability of PS e-beams for millimetre-wave generation. A movable inner conductor allowed the cathode depth to be adjusted, with previous experiments performed at the University of Strathclyde concluding that the depth should be equal to the inner diameter. The anode was constructed from 12 mm-thick stainless steel fitted with an NW-10 flange to allow for vacuum evacuation of the discharge chamber. A 3 mm diameter aperture ran through both cathode and anode, the gap between the cathode and anode faces separated by a Perspex insulating disc, with the possibility of extending the gap separation via the addition of further insulating discs interspersed with stainless steel intermediate electrodes. The discharge was triggered by applying a charging voltage directly to the cathode body via a 3 MΩ charging resistor, while the pulse was extended through the addition of a 428 pF external capacitance.

Measurement of the PS-generated electron beam was achieved through a number of diagnostic methods. These included a ferrite-core Rogowski coil for the instantaneous measurement of beam current and a self-integrating voltage divider circuit for the monitoring of discharge voltage. The beam cross-sectional area was

monitored by means of a molybdenum witness plate and via a phosphorous-coated scintillator in conjunction with a long-exposure digital camera.

Using a stainless steel disc of 0.5 mm thickness and 0.5 mm radius central aperture affixed to the anode, PS-generated electron beams were successfully reduced in cross-sectional diameter for use in the generation of 200 GHz radiation in a backward wave oscillator. Using a 2-gap PS configuration at a charging voltage of 10 kV, a 4 A electron beam current was detected via a Rogowski coil. An image of the cross-sectional beam profile was captured using a scintillator disc using a 3-gap PS discharge at 34 kV, with a beam current of approximately 14 A measured. Attempts were also made to reduce the electron beam to diameters of as low as 140 μm using similar collimating structures. While current measurements showed electron propagation downstream of the anode, current values were not cross-correlated with scintillator witness plate diagnostic measurements, indicating that the scintillator measurement system was not sensitive enough to accurately measure the cross sectional profile of the pseudospark electron beam.

The beam's capacity as a generator of X-rays was examined using a 46 kV, 3 mm-diameter electron beam directed towards a 0.1 mm thick molybdenum target. An X-ray photodetector was placed 52 mm downstream of the anode and target, while two 0.1 mm diameter copper wires were crossed and attached to the photodetector for use as an imaging target. Following numerous successive PS discharge pulses, an image of the target was detected via the X-ray photodetector, with X-ray photons possessing an average energy of 17.8 keV. These energy levels lie within the expected parameters of molybdenum-based X-ray generators and performance shows the potential of the PS discharge as a small-spot X-ray imaging source.

6.2.2 W-band Frequency Generation

A backward wave oscillator for operation at a frequency of 67 GHz was designed and tested. Using a sinusoidally-rippled slow wave structure of mean radius,

amplitude and period of 2.75 mm, 1.375 mm and 1.75 mm respectively, the BWO was manufactured by means of the electrodeposition of copper on an aluminium mandrel machined via the use of high-speed grinding techniques before the chemical dissolution of the aluminium base. The structure was machined to allow insertion into the PS anode and was tested using a 100 kV, 25 A PS electron beam generated using a cable pulser to apply the enhanced charging voltage to a 14-gap PS configuration. Using a W-band detector with a cut-off frequency of 59 GHz, a millimetre wave pulse was successfully measured. At the time, a lack of a calibrated W-band detectors and W-band mm-wave diagnostic apparatus meant that obtaining an exact frequency and power measurement for the pulse was not possible, but the successful generation of the mm-wave pulse provided the necessary justification for the research contained within this thesis, namely the design, manufacture and testing of the W-band klystron and G-band BWO.

A 3-cavity klystron with an operating frequency of 94 GHz was likewise designed and simulated in MAGIC. Using three irregularly-spaced pillbox cavities and a microwave signal power of 4.7 mW, a pulsed electron beam driven by an accelerating voltage of 8 kV and current of 15 mA predicted a peak output power of 8.4 W, with a gain and efficiency of 20 dB and 7% respectively. A novel method of coupling to and from these cavities was devised, using a tapered waveguide to couple to the cavity via a dielectric insert, thus compensating for cut-off effects. A prototype coupling system was simulated in CST Microwave Studio and subsequently constructed and tested with two dielectric materials: alumina and BNP2, a machinable form of aluminium nitride. In simulations, alumina was shown to perform better at lower frequencies (19 dB, as opposed to 27 dB) while both materials demonstrated similar losses at the upper end of the frequency band (~4 dB). In experiments, alumina was shown to exhibit lower losses both at the lower and upper ends of the frequency band. Due to these lower losses, the decision was made to use alumina as the dielectric for the W-band coupler.

Due to large losses within the X-band coupling system, the design was revised for W-band experiments. An asymmetrical design, with one wall retaining a constant profile while the other tapered inwards, was found to reduce transmission losses by several dB, while reflection was similarly reduced. The klystron interaction region was machined from ten copper slates, stacked together to form major features, and placed within a copper housing structure which was vacuum sealed using Mylar windows and connected directly to the PS anode. During cold testing of the microwave cavities, it was difficult to match the input and output frequencies and tightening of the structure caused a degree of misalignment between coupling slots and cavities. The system was nonetheless tested using an electron beam generated from a two-gap PS discharge with applied voltages ranging from 6-14 kV. While the frequency of the input signal was varied between 93 GHz and 96 GHz, no millimetre wave signal or beam trace observed. As such, work on this device is still ongoing.

6.2.3 G-band Frequency Generation

A BWO with a 30-period, sinusoidally-rippled SWS of mean radius, amplitude and periodic length of 0.5 mm, 0.1 mm and 0.467 mm respectively was simulated in MAGIC-3D. Driven by a pulsed, 35 kV electron beam carrying a current of 1.5 A, the device showed an expected output of ~ 2W at 200 GHz. This frequency was verified by numerical calculation of the SWS dispersion relation. In order to retrieve the amplified signal, a cylindrical horn antenna of outer radius 3.5 mm and length 18 mm was modelled in CST Microwave Studio, with a predicted TM_{01} gain of 17 dB. As with the W-band device, the device structure was manufactured through the electrodeposition of copper on an aluminium mandrel machined via high-speed milling, with the aluminium dissolved in an alkaline solution after machining of the BWO outer diameter for insertion into the PS anode. The launching antenna was machined separately by means of wire-spark erosion. The machined former's dimensions were out by ~100 μms, so the dispersion relations were adjusted to take account of this, as well as the presence of the ion channel within the SWS. These two factors combined effectively cancelled each other out, again showing interaction at ~200 GHz for a 35 kV electron beam.

The assembled BWO was attached to a 4-gap PS discharge chamber, with a tungsten mesh adjacent to the inner surface of the anode allowing for reflection of the microwave signal towards the launching antenna. Discharge occurred at a charging voltage of 42 kV and a pressure of 600 mTorr; a microwave signal of 1 mW was detected from a G-band detector situated 55 mm downstream of the horn, at an angle of 5º from the normal. Integrating over the normalised profile of the launching horn, the device output was calculated as 2.7 W, confirming the MAGIC simulations. A 2nd-harmonic frequency mixer using a W-band local oscillator source showed the BWO to have an output frequency range of 188 - 202 GHz.

Due to the sweeping nature of the voltage pattern for PS discharges, the pulses obtained from the PS-BWO do have a peak frequency but generally range over a spectrum of frequencies, with the results varying slightly from shot-to-shot. In addition, it was found that achieving repeatability in these experiments can be difficult, both in terms of the microwave pulse and in the stability of the discharge. As part of this may lie with the observed variation in shot performance due to deterioration of the gas within the system, with multiple shots often leading to degradation of shot stability, it is possible that a better method of monitoring gas uniformity within the discharge system and of refreshing the working gas itself may resolve this issue.

6.3 Future Work

6.3.1 Pseudospark Beam

While the pseudospark beam has been thoroughly investigated, little work has been done on the properties of the pseudospark discharge itself. One avenue which may be considered is the determination of the plasma parameters, in particular the plasma density and temperature, through the use of plasma spectroscopy, a form of emission spectroscopy. This involves observing the light emitted by the plasma when discharge occurs with a known gas, with the light intensity varying with the electron density at the point of emission. By capturing a sample of the spectra using a fast-

shutter feed triggered to coincide with the discharge and through the subsequent analysis of the emission spectra, it is possible to obtain a profile of the generated plasma.

One feature of the pseudospark beam which has not been directly measured is that of the beam energy. It may be inferred from the measurements already available but this could be confirmed through the use of an energy analyser. While many techniques exist for the measurement of electron beam energy, including the use of magnetic spectrometers, the determination of energy from electron velocities and the measurement of electron penetration into various materials, it is unknown which method would be the most suitable. An estimate of electron energy may be given by the measurement of radiation-stimulated dendroid cracks in acrylics under bombardment by electrons, which would be a simple, though not highly accurate, method, though all techniques may be considered [103].

The use of the PS beam as a generator of X-rays is an interesting application, though one with potential for further improvement. One improvement could be to reduce the beam's cross-sectional diameter and thus to reduce the X-ray spot size. This would allow for the scanning of smaller areas, a highly desirable trait as it effectively reduces the surface area being irradiated at any one time. Another possibility is to allow for the scanning of an object from several angles simultaneously, which could be achieved by splitting the electron beam into numerous, non-parallel beamlets and refracting these using a target material surrounding the object. In such a way, it may be possible to image an object from several separate viewpoints.

Finally, one criticism of the PS discharge is that the stability of the system is often upset with repeated shots. An improved method of monitoring gas equilibrium within the system could help remedy this, although an increased knowledge of the PS

discharge via the investigations previously suggested could likewise improve discharge stability.

6.3.2 High-frequency Generation

Both types of device examined in the course of this work have the potential for further improvement. Progress showed that whilst the theory of the klystron was beyond reproach, the physical construction of a multiple-cavity klystron using fundamental harmonics at high frequencies is a difficult process which pushes manufacturing tolerances to their limits. One method of overcoming this would be to use micro-electromechanical systems (MEMS) techniques to create the interaction region. This allows for the creation of minute structures at high aspect ratios, and with excellent tolerances, though it is generally a costly route and would not circumvent the problems faced in regards material tolerances and stresses. Rather, an improved method of aligning the cavity structures and securing to the PS anode would be preferable.

Reflex and extended interaction klystrons (EIKs) may also be considered, due to the fact that EIKs may use distributed coupling systems, eliminating the need for the dielectric based method and thus granting more freedom in design and reflex klystrons use only a single cavity which, again, offers greater freedom in design and construction, particularly in regards alignment. The multiple-cavity klystron may still be viable by using larger cavities resonating at higher-order modes. By allowing for larger dimensions, coupling and manufacture are simplified and the quality of the finished device (surface polish, etc.) will be improved.

In regards the G-band BWO, it would be beneficial to perform further simulations on the structure to confirm the findings of both MAGIC and experimentally-observed results. Whilst CST Studio suite was only used in the design and measurement of the output horn gain and for the determination of the single-period SWS dispersion, using CST Particle Studio it would be possible to gain a complete impression of the

workings of the device, including the effect of horn reflections and their contribution to the bunching effects within the SWS, an aspect which cannot be confirmed in the current decoupled horn-BWO simulations. Having such a model in place would allow for optimisation of the structure, including alternative cut-off designs for reflection of the generated signal within the device, and to design improved horn structures which may help eliminate additional modes in the TM_{01} output mode pattern. The most likely alternative to the conical horn would be the corrugated horn to produce a Gaussian beam, which generates smaller side-lobes, though machining of such a structure could be difficult and will require further investigation.

It would be most useful to obtain more information on the microwave signal generated by the W-band BWO, particularly the pulse power and frequency. The techniques for obtaining this have been established in this work and the information obtained would provide a useful point of comparison with the results obtained from the G-band device.

References

[1] C.-L. Ko, C.-H. Li, C.-N. Kuo, M.-C. Kuo and D.-C. Chang, "A 210 GHz amplifier in 40-nm digital CMOS technology," *IEEE Trans. Microw. Theory. Techn.,* vol. 6, no. 16, pp. 2438-2446, 2013.

[2] H. Eisele, "State of the art and future of electronic sources at terahertz frequencies," *Electron. Lett. - Special Supplement: Terahertz Technology,* pp. S8-S11, 2010.

[3] W. Fu, Y. Yan, X. Li and S. Liu, "The experiment of a 220 GHz gyrotron with a pulse magnet," *J. Infrared Milli. Terahz. Waves,,* vol. 31, no. 4, pp. 404-410, 2010.

[4] T. Saito, N. Yamada, S. Ikeuti, S. Ogasawara, Y. Tatematsu, R. Ikeda, I. Ogawa, T. Idehara, V. N. Manuilov, T. Shimozuma, S. Kubo, M. Nishiura, K. Tanaka and K. Kawahata, "Generation of high-power sub-terahertz radiation from a gyrotron with second harmonic oscillation," *Phys. Plasmas,* vol. 19, no. 6, pp. 063106-1-063106-9, 2012.

[5] M. H. Beringer, S. Kern and M. Thumm, "Mode selection and coaxial cavity design for a 4-MW 170-GHz gyrotron, including thermal aspects," *IEEE Trans. Plasma Sci.,* vol. 41, no. 4, pp. 853-861, 2013.

[6] T. Rzesnicki, B. Piosczyk, S. Kern, S. Illy, J. Jin, A. Samartsev, A. Schlaich and M. Thumm, "2.2-MW record power of the 170-GHz European preprototype coacial-cavity gyrotron for ITER," *IEEE Trans. PLasma Sci.,* vol. 38, no. 6, pp. 1141-1149, 2010.

[7] Microtech Instruments, Inc., [Online]. Available: http://www.mtinstruments.com/thzsources/. [Accessed 2 July 2013].

[8] D. M. Vavriv, "Potential of the clinotron for THz-generation," in *7th Workshop on High Energy Density and High Power RF,* Kalamata, Greece, 2005.

[9] V. L. Bratman, V. A. Gintsburg, Y. A. Grishin, B. S. Dumesh, F. S. Rusin and A. E. Fedotov, "Pulsed wideband orotrons of millimeter and submillimeter waves," *Radiophys. Quantum El.,* vol. 49, no. 11, pp. 866-871, 2006.

[10] J. C. Tucek, M. A. Basten, D. A. Gallagher and K. E. Kreischer, "220 GHz power amplifier testing at Northrop Grumman," in *14th IEEE International Vacuum Electronics Conference*, Paris, France, 2013.

[11] C. D. Joye, A. M. Cook, J. P. Calame, D. K. Abe, K. T. Nguyen, E. L. Wright, A. N. Vlasov, I. A. Chernyavskiy, T. Kimura and B. Levush, "Demonstration of a high power, wideband 220 GHz serpentine waveguide amplifier fabricated by UV-LIGA," in *14th IEEE International Vacuum Electronics Conference*, Paris, France, 2013.

[12] Communications & Power Industries, Ltd., [Online]. Available: http://www.cpii.com/docs/related/40/Family%20of%20MMW%20Products.pdf. [Accessed 3 July 2013].

[13] N. I. Avtomonov, V. D. Naumenko, D. M. Vavriv, K. Schünemann, A. N. Suvorov and V. A. Markov, "Towards terahertz magnetrons: 210-GHz spatial-harmonic magnetron with cold cathode," *IEEE Trans. Electron Devices,* vol. 59, no. 12, pp. 3608-3611, 2012.

[14] J. H. Booske, R. J. Dobbs, C. D. Joye, C. L. Kory, G. R. Neil, G.-S. Park, J. Park and R. J. Temkin, "Vacuum electronic high power terahertz sources," *IEEE Trans. THz Sci. Technol.,* vol. 1, no. 1, pp. 54-75, 2011.

[15] J. Christiansen and C. Schultheiss, "Production of high current particle beams from low pressure spark discharges," *Z. Physik A.,* vol. 290, no. 1, pp. 35-41, 1979.

[16] A. W. Cross, H. Yin, W. He, K. Ronald, A. D. Phelps and L. C. Pitchford, "Generation and application of pseudospark electron beams," *J. Phys. D: Appl. Phys.,* vol. 40, no. 7, pp. 1953-1956, 2007.

[17] K. Frank, E. Boggasch, J. Christiansen, A. Goertler, W. Hartmann, C. Kozlik, G. Kirkman, C. Braun, V. Dominic, M. A. Gundersen, H. Riege and G. Mechterscheimer, "High-power pseudospark and BLT switches," *IEEE T. Plasma Sci.,* vol. 16, no. 2, pp. 317-323, 1998.

[18] C. S. Wong, H. J. Woo and S. L. Yap, "A low energy tunable pulsed X-ray source based on the pseudospark electron beam," *Laser Part. Beams,* vol. 25, no. 5, pp. 497-502, 2007.

[19] W. Benker, J. Christiansen, K. Frank, H. Gundel, W. Hartmann, T. Redel and M. Stetter, "Generation of intense pulsed electron beams by the pseudospark discharge," *IEEE. T. Plasma Sci.,* vol. 17, no. 5, pp. 754-757, 1989.

[20] A. W. Cross, S. N. Spark and A. D. R. Phelps, "Gyrotron experiments using cavities of different ohmic Q," *Int. J. Electron.,* vol. 79, no. 4, pp. 481-493, 1995.

[21] N. S. Ginzburg, N. Y. Peskov, A. D. R. Phelps, A. W. Cross, W. He and P. Winning, "Theoretical and experimental studies of a Ka-band free electron laser with a guide magnetic field," in *23rd Annual Plasma Physics Conference (IoP),* Crieff, Scotland, 1996.

[22] S. J. Cooke, A. W. Cross, W. He and A. D. R. Phelps, "Experimental operation of a cyclotron autoresonance maser oscillator at the second harmonic," *Phys. Rev. Lett.,* vol. 77, no. 23, pp. 4836-4839, 1996.

[23] V. L. Bratman, A. W. Cross, G. G. Denisov, W. He, A. D. R. Phelps, K. Ronald, S. V. Samsonov, C. G. Whyte and A. R. Young, "High-gain wide-band gyrotron traveling wave amplifier with a helically corrugated waveguide," *Phys. Rev. Lett.,* vol. 84, no. 12, pp. 2746-2749, 2000.

[24] D. C. Speirs, K. Ronald, S. L. McConville, K. M. Gillespie, A. D. R. Phelps, A. W. Cross, R. Bingham, C. W. Robertson, C. G. Whyte, W. He, I. Vorgul, R. A. Cairns and B. J. Kellett, "Numerical investigation of auroral cyclotron maser processes," *Phys. Plasmas,* vol. 17, no. 5, p. 056501, 2010.

[25] I. V. Konoplev, P. McGrane, W. He, A. W. Cross, A. D. R. Phelps, C. G. Whyte, K. Ronald and C. W. Robertson, "Experimental studies of coaxial free-electron maser based on two-dimensional distributed feedback," *Phys. Rev. Lett.,* vol. 96, no. 3, p. 035002, 2006.

[26] M. Garven, S. N. Spark, A. W. Cross, S. J. Cooke and A. D. R. Phelps, "Gyrotron experiments employing a field emission array cathode," *Phys. Rev. Lett.,* vol. 77, no. 11, pp. 2320-2323, 1996.

[27] K. Ronald, A. W. Cross, A. D. R. Phelps, W. He, H. Yin and S. N. Spark, "Explosive cathode gyrotron experiments," *IEEE Trans. Plasma Sci.,* vol. 26, no. 3, pp. 375-382, 1998.

[28] H. Yin, Pseudospark discharge and Cherenkov maser experiments, Glasgow: PhD Thesis, University of Strathclyde, 1998.

[29] H. Yin, W. He, A. W. Cross, A. D. R. Phelps and K. Ronald, "Single-gap pseudospark discharge experiments," *J. Appl. Phys.*, vol. 90, no. 7, pp. 3212-3218, 2001.

[30] H. Yin, A. D. R. Phelps, W. He, G. R. M. Robb, K. Ronald, P. Aitken, B. W. J. McNeill, A. W. Cross and C. G. Whyte, "A pseudospark cathode Cherenkov maser: theory and experiment," *Nucl. Instr. and Meth. in Phys. Res. A*, vol. 407, no. 1-3, pp. 175-180, 1998.

[31] H. Yin, W. He, G. R. M. Robb, A. D. R. Phelps, K. Ronald and A. W. Cross, "Coherent microwave generation from a pseudospark cathode Cherenkov maser," *Phys. Rev. ST Accel. Beams*, vol. 2, no. 2, p. 020701, 1999.

[32] H. Yin, A. W. Cross, W. He, A. D. R. Phelps and K. Ronald, "Pseudospark experiments: Cherenkov interaction and electron beam post-acceleration," *IEEE T. Plasma Sci.*, vol. 32, no. 1, pp. 233-239, 2004.

[33] M. Faraday, "Experimental researches in electricity," *Seventh Series Transactions of the Royal Philosophical Society of London*, p. 124, 1776-1786.

[34] J. P. Birk, Chemistry, Houghton Mifflin, 1994.

[35] J. D. Ryder, Electronic Fundamentals and Applications, Pitman Publishing, 1976.

[36] T. A. Edison, "Electric-lamp". Patent 223,898, 27 January 1880.

[37] T. A. Edison, "Electrical indicator". Patent 307,031, 21 October 1884.

[38] A. S. Gilmour, Jr., Microwave Tubes, Artech House, 1986.

[39] R. W. Wood, "A new form of cathode discharge and the production of X-rays, together with some notes of diffraction," *Phys. Rev.*, vol. 5, no. 1, pp. 1-10, 1897.

[40] W. Schottky, "Über kalte und warme elektronenentladungen," *Z. Phys. A-hadron Nucl.*, vol. 14, no. 1, pp. 63-106, 1923.

[41] D. A. Davies, Waves, atoms and solids, Longman, 1978.

[42] W. E. Spicer and A. Herrera-Gómez, "Modern theory and applications of

photocathodes," in *Proc. SPIE International Symposium on Optics, Imaging and Instrumentation*, San Diego, CA, 1993.

[43] Y. E. Kreindel, Plasma Electron Sources, Atomizdat, 1977.

[44] E. M. Oks and p. M. Schanin, "Development of plasma cathode electron guns," *Phys. Plasmas,* vol. 6, no. 5, pp. 1649-1654, 1999.

[45] V. Burdovitsin and E. Oks, "Hollow-cathode plasma electron gun for beam generation at forepump gas pressure," *Rev. Sci. Instrum.,* vol. 70, no. 7, pp. 2975-2978, 1999.

[46] R. Mavrodineanu, "Hollow cathode discharges – analytical applications," *J. Res. Nat. Bur. Stand.,* vol. 89, no. 2, pp. 143-187, 1984.

[47] A. M. Howatson, An Introduction to Gas Discharges, Pergamon Press, 1976.

[48] J. S. E. Townsend, Electricity in Gases, Oxford: Clarendon Press, 1915.

[49] K. Frank, "Review of superdense glow discharge," in *Physics and Applications of Psuedosparks*, NATO ASI Series, Plenum Press, 1990, pp. 15-54.

[50] R. J. Carman, DC Glow Discharge Electron Guns for the Excitation of Rare Gases, St. Andrew's: Thesis submitted for the title of Ph.D., 1986.

[51] P. Gill and C. E. Webb, "Electron energy distributions in the negative glow and their relevance to hollow cathode lasers," *J. Phys. D: Appl. Phys.,* vol. 10, no. 3, p. 299, 1977.

[52] R. M. Chaudhari and M. M. Chaudhari, "Energy spectrum of cathode rays in glow discharge in gases at low pressures," in *International Conference on Phenomena in Ionized Gases, Vol. I*, Belgrade, 1965.

[53] R. Warren, "Interpretation of field measurements in the cathode region of glow discharges," *Phys. Rev.,* vol. 98, no. 6, p. 1655, 1958.

[54] K. G. Emeleus, "The negative end of cold cathode glow discharges," *J. Phys. D: Appl. Phys.,* vol. 14, no. 12, p. 2179, 1981.

[55] W. Hartmann and M. A. Gundersen, "Cathode-related processes in high-current density, low pressure glow discharges," in *Physics and Applications of Pseudosparks*, NATO ASI Series, Plenum Press, 1990, pp. 77-88.

[56] A. Anders, S. Anders and M. A. Gundersen, "Model for explosive emission in a

pseudospark "superdense glow",” *Phys. Rev. Lett.*, vol. 71, no. 3, pp. 364-367, 1993.

[57] V. K. Zworykin, Electron Optics and the Electron Microscope, John Wiley & Sons, 1945.

[58] G. M. Glasford, Fundamentals of Television Engineering, McGraw Hill, 1955.

[59] C. Vieu, F. Carcenac, A. Pépin, Y. Chen, M. Mejias, A. Lebib, L. Manin-Ferlazzo, L. Couraud and H. Launois, “Electron beam lithography: resolution limits and applications,” *Appl. Surf. Sci.*, vol. 164, no. 1-4, pp. 111-117, 2000.

[60] S. Humphries Jr., Charged Particle Beams, John Wiley & Sons, 1990.

[61] C. Lejeune and J. Aubert, “Emittance and brightness: definitions and measurements,” *Adv. Electron. Electron Phys.*, vol. Suppl. 13A, p. Pt. A, 1980.

[62] J. T. Mendel, C. F. Quate and W. H. Yocom, “Electron beam focusing with periodic permanent magnet fields,” *Proc. IRE*, vol. 42, no. 5, pp. 800-810, 1954.

[63] D. H. Whittum, A. M. Sessler and J. M. Dawson, “Ion-channel laser,” *Phys. Rev. Lett.*, vol. 64, no. 21, pp. 2511-2514, 1990.

[64] D. Su and C. J. Tang, “Electromagnetic instability in an electron beam-ion channel system,” *Phys. Plasmas*, vol. 16, no. 5, p. 053101, 2009.

[65] D. W. Kerst and R. Serber, “Electron orbits in the induction accelerator,” *Phys. Rev.*, vol. 60, no. 1, pp. 53-58, 1941.

[66] E. Boggasch and M. J. Rhee, “High-brightness pseudospark-produced electron beam,” *Appl. Phys. Lett.*, vol. 56, no. 18, pp. 1746-1748, 1990.

[67] R. Ganter, R. J. Bakker, M. Dehler, J. Gobrecht, C. Gough, E. Kirk, S. C. Leemann, K. Li, M. Paraliev, M. Pedrozzi, F. Le Pimpec, J.-Y. Raguin, L. Rivkin, V. Schlott, H. Sehr, S. Tsujino and A. Wrulich, “High current electron emission from microscopic tips,” in *Proceedings of FEL 2006*, Berlin, Germany, 2006.

[68] J. Benford, J. A. Swegle and E. Schamiloglu, High Power Microwaves, Boca Raton, FL: Taylor & Francis, 2007.

[69] R. G. Carter, Electromagnetic waves: Microwave components and devices,

Chapman and Hall, 1990.

[70] H. R. Johnson, “Backward-wave oscillators,” *Proc. IRE,* vol. 43, no. 6, pp. 684-697, 1955.

[71] S. E. Tsimring, Electron Beams and Microwave Vacuum Optics, Hoboken, New Jersey: Wiley-InterScience, 2007.

[72] H. Heffner, “Analysis of the backward-wave travelling-wave tube,” *Proc. IRE,* vol. 42, no. 6, pp. 930-937, 1954.

[73] J. R. Pierce, “Travelling Wave Tubes,” *AT&T Tech. J.,* vol. XXIX, no. 1, pp. 1-59, 1950.

[74] J. M. Butler, C. B. Wharton and S. Furukawa, “Dependence of relativistic backward wave oscillator parameters on effective beam gamma,” *IEEE Trans. Plasma Sci,* vol. 18, no. 3, pp. 490-496, 1990.

[75] R. H. Varian and S. F. Varian, “A high-frequency oscillator and amplifier,” *J. Appl. Phys.,* vol. 10, no. 5, pp. 321-327, 1939.

[76] G. Caryotakis, “High power klystrons: Theory and practice at the Stanford Linear Accelerator Center Part I,” SLAC Publishing, Stanford, CA, 2005.

[77] R. G. Carter, “Accelerator technologies for charged particles: an introduction,” *Contemp. Phys.,* vol. 52, no. 1, pp. 15-41, 2011.

[78] R. Warnecke and P. Guénard, “Les tubes à commande par modulation de vitesse,” *Ann. Telecommun.,* vol. 7, no. 3, p. 152, 1952.

[79] G. M. Branch and T. G. Mihran, “Plasma frequency reduction factors in electron beams,” *IRE Trans. On Elec. Dev.,* vol. 2, no. 2, pp. 3-11, 1955.

[80] A. S. Gilmour, Jr., Klystrons, traveling wave tubes, magnetrons, crossed-field amplifiers and gyrotrons, Norwood, MA: Artech House, 2011.

[81] K. Fujisawa, “General treatment of klystron resonant cavities,” *IRE Trans. Microw. Theory Techn.,* vol. 6, no. 4, pp. 344-358, 1958.

[82] R. G. Carter, J. Feng and U. Becker, “Calculation of the properties of reentrant cylindrical cavity resonators,” *IEEE Trans. Microw. Theory Techn.,* vol. 55, no. 12, pp. 2531-2538, 2007.

[83] P. H. Harms, J. -F. Lee and R. Mittra, “A study of the nonorthogonal FDTD

method versus the conventional FDTD technique for computing resonant frequencies of cylindrical cavities," *IEEE Trans. Microw. Theory Techn.*, vol. 40, no. 4, pp. 741-746, 1992.

[84] M. Clemens and T. Weiland, "Discrete electromagnetism with the finite integration technique," *Prog. Electromagn. Res.,* vol. 32, pp. 65-87, 2001.

[85] B. Goplen, L. Ludeking, D. Smith and G. Warren, "User-configurable MAGIC for electromagnetic PIC calculations," *Comput. Phys. Commun.,* vol. 87, no. 1-2, pp. 54-86, 1995.

[86] J. P. L. Neto and J. J. Barroso, "The Sinusoid as the Longitudinal Profile in Backward-Wave," *Braz. J. Phys.,* vol. 34, no. 4B, pp. 1577-1582, 2004.

[87] K. Minami, Y. Carmel, V. L. Granatstein, W. W. Destler, W. Lou, D. K. Abe, R. A. Kehs, M. M. Ali, T. Hosokawa, K. Ogura and T. Watanabe, "Linear theory of electromagnetic wave generation in a plasma-loaded corrugated-wall resonator," *IEEE Trans. Plasma Sci.,* vol. 18, no. 3, pp. 537-545, 1990.

[88] H. Yin, D. Zhu, A. D. R. Phelps, W. He, A. W. Cross, G. R. M. Robb and K. Ronald, "Pseudospark-based electron beam production and post-acceleration," *J. Appl. Phys.*, vol. 91, no. 8, pp. 5419-5422, 2002.

[89] H. Yin, A. W. Cross, W. He, A. D. R. Phelps, K. Ronald, D. Bowes and C. W. Robertson, "Millimeter wave generation from a pseudospark-sourced electron beam," *Phys. Plasmas,* vol. 16, no. 6, p. 063105, 2009.

[90] T. Tasuku and T. Yoneyama, Modern millimeter-wave technologies, USA: IOS Press, 2001.

[91] W. He, D. Bowes, H. Yin, L. Zhang, C. R. Donaldson, G. Liu, D. Speirs, K. Ronald, A. D. R. Phelps, X. Chen, D. Li and A. W. Cross, "Frequency Swept Terahertz Pulse Generation using," *Prepared for publication.*

[92] L. W. Hinderks and A. Maione, "Copper conductivity at millimeter-wave frequencies," *Bell Syst. Tech. J.,* vol. 59, no. 1, pp. 43-65, 1980.

[93] H. A. Wheeler, "Coupling holes between resonant cavities or wave-guides evaluated in terms of volume ratios," *IEEE Trans. Microw. Theory Tech.,* vol. 12, no. 2, pp. 231-244, 1964.

[94] D. C. Wunsch and A. Erteza, “Kerr cell measuring system for high voltage pulses,” *Rev. Sci. Instrum.,* vol. 35, no. 7, pp. 816-820, 1963.

[95] L. L. Altgilbers, J. Baird, B. L. Freeman, C. S. Lynch and S. I. Shkuratov, Explosive Pulsed Power, Imperial College Press, 2010.

[96] P. Horowitz and W. Hill, The Art of Electronics, Cambridge University Press, 1989.

[97] M. Argüeso, G. Robles and J. Sanz, “Implementation of a Rogowski coil for the measurement of partial discharges,” *Rev. Sci. Instrum.,* vol. 76, no. 6, p. 065107, 2005.

[98] D. B. Williams and C. B. Carter, Transmission Electron Microscopy: A Textbook for Materials Science, 2nd Edition, Springer, 2009.

[99] S. N. Sparks and A. D. R. Phelps, “Witness plate electron beam diagnostic for electron cyclotron maser research,” *Meas. Sci. Technol.,* vol. 1, no. 4, pp. 352-355, 1990.

[100] N. Chatterjee, Electron microprobe analysis by wavelength dispersive x-ray spectroscopy, Massachusetts Institute of Technology, Cambride, MA: Course Notes, 2010.

[101] N. Bethe, Handbook of Physics, Berlin: Springer, 1933.

[102] G. H. Bryant, Principles of microwave measurements, IEEE Electrical Measurement Series 5, 1988.

[103] E. I. Knizhnik, V. A. Moskalev and A. D. Onisko, “A simple method for the measurement of electron-beam energy,” *Sov. Atom. Energy,* vol. 60, no. 3, pp. 279-281, 1986.

[104] T. Idehara, H. Tsuchiya, L. Agusu, S. Mitsudo, H. Murase, H. Mori, T. Kanemaki and T. Saito, “Development of a THz gyrotron with 20 T pulsed magnet,” *J. Phys. Conf. Ser.,* vol. 51, pp. 553-556, 2006.

[105] M. Y. Glyavin, A. G. Luchinin and G. Y. Golubiatnikov, “Generation of 1.5-kW, 1-THz coherent radiation from a gyrotron with a pulsed magnetic field,” *Phys. Rev. Lett.,* vol. 100, no. 1, p. 015101, 2008.

[106] B. P. Gorshunov, A. A. Volkov, A. S. Prokhorov, I. E. Spektor, J. Akimitsu, M.

Dressel, G. Nieuwenhuys, S. Tomic and S. Uchida, “Terahertz BWO spectroscopy of conductors and superconductors,” *Quantum Electron.,* vol. 37, no. 10, pp. 916-923, 2007.

[107] M. Philipp, U. U. Graf, A. Wagner-Gentner, D. Rabanus and F. Lewen, “Compact 1.9 THz BWO local-oscillator for the GREAT heterodyne receiver,” *Infrared Phys. Techn.,* vol. 51, no. 1, pp. 54-59, 2007.

[108] A. Dobroiu, M. Yamashita, Y. N. Ohshima, Y. Morita, C. Otani and K. Kawase, “Terahertz imaging system based on a backward-wave oscillator,” *Appl. Optics,* vol. 43, no. 30, pp. 5637-5646, 2004.

[109] R. E. Miles and M. Naftaly, “Terahertz Sources,” in *Microwave Photonics: Devices and Applications,* John Wiley & Sons, 2009, pp. 111-129.

[110] O. A. Klimenko, Y. A. Mitayagin, S. A. Savinov, V. N. Murzin, N. V. Dyakonova, P. Solignac and W. Knap, “Terahertz wide range tunable cyclotron resonance p-Ge laser,” *J. Phys. Conf. Ser.,* vol. 193, no. 1, p. 012064, 2009.

[111] G. Ramian, “The new UCSB free-electron lasers,” *Nucl. Inst. Meth. A,* vol. 318, no. 1, pp. 225-229, 1992.

[112] A. Gover, A. Faingersh, A. Eliran, M. Volshonok, H. Kleinman, S. Wolowelsky, Y. Yakover, B. Kapilevich, Y. Lasser, Z. Seidov, M. Kanter, A. Zinigrad, M. Einat, Y. Lurie, A. Abramovich, A. Yahalom, Y. Pinhasi, E. Weisman and J. Shiloh, “Radiation measurements in the new tandem accelerator FEL,” *Nucl. Inst. Meth. A,* vol. 528, no. 1-2, pp. 23-27, 2004.

[113] N. e. a. Gavrilov, “Status of the Novosibirsk high-power terahertz FEL,” *Nucl. Inst. Meth. A,* vol. 575, no. 1-2, pp. 54-57, 2007.

[114] A. G. G. G. E. M. G. a. S. I. Doria, A. Doria, G. P. Gallerano, E. Giovenale, G. Messina and I. Spassovsky, “Enhanced coherent emission of terahertz radiation by energy-phase correlation in a bunched electron beam,” *Phys. Rev. Lett.,* vol. 93, no. 26 Pt 1, p. 264801, 2004.

[115] D. Dragoman and M. Dragoman, “Terahertz fields and applications,” *Prog. Quant. Electron.,* vol. 28, no. 1, pp. 1-66, 2004.

[116] B. Ferguson and X.-C. Zhang, “Materials for terahertz science and technology,”

Nature Mater., vol. 1, pp. 26-33, 2002.

[117] M. R. Stone, M. Naftaly, R. E. Miles, J. R. Fletcher and D. P. Steenson, "Electrical and radiation characteristics of semilarge photoconductive terahertz emitters," *IEEE T. Microw. Theory*, vol. 52, no. 10, pp. 2420-2429, 2004.

[118] Y. C. Shen, P. C. Upadhya, E. H. Linfield, H. E. Beere and A. G. Davies, "Ultrabroadband terahertz radiation from low-temperature-grown GaAs photoconductive emitters," *Appl. Phys. Lett.*, vol. 83, no. 15, pp. 3117-3119, 2003.

[119] M. R. Stone, M. Naftaly, R. E. Miles, I. C. Mayorga, A. Malcoci and M. Mikulics, "Generation of continuous-wave terahertz radiation using a two-mode titanium sapphire laser containing an intracavity Fabry-Perot etalon," *J. Appl. Phys.*, vol. 97, no. 10, p. 103108, 2005.

[120] J.-i. Nishizawa, K. Suto, T. Sasaki, T. Tanabe and T. Kimura, "Spectral measurement of terahertz vibrations of biomolecules using a GaP terahertz-wave generator with automatic scanning control," *J. Phys. D: Appl. Phys.*, vol. 36, no. 23, pp. 953-957, 2003.

[121] T. Taniuchi, S. Okada and H. Nakanishi, "Widely tunable terahertz-wave generation in an organic crystal and its application," *J. Appl. Phys.*, vol. 95, no. 11, pp. 5984-5987, 2004.

[122] H. Eisele, "355 GHz oscillator with GaAs TUNNETT diode," *Electron. Lett.*, vol. 41, no. 6, pp. 329-311, 2005.

[123] K. Chang, W. F. Thrower and G. M. Hayashibara, "Millimeter-wave silicon IMPATT sources and combiners in the 110-260-GHz range," *IEEE T. Microw. Theory*, vol. 29, no. 12, pp. 1278-1284, 1981.

[124] E. Alekseev and D. Pavlidis, "GaN Gunn diodes for THz signal generation," *IEEE MTT-S International Symposium Digest 3*, pp. 1905-1908, 2000.

[125] E. R. Brown, J. R. Söderström, C. D. Parker, L. J. Mahoney, K. M. Molvar and T. C. McGill, "Oscillations up to 712 GHz in InAs/AlSb resonant-tunneling diodes," *Appl. Phys. Lett.*, vol. 58, no. 20, pp. 2291-2293, 1991.

[126] E. e. a. Schomburg, "Millimeter wave generation with a quasi planar

superlattice electronic device," *Solid-State Electron.*, vol. 42, no. 7-8, pp. 1495-1498, 1998.

[127] A. Tredicucci, R. Köhler, L. Mahler, H. E. Beere, E. H. Linfield and D. A. Ritchie, "Terahertz quantum cascade lasers – first demonstration and novel concepts," *Semic. Sci. Technol.*, vol. 20, no. 7, pp. S222-S227, 2005.

[128] P. Lorrain and D. Corson, Electromagnetic Fields and Waves, W.H. Freeman and Company, 1970.

[129] J. D. Kraus and K. R. Carver, Electromagnetics, McGraw-Hill, 1973.

Appendix I:

An Overview of mm-Wave Sources

I.1 Introduction

To date, the market for devices operating in the mm and sub-mm spectra has increased dramatically due to an increasing number of applications within these frequency bands. These can roughly be classed as falling into one of a number of categories:

- Vacuum sources
- Laser sources
- Electronic sources

In addition, other 'short-cuts' may be taken, for example through the use of frequency multipliers. What follows is merely a brief summary of what has been achieved to date using these methods.

I.2 Vacuum Sources

- ***Gyrotrons***

Gyrotrons are a form of free electron maser whose operation is based on the Cyclotron Resonance Maser instability which bunches electrons with cyclotron motion within a strong magnetic field. They are well suited for millimetre-wave generation due to the fact that their cavity size may be larger than the electron wavelengths and reducing the limitations imposed by material properties such as conductivity.

There are currently two gyrotron devices which have achieved operation at 1 THz. The first of these is the FU series gyrotron at the Research Center for Development of Far Infrared Region, University of Fukui, Japan [104]. In 2006, this achieved operation at a frequency of 1.005 THz (at second harmonic). The magnetic field required was 19.1 T.

The other system in operation is at the Institute of Applied Physics, Russian Academy of Sciences and it also broke the 1 THz barrier in 2007 [105]. This generated coherent radiation at 1.022 THz in 50 μs pulses with a microwave power per pulse of 5 kW, and at the fundamental harmonic of 1.3 THz in 40 μs pulses with a power of 0.5 kW. The required magnetic fields were 38.5 T and 48.7 T respectively, and the gyrotron tube is relatively compact at 400 mm in length.

- ***Backward Wave Oscillators (BWOs)***

BWOs are a form of travelling wave tube in which an electron beam interacts with a slow-wave structure, sustaining oscillations by propagating a travelling wave backwards against the beam. The output power is coupled out near the beam source or reflected and coupled out in the forward direction.

BWOs normally emit in the sub-THz region and the emitted radiation is then passed through one or more frequency multipliers. They are predominately found in THz spectroscopy systems [106] in the form of, for example, BWOs operating at 633 GHz then run through a 3X multiplier. These systems typically output ~100 μW of power and while they do work for spectroscopy systems they are bulky, require water cooling and are largely inefficient. Similar sources are employed in some astrological detection systems such as the 1.9 THz BWO system used in the GREAT heterodyne receiver [107].

BWOs operating in the sub-THz regime have found some use in imaging systems, with one tunable BWO operating in the 520-710 GHz frequency range being used for a variety of THz imaging purposes. The device has an estimated 15 mW output power [108].

I.3 Laser Sources

- ***Far Infrared Lasers (FIRs)***

The broad group of FIRs are one of the longest-known sources of coherent sub-mmW radiation, and they may be further sub-divided into three specific categories: molecular lasers, p-Ge lasers and free-electron lasers (FELs).

Molecular lasers are a source of discrete frequencies of THz radiation, using THz emitting transitions occurring between adjacent rotational levels of the same vibrational state within active gases which have a permanent dipole moment. Excitation is performed using optical pumping, often with a high-power CO_2 laser [109]. The frequency lines generated depend on the gas being used, with some gases able to generate several discrete lines. However, these devices are not continuously tunable and as such are limited in their usage, particularly in regards most spectroscopic applications. They have been known to generate frequencies in the range of 0.25-7.5 THz, with CW power levels in the order of mWs.

p-Ge laser are sub-mmW sources possessing high tunability, consisting of a cryogenically cooled p-doped Ge crystal mounted within a superconducting magnet. By altering the magnetic field strength, it is possible to tune the frequency of the laser, with a general range of 1.5-4.5 THz. These devices are usually pulsed, with repetition rates of tens of Hz, and have reasonable peak output powers in the order of watts. The cyclotron resonance mode p-Ge laser developed at the Lebedev Physical Institute in Moscow is tunable in the range 1.2-2.8 THz with a linewidth of approximately 6 GHz. Pulse duration and repetition rate are 1 μs and 10 Hz respectively. A very large magnetic field is required (2-4.8 T) for operation but this is true with all p-Ge lasers. Output powers of 10 mW were observed [110].

Free electron lasers (FELs) are a type of highly tunable lasers which use a highly relativistic electron beam moving freely through a magnetic medium as the lasing medium, rather than gas or semiconductor lasers in which all electrons are bound. They have the widest frequency range of any laser type and examples include the LCLS at SLAC. The first THz-FEL was the UCSB-FEL which allows for tunable operation from 0.12-4.8 THz with power output of 500-5000 W and pulse duration of 1-20 μs at 1 Hz repetition rate [111]. There are several others in operation throughout the world such as the 100 GHz EAFEL in Israel [112], but notably there is the development of the THz-FEL at Novosibirsk which aims to produce around 100 W of power [113]. Work is also being undertaken on 'compact FEL' devices, most notably the FEL-CATS device at ENEA-Frascati, which operates between 70-700 GHz, with a measured macro-pulse power of 1.5 kW at 0.4 THz. The radiation emitted has a pulsed structure composed of wave-packets of 3-10 ps, spaced at a repetition frequency of 3 GHz [114].

- ***Broadband laser generation***

Broadband generation uses ultrafast lasers which are mode-locked and typically have pulse lengths of under 100 fs, though some are as short as 10 fs. Repetition rates are in the order of 50-100 MHz and powers are around 0.2-2 W, with peak powers of 10^8 W possible. There are two general types of broadband emitter: those using optical rectification by electro-optic crystals and those based on biased photoconductive emitters.

Optical rectification as a generator of THz radiation has been in use since the 1980s, using crystals possessing bandgaps shorter than the laser wavelength. One common combination is to use zinc-blende semiconductors (bandgaps of 2-2.5 eV) with Ti-sapphire lasers (wavelength of 800 nm). When a short, high-intensity laser pulse interacts with the crystal, transient polarisation occurs which gives rise to optical rectification, with the THz power being generated proportional to the square of the optical power, varying with crystal and laser orientation and being varied by the second-order non-linear coefficient, $\chi^{(2)}$ [115]. Optical rectification usually generates

bandwidths of 0.1-3 THz, although wider bandwidths of up to 40 THz have been observed [116].

Much like optical rectification, the used of biased photoconductive emitters was pioneered in the 1980s and utilises ultrafast lasers. In this case, the laser is incident on a semiconductor wafer (e.g. GaAs) with bias electrodes deposited on its surface. The wavelength of the laser radiation must be shorter than the semiconductor's band gap which results in the semiconductor absorbing photons from the incident radiation and generating photocarriers. The bias field serves to accelerate these, whilst the laser intensity alters their density. In this way, high-current ultra-short currents are generated within the material, radiating into free space at THz frequencies [117]. Emitted powers average in 10s of μWs, which is much higher than those from optical rectification, but comes at the expense of bandwidth. A sample photoconductor could provide a working spectrum of 4 THz, but the power drops off exponentially with frequency. Nonetheless, some devices sacrifice power for bandwidth and biased photoconductive emitters exist with usable bandwidths of 20 THz [118].

- ***Difference Frequency Generation (DFG)***

Difference Frequency Generation uses near-infrared lasers, with one detuned by the required THz frequency and therefore relying on frequency mixing in order to generate THz radiation. There are two distinct types of DFG, continuous wave DFG using photoconductive emitters and pulsed DFG using electro-optic crystals.

When using photoconductive emitters, the process is similar to that of broadband emission but here two CW lasers are used rather than a pulsed source, and THz emission is caused by fluctuations in carrier density due to laser intensities and frequencies. Again, power scales with the square of the optical power and applied voltage but also on antenna efficiency and the material's carrier lifetime, the shorter the better. Power and bandwidth for CW DFG systems are limited to roughly 1 μW and 1.5 THz respectively [119].

For pulsed operation using electro-optic crystals, a sample setup would be a Q-switched laser pumping an optical parametric oscillator to provide the two required wavelengths to generate the THz frequencies, which shall be focused onto an electro-optic crystal. Via three-wave mixing, the THz difference frequency may now be generated. As the THz frequency being generated increases, so too do the efficiency and the THz power. As such, it is possible to achieve peak THz powers in the hundreds of milliwatts and to generate frequencies above 3 THz. Using GaP crystals, frequencies of 0.5-7 THz have been generated, with peak powers of ~100 mW [120] whilst organic DAST crystals have achieved continuous tuning at up to 20 THz with peak powers of 13.8 W [121].

I.4: Electronic Sources

Electronic devices such as Gunn, IMPATT and TUNNETT diodes are gradually receiving more attention as THz sources in recent years. They operate by the application of a high DC voltage to send the device into a state of negative differential resistance (NDR). This creates an intrinsically unstable state, sending the device into oscillation, the maximum frequency achievable limited by the time taken to transfer electrons from the light to the heavy mass conduction bands. GaAs TUNNETT diodes have been operated at 355 GHz, producing 140 μW of power [122] whilst Si IMPATT diodes have been achieving THz generation, predominately in the 100-300 GHz region, for many years with some generating 3 W (pulsed) and 110 mW (CW) outputs [123]. GaN Gunn diodes have also been employed with a frequency range of 148-162 GHz and an output power density of 10^5 W/cm^2 [124]. Such devices have much potential in some respects but are largely limited in frequency, often requiring frequency multiplication for operation nearer 1 THz. Low output powers may also be an issue.

- ***Resonant Tunnelling Diodes***

Resonant tunnelling diodes have the distinctive feature of possessing a double potential barrier structure and in the small space between barriers energy levels are quantised. At a given DC bias, the left-hand levels align with the lowest distinct level of the well, allowing for a resonant state at which electrons can tunnel through the barriers. As the bias is increased, the current falls due to the collapse of the resonant condition yet eventually the current increases once more due to the combined tunnelling through, and excitation over, the barriers. The final result is an I-V curve possessing an NDR region which can lead to oscillations. To date, the highest achieved frequency has been 712 GHz in an InAs/AlSb diode, but this was in the region of μWs of power [125]. As such, there are few applications for resonant tunnelling diodes but work continues on them with differing structures.

- ***Superlattice Electron Devices (SLEDs)***

It is possible to generate an NDR state without the transfer of electrons between bands in the event that electrons gain extra transfer without mass. This occurs in SLEDs where a momentum increase results in increased electron mass due to its particular band structure. At a high enough bias, electrons will slow down and as a result enter an NDR state but given that no transfer takes place, the frequency is not limited by transfer time. To date, SLEDs have only achieved 200 GHz at a power of sub-microwatts but progress with these devices continues to occur [126].

- ***Quantum Cascade Lasers (QCLs)***

QCLs utilise semiconductor lasers which emit in the mid-to-far-infrared region of the EM spectrum. Rather than relying on interband transitions, as with traditional semiconductor lasers, they instead are unipolar and operate via intersubband transitions in a repeated stack of semiconductor quantum well heterostructures. QCLs have proven to be a noteworthy THz source since breaking the THz mark in 2003 and as of 2005 they were able to achieve CW operation at room temperature and at frequencies of up to 4.4 THz. Such systems achieve mW of power and current densities of 100s of A/cm^2, but despite this they have limitations: the lower cut-off frequencies lie at around 1 THz, meaning operation at lower frequencies is difficult;

operation at lower frequencies requires additional magnetic fields and cooling; higher temperature operation results in reduced output power; and tunability is limited [127].

Appendix II:

Electromagnetic Theory

II.1 Electromagnetic Waves

Electromagnetic waves, as the name suggests, are self-propagating waves which possess both an electric and a magnetic component [128]. They propagate through free space with a velocity comparable to that of light and a wavelength given by

$$\lambda = \frac{c}{f} \tag{II.1}$$

where λ is the wavelength of the radiation, f the frequency and c the velocity of light. EM waves tend to be periodic and their waveforms may be broken down into sinusoidal components with fundamental and harmonic frequencies. As such, a wave's harmonics' effects within a circuit may be analysed for each harmonic and subsequently added back together to ascertain the complete effects of the waveform.

A wave's propagation may be given by

$$E = E_0 \sin(\omega t \pm \gamma z) \tag{II.2}$$

whereE_0 is the peak electric field, ω the angular frequency, γ the propagation constant, t the time and z the distance. An illustration of this is to choose a constant value of E, $E1$. For the field to remain constant, the sine wave's angle must remain constant, i.e.

$$\phi_0 = \omega t \pm \gamma z \tag{II.3}$$

Choosing the minus sign first,

$$z = \frac{\omega t - \phi_0}{\gamma} \tag{II.4}$$

This equation shows that as t increases so too does z and the wave is therefore propagating in the z-direction. It can also be shown that the reverse is true.

The wave's velocity may be given by taking the derivative of (1.4) with respect to time,

$$u = \frac{dz}{dt} = \frac{\omega}{\gamma} \tag{II.5}$$

and therefore the propagation constant can be found from

$$\gamma = \frac{\omega}{u}\text{radians/metre} \tag{II.6}$$

which is a measure of the phase characteristic of a wave progressing through a medium.

Often, γ may be used to determine the attenuation or growth of a wave, and in these cases

$$\gamma = \beta + j\alpha \tag{II.7}$$

where β is now the phase characteristic and α a measure of the rate of growth or attenuation. As such, the propagation of a wave may be expressed as

$$E = E_0 e^{-\alpha z} \sin(\omega t - \gamma z) \tag{II.8}$$

Given that EM waves contain both electric and magnetic components, it can be said that, in the case of a wave in free space, both the electric and magnetic waves are sinusoidal and proceed in the z direction with the magnetic field's direction at a right angle to the electric field.

II.2 Waves in a Rectangular Waveguide

To begin understanding the transference of electromagnetic waves through a waveguide, it is necessary to understand Maxwell's equations which, in their basic forms, are given as

$$\boldsymbol{\nabla} \cdot \boldsymbol{E} = \frac{\rho}{\varepsilon} \tag{II.9}$$

$$\boldsymbol{\nabla} \cdot \boldsymbol{B} = 0 \tag{II.10}$$

$$\boldsymbol{\nabla} \times \boldsymbol{E} = -\frac{\partial \boldsymbol{B}}{\partial t} \tag{II.11}$$

$$\boldsymbol{\nabla} \times \boldsymbol{B} = \mu \boldsymbol{J} + \varepsilon\mu \frac{\partial \boldsymbol{E}}{\partial t} \tag{II.12}$$

where **E** and **B** are the vector forms of the electric and magnetic fields respectively, and **J** and ρ are the current and charge densities respectively. Equations II.9 and II.10 represent Gauss's laws for electric and magnetic fields, equation II.11 represents Faraday's law and II.12 represents Faraday's law. In some cases, constituent forms of these equations may be used, with

$$\boldsymbol{D} = \varepsilon \boldsymbol{E} \tag{II.13}$$

$$\boldsymbol{H} = \frac{\boldsymbol{B}}{\mu} \tag{II.14}$$

From the above equations and their relationships it is possible to express the equations for propagation of electric and magnetic waves, assuming zero charge and current,

$$\nabla^2 \boldsymbol{E} = \mu\varepsilon \frac{\partial^2 \boldsymbol{E}}{\partial t^2} \tag{II.15}$$

$$\nabla^2 \boldsymbol{B} = \mu\varepsilon \frac{\partial^2 \boldsymbol{B}}{\partial t^2} \tag{II.16}$$

When considering Maxwell's equations within a bound medium, it is necessary to also consider boundary conditions. Within a metallic medium, it is necessary that the tangential component of the electric field goes to zero at the walls, due to the walls shorting the field, as must the normal component of the magnetic field due to current flow negating the field. These boundary conditions therefore only allow the propagation of either transverse electric (TE) or transverse magnetic (TM) modes within a hollow waveguide and exclude the propagation of transverse electro-magnetic (TEM) modes (Carter 2010).

II.2.1 Rectangular waveguides

The dispersion relation for an electromagnetic wave within a smooth-walled rectangular waveguide is given as

$$\omega_W = c\sqrt{k_z^2 + k_\perp^2} \tag{II.17}$$

where k_z is the propagating wavenumber and $k_\perp$ is the perpendicular wave vector.

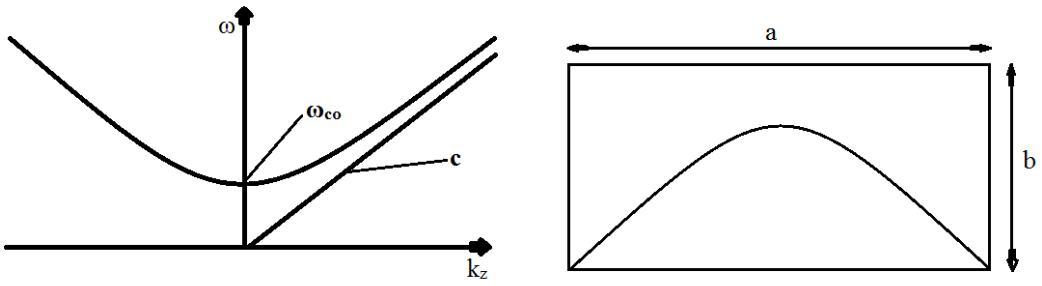

Figure II.1 (a) and (b): Dispersion diagram showing normal modes of a waveguide and a beam travelling at the speed of light, left; and the electric field profile of the x-y plane of a rectangular waveguide, where *a* is the waveguide width and *b* the height, right.

The minimum frequency, ω_{co} (also known as the angular cut-off frequency), capable of propagation within a rectangular waveguide is given as

$$\omega_{co} = ck_\perp = c\sqrt{\left(\frac{m\pi}{a}\right)^2 + \left(\frac{n\pi}{b}\right)^2} \tag{II.18}$$

where m and n are the waveguide mode numbers, a and b denote the waveguide dimensions.

In practice, the numbers m and n are used to indicate the number of half-wave variations over the length and height of the waveguide cross-section respectively. Substituting the above into equation II.17 results in

$$\omega = c\sqrt{k_z^2 + \left(\frac{m\pi}{a}\right)^2 + \left(\frac{n\pi}{b}\right)^2} \tag{II.19}$$

II.2.1.1 TE Waves

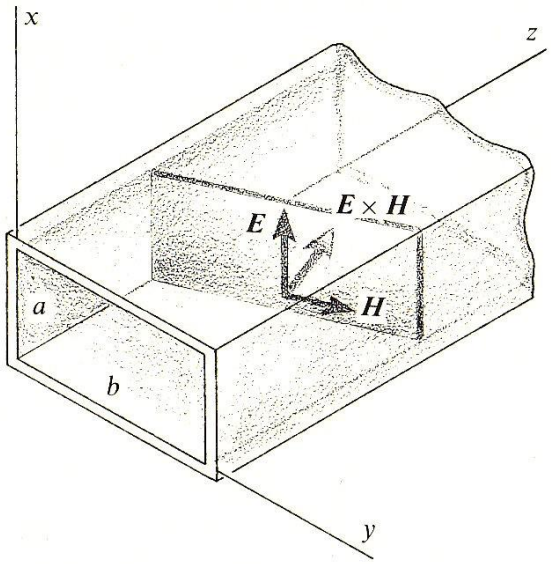

Figure II.2: E and H field orientation of a TE wave within a rectangular waveguide.

A TE wave is one in which the E and H fields are oriented as shown in figure II.2 and are reflected on the walls parallel to the x-z plane. The equations governing the electric and magnetic field components may be given from the wave equation and from boundary conditions.

$$B_z = A\cos\left(\frac{m\pi}{a}x\right)\cos\left(\frac{n\pi}{b}y\right) \tag{II.20}$$

$$E_z \equiv 0 \tag{II.21}$$

$$E_x = i\frac{\omega}{k_\perp^2}\frac{\partial B_z}{\partial y} \tag{II.22}$$

$$E_y = -i\frac{\omega}{k_\perp^2}\frac{\partial B_z}{\partial x} \tag{II.23}$$

$$B_x = i\frac{k_z}{k_\perp^2}\frac{\partial B_z}{\partial x} \tag{II.24}$$

$$B_y = i\frac{k_z}{k_\perp^2}\frac{\partial B_z}{\partial y} \tag{II.25}$$

where *A* is a constant related to the amplitude of the wave. It should be noted that, for the case of TE_{mn} modes, either m or n can be zero, but both cannot.

II.2.1.2 TM Waves

Transverse magnetic modes vary in two ways from TE modes; firstly, in that they have no axial component of B ($B_z = 0$); and secondly in that while TE modes may have values of m or n equalling 0, the fundamental TM mode is TM_{11} (i.e. $m, n \neq 0$). Other than this, the field distribution equations for a TM mode are similarly obtained to those of in TE waves.

$$E_z = D \sin\left(\frac{m\pi}{a}x\right) \sin\left(\frac{n\pi}{b}y\right) \tag{II.26}$$

$$B_z \equiv 0 \tag{II.27}$$

$$E_x = i\frac{k_z}{k_\perp^2}\frac{\partial E_z}{\partial x} \tag{II.28}$$

$$E_y = -i\frac{k_z}{k_\perp^2}\frac{\partial E_z}{\partial y} \tag{II.29}$$

$$B_x = -i\frac{\omega}{\omega_{co}^2}\frac{\partial E_z}{\partial y} \tag{II.30}$$

$$B_y = i\frac{\omega}{\omega_{co}^2}\frac{\partial E_z}{\partial x} \tag{II.31}$$

with *D* a constant indicating the wave amplitude [68].

II.3 Waves in a Circular Waveguide

While circular waveguide is not explicitly used during the course of this work, it is useful to analyse the construction and propagation of waves in such a structure as it enables us to better understand the operating principles of the backward wave oscillator.

In a circular waveguide with perfectly conducting walls and radius $r = r_0$, $x_\perp$ lies in the r-θ plane. *E* may now be expressed as

$$E(r, \theta, z, t) = E(r, \theta)e^{i(k_z z - \omega t)} \tag{II.32}$$

while the boundary conditions state that B_r, E_θ and E_z all equal zero at the conducting wall (i.e. when $r = r_0$).

The equations governing the electric and magnetic field components for TE_{nm} waves in a circular waveguide are expressed as

$$B_z = AJ_m(k_\perp r)\sin(m\theta) \tag{II.33}$$

$$E_z \equiv 0 \tag{II.34}$$

$$E_r = i\frac{\omega}{k_\perp^2}\frac{1}{r}\frac{\partial B_z}{\partial \theta} \tag{II.35}$$

$$E_\theta = -i\frac{\omega}{k_\perp^2}\frac{\partial B_z}{\partial r} \tag{II.36}$$

$$B_r = i\frac{k_z}{k_\perp^2}\frac{\partial B_z}{\partial r} \tag{II.37}$$

$$B_\theta = i\frac{k_z}{k_\perp^2}\frac{1}{r}\frac{\partial B_z}{\partial \theta} \tag{II.38}$$

and, for TM_{nm} modes,

$$E_z = DJ_m(k_\perp r)\sin(m\theta) \tag{II.39}$$

$$B_z \equiv 0 \tag{II.40}$$

$$E_r = i\frac{k_z}{k_\perp^2}\frac{\partial E_z}{\partial r} \tag{II.41}$$

$$E_\theta = i\frac{k_z}{k_\perp^2}\frac{\partial E_z}{\partial \theta} \tag{II.42}$$

$$B_r = -i\frac{\omega}{k_\perp^2}\frac{1}{r}\frac{\partial E_z}{\partial \theta} \tag{II.43}$$

$$B_\theta = i\frac{\omega}{k_\perp^2}\frac{\partial E_z}{\partial r} \tag{II.44}$$

where J_m is the Bessel function of the m^{th} order.

In rectangular modes, the cut-off frequencies do not vary between TE and TM modes and thus can be calculated through equation II.18. For circular waveguide, separate equations exist to calculate the cut-off frequency for a TE and for a TM mode. For TE modes:

$$\omega_{co} = \frac{c\chi'_{nm}}{r_0} \tag{II.45}$$

where χ'_{mn} is the derivative of the Bessel root of the first kind of order nm.

Meanwhile, for TM modes,

$$\omega_{co} = \frac{c\chi_{nm}}{r_0} \tag{II.46}$$

where χ_{mn} is the Bessel root of the first kind of order nm.

II.4 Waves in Dielectric Media

While the above equations all hold for a plane electromagnetic wave travelling in space, it is sometimes necessary for dielectric media to be used. Situations where this may arise are in slow wave structures, where a waveguide may be lined with a dielectric media to induce slow space-charge waves; in RF windows, where both RF transmission and vacuum integrity are of high import and, in the case examined within this work, to use the dielectric's propagation properties as an aid in coupling structures.

Electromagnetic propagation within a dielectric is almost identical to that within free space with the exception that the material has an associated dielectric constant, ε_r. Thus, if we take the speed of propagation in free space to be

$$c = \frac{1}{\sqrt{\mu_0 \varepsilon_0}} \tag{II.47}$$

then, in a dielectric

$$c = \frac{1}{\sqrt{\mu \epsilon}} \tag{II.48}$$

where $\mu = \mu_0 \mu_r$ and $\varepsilon = \varepsilon_0 \varepsilon_r$.

From equations II.19, II.46 and II.48 we may ascertain that if a material of high ε_r is used in place of free space, the effective cut-off frequency in a waveguide increases in proportion to the square root of the dielectric constant (i.e. $\omega_{co} \propto \sqrt{\mu\varepsilon}$).

While losses within a dielectric may be negligible in the case of DC fields, for AC currents there arises the issue of dielectric hysteresis. If the permittivity is written as

$$\varepsilon = \varepsilon' + \varepsilon'' \tag{II.49}$$

where ε' and ε'' reflect the real and imaginary components of the permittivity and both are dependent on frequency, Maxwell's equation for faraday's law is rewritten as

$$\boldsymbol{\nabla} \times \boldsymbol{H} = j\omega\varepsilon'\boldsymbol{E} + (\sigma + \omega\varepsilon'')\boldsymbol{E} \tag{II.50}$$

where σ is the conductivity. If ε' reflects the real, lossless, component of the dielectric permittivity and ε'' reflects the losses due to bound charge and dipole relaxation, the loss tangent may be given as the ratio of the two [129],

$$tan\delta = \frac{\omega\varepsilon'' + \sigma}{\omega\varepsilon'} \tag{II.51}$$

Appendix III:

Pseudospark Risk Assessment

SPECIFIC PROJECT RISK ASSESSMENT FORM

Section A

Department Physics

Project/Works Title **Controlled lab area 1 – millimetre wave source**

Description of Work Activity A pulsed power supply driving a thermionic cathode is used to accelerate electrons from the cathode of an electron gun producing a beam of 40kV and 2A travelling in a high vacuum environment. The beam interacts with a high magnetic field from a DC solenoid to produce short pulses of microwave radiation. The expended electrons are allowed to impact on the walls of the vacuum chamber.

Section B

Description of significant hazards: (eg slipping/tripping; fire; work at height; pressure systems; electricity; dust; fumes; manual handling; noise; poor lighting; low temperatures; vehicles; moving parts of machinery

There are several hazards relating to electromagnetic safety: Firstly and at the highest frequency are X-rays, then there is the microwave output from the experiment and lastly the low frequencies of the pulsed and DC power supplies.

High pressure and vacuum chambers/pumps are used giving rise to pressure vessel issues.

Tripping and slipping can be an issue.

A hazard exists from the use of lead X-ray shields

Section C

Groups who may be at risk: Staff/Students with Special Needs ❒ Inexperienced Staff ❒

Academic Staff X❒ Office Staff ❒ Maintenance Staff ❒ Technicians X❒

Postgraduates X❒ Undergraduates ❒ Lone Workers ❒ Contractors ❒

Visitors ❒ Members of Public X❒ Other ❒ Specify _____

Section D

Assess the foreseeable risks from the hazards identified and state the controls to be implemented to eliminate or minimise the risk where it is reasonably practicable to do so.

Give priority to those risks which affect large numbers of people and/or could result in serious harm. Apply the following principles, if possible, in the following order:

- ✓ **Remove the risk completely**
- ✓ **Try a less risky option**
- ✓ **Prevent access to hazard (eg guarding)**
- ✓ **Organise work to reduce exposure to hazard**
- ✓ **Issue personal protective equipment**
- ✓ **Provide welfare facilities (eg washing facilities for removal of contamination)**

This section should be used to specify the scheme of work which should include details of the significant controls, safety procedures and working methods which need to be adhered to. It should also refer to existing safety procedures, eg already contained in the departmental safety regulations or University local rules. The following should also be considered in the risk assessment process:

Do the control measures - meet the standards set by the legal requirements?
- comply with a recognised industry standard?
- represent good practice?
- reduce risk as far as reasonably practicable?

Risk Analysis for controlled lab area 1– W-band microwave source
This analysis is submitted to the records to describe the assessment of the risks
involved in the thermionic cathode pulsed vacuum diode with respect to incidental
X-Ray production, low and intermediate frequency electromagnetic safety issues,
vacuum and gas pressure concerns. Where action has been deemed necessary,
the appropriate provisions are described.

X-Ray shielding for controlled laboratory area 1, W-band microwave source

At legally required levels (indeed even at levels somewhat above this) the probability of undesirable effects is low. However since the consequences may be severe, in order to ensure meeting the legal requirements with this experiment it is necessary to consider X-ray shielding.

The X-ray's are produced incidentally in the experiments in Vacuum Electronics when the electron beam impacts with the collector surface (usually the anode) as a result of decelerating bremstrahlung interactions between the electrons and the atoms forming the crystal lattice of the collector.

The rate of radiation production may be estimated using formula 1, used in the Atoms, Beams and Plasma's (ABP) group and as approved by the radiation safety office for estimating of X-Ray flux rate at a given distance D from the source, assuming that the radiation is distributed evenly over a sphere. To obtain a daily dose this is multiplied by the pulse duration of the diode voltage signal and the planned no. of pulses per day. This is then compared to the allowed daily dose rate calculated by dividing the annual limit of 1mSv by a working year based on 5 days by 52 weeks (converted to rads on the basis of 1Sv=100Rads). This gives the amount of shielding required and the thickness of lead based on an 10-folding length (this is only an approximation as the actual curves are not quite exponential, and are checked to determine the amount of shielding required), data from the publication "Handbook of radiological protection, Part 1, Data", HM Stationary Office 1971. A mechanical counting device allows the number of pulses per day to be recorded.

$$\text{Dose(rads per s)} = 5000\left(\frac{VIZ}{D_{mm}{}^{2}\,x74}\right)\left[\frac{RAD}{SEC}\right]$$

Where

V is the accelerating potential (in Volts)
I is the current (in Amps)
Z is the atomic number of the collector material
D is the range to the personnel (in mm)

The formula used to obtain the following **estimation of radiation dose levels** and **required shielding** were performed in the **units of Rads**. This is to **facilitate comparison with the exposure charts published in the handbook of radiological protection (part 2)**, Data issued by the NRPB. These charts are given in units of Roentgen/mA per unit time. The Roentgen is a measure of X-ray energy that is the product of power contained in the beam and time of exposure – defined as the total number of charge pairs produced in 1 cc of air under standard conditions i.e. at 760mm Hg ambient pressure and 0 degrees C). All radiation calculations were carried out in Radiation Absorbed Dose (RADS) which were then converted to Sieverts. The Rad defines the amount of radiation actually absorbed by a medium, one rad means that 0.01 joule of energy is absorbed by 1 kg of material.

We assume for the purpose of calculating the required shielding that all the X-rays are produced at the peak voltage of the experiment (40kV in this case). As a typical electron will undergo multiple bremstrahlung interactions during its deceleration, this is an overestimate of the shielding required. Furthermore we assume the voltage is constant over the pulse duration (0.4μs), and a constant current of 2A. So we base the calculation on 40kV and 2A for 100 pulses each day of 0.4μs duration. Lastly we assume the electrons impact onto a copper collector as the highest Z component of the vacuum chamber. There are two zones of "closest approach" for people which are considered 1) the front, back and side and 2) the up and the down direction. For all directions front, back, sides, up and down the minimum distance of "closest approach" (Room 2.03 floor to roof height 5m, Room 1.03 basement floor to roof height 3.7m) to the experiments is taken to be 1.5m. The requirements for their protection to 1mSv/annum are worked out in sheet 1. The hazards associated with operation of controlled laboratory area 2 – thermionic cathode pulsed vacuum diode system has been assessed. The shielding factor required by the Radiation Protection Service was set at an attenuation 2717. The shielding would either be provided by 44cm thick concrete or 7mm thick lead walls surrounding each experimental area.

Low Frequency Electromagnetic Safety issues
These hazards apply only to staff and students working in the laboratory. Precautions are required because of the consequences of an error/fault could be lethal.

The experiments use high voltage pulses of amplitude up to 40kV and current of up to 2A. To generate these pulses a DC power supply with a capacity for 100kV and 40mA will be used to charge a pulsed transformer. This pulsed power supply will be switched by a spark-gap giving a high voltage output pulse.

In addition to these items there are conventional CW solenoids which generate magnetic fields not exceeding 2.1T.

Basic safety concerns are:

(a) Failure of HV pulsed. The pulsed transformer is enclosed in a physical barrier in the form of a 44cm concrete wall and a 7mm lead roof, door and a 7mm lead floor encased in a 50mm concrete screed also surrounds the experimental area.
(b) Danger of high magnetic fields: The magnetic field is quite high at 2.1T and operated DC. Efforts have been made use non-magnetic metals where possible in the construction of the experiment. However, care is required to prevent items of ferrous construction being placed too near the magnets.
(c) Danger due to the high power DC electrical power supplies charging the pulsed high voltage storage units and driving the magnet coils, and danger posed by the energy stored in the magnet coils must be taken into consideration. A pneumatic high voltage switch is provided to short out the HV power supplies and its charging line to ground remotely through suitable resistors. This switch is controlled by a safety device which provides a clear visual indication of the state of the switch (or switches, there can be up to three depending on how many independent HV circuits are in use) and an audible warning when changing state. The safety locking box can also induce an automatic shutdown of the DC power supplies. The locking box monitors the condition of the access door to the experimental area and will shut the experiment down in the event that the door is

opened. A lockout switch is provided inside each experimental area which may be pressed by any member of staff working in the area to prevent the inadvertent arming of the system. All visual indicators are provided by gas-discharge technology for proven longevity and reliability. Earthing sticks capable of dealing with the full energy of the pulsed HV power supplies are provided at the entrance of the experimental area and are used by the researchers to ensure the circuit is properly earthed.

The researchers are fully aware that the automated safety locking box must be subject to frequent tests and they must be vigilant to observe any faults which might occur. They are also aware that the locking box is provided as a last resort safety net in the event that all else fails and that care and vigilance by the staff to the safe operation of the experiment is paramount.

Pressure systems (a), (b), and (c)

(a) Gas
The experiments require the use of substantial quantities of gas. These gases are supplied by BoC in suitable containers and appropriate regulators (changed are regular intervals as specified) which are used to control the output pressure. The gas cylinders are secured to a wall in Col 1.03 with chains and brackets. The gas is plumbed to each experimental area using pressure tested piping. Provided the cylinders are handled properly there is little risk associated with this activity.

(b) Water System
The DC driven coils are cooled by the use of a recirculating water cooled heat exchanger system located in Col 1.03. The maximum pressure of the water system in experimental lab area 1 is 4Bar. Issues can occur if there is a failure of the high pressure water system leading to a hot water jet escaping into the lab. This can occur either due to failure of the nylon connectors or boiling of the water in the solenoid if it becomes blocked. The water is subject to frequent filtration. Failure of the water system is most likely when the coil is energised. Experimenters cannot gain access to these areas at these times. The water pump may be stopped from a position remote from the experiment. Normally the water does not exceed 65^0C. Interlocking systems disable the power supplies heating the water in the event of the water temperature in the outlet being too high or a water flow fault.

(c) Vacuum pumps
The vacuum required for the experiments are maintained by a scroll backing a turbomolecular pump with an ion pump. The fluid pumped is primarily air or nitrogen. The exhaust gases are filtered.

The microwave power levels
The microwave radiation generated can have a power of up to 10kW. The pulse duration is however 400ns and with a maximum number of pulses per day of 100, the average power output of the experiment is therefore of the order of 4 mJoules/pulse or 400mJ per day. The nearest people are the experimenters at >1.5m away and behind a lead wall. This average exposure is less than one might expect of a mobile phone.

Tripping
The need to provide the range of other safety measures listed above means that trip hazards unavoidably exist however these have been minimised by feeding all service lines in at the back of each experimental area via no-line of sight access holes at the back of each laboratory area. The service corridor at the back of each experimental area is closed off with each door tripping the interlock system if opened while an experiment is operating. The areas around the experiment are not thoroughfares and efforts are made to minimise the number of trip hazards associated with each experiment. This affects the people in the lab area, who are all aware of the issue and the need to take care when working in the areas concerned.

Moving of Lead Roof
Panels can only be moved by Dr. C.G. Whyte, Dr. K. Ronald, Dr. W. He, Dr. A.W. Cross, Dr. C.W. Robertson, Dr. I.V. Konoplev, Dr. D.C. Speirs, Dr. H. Yin, Dr. P MacInnes, Dr. S. McConville and Dr. C.R. Donaldson (who have all been trained in how to move the panels) and one other experimenter. Before commencing with the moving of roof panels each person present must read the Risk Assessment that has been prepared for the moving of the lead roof.

Sheet 1 - Controlled lab area 2-Cold Cathode Pulsed Vacuum diode

Define Here the Beam Voltage (V in Volts), Current (A in Amps), Target Atomic Number (Z), Pulse Duration (T in seconds), The Number of Pulses Per Day (P) the Maximum Allowed Radiation Dose (M in mSv), the Range to the personnel (R in m) and the Tenth Value Length of lead/concrete for the peak energy (mm). Note the TVL approach is only an approximation, as only thick shields really exhibit e-folding behaviour. See published graphs

```
> V:=40E3; A:=2; Z:=29; T:=400E-9; P:=100;
R:=1.5; M:=1; TVL:=0.23; TVC:=13.5;
```

$$V := 40000.$$

$$A := 2$$

$$Z := 29$$

$$T := 4.00\,10^{-7}$$

$$P := 100$$

$$R := 1.5$$

$$M := 1$$

$$TVL := 0.23$$

$$TVC := 13.5$$

Calculate the peak dose rate in Rads/sec using our usual formula

```
> PEAKDOSE:=5000*V*A*Z/(((R*1000)^2)*74);
```

$$PEAKDOSE := 69.66966960$$

Convert the Annual dose limit in mSv to Rads (1Sv=100Rads) and divide by days in the year

```
> ALLOWEDDAILY:=M*100/(52*5*1000);
```

$$ALLOWEDDAILY := \frac{1}{2600}$$

Calculate the daily peak dose based on the peak dose rate, the duration of each pulse and the number of pulses per day

```
> DAILY:=PEAKDOSE*T*P;
```

$$DAILY := 0.002786786780$$

Calculate how much attenuation is required over and above the D-squared term to obtain the required dose rate

```
> SHIELD:=DAILY/ALLOWEDDAILY;
```

$$SHIELD := 7.245645648$$

Estimate the thickness of shield required based on the Tenth Value Length provided (this is crude as lead does better than exponential

initially, therefore see real graphs from the Handbook of Radiological Protection, Part 1, Data. HM Stationary Office, 1971

```
> LEADTHICKNESS:=TVL*log[10](SHIELD);
CONCRETETHICKNESS:=TVC*log[10](SHIELD);
```

$$LEADTHICKNESS := 0.197817730$$

$$CONCRETETHICKNESS := 11.6110407$$

Reciprocal of shield (it is easier to read this on the graphs)

```
> TRANS:=1/SHIELD;
```

$$TRANS := 0.138013925$$

Section E

Accreditation

Assessor:	Kevin Ronald (Dr.)	
Signature	Print	Date
Radiation Protection Supervisor:	Adrian W. Cross (Prof.)	
Signature	Print	Date

Signature of all persons receiving a copy of this risk assessment.

Signature	Print	Date
Signature	Print	Date
Signature	Print	Date
Signature	Print	Date
Signature	Print	Date
Signature	Print	Date
Signature	Print	Date

Date of next assessment(s)

1. 1/06/2010 2. _____ 3. _____

Note:

1. **The completed risk assessment form must be kept by the assessor and supervisor with a copy given to Departmental Safety Convener.**
2. **The assessment must be reviewed and where appropriate revised if there is reason to suspect it is no longer valid or there has been a significant change to the task procedure.**
3. **The responsibility for ensuring that the risk assessment is suitable and sufficient lies with the Supervisor <u>not</u> with the Departmental Safety Convener.**
4. **A copy of this assessment must be retained by the Department for as long as is relevant (in case of the form being used as a COSHH risk assessment this must be kept for 30 years and in some cases 40 years after the project or works are terminated).**

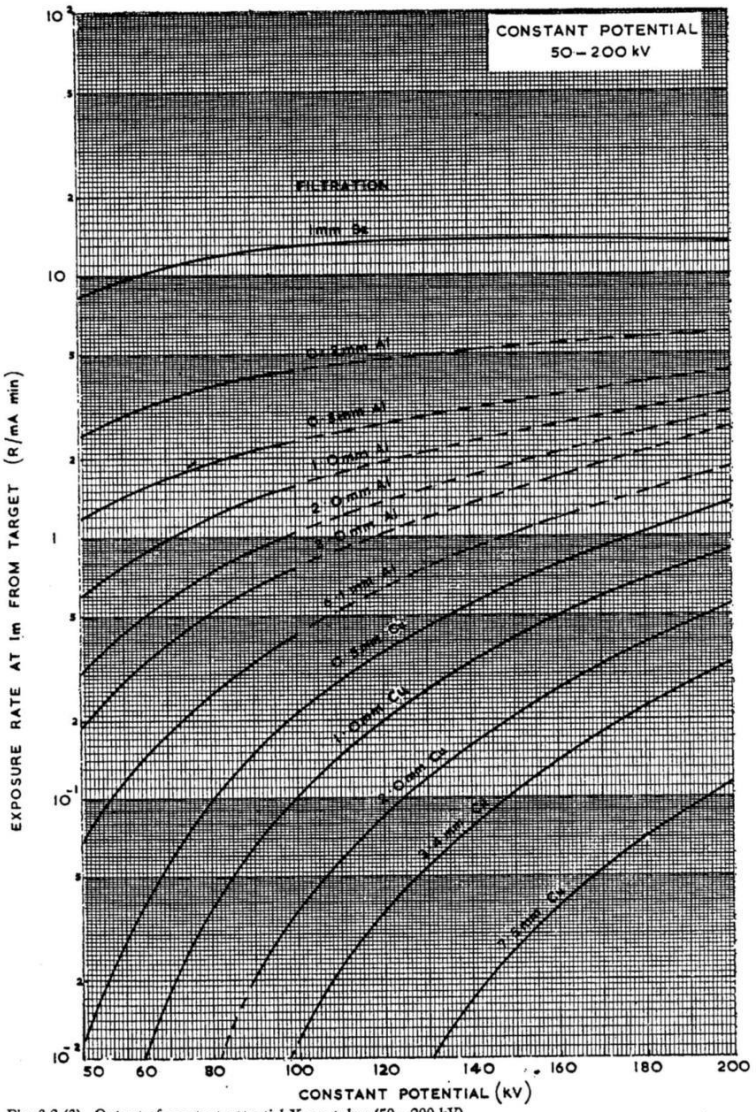

Fig. 3.2 (3). Output of constant potential X-ray tubes (50 – 200 kV).
For half-wave generators, the output is about $\frac{1}{3}$ to $\frac{1}{4}$ of that plotted.

Fig. 4.3
(7)

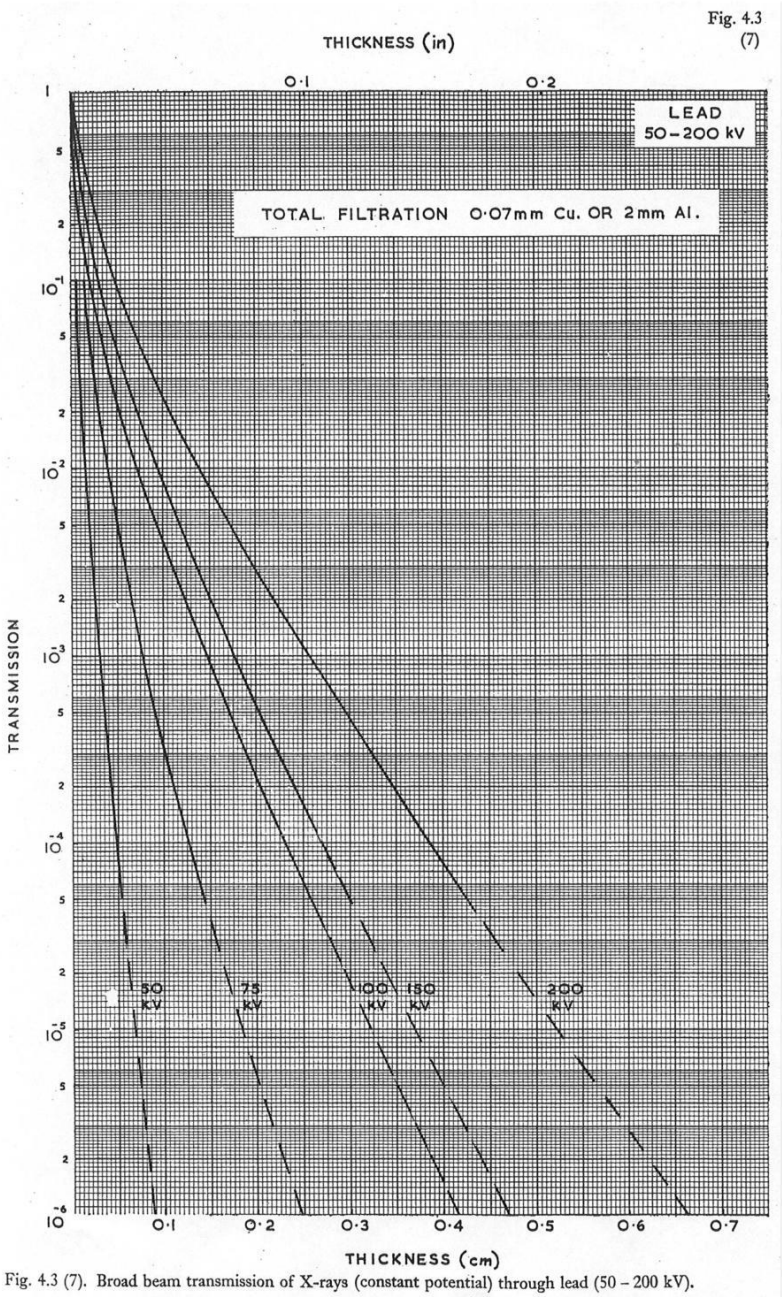

Fig. 4.3 (7). Broad beam transmission of X-rays (constant potential) through lead (50 – 200 kV).

RP—F

Fig. 4.3
(1)

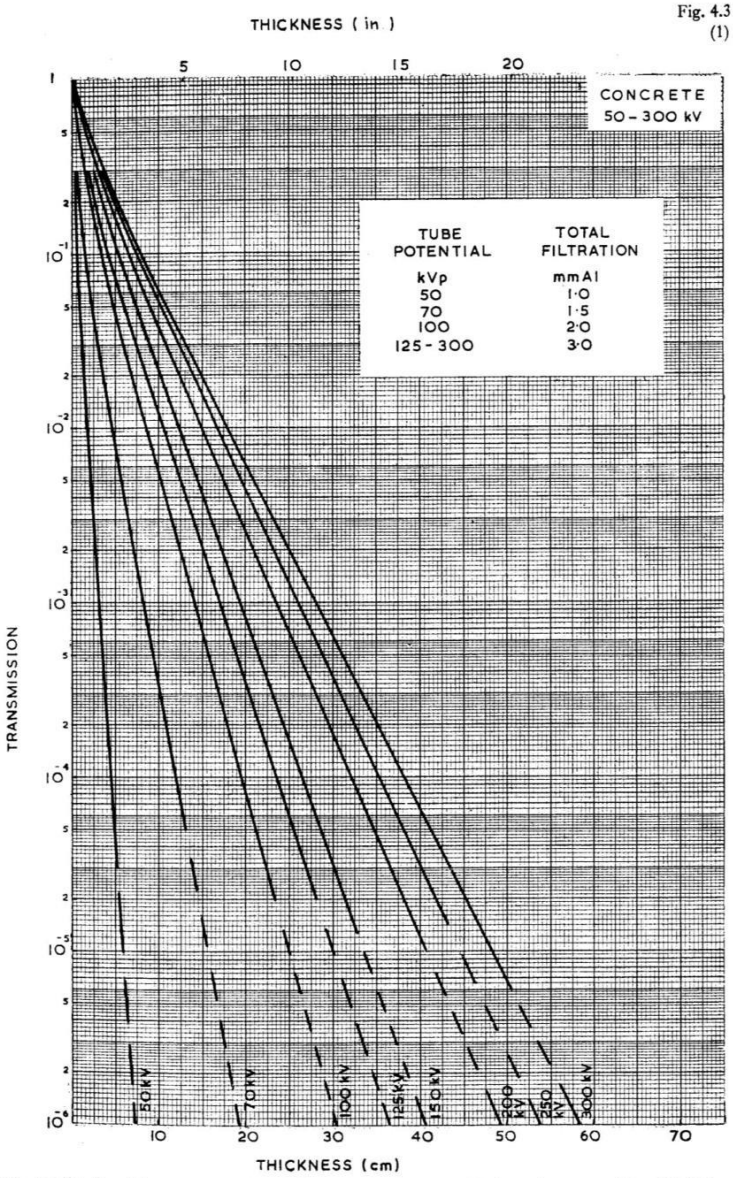

Fig. 4.3 (1). Broad beam transmission of X-rays (pulsating potential) through concrete (50 – 300 kV). These curves may also be used for constant potential, if necessary.

Table 4.8 (1) shows half-value and tenth-value thicknesses for heavily filtered X-radiation under broad beam conditions. The values are taken from the exponential parts of the transmission curves in Section 4.3. Table 4.8 (2) shows similar figures for gamma radiation and bremsstrahlung from a number of nuclides and, in this case, values are taken wherever possible from the exponential sections of the curves in Section 4.4. In a few cases, marked 'Approximate', the results are taken from parts of the curve which are not linear on the semilogarithmic plot.

TABLE 4.8 (1): Half-Value Thicknesses and Tenth-Value Thicknesses for Heavily Filtered X-radiation (Broad Beam Conditions)

Source	*Half-Value Thickness*			*Tenth-Value Thickness*		
	Lead (*mm*)	*Concrete* (*mm*)	(*in*)	*Lead* (*mm*)	*Concrete* (*mm*)	(*in*)
50 kVp	0·07	8·8	0·15	0·23	13·5	0·53
50 kVcp	0·06			0·20		
70 kVp		10·2	0·4		35·6	1·40
75 kVp	0·17			0·58		
75 kVcp	0·19			0·63		
100 kVp	0·26	16·5	0·65	0·87	54·2	2·17
100 kVcp	0·30			0·95		
125 kVp	0·29	19·1	0·75	0·96	64	2·52
150 kVp	0·30	21·8	0·85	1·00	69·9	2·75
150 kVcp	0·32			1·04		
200 kVp	0·43	25·9	1·02	1·42	85·5	3·37
200 kVcp	0·43			1·42		
250 kVp	0·9	27·7	1·09	3·0	90·4	3·56
250 kVcp	0·98			3·18		
300 kVp	1·48	30·2	1·2	4·90	102	4·0
300 kVcp	1·33	28·7	1·13	4·4	94·5	3·72
400 kVcp	2·47	29·7	1·17	8·25	99·8	3·93
0·5 MV	3·1	35·6	1·4	10·3	119	4·7
1·0 MV	7·6	45·7	1·8	25·2	150	5·9
2·0 MV	11·5	61	2·4	39·0	200	7·9
3·0 MV		68·6	2·7		226	8·9
4·0 MV		83·8	3·3		274	10·8
6·0 MV		102	4·0		338	13·3
10 MV		117	4·6		386	15·2
20 MV		137	5·4		457	18·0
30 MV		137	5·4		457	18·0
38 MV		137	5·4		457	18·0

Appendix IV:

Publications

Millimeter wave generation from a pseudospark-sourced electron beam

H. Yin, A. W. Cross, W. He, A. D. R. Phelps, K. Ronald, D. Bowes, and C. W. Robertson
Department of Physics, Scottish Universities Physics Alliance, University of Strathclyde, Glasgow G4 0NG, United Kingdom

(Received 14 January 2009; accepted 27 May 2009; published online 23 June 2009)

Experimental studies of the production and propagation of an electron beam from a multigap pseudospark discharge are presented. From a three-gap pseudospark, a beam up to 680 A was measured at the anode at an applied dc voltage of 23 kV. This beam can propagate downstream as far as 20 cm in a gaseous environment with no guiding magnetic field, which confirms that the transport of the electron beam was based on the neutralization of the space charge of the electron beam due to the ionization of the gas molecules by the beam itself. The beam is of very small size of 1–3 mm in diameter and is ideal to drive high frequency radiation. Higher energy electron beam pulses were generated using a 14-gap pseudospark discharge powered by a cable pulser capable of producing 120 ns duration and 170 kV voltage pulses. The beam measured had a current of up to 110 A. Interactions between the produced beam and a Ka-band Cherenkov maser and a W-band backward wave oscillator slow wave structure were simulated and designed. Millimeter wave pulses were detected from the Cherenkov maser and backward wave oscillator beam-wave interaction experiments. © *2009 American Institute of Physics*. [DOI: 10.1063/1.3155444]

I. INTRODUCTION

In recent years pseudospark discharges[1–6] attracted significant attention from diverse fields such as pulsed-power switching, electron and ion beam generation, free electron masers, extreme-ultraviolet radiation sources, and microthrusters due to their unusual and interesting discharge properties. A pseudospark is an axially symmetric, self-sustained, transient, low pressure (typically 50–500 mTorr) gas discharge in a hollow cathode/planar anode configuration, which operates on the low pressure side of the hollow-cathode analogy to the Paschen curve. A potentially useful property of this type of discharge is the formation of an electron beam during the breakdown process.[7,8] During a pseudospark discharge, low temperature plasma is formed as a copious source of electrons and ions and can be regarded as a low work function surface that facilitates electron or ion extraction by applying voltages of different polarities.

Pseudospark discharge experiments previously carried out in this laboratory consisted of electron beam generation from a single-gap pseudospark system, which was adjusted over a wide range of parameters, including cathode cavity length, cathode hole size, applied voltage, external capacitance, and the inductance in the discharge circuit.[9] In this paper, (i) electron beam experiments using a three-gap pseudospark discharge are presented in Sec. II and (ii) Cherenkov maser and backward wave oscillator (BWO) beam-wave interaction experiments from a 14-gap pseudospark discharge are compared with the simulations in Sec. III. Finally conclusions are drawn in Sec. IV.

II. ELECTRON BEAM EXPERIMENTS WITH A THREE-GAP PSEUDOSPARK

The three-gap pseudospark electron beam experiments were conducted using the experimental setup as shown in Fig. 1. The hollow cathode was connected to the dc power supply (30 kV, 1 mA) through a 30 MΩ charging resistor. The anode was grounded. There was no external applied guide magnetic field.

The charging voltage was measured using a capacitive voltage probe. Measurements of the beam current were realized using two Rogowski belts, one located at the anode and a second movable belt further downstream. A Faraday cup in series with 0.33 Ω impedance was also put into the drift tube to measure the beam current. A fine tungsten mesh of vacant area divided by total area of 90% was inserted before the Faraday cup to exclude the plasma from entering it. Another Rogowski coil was connected to the discharge circuit to measure the discharge current. The external energy storage capacitance was 600 pF.

The typical temporal evolution of the beam produced is shown in Fig. 2. With an applied voltage of 23 kV, the peak discharge current was 950 A, while the peak beam current measured by the first Rogowski belt was 680 A and the peak beam current recorded by the Faraday cup was 340 A. This means about 50% of the beam reached the Faraday cup. The loss of the beam is due to the collisions between the beam electrons and the background gas molecules during the beam propagation from the anode to the Faraday cup and 10% of the Faraday cup is obscured by the tungsten mesh. With no tungsten mesh, the measurement of the Faraday cup would be about 80% of the beam measurement from the first Rogowski belt at the anode. For example, when the current measured by the first Rogowski belt was 560 A, the current measured by the Faraday cup was 480 A.

The cross-sectional image of the electron beam was obtained by inserting a scintillator disk (1 μm thickness copper foil coated with scintillation powder) after the first Rogowski belt and taking a picture with a high-speed digital camera located at the end of the drift tube. Figure 3 is a single-shot image of the electron beam at an applied voltage of 23 kV. The electron beam diameter represented by a central bright spot was around 1 mm in a drift tube of diameter

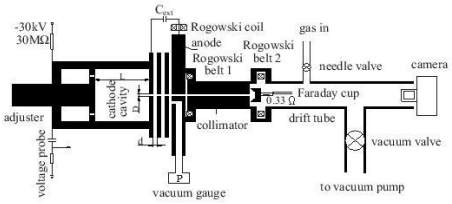

FIG. 1. Three-gap pseudospark electron beam experimental setup.

22.5 mm (represented by the fine circle). Figure 4 is a three-shot image of the electron beam at the same applied voltage of 23 kV. The electron beam moves around from shot to shot and as a consequence the diameter of the central spot is about the same as that of the anode aperture (3 mm), which is broader than the beam. The bright specks are caused by the scintillation disk holder. From Fig. 4, it can be seen that it is a very bright beam surrounded by a distributed bright circle (the outer circular glow of diameter 22.5 mm in Fig. 4). The occurrence of the circular glow confirms the formation of an ion channel.[10,11] At the start of the pseudospark discharge the initial high-energy electrons ionize the background gas to form a plasma channel. When the electron beam subsequently generated by the pseudospark discharge is then injected into the plasma channel, the space charge of the beam expels the channel plasma electrons while the much more massive ions remain relatively fixed. The expelled plasma electrons strike the scintillation disk and drift tube resulting in a bright outer circle. The resulting positive ion channel acts to focus and guide the pseudospark electron beam. This

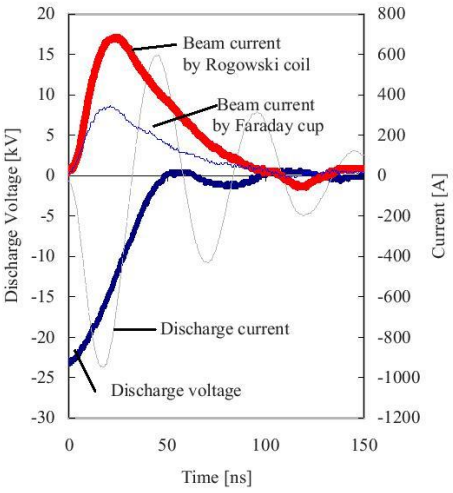

FIG. 2. (Color online) Temporal evolution of the beam produced from a three-gap pseudospark discharge chamber.

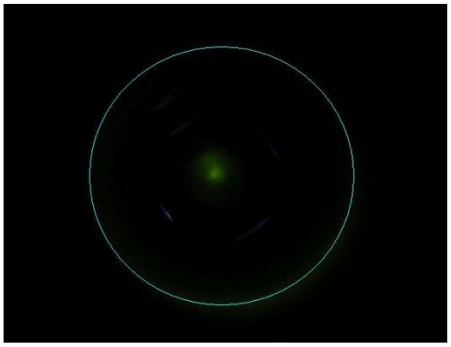

FIG. 3. (Color online) Image of electron beam imprint on phosphor scintillator for a single pulse. The electron beam diameter (represented by the central bright spot) was around 1 mm.

agrees with the simulation in Ref. 12, which implies that a favorable ion background exists along the beam channel. The brightness of the electron beam was measured again using a magnetic-field-free collimator technique.[12,13] The collimator length was 5 cm with an axial aperture 3.5 mm in diameter. A time dependent beam brightness of up to 10^{11-12} A m^{-2} rad^{-2} was measured. This beam has higher combined current density ($>10^4$ A cm^{-2}) and brightness (up to 10^{12} A m^{-2} rad^{-2}) than any other type of electron source, including thermionic, explosive emission, field emission, and photocathodes.

The dependence of the discharge current and electron beam current on the hollow cathode cavity length L was studied. It was found that when L was less than 3 mm, which was equal to the cathode aperture diameter D, the beam current was small while the discharge current was high. Both the discharge and beam current were insensitive to L when it

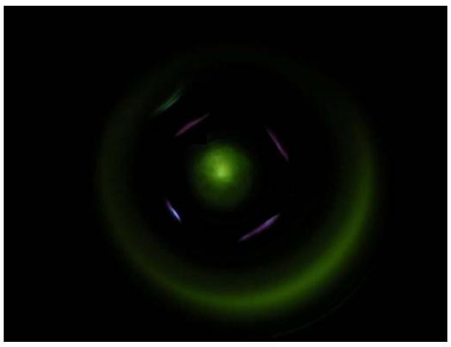

FIG. 4. (Color online) Image of electron beam imprint on phosphor scintillator integrated over three pulses. Note that the central spot is broader than the electron beam.

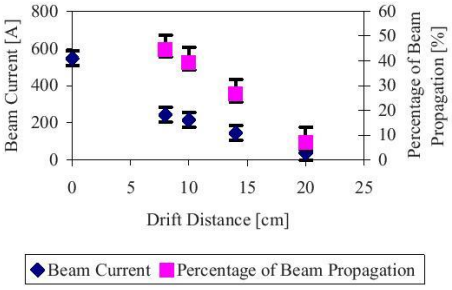

FIG. 5. (Color online) Electron beam current and its propagation percentage along the axis after the anode.

was larger than 3 mm. At the extreme situation when L was close to 0 mm, i.e., no hollow cathode region, both the discharge and beam current were small. The pseudospark configuration, which produced the best beam current pulse, was when the cathode aperture diameter D (3 mm) was equal to the gap separation d (3 mm) with L (30 mm) approximately a factor of 10 greater than D. The dependence of the electron beam current on the axial distance from the anode was investigated using the beam measurements from two Rogowski belts, one at the cathode and the other which could be moved downstream along the axis. It was found that even though there was no guiding magnetic field, about 10% of the beam propagated as far as 20 cm from the anode, as shown in Fig. 5. These currents were measured with the second Rogowski belt with the Faraday cup removed. The beam loss was due to the collisions between the beam electrons and gas molecules.[14–16] For the experiment at an operating pressure of 60 mTorr, the molecular number density was $\sim 10^{20}$ cm^{-3}. For a molecule size of ~0.3 nm, the mean free path for an electron in this environment was calculated to be about 1.3 cm, which supports the argument that the beam was attenuated due to the collisions.

III. MILLIMETER WAVE GENERATION EXPERIMENTS WITH A 14-GAP PSEUDOSPARK

From the electron beam experiments with the three-gap pseudospark, it can be seen that the beam can propagate downstream as far as 20 cm in a gaseous environment even though there was no guiding magnetic field. The beam is of very small size, 1–3 mm in diameter, which makes it ideal to drive high frequency radiation sources. In order to generate high power, high frequency radiation, a higher energy beam is needed. In our experiment higher energy electron beam pulses were generated using a 14-gap pseudospark discharge powered by a cable pulser capable of producing 120 ns duration and 170 kV voltage pulses. The beam-wave interaction experiments were conducted using the 14-gap pseudospark discharge as shown in Fig. 6. The cable pulser was based on the principle of addition of the output voltages from two Blumlein circuits made from high voltage cables. It can produce a nominal four times multiple of its charging voltage

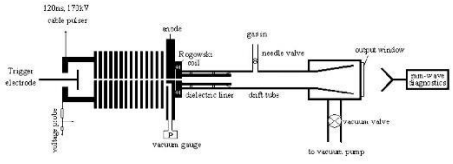

FIG. 6. Beam-wave interaction experimental setup using a 14-gap pseudospark. The dielectric liner in the interaction region for the Cherenkov maser experiments was replaced by a corrugated waveguide for the BWO experiments.

from a dc power supply when the load impedance is much larger than its characteristic impedance of 200 Ω. The pseudospark discharge was initiated by the application of a 20 kV pretrigger pulse to the hollow cathode region of the pseudospark chamber. Careful adjustment of two delay units ensured that the initiation of the pseudospark discharge was followed by the generation of the voltage pulse by the cable pulser with both being time correlated producing an electron beam.

In the beam-wave interaction region, a Cherenkov maser slow wave structure and a copper BWO slow wave structure were used for the beam-wave interaction experiments. The Cherenkov maser slow wave structure was made of a section of cylindrical waveguide, 9.5 mm in diameter and 10 cm in length, lined with a 1.75 mm thick layer of dielectric (alumina, ε_r=9.5). The dielectric liner was used to slow down the normal electromagnetic modes in the cylindrical waveguide. The BWO interaction region was made of a corrugated copper structure of mean radius of 3.75 mm, length of 24.5 mm, period of 1.75 mm, and depth of 0.375 mm. The structure was manufactured by machining a positive aluminum former and chemically depositing a 3 mm thick layer of copper on the aluminum former, which was later dissolved away in an alkali solution. The millimeter wave launching horn was located just downstream of the interaction region.

A. Cherenkov maser interaction results compared with simulations

Interaction between the electron beam and a Cherenkov maser slow wave structure was studied. The electromagnetic wave frequency versus axial wave number dispersion diagram for the Cherenkov maser in the TM_{01} mode was calculated using analytical theory (broken line) as well as simulated using the particle-in-cell code MAGIC (squares), and is shown in Fig. 7. They are in very good agreement. The electron beam dispersion relation for the beam of current 25 A and voltage 60 kV was also calculated using MAGIC and plotted in Fig. 7. Bunching of the electrons and coherent energy exchange between the beam electrons and the wave can only occur when the beam and the wave dispersions intersect. The MAGIC simulations show that the interaction between the TM_{01} mode and a 25 A, 60 kV electron beam can be expected around 25 GHz.

The experimental setup of the Cherenkov maser is shown in Fig. 6 and a 14-gap pseudospark discharge cham-

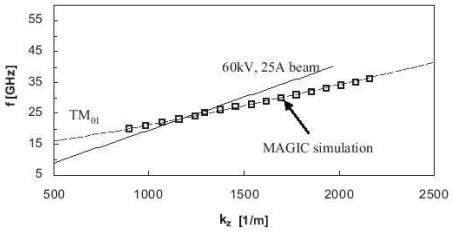

FIG. 7. Dispersion diagrams of the Cherenkov maser with the beam line (60 kV, 25 A) interacting with the TM_{01} mode.

ber was used in the experiment for the electron beam generation. Figure 8 shows the time-correlated electron beam pulse, the applied voltage pulse, and millimeter wave pulse measured using a Ka-band detection system, which had a cutoff frequency of 21 GHz. Millimeter wave pulses above 21 GHz frequency were detected from the Cherenkov maser beam-wave interaction powered by this 14-gap pseudospark-sourced electron beam.

B. BWO interaction results compared with simulations

Figure 9 shows the dispersion relations of the TM_{01} mode and its first spatial harmonic in a waveguide with a small, but nonvanishing, corrugation amplitude, the operating TM_{01} eigenmode in the BWO slow wave structure, and the dispersion of the beam. The waveguide mode (hyperbolic curves) was calculated using analytical theory and the operating TM_{01} eigenmode (circles) was calculated using MAGIC along with the linear beam dispersion line for an electron beam of energy of 100 keV and current of 25 A. The beam line intersects the operating eigenmode dispersion relation at about 70 GHz. The coupling factor between the TM_{01} mode

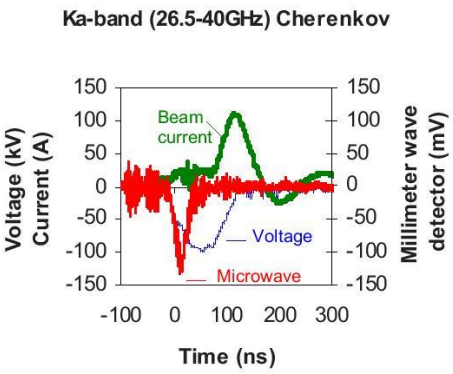

FIG. 8. (Color online) Time-correlated electron beam current pulse, the applied voltage pulse, and millimeter wave pulse (using a Ka band detector) from the Cherenkov maser.

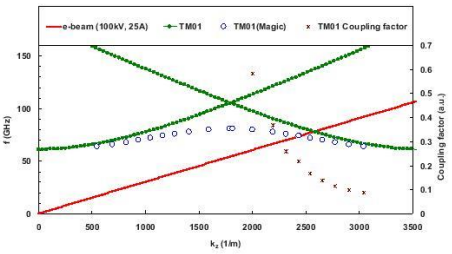

FIG. 9. (Color online) Dispersion diagrams of the BWO structure where * is the simulated coupling factor between the TM_{01} mode and its first spatial harmonic

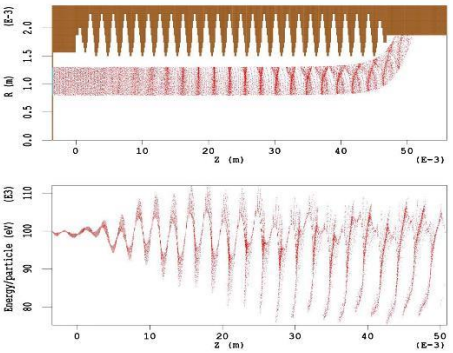

FIG. 10. (Color online) MAGIC simulation of the electron trajectories when interacting with the corrugated backward traveling wave structure (top, solid color) with the beam electron bunches (top lower) and beam electron energy (bottom).

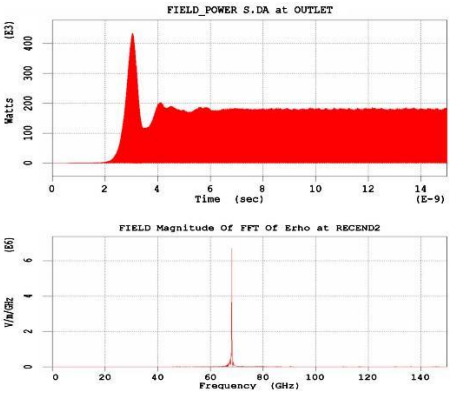

FIG. 11. (Color online) Predicted millimeter wave output power (top) and frequency (bottom) from the BWO.

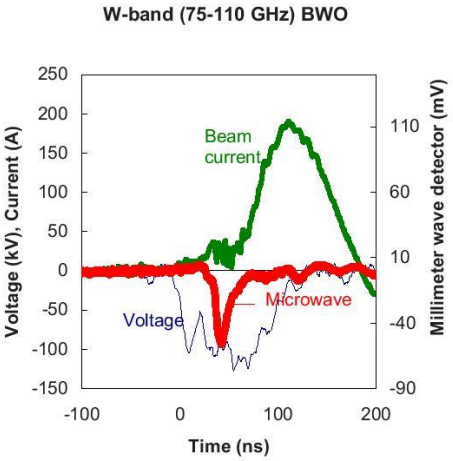

FIG. 12. (Color online) Time-correlated electron beam pulse, the applied voltage pulse, and millimeter wave pulse from the BWO (using a W-band detection system).

and its first spatial harmonic was also calculated using MAGIC and shown in Fig. 9 (*). The larger the coupling factor, the stronger the resulting beam-wave interaction.

The electron trajectories when interacting with the backward traveling wave were simulated using MAGIC (Fig. 10). The predicted millimeter wave output power and frequency (67 GHz, in good agreement with the calculation) from the BWO are shown in Fig. 11. Millimeter wave pulses were measured using a W-band detection system (cutoff frequency of 59 GHz) with Fig. 12 showing the time-correlated electron beam pulse, millimeter wave pulse, and the applied voltage pulse.

It can be seen for both the Cherenkov maser and the BWO the electron beam had a first step hollow cathode current of 25 A, followed by a conductive phase beam of current over 100 A. Millimeter waves were generated during the first step of the beam current (25 A) at a voltage of 60 kV for the Cherenkov maser and at a voltage of 100 kV for the BWO, as a consequence of these electrons having the energy required to satisfy their respective beam-wave resonance conditions.

IV. CONCLUSIONS

In summary, a three-gap pseudospark-sourced electron beam was studied to determine its beam quality as well as its propagation. Electron beams of up to 680 A were measured at the anode from the three-gap pseudospark discharge. It was found that the electron beam brightness could be as high as 10^{12} A m^{-2} rad^{-2}. About 10% of the beam propagated a distance of up to 20 cm without a magnetic guiding field. The research resulted in a pseudospark-produced electron beam that has the highest simultaneous electron beam current density (10 kA cm^{-2}) and brightness (10^{11} to 10^{12} A m^{-2} rad^{-2}) when compared to all other sources. Theoretical modeling and experimental investigation of the propagation of a pseudospark electron beam in the background gas environment was carried out. Comparison between numerical models and pseudospark-sourced electron beam experiments with no external applied guide magnetic field resulted in a better understanding of the beam formation and transportation dynamics. As predicted in Ref. 12, the results here are consistent with the initial high-energy electrons generated by the pseudospark discharge ionizing the background gas to form a plasma channel and the electron beam subsequently generated by the pseudospark discharge then propagating along the plasma channel.

The unique electron beam pulses generated by a pseudospark discharge were used to generate coherent, millimeter wave radiation above 21 GHz from a Cherenkov maser and 67 GHz from a BWO millimeter wave radiation has been measured from both the Cherenkov maser and the BWO. A pseudospark discharge is a very promising electron beam source for use in the generation of high frequency terahertz radiation. As the frequency increases it becomes increasingly difficult (if not impossible) using conventional cathodes to focus and form high current density, high quality electron beams through the small interaction region of a terahertz maser. We plan to scale down in size the pseudospark discharge chamber to generate submillimeter diameter electron beam pulses of current density 1 kA/cm^2, which can be propagated through the beam-wave interaction region of a high frequency (200 GHz) reflex klystron and a BWO (390 GHz) and to investigate the scaling of these radiation sources to the terahertz frequency range.

ACKNOWLEDGMENTS

The authors would like to thank the Engineering and Physical Sciences Research Council (EPSRC) for supporting this work and the UK High Power Radio Frequency Faraday Partnership for supplying the simulation package.

[1] J. Christiansen and C. Schultheiss, Z. Phys. **A290**, 35 (1979).
[2] M. A. Gunderson and G. Schaefer, "Physics and Applications of Pseudosparks," *NATO ASI Ser. B* (Plenum, New York, 1990).
[3] K. Frank and J. Christiansen, IEEE Trans. Plasma Sci. **17**, 748 (1989).
[4] H. Yin, G. R. M. Robb, W. He, A. D. R. Phelps, A. W. Cross, and K. Ronald, Phys. Plasmas **7**, 5195 (2000).
[5] A. W. Cross, H. Yin, W. He, K. Ronald, A. D. R. Phelps, and L. C. Pitchford, J. Phys. D **40**, 1953 (2007).
[6] H. Yin, A. W. Cross, W. He, A. D. R. Phelps, and K. Ronald, in *Pseudospark Physics and Applications*, special issue of IEEE Trans. Plasma Sci. **32**, 233 (2004).
[7] K. K. Jain, E. Boggasch, M. Reiser, and M. J. Rhee, Phys. Fluids B **2**, 2488 (1990).
[8] E. Dewald, K. Frank, D. Hoffmann, R. Stark, M. Ganciu, B. Mandache, M. Nistor, A. Pointu, and I. Popescu, IEEE Trans. Plasma Sci. **25**, 272 (1997).
[9] H. Yin, W. He, A. W. Cross, A. D. R. Phelps, and K. Ronald, J. Appl. Phys. **90**, 3212 (2001).
[10] K. Ramaswamy, W. W. Destler, and J. Rodgers, J. Appl. Phys. **83**, 3514 (1998).
[11] M. C. Myers, J. A. Antoniades, R. A. Meger, D. P. Murphy, and R. F. Fernsler, J. Appl. Phys. **78**, 3580 (1995).

[12]H. Yin, A. W. Cross, A. D. R. Phelps, D. Zhu, W. He, and K. Ronald, J. Appl. Phys. **91**, 5419 (2002).
[13]G. J. Caporaso and D. L. Birx, IEEE Trans. Nucl. Sci. **32**, 2608 (1985).
[14]G. P. Gupta and V. K. Rohatgi, J. Appl. Phys. **64**, 6626 (1988).
[15]M. A. Mostrom, D. Mitrovich, and D. R. Welch, Phys. Plasmas **3**, 3469 (1996).
[16]P. W. Werner, E. Schamiloglu, J. R. Smith, K. W. Struve, and R. J. Lipinski, Phys. Rev. Lett. **73**, 2986 (1994).

- Accepted for publication, 7th Triennial Special Issue of the IEEE Transactions on Plasma Science: Images in Plasma Science (August 2014)

Visualization of a Pseudospark-Sourced Electron Beam

D. Bowes, H. Yin, W. He, K. Ronald, A.D.R. Phelps, D. Chen, P. Zhang, X. Chen, D.Li, A.W. Cross

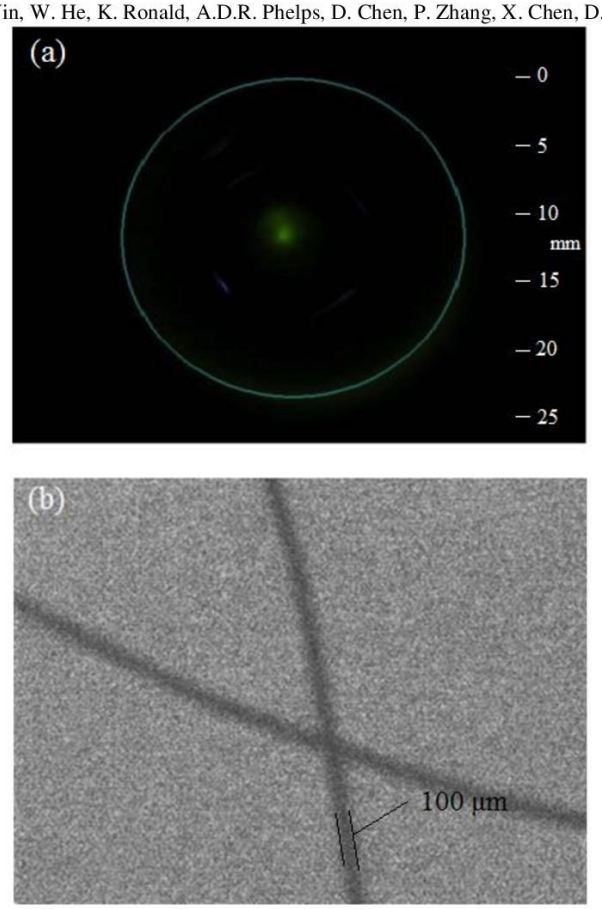

Fig. 1.(a) Cross-sectional image of 3 mm-diameter pseudospark electron beam captured by means of a scintillator, and (b) image captured via the use of an X-ray photodetector.

Manuscript received 1 November 2013; revised 1 February 2014.
D. Bowes, H. Yin, W. He, A.W. Cross, K. Ronald, and A.D.R. Phelps are with Department of Physics, SUPA, University of Strathclyde, Glasgow G4 0NG, UK
D. Chen and P. Zhang are with Computed Tomography Lab, School of Mathematical Sciences, Capital Normal University, Beijing 100048, China
X. Chen and D. Li are with Department of Electronic Engineering, Queen Mary University of London, London E1 4NS, UK
Work was supported by the Engineering and Physical Sciences Research Council (EPSRC)
Publisher Identifier S XXXX-XXXXXXX-X

Abstract – A pseudospark (PS)-sourced electron beam of 3 mm diameter has been experimentally investigated. Emission of X-rays was detected during a PS discharge and clear X-ray images were formed using the PS-sourced electron beam impacting on a 0.1 mm-thick molybdenum target at an applied voltage of 46 kV. Using a phosphor-coated scintillator, the beam's cross-sectional profile and surrounding ion channel were also observed. These results confirm the presence of an electron beam.

The pseudospark discharge is a relatively new class of gas discharge, having only been discovered in the late 1970's. It is a self-sustained, transient, low pressure (typically 6.5 - 65 Pa) gas discharge in a hollow cathode / planar anode configuration, whose behavior varies with geometry and external circuit configuration. Additionally, an electron beam which requires no guiding magnetic field due to the presence of an ion channel is formed during the breakdown process [1-2]. Pseudospark discharges have gained considerable attention during the last 30 years particularly with regard to their breakdown characteristics and the underlying plasma physics responsible for high current emission and potential applications in various fields. In addition, they have been shown to act as a source of soft X-rays by means of X-ray fluorescence [3].

A four-gap, PS discharge structure with anode and cathode apertures of 3 mm diameter was constructed. The hollow cathode cavity was made of stainless steel, with a length of 50 mm and inner diameter of 50 mm. These dimensions were based on the requirements of the hollow cathode effect [4]. An external energy storage capacitor of 428 pF was across the cathode and anode in the discharging circuit while a mechanical rotary pump evacuated the experimental system from the anode end through a vacuum valve. The working gas (argon) entered the chamber through a fine-controlled needle valve at the anode side, with pressure measured at the anode via a Baratron-type pressure gauge. The experimental setup and diagnostics are similar to reference [5].

A cross-sectional image of a pseudospark-sourced, axially symmetric electron beam (Fig. 1 (a)) was captured via the use of a long-exposure digital camera together with a scintillator disc consisting of 1 µm-thick copper foil coated in a fine layer of phosphorous powder and situated in a drift tube downstream of the PS anode. The image shows an image captured from a 3 ± 0.3 mm-diameter PS electron beam where the central beam spot can clearly be seen, along with a surrounding 'halo', circled in figure 1 (a). This ring of light forms as plasma electrons, generated from the ionization of background gas by the beam front, are expelled towards the edge of the drift tube by subsequent beam electrons so that an ion channel is formed for further beam propagation. The presence of this ring in the captured image shows that both the electron beam and the ion channel are present during pseudospark beam propagation.

While this is one method of indicating the presence of an electron beam, another is to detect the presence of X-rays from electron impact on a suitable target. To this end, the scintillator was removed and a 0.1 mm-thick molybdenum target was placed immediately after the PS anode. The molybdenum target was also serving as a witness plate for the PS electron beam. An X-ray photodetector was located 52 mm from the anode with a micro-sized object made of two crossed metal wires of 100 µm in diameter attached as a test object for X-ray imaging.

The pseudospark was configured for operation in a free-running, as opposed to triggered, mode. Critical breakdown pressure was noted from the previous experiment and maintained by adjusting the needle valve while pumping before voltage was applied and increased until breakdown occurred and kept on for repetitive breakdowns. In this way, the X-ray detector was able to continue to acquire the image data instantaneously one shot after another with a repetition rate of 1 Hz. By adjusting the gas pressure, X-ray images at a different discharge voltage, i.e., at different beam energy, were recorded.

Mean X-ray photon energies were calculated to be in the region of 19.8 keV. The integration time of the charge-coupled device (CCD) detector was selected to be 800 ms, with obtained images being captured from a single discharge pulse. X-ray images of the crossed metal wires were recorded at voltages between 22 and 46 kV with the clearest image (Fig. 1 (b)) obtained at an applied voltage of 46 kV, corresponding to the production of a 300A, 34kV PS-beam. The reduced clarity of the obtained images at lower voltages effectively set a threshold voltage for the effective capture of X-ray images from PS-sourced beams. In this way, the presence of the electron beam and its suitability as a small-spot X-ray imaging source were confirmed.

REFERENCES

[1] H. Yin, A.W. Cross, A.D.R. Phelps, D. Zhu, W. He and K. Ronald,"Propagation and post-acceleration of a pseudospark-sourced electron beam", J. Appl. Phys. 91 5419-5422 (2002)

[2] H. Yin, A.W. Cross, W. He, A.D.R. Phelps and K. Ronald, "Pseudospark Experiments: Cherenkov Interaction and Electron beam Post-acceleration", 2nd Special Edition of the IEEE Transactions on Plasma Science on Pseudospark Physics and Applications, PS-32, pp233-239, 2004.

[3] C.S. Wong, H.J. Woo and S.L. Yap, "A low energy pulsed X-ray source based on the pseudospark electron beam", Laser Part. Beams 25 497-502 (2007)

[4] M.A. Gunderson and G. Schaefer,"Physics and applications of pseudosparks", NATO Advanced Study Institute, Series B: Physics 219 Plenum (1990)

[5] H. Yin, A.W. Cross, W. He, A.D.R. Phelps, K. Ronald, D. Bowes, and C.W. Robertson, "Millimeter wave generation from a pseudospark-sourced electron beam", Phys. Plasmas, 16, 063105, 2009.